

Burning Behavior of Fuel on Water Under the Influence of Waves.

by

Nathaniel G. Sauer

A Dissertation

Submitted to the Faculty

of the

WORCESTER POLYTECHNIC INSTITUTE

in Partial Fulfillment of the Requirements for the

Degree of Doctor of Philosophy

in

Fire Protection Engineering
May 2023

Approved:

Ali S. Rangwala, Professor, Department of Fire Protection Engineering, WPI, Advisor

Morris Flynn, Professor, Department of Mechanical Engineering, UAlberta

Jose Torero, Professor & Head of Civil, Environmental & Geomatic Engineering, UCL

Leonard Zabilansky, Principal Engineer, National Oil Spill Response Research & Renewable Energy Test Facility

Albert Simeoni, Professor & Department Head, Fire Protection Engineering, WPI

I would like to dedicate this work to my family, especially to my parents, Deborah and Jeffrey. Your endless love and support are the foundation upon which this work was made possible. You sparked my ambition for science and engineering, and you helped nurture my curiosity however tiring it may have been. I love you both dearly and owe you more than I can ever repay.

Acknowledgement

I would first like to sincerely thank my advisor, Professor Ali S. Rangwala. Your passion for research is admirable, and your guidance and knowledge are invaluable tools for us as growing researchers. I feel a sense of great pride that I was able to spend my time as a PhD student in the combustion lab, working with great people and under a great mentor.

I would also like to thank the members of my committee Prof. Morris Flynn, Prof. Jose Torero, Leonard Zabilansky, and Prof. Albert Simeoni. All of whom have provided invaluable guidance and feedback as my PhD has matured.

I worked with many great researchers in my time at WPI, all of whom have contributed in some form or another to the development of my PhD. Dr. Sharanya Nair in particular helped conduct many experiments and guided much of the mathematical modeling throughout. I would also like to particularly thank Mahesh Kottalgi and Hsin-Hsiu Ho who both provided me with camaraderie and lent a hand during many an experiment, I wish you both success in your future endeavors. I would also like to thank my other colleagues: Veronica, Li, Rayna, Gio, Suhas, Chuming, Kemal, and Pi. As well I would like to thank the undergraduate members who contributed especially large portions to this work, going above and beyond the standards for undergraduate research, Julia, Adam, Dennis, and Camden.

Finally, I would also like to thank other members of the Dept. of Fire Protection Engineering at WPI. Ray and Fritz who allowed us to build a functioning wavetank in their lab, I am grateful. As well as the other members of the FPE department who all helped contribute in more ways than can be named: Juan, Suryansh, Muthu, Abhinandan, Reza, Jon, and of course Diane.

I cannot express the gratitude I feel that I was able to spend my graduate time surrounded by such outstanding people, thank you all.

Abstract

BURNING BEHAVIOR OF FUEL ON WATER UNDER THE INFLUENCE OF WAVES.

As the world's energy production continues to rely on fossil fuels, environmental spills will pose a significant hazard to marine and shoreline ecosystems. A quick and effective response to ocean oil spills is critical to minimizing the subsequent environmental damage. In-situ burning (ISB) is a method of cleanup and containment of this spilled fuel by collecting and burning the fuel in-place on the ocean surface. ISB is particularly well regarded for its speed, effectiveness, and low cost, and as such has become the focus of much research. Limited research has been completed on the impact of waves on hydrocarbon pool burning. This study attempts to investigate the influence of surface water waves on the burning characteristics of hydrocarbon fuels floating on water at three distinct scales. For each scale, a separate wavetank was used, two of which were specifically designed and constructed for this work.

The primary guideline for informing in-situ burning operations is the Beaufort scale, which correlates wind speed with wave height (Fig. 1). A common threshold for in-situ burning is a Beaufort sea state of 3 or less for conducting in-situ burn operations. However, this is only in reference to boom performance and ability to collect and ignite the oil and makes no reference to potential burn performance [1], [2]. Using typical ocean wave distributions for corresponding wavelengths and periods such as from Trujillo & Thurman [3], the corresponding approximate wave steepness for each Beaufort sea state is calculated (Fig. 1). The primary goal of this study is to quantify the potential effect on burning that each sea state could produce. Wave steepness is the dimensionless parameter that will be used throughout this work, and is defined as wave height divided by wavelength, presented in Eqn. 2. It is hypothesized that two factors are most greatly affecting the heat loss induced by the wave: the distance of water motion across the bottom of the fuel, and the frequency of this water motion. For linear water waves of regular period and wavelength and with a known water depth; the wavelength λ is traditionally calculated with a form of the dispersion equation (Eqn. 1). Where the wavelength is an iterative solution depending only on the period t_p and the

tank depth z [4], [5].

$$\lambda = \frac{gt_p^2}{2\pi} \tanh \frac{2\pi z}{\lambda_{old}}, \quad (1)$$

In this way the wave steepness (Eqn. 2) captures both the distance and frequency of the wave motions. The distance of the motion is captured in the wave height, which for deep water waves the horizontal motions are approximately equal to the vertical motions. Additionally, the frequency of oscillations is captured in the wavelength, as the wavelength is a function of the wave period as shown in Eqn. 1.

$$S = \frac{H}{\lambda}. \quad (2)$$

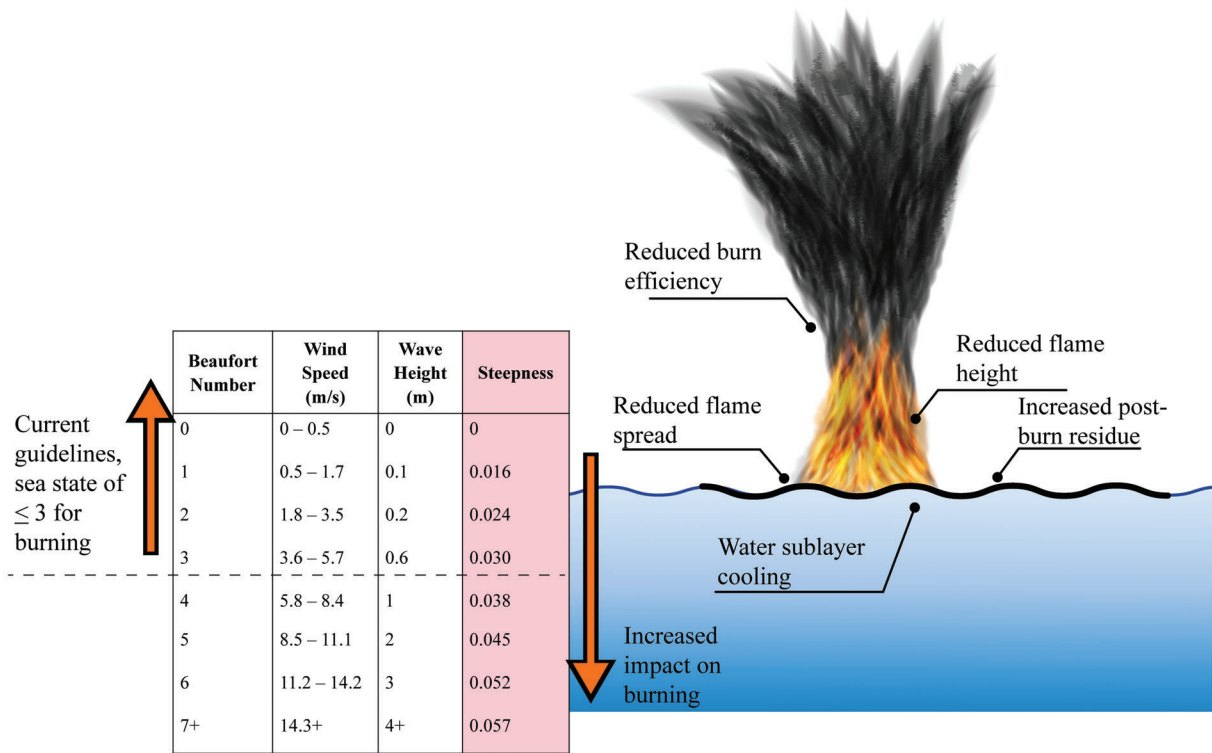


Figure 1: Wave interaction with in-situ burn overview and basic scope.

This work experimentally examines the interaction of waves with burning pools at three distinct sizes: 10 cm, 80 cm, and 2 m. Three wave tanks were used to investigate the burning of floating hydrocarbon fuels. Two of these wave tanks were custom-built at Worcester Polytechnic Institute

for this study. The third and largest tank used in this study is located at the US Army Cold Regions Research Facility in Hanover, NH. Current data is available for kerosene fuel at 10 cm and 80 cm, and crude oil at 2 m.

Small-scale experiments were conducted in a wavetank 2.4 m long, 0.24 m wide, and 0.28 m tall and filled with fresh water. A custom-made Arduino-based wavemaker generated wave profiles based on the height and period of the experimenters' choosing. Thin layers (0.6 cm) of kerosene were burned at a 10 cm diameter, and examined against 9 different wave profiles, with wave steepness (S) ranging from ($S = 0.003 - 0.080$). The no wave cases experienced a burn rate on average of approximately 0.5 mm/min, with the worst-case wave burning at approximately 0.35 mm/min a decrease of 30%. A study on subsurface water velocities and wave motion displacement was also conducted in the small-scale wavetank, using Particle Image Velocimetry (PIV) and particle tracking.

Medium-scale experiments were conducted in a modular wavetank built exclusively for examining the burning rate of a fuel floating on water. This wavetank was 3.66 m (12 ft) long, 1.83 m (6 ft) wide, and 0.91 m (3 ft) tall, and filled with freshwater to a static depth of 0.61 m (2 ft). Waves generated in this tank had a more than 0.86 R^2 agreement with their ideal sinusoidal profiles. Kerosene pools 80 cm in diameter were examined at 1, 2, and 3 cm thicknesses and with 4 different wave profiles with steepness (S) ranging from ($S = 0.008 - 0.0174$). At this scale, fuel layer thickness was maintained at steady state using a pump and flowmeter. Surface heat flux was also measured and a burning model incorporating the measured regression rate and heat flux allowed for the calculation of heat loss to the water sublayer. Flame heights and centerline heat flux experienced reductions with increasing wave steepness. Experimentally determined regression rates were also observed to decrease with increasing waves. The regression rate for 1 cm thick fuel layers was reduced by a maximum of 27%, for 2 cm layers a maximum of 19%, and for 3 cm layers a maximum of 12%. The calculated heat loss to the water sublayer also increased with increasing wave steepness.

Large-scale experiments were conducted at the U.S. Army Cold Regions Research Facility in Hanover, NH. The above-ground wavetank used measured 13.7 m long, 2.4 m wide, and 2.25 m tall and during testing was filled with 30 parts per thousand saltwater. Crude oil in 8 cm thick layers was examined

for a baseline and two wave cases, with wave steepness (S) values of ($S = 0.008$ & $S = 0.009$). The burn area for these experiments was a 1.9 m x 1.7 m pool with an approximated equivalent diameter of 2.03 m. Thermocouple data from these experiments was used to evaluate the rate at which a hot thermal wave progressed through the burning fuel layer. Flame heights and global burn rates were observed to decrease with increasing wave steepness. Calculated thermal penetration rates were also seen to decrease with increasing wave steepness.

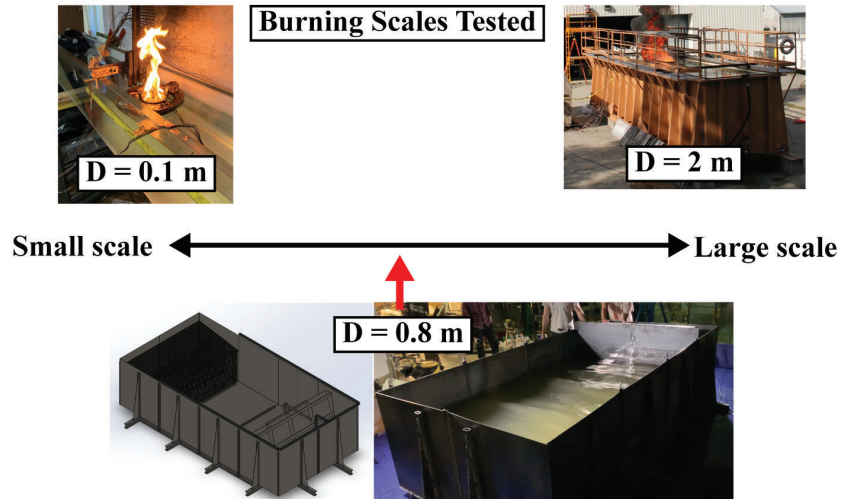


Figure 2: Images and summary of the burning scales examined in this work.

Burning rate models for each scale are presented and are based primarily on experimentally captured temperature data. Results across the three scales show a decrease in fuel temperatures, a decrease in flame height, and a decrease in burning rate with the addition of waves. Burning rate models show good agreement between calculated and experimentally determined values, especially for the medium scale where fuel layer thickness was maintained, and regression rate was measured. Thicker fuels tend to experience less of a reduction in burning behavior with waves. Changes in boilover occurrence and behavior were also observed with the addition of waves. Although it is hard to determine the precise impact of waves at ISB scales, this study presents reasonable ranges for sea-state equivalent waves.

TABLE OF CONTENTS

Acknowledgement	iii
Abstract	iv
Table of Contents	viii
List of Tables	xii
List of Figures	xiii
Nomenclature	xix
CHAPTER 1 : Introduction & Background	1
1.1 Literature Review	1
1.1.1 In-Situ Burning (ISB)	1
1.1.2 Burning on Water	2
1.1.3 ISB History	4
1.1.4 Oil Slicks and Waves	5
1.1.5 Burning and Waves	5
1.1.6 Wavetank Construction	7
1.1.7 Measurement of Wave Velocity	7
1.2 Research Objectives	9
CHAPTER 2 : Transient Burning Behavior of an Oil Slick with Waves ($D = 0.1$ m)	11
2.1 Introduction	11
2.2 Experimental Apparatus	11
2.3 Wave Generation	13
2.4 Results	16
2.4.1 Visual Timeline	16

2.4.2	Average Burn Time	18
2.4.3	Liquid temperature history	18
2.5	Interface Temperature Model	20
2.6	Conclusions	29
CHAPTER 3 : Transient and Steady State Burning Behavior of an Oil Slick with		
 Waves (D = 0.8 m)		30
3.1	Introduction	30
3.2	Experimental Apparatus	30
3.3	Results - Dynamic Fuel Layer Thickness	40
3.3.1	Time to Boilover & Boilover Duration	41
3.3.2	Global Regression Rate	44
3.3.3	Interface Temperature Model	46
3.4	Results - Constant Fuel Layer Thickness	51
3.4.1	Flowmeter Regression Rate	51
3.4.2	Flame Height and Flame Heat Flux	52
3.4.3	Temperatures	59
3.5	Burning Rate Formulation	63
3.6	Conclusions	74
CHAPTER 4 : Burning Behavior of an Oil Slick with Waves (D = 2 m)		76
4.1	Introduction	76
4.2	Experimental Apparatus	76
4.3	Results	82
4.3.1	Flame Height & Smoke Color Intensity	82
4.3.2	Temperatures	84
4.3.3	Thermal Penetration Rate	86
4.4	Burning Rate Formulation	87
4.5	Conclusions	90

CHAPTER 5 : Conclusions	92
5.1 Summary	92
5.2 Future Works	96
Bibliography	99
APPENDIX A : Wave Turbulence	106
A.1 Purpose	106
A.2 Experimental Setup	107
A.2.1 Wavetank and Pan	107
A.2.2 Wave Tank Preparation	108
A.2.3 Particle Image Velocimetry	109
A.2.4 Particle Tracking	112
A.2.5 Heat Transfer Coefficient	113
A.3 Experimental Matrix/ Waves Examined	114
A.4 Results	115
A.4.1 Wave Motion without Pan	115
Circular Paths	115
Elliptical Paths	117
A.4.2 Wave Motion with Pan	119
A.4.3 Experimental Heat Transfer Coefficient	123
A.4.4 Vortices Induced at Pan Edge	128
A.5 Conclusions	129
APPENDIX B : Evaporation Study	130
B.1 Experimental Apparatus	130
B.2 Results & Analysis	133
B.3 Conclusions	142
APPENDIX C : Experimental Equipment/ Codes	143

C.1	Wave Turbulence	143
C.1.1	PIV Particle Count Code	143
C.1.2	PIV Frames and Laser Visualization Code	143
C.2	Small Scale	146
C.2.1	Overview	146
C.2.2	Flume Construction	146
C.2.3	Wave Generator Design and Construction	147
	Basic Operation	149
	Operation Checklist	149
C.2.4	Small Wavemaker Arduino Code	151
C.2.5	Wavetank Construction Photos	164
C.3	Medium Scale	167
C.3.1	Wave Generator Design Graphs	167
C.3.2	Wavetank Assembly and Operation Checklists	168
C.3.3	Additional Data	171
C.3.4	Flowmeter Arduino Code	173
C.3.5	Flame Height MATLAB Code	180
C.3.6	Wavetank Construction Photos	182
C.4	Large Scale	187
C.4.1	Data Separation Matlab Code	187
C.4.2	Data Averaging in Excel	188
C.4.3	Thermal Penetration Rate in Excel	189

LIST OF TABLES

TABLE 2.1	Small scale wave profiles tested.	16
TABLE 2.2	Small scale average burn times.	18
TABLE 2.3	Surface Absorption Models from other works, adapted from Hristov 2001 [82].	23
TABLE 3.1	Medium scale wave profiles tested.	39
TABLE 3.2	Comparison of burn parameters and results between small and medium scales.	41
TABLE 3.3	Heat flux vs. normalized position for 1 cm thickness tests. Values obtained from steady-state regions of experiments and averaged over repeat cases.	57
TABLE 4.1	Large Scale Wave Profiles Tested.	81
TABLE 4.2	Regression rates and flame heights of 3 experiments, flame heights are averages of data taken from 5 – 15 minutes post ignition.	84
TABLE A.1	Waves examined in the PIV section.	114
TABLE B.1	Evaporation study wave profiles.	133

LIST OF FIGURES

FIGURE 1.1	(a) Regression rate and flame height data for liquid pool fires compared to fire diameter, adapted from Blinkov & Khudyakov 1961, and Hottel 1959 [12], [13] (b) data from Modak and Iqbal [14], [15], adapted from Quintiere [16]	3
FIGURE 1.2	<i>Left</i> , purely progressive (0% reflection) waves, white reflective particles photographed over one wave period. <i>Right</i> , wave paths of a short wavelength wave remain mostly circular, wave paths of long wavelength waves are mostly elliptical.	8
FIGURE 2.1	(a) Side view sketch of cross-section of fuel pan and floating ring, (b) Top view of fuel pan and floating ring, (c) Sketch of the experimental set-up.	12
FIGURE 2.2	Top, side view of wavetank without waves showing wave generator and wave absorbing beach. Wave absorbing rubberized horsehair mat was used both on the beach and behind the wave paddle to suppress disruptive reflections. . .	13
FIGURE 2.3	Image of the burn pan and floating ring during the experiment.	13
FIGURE 2.4	Visual timelines for three different wave profiles: (a) no-wave, (b) wave 2, (c) wave 9.	17
FIGURE 2.5	Temperature vs. depth plot showing both no-wave and worst-case wave (wave 9, steepness 0.08). Standard deviation for these temperature measurements ranged 2 – 12°C across the three repeats.	19
FIGURE 2.6	Experimentally determined heat transfer coefficient (HTC) from Sec. A.4.3 vs. wave steepness.	24
FIGURE 2.7	Comparison of interface temperature, (T_δ) over the duration of the burn. Shown for the no-wave case and three different steepness waves.	27
FIGURE 2.8	(a) Experimental and wave-model heat transfer coefficients as a function of wave steepness. (b) Agreement between burn model heat transfer coefficient and experimentally determined heat transfer coefficient.	28
FIGURE 3.1	Schematic of wavetank used for testing.	32
FIGURE 3.2	(a) Side view of wavetank during testing. (b) Looking towards the wave generation paddle during a burn test with waves. (c) Empty wave flume before installing wave generation mechanism, wave paddle, and wave absorbing section. (d) Wave generation mechanism attached to the paddle pushing arm. . .	33
FIGURE 3.3	<i>Top</i> , top-down schematic of the fuel containment pan used in the experiments. <i>Bottom</i> , side view of fuel pan showing radial positions of thermocouples and heat flux gauges.	34
FIGURE 3.4	(a) Thermocouple arrays used for measuring gas, fuel, and water temperatures. (b) View from underwater camera showing measurement lines used for maintaining fuel thickness, the bottom of kerosene layer is differentiable from water and partially marked with a red dashed line. (c) Floating burn ring in the wavetank, fuel filling apparatus visible below the water surface. (d) Fuel filling ring during construction.	35
FIGURE 3.5	Position of the fuel layer relative to the pan wall for the three thickness cases examined in this section: 1 cm, 2 cm & 3 cm.	36

FIGURE 3.6	Ideal vs. measured heat flux for the two heat flux gauges used during burn experiments.	38
FIGURE 3.7	(a) Ideal wave profile shown with measured wave profile in experimental apparatus ($S = 0.008$) (b) Ideal wave heights vs. their corresponding measured wave heights.	39
FIGURE 3.8	Timelines of the dynamic burn experiments with 2 cm fuel layers of kerosene. Blue portions show burning and red portions show boilover.	41
FIGURE 3.9	Time to boilover vs. wave steepness. Burns took longer to reach boilover with increasing steepness waves.	43
FIGURE 3.10	Boilover duration plotted vs. wave steepness for dynamic fuel layer experiments.	44
FIGURE 3.11	Global regression rate calculated from Eqn. 3.7 plotted vs. wave steepness S for both the medium and small scales. Showing a decrease in global regression rates with waves steepness.	45
FIGURE 3.12	In-depth temperature profiles for the dynamic fuel layer thickness case without wave and with $S = 0.009$ wave, data from 5 & 7 minutes post-ignition. Gray region shows the initial fuel thickness of 2 cm.	46
FIGURE 3.13	Comparison of interface temperature (T_δ) over the duration of the burn for the medium scale dynamic fuel layers. Shown for the no-wave case and three different steepness waves.	49
FIGURE 3.14	(a) Heat transfer coefficients calculated from the dynamic fuel thickness experiments examined, black dots show the linear fit values obtained from Sec. A.4.3. (b) Agreement between burn model heat transfer coefficient and experimentally determined heat transfer coefficient.	50
FIGURE 3.15	Experimental regression rate from flowmeter data vs. wave steepness for the 3 thicknesses. 1 cm thickness case as blue crosses, 2 cm as green dots, and 3 cm as red diamonds.	52
FIGURE 3.16	Flame height vs. time for the no wave case (squares), and two waves from this study: $S = 0.009$ (circles) and $S = 0.017$ (triangles), data from 1 cm thickness cases. Shaded regions show 90% confidence intervals of the flame oscillations.	54
FIGURE 3.17	<i>Left</i> No wave, <i>middle</i> moderate wave ($S = 0.009$), and <i>right</i> worst-case wave ($S = 0.017$), displaying different flame behavior with and without the waves, different flame shapes being indicators of the different heat feedback distributions across the radius of the pool. Images taken every 30 seconds during burn, boilover excluded.	55
FIGURE 3.18	Heat flux vs. normalized position for 1 cm thickness tests. Values are obtained from steady-state regions of experiments and averaged over repeat cases.	56
FIGURE 3.19	Heat flux vs. normalized position for 2 cm thickness tests. Values are obtained from steady-state regions of experiments and averaged over repeat cases.	57
FIGURE 3.20	Heat flux vs. radial position for the no wave case compared to similar fires where data is available in literature.	58
FIGURE 3.21	Temperature vs. time for the 2 cm thickness no wave case, showing regions of fuel heating, and steady-state burning. A clear period of fuel layer thinning is visible after fuel feeding is shut off.	60

FIGURE 3.22	Temperature vs. depth for baseline and highest steepness wave case at 1 cm fuel thickness. Wave case demonstrates overall lower temperatures in the fuel layer, with nearly identical surface temperatures. Temperature data taken from a 1-minute average at 4-minutes post ignition.	61
FIGURE 3.23	Temperature vs. depth for baseline and highest steepness wave case at 2 cm fuel thickness.	62
FIGURE 3.24	Temperature vs. depth for baseline and highest steepness wave case at 3 cm fuel thickness.	63
FIGURE 3.25	Diagram of energy balance under consideration. \dot{Q}_s is the heat input, \dot{Q}_{sens} is the heat used to raise the temperature of the replenished fuel from ambient to T_B , and $\dot{Q}_{loss,water}$ is the heat lost from the fuel to the water sublayer.	64
FIGURE 3.26	1 cm fuel thickness fuel-water interface temperatures. Lines calculated from model, points obtained from experimental thermocouple data.	67
FIGURE 3.27	2 cm fuel thickness fuel-water interface temperatures. Lines calculated from model, points obtained from experimental thermocouple data.	68
FIGURE 3.28	3 cm fuel thickness fuel-water interface temperatures. Lines calculated from model, points obtained from experimental thermocouple data.	69
FIGURE 3.29	(a) Heat transfer coefficients calculated from each fuel thickness examined in this section, black dots show the linear fit values obtained from Sec. A.4.3. (b) Agreement between burn model heat transfer coefficient and experimentally determined heat transfer coefficient.	70
FIGURE 3.30	Experimentally measured \dot{Q}_s in red, and $\dot{Q}_{loss,water}$ in blue. Increasing thickness demonstrated both an increase in heat return to the fuel layer, and a decrease in heat loss. Calculated regression rates are black-and-white crosses on the secondary y-axis. Bars are grouped by wave steepness, and shaded by fuel thickness.	72
FIGURE 3.31	Calculated vs. experimental regression rates show relatively good agreement between the two values, with a tendency for the energy balance to over predict the regression rate.	73
FIGURE 3.32	Schematic of altered flame and burn behavior with the addition of waves. <i>Left</i> , no wave case demonstrating a more gravity-driven plume. <i>Right</i> , wave case demonstrating a shorter flame and lower burn rate.	74
FIGURE 4.1	Overview of the wave tank used for these burn experiments at the U.S. Army Cold Regions Research and Engineering Laboratory facility.	77
FIGURE 4.2	Schematic showing dimensions of the CRREL wave tank used in this study.	77
FIGURE 4.3	Top-down view of wavetank site during a burn, showing linear distances to key locations.	78
FIGURE 4.4	View of fully prepared testing location before experiments, showing fuel containment boom and other testing apparatus.	78
FIGURE 4.5	<i>Left</i> , grid-style FRs inside of the containment boom in the wave tank. <i>Right</i> , schematic of grid FR showing major dimensions.	79
FIGURE 4.6	Primary instrumentation for these experiments was the thermocouples. <i>Left</i> , TC locations in the burning pool, one center and one edge location. <i>Right</i> , thermocouple tree showing the number and spacing of TCs.	80

FIGURE 4.7	Water surface location vs. time showing one of the waves tested. The non-linear profile is due to reflections inside the burn area from the heavy oil containment boom.	81
FIGURE 4.8	Images from the first 20 minutes of burning, for the no-wave case <i>top</i> and wave 2 case <i>bottom</i>	83
FIGURE 4.9	<i>Left</i> , flame height vs. time for the grid Flame Refluxer with no wave and with the wave showing the decrease in flame height with the presence of the wave, indicating a decrease in burn performance with the wave. <i>Right</i> , flame height averages from 5 – 15 minutes during the burn experiment, error bars display standard deviation in the dataset.	83
FIGURE 4.10	Temperature vs. depth plot for the grid without waves (white) and with waves (green and black). Without waves show a progressive temperature development throughout the experiment. Cases with waves show a much steadier linear temperature gradient through the depth of the fuel over the experiment. . . .	85
FIGURE 4.11	<i>Left</i> , temperature vs. time plot for a burn experiment, regions outlined in red indicate thermal penetration events of interest. <i>Right</i> , thermocouple diagram showing descending thermal front heating TCs at different times.	86
FIGURE 4.12	<i>Left</i> , depth from surface vs. time from ignition for the grid with no wave, points are plotted for the time at which the thermocouple at that depth rises above 120°C. The slope of this line is the thermal penetration rate in mm/min. <i>Right</i> , thermal penetration rates for the grid FR at stagnant water, wave 1, and wave 2. Demonstrating a clear decrease in thermal penetration rate with increasing wave steepness.	87
FIGURE 4.13	Interface temperature T_δ over time, point represent experimentally measured data, lines represent model best-fit interface temperatures from Eqn. 4.3 . . .	89
FIGURE 4.14	(a) Experimental and wave-model heat transfer coefficients vs. wave steepness. (b) Agreement between burn model heat transfer coefficient and experimentally determined heat transfer coefficient.	90
FIGURE 5.1	Normalized regression rate for the 3 different scales vs. wave steepness. . . .	93
FIGURE 5.2	Heat transfer coefficient (HTC) vs. wave steepness. Heat transfer coefficient is the calculated value from each phase. Dashed line is from linear fit to sphere experiments data from Sec. A.4.3.	94
FIGURE 5.3	Heat transfer coefficient determined from burning models and from sphere experiments data.	95
FIGURE 5.4	(a)Regression rate determined from medium scale burning model with discrete h values calculated for each case (triangles) and regression rates determined from the sphere linear fit approximation (blue squares). (b) Regression rates from the medium scale, x-axis calculated from linear fit to sphere experimental HTC data, y-axis calculated from burning model HTC as presented in Ch. 3.5.	96
FIGURE 5.5	Various wave profiles defined by differing wave theory, compared with the linear sinusoidal wave examined in this work.	97
FIGURE 5.6	(a) Irregular water surface location measured during Hurricane Andwer, in contrast to the regular sinusoidal wave profiles examined in this study. (b) Distribution of ocean wave heights observed during Hurricane Andrew 1992. Data from both plots adapted from Judge 2019 [94].	98

FIGURE A.1	Sketch of wavetank showing planes of interest and approximate size and location of the footprint of the floating ring for burn experiments denoting the measurement region of interest.	106
FIGURE A.2	Image of the pan with the laser sheet at the edge, used for capturing information about vortices generated due to the pan lip.	107
FIGURE A.3	Image of the pan with the laser sheet at the edge, used for capturing information about vortices generated due to the pan lip.	108
FIGURE A.4	Polished surfaces on the bottom of the wavetank where the laser enters from the bottom.	109
FIGURE A.5	Laser sheet optics used in PIV investigation.	110
FIGURE A.6	Image of PIV setup in use in small wavetank, laser and optics configuration visible at the bottom, laser sheet visible center.	112
FIGURE A.7	<i>Clockwise from top-right</i> , sphere suspended from TC wire as configured during experiments, hot-plate and beaker used for hot-water bath, 2017 aluminum sphere with thermocouple wire protruding.	114
FIGURE A.8	Images taken with (shutter speed = $1 \cdot t_p$), paths are traced by PIV particles. Wave shown all have a period of 0.4s and mostly circular paths.	116
FIGURE A.9	Calculated wave path radius vs. Depth from surface for the $t_p = 0.4$ s wave. . .	117
FIGURE A.10	(a) Component radius vs. depth from surface for $t_p = 1$ s and $t_p = 2$ s waves, crosses signify measurements from images. Solid lines generated from Eqn. A.7, dashed lines generated from Eqn. A.8. (b) Ratio of major component to minor component ($\frac{major}{minor}$) of ellipse plotted vs. depth from surface, showing a flattening ellipse with depth towards bottom.	118
FIGURE A.11	Images taken with (shutter speed = $1 \cdot t_p$), paths are traced by PIV particles and measured using a pixel scaling then compared to calculated values.	119
FIGURE A.12	Horizontal (u) velocity component inside of the pan vs. time for $t_p = 1$ s, $H = 1$ cm wave from Table A.1.	120
FIGURE A.13	Horizontal (u) velocity component inside of the pan vs. time for $t_p = 2$ s, $H = 1$ cm wave from Table A.1.	121
FIGURE A.14	Horizontal (u) velocity component inside of the pan vs. time for $t_p = 0.4$ s, $H = 0.3$ cm wave from Table A.1.	121
FIGURE A.15	(a) Wave theory horizontal displacement vs. PIV measured horizontal displacement inside of the floating pan. (b) Ratio of measured displacement to calculated displacement vs. wave steepness.	123
FIGURE A.16	Experimental and calculated temperature vs. time curves for the convective cooling of the aluminum sphere. Calculated curve obtained from Eqn. A.20. .	125
FIGURE A.17	Experimentally determined heat transfer coefficient (HTC) from sphere experiments versus wave steepness. Showing an increase in heat transfer coefficient with increasing wave steepness.	126
FIGURE A.18	Experimentally determined heat transfer coefficient (HTC) from the sphere experiment with different conditions. Pan indicates with the pan in place, measured in the center. 1/2 indicates measuring across the width of the tank, 1/2 from the edge of the tank to the center. 3/4 indicates a measurement 3/4 of the distance from the center to the wall of the wavetank.	127

FIGURE A.19	PIV images taken next to pan wall, colormap shows vortex intensity. Period 0.4 s and 2 s wave are shown, with images taken at time intervals of fractions of the total wave period. Shows vortex generation and decay on the edge of the pan with a frequency equal to the wave period.	128
FIGURE B.1	Dimensioned wavetank schematic of the wavetank used for these experiments.	130
FIGURE B.2	(a) Side view of 5.08 cm diameter evaporation plastic ring (b) Top view of small evaporation ring.	131
FIGURE B.3	Wind speed measurements taken inside of the wavetank measured in m/s with a rotating vane anemometer. Initial layout of 5 evaporation locations is shown in red with final chosen location shown in light blue. Dashed line denotes an 80cm circle.	132
FIGURE B.4	(a) Raw video footage obtained from FLIR showing the uncentered fuel ring units show degrees Celsius (b) Cropped and stabilized video footage showing just the center of the fuel ring and the cold n-Pentane undergoing evaporation.	134
FIGURE B.5	Mean RGB level plotted vs. frame number for a no wave case.	135
FIGURE B.6	Regression rate vs. steepness for the evaporation of n-Pentane with waves. . .	136
FIGURE B.7	Model parameters and boundary conditions	137
FIGURE B.8	Calculated surface temperature vs. wave steepness. Surface temperature is predicted to rise with increasing wave steepness.	140
FIGURE B.9	(a) Convective heat transfer coefficient vs. wave steepness, triangles calculated in this section. (b) Convective heat transfer coefficient (HTC) values calculated in this section plotted vs. HTC from the sphere experiments Sec. A.4.3	141
FIGURE C.1	The flow of data from the user input to the output signals to the motor. . . .	147
FIGURE C.2	Variables used when calculating stroke length.	148
FIGURE C.3	(a) Stepper motor controller hardware, (b) Stepper motor and gear configuration, (c) Wide view of stepper motor and wave paddle.	149
FIGURE C.4	VFD controller frequency vs. gearbox output in revolution per second.	167
FIGURE C.5	Controller frequency vs. output wave period.	167
FIGURE C.6	In-depth fuel temperature profile information taken during the wave case in the medium scale, showing temperature fluctuations with the wave.	172
FIGURE C.7	In-depth fuel temperature data taken with the wave, now with the 1-minute moving average applied.	172
FIGURE C.8	Sheet and formula for generating ‘timecodes’ for averaging.	189
FIGURE C.9	Calculation of time window on the averaged data sheet.	189
FIGURE C.10	Calculation of the averaged data point.	189
FIGURE C.11	Excel formula for determining if a thermocouple has passed a threshold temperature or not, for this case this threshold is 120°C	190
FIGURE C.12	Excel formula used for determining the first time at which the thermocouple crosses the threshold temperature.	191
FIGURE C.13	Thermal penetration analysis, increasing time to threshold temperature with increasing TC depth.	191

NOMENCLATURE

This list describes symbols that will later be used within the body of the document.

Standard

A	Area, or Amplitude
C_p	Specific heat
D	Diameter
g	Gravitational acceleration
H	Wave height
h	Convective heat transfer coefficient
k	Thermal conductivity
L	Latent heat of vaporization, or length
l	Boundary layer thickness
MW	Molecular weight
r	Radius
R_u	Ideal gas constant
S	Wave steepness
St	Stokes value
T	Temperature
t	time
t_p	Wave period
v	Regression rate
v_p	Thermal penetration rate
X	Mole fraction
Y	Mass fraction
y	Depth
\dot{m}	Mass loss per unit time
\dot{m}''	Mass loss per unit area per unit time
\dot{Q}	Heat transfer
\dot{q}''	Heat transfer per unit area

\bar{t}	Average of times
\bar{y}	Average of depths
Δh_{fg}	Enthalpy of formation of gas
Le	Lewis number
Re	Reynolds number

Greek Alphabet

α	Thermal diffusivity
χ	Heat feedback fraction
γ	Kinematic viscosity
λ	Wavelength
\mathcal{D}_{AB}	Binary diffusivity of species pair
ν	Dynamic viscosity
ω	Angular velocity
ρ	Density
τ_f	Flow timescale
τ_p	Particle response time

Common Subscripts

+	Above surface
–	Below surface
∞	Ambient
<i>air</i>	ambient air
<i>B</i>	Boiling point
<i>burn</i>	Burn, usually area
<i>F</i>	Fuel
<i>g</i>	Gas
<i>HRR</i>	ambient air
<i>int</i>	Interface
<i>l</i>	Liquid
<i>p</i>	Particle

r, rad Radiation
 s Surface
 w Water
 $w - F$ Water to fuel interface

CHAPTER 1

Introduction & Background

1.1 Literature Review

This literature review will attempt to provide context to the various disciplines in this work, beginning with environmental fuel spills and their cleanup and containment methods. It will then focus examining on in-situ burning, the primary mode examined in this work. Following this, it will focus on examining the body of work focusing on burning fuels on a water sublayer, all of which are stagnant water sublayers. The literature review will then examine research pertaining to oil slicks interacting with waves without burning, and then oil slicks and waves with burning. The literature review will continue with the research examined as part of designing the wavetanks required for this study. Finally, concluding with some research reviewed which laid the groundwork for PIV and particle tracking in wavetanks, a method also used in this study.

1.1.1 In-Situ Burning (ISB)

Environmental oil spills are an incredibly costly and dangerous consequence of modern energy. As the world continues to rely heavily on these hydrocarbon-based fossil fuels, industrial accidents that put sensitive ocean ecosystems at extreme risk will continue to occur. Although accidental oil spills have been reducing in frequency and size, their impact remains devastating on the affected environments [6]. The harm caused by the 2010 Deepwater Horizon (DWH) spill, for example, is still being observed and studied in marine and coastal ecosystems years after its occurrence [7]. Unusually high mortality rates in bottlenose dolphins were observed at the time of DWH and higher rates of unusual diseases were observed in these dolphins as well [8]. Since dolphins are a critically important keystone species, a collapse in their population can have severe negative effects on their local marine ecosystems.

In-situ burns are a frequently used method of environmental fuel spill cleanup and containment. In-situ burning operations accounted for the removal of approximately 5% of the 4.9 million barrels of oil spilled during the Deepwater Horizon spill [9]. This equated to roughly 245,000 barrels of

oil removed from the environment. Concern about the efficacy and safety of ISBs is always at the forefront of these large, smokey, and photogenic burns [10], [11]. The nature of ISBs means that they take place on the ocean surface, which almost always has wave action present. However, very little research has been conducted into how these waves impact ISBs. Waves have been observed to negatively impact burning, and guidelines for in-situ burning mention the sea state as a critical consideration for if or when an ISB can be conducted [2]. However very little is understood about how waves change the burning dynamics of a fuel floating on water.

1.1.2 Burning on Water

Much research has been conducted in the field of liquid pool fire burning. One of the most cited works still today, by Blinov and Khudyakov 1961 and summarized by Hottel 1959, was one of the first works to study the regression rates of various fuels extensively (gasoline, kerosene, diesel, and solar oil) [12], [13]. Blinov and Khudyakov also examined burning liquids in tanks, extinction of burning liquids, flash temperature, and surface flame spread among other topics. Blinov and Khudyakov solidified the idea of maximum burn rates for various fuel types as a function of burning pool diameter, a concept that is key in this investigation. The transition between laminar and turbulent flow regimes is shown to be accompanied by a plateau in the maximum regression rate for all fuels tested at diameters greater than 1 m (Fig. 1.1a). Similarly Modak and Croce 1977 as well as Iqbal and Quintiere (2016) contributed to the understanding that incident flame heat flux is also a function of burning pool diameter. Finding that the larger diameter of a burning pool, the more radiation dominant the incident flame heat flux becomes (Fig. 1.1a) [14], [15].

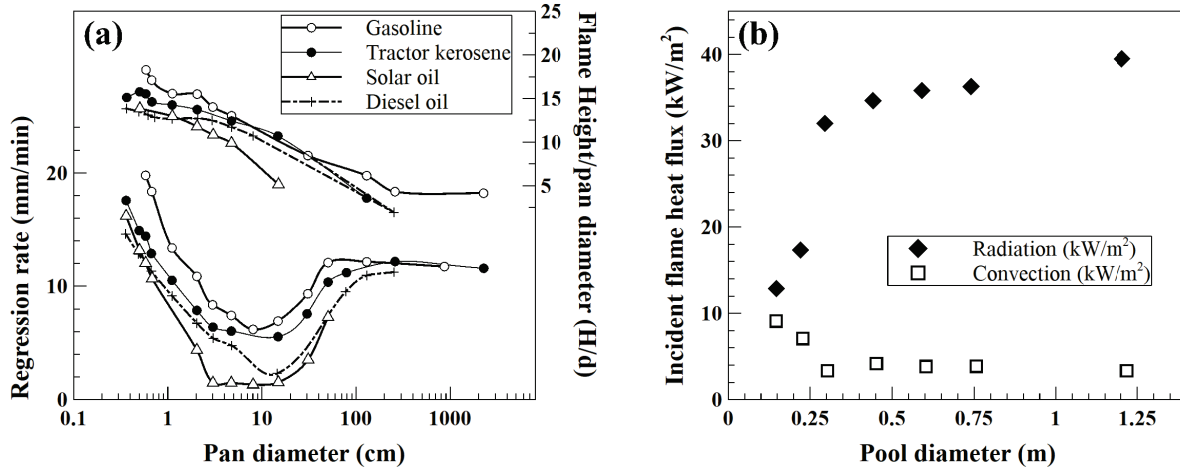


Figure 1.1: (a) Regression rate and flame height data for liquid pool fires compared to fire diameter, adapted from Blinkov & Khudyakov 1961, and Hottel 1959 [12], [13] (b) data from Modak and Iqbal [14], [15], adapted from Quintiere [16]

One of the first studies of a burning fuel floating on water also introduced an early thermal model for the scenario. The simple 1-dimensional model of a thin layer of fuel floating on water, developed in Twardus and Bruztowski 1982, was later extended to include radiation absorption and tilting wind effects on the burning pool [17]. Later in 1983, Petty published results from a series of large-scale (2 m) test burns of crude oil floating on water, showing that burning of crude oil could potentially be used to clean up spilled fuel [18]. Following this study, Arai et al. 1990 examined simple and multicomponent fuel mixtures, investigating the impact of a boiling water sublayer on a burning pool. Arai et al. demonstrated that for at least relatively small pools (4.8 – 20.3 cm), boilover would cause a significant decrease in flame height and mass burning rate, while larger pools showed opposite results [19]. Garo et al. 1994 studied the impact of pan diameter and initial fuel thickness on burning rate, time to boilover, and liquid temperature history, discovering that a water sublayer does have a significant impact on burning and that surface temperatures and fuel-water interface temperatures also see slight variations across experiments [20]. Further studies have examined the effect of fuel thickness and fuel boiling point on time to boilover of a burning fuel floating on water [21]–[24]. Laboureur et al. 2013 for example, investigated the influence of pan diameters, water and fuel thicknesses, lip heights, and pan materials on a burning layer of 30% oil 70% diesel mix

floating on water [24]. Garo et al. 1999 showed again that simple thermal models could predict in-depth liquid temperature histories with “reasonable agreement” [23]. Torero et al. 2003 examined existing simple surface absorption heat conduction models of a liquid fuel burning on water. Results in this study showed that only a very small portion of the heat released by combustion returns to the fuel layer ($\sim 1\%$) [25]. Ajay Walavalkar’s 2001 PhD thesis examined the combustion of various fuels and states of fuels floating on water. Examined fuels included diesel, diesel-water emulsions, crude, crude-water emulsions, and weathered crude and crude emulsions. Walavalkar found that increasing water contents reduced burn rate, burn duration, oil residue, and burn efficiency; whereas weathering decreased burn rate and burn efficiency, but also increased total burn time and oil residue remaining [26]. Laurens van Gelderen’s 2017 PhD thesis also examined in-situ burning of crude oil floating on water, focusing on the effects of initial thickness, vaporization order, weathering state, burning area, and the impact of the water on the burning crude oil slick. The initial fuel layer thickness and weathered state were noted to be of importance for the ignitability of the fuel layer, and once ignited, most independent variables studied had limited effects on the burning efficiency at the operational scale [27]. Recent work by Chen et al. in 2023 reviewed pool fire research and models, and acknowledged other studies which have examined the influence of a water sublayer. However, made no measurements or mention of a water-sublayer other than quiescent [28]. Chang 2022 examined the burning behavior of a thin oil slick burning on a turbulent water sublayer, finding that increasing turbulence intensity corresponded to an increased heat transfer rate at the fuel-water interface. This study also measured a maximum mass loss rate reduction of about 34% from the baseline with the highest turbulence condition [29].

1.1.3 ISB History

The framework for in-situ burning began to develop in the early 1970’s, as researchers started investigating the use of combustion as a method for cleanup of spilled fuels [30]–[32]. While combustion science was investigating the influence of a water sublayer on liquid fuel burning, oil spill research was simultaneously investigating the use of in-situ burning as a method for oil spill cleanup. Labelle et al. 1993 was one of the first works to formally consider in-situ burning for mitigation of an offshore environmental spill, in this case off the Tampa Bay coast [33]. The following year a paper

by Lindstedt-Siva called for more experiment-based research in the field of oil spills and specifically in-situ burning [34]. Buist et al. 1998 summarized requirements for ignition as well as outlined flame temperatures, slick thicknesses, burn rates, flame spread, and other factors associated with successful in-situ burns [35].

1.1.4 Oil Slicks and Waves

Researchers have also investigated the interaction of oil slicks with waves, with an emphasis on the breakup and emulsion of oils in ocean conditions [36]–[40]. For example, Belore 2002 conducted a series of experiments in a wave tank to examine the effectiveness of dispersants on Hibernia crude oil under cold water wavy conditions [40]. Additional studies have examined in-situ burning in coastal marshes [41], [42] and for inland freshwater regions [43]. The reach of in-situ burning studies is broad, and yet the amount of research conducted on the influence of waves on open water in-situ burns is scarce.

1.1.5 Burning and Waves

In one of the first studies to examine the impact of waves on burning, Bech et al. 1993 conducted a series of small and mesoscale tests to study how ice, waves, and wind affect in-situ burning. The study found that the presence of waves in some cases reduced burn efficiency and, in other cases, made emulsions impossible to ignite [44]. McCourt et al. 1998 conducted laboratory-scale experiments with six crude oils to determine ignition limits, the likelihood of sinkage, and wave action on the combustion of emulsified slicks. Burn tests with waves were conducted with a 40 cm floating burn ring and with two distinct wave profiles tested. In many cases, adding waves caused a decrease in burn rate and burn efficiency; however, it was not uncommon in their results to see one of the wave profiles increase the burn rate or burn efficiency [45]. During this same time, Buist and McCourt would publish and contribute numerous works to the field of in-situ burning and particularly in-situ burning interacting with waves. One study published by Buist and McCourt in 1998 examined the interaction at a larger scale (1.7 m diameter) and with accompanying larger waves. Results were not as conclusive but noted an observable increase in post-burn residues with increasing wave steepness, and a slight decline in oil removal efficiency with increasing waves, in

agreement with their earlier small-scale results [46]. Another study authored by Buist in 1998 tested ‘mid-scale’ 1.7 m diameter ANS and Milne Pt. crude oils with waves, finding that increasing wave steepness reduced burn rate and burn efficiencies [35]. Again, in another study about the same time, Buist et al. noted increased post-burn residues with increasing wave steepness, hypothesizing that their observed changes in burning behavior were related to an increase in heat transfer through the fuel slick with waves [47]. Another set of experiments by Buist et al. in 2003 aimed to investigate the limits of in-situ burning thin slicks in icy conditions. Waves were again introduced as an additional independent variable in this study. Again, it was found that waves overall negatively impacted the burns, reducing the oil removal rate to around 66% of the calm water removal rate [48]. In 2011 Buist noted that steeper and potentially cresting waves reduce burn efficiency but made no detailed measurements for the waves used [49]. Lin et al. 2005 recognized that waves may decrease burn efficiency and increase burn residues but made no measurements to substantiate the claim [41]. Brandvik et al. 2006 noted that waves during large-scale burns could prevent flame spread, either by reducing fuel thickness or by internal mixing of colder oil with hotter surface oil [50]. Aurell et al. 2021 examined emissions from crude oil burns with varying boom configurations and air injection nozzles with and without waves. Aurell found that waves reduce oil mass loss rate in all cases, providing that heat loss due to increased heat transfer between the water and oil is a likely explanation [51].

These studies examining the impact of waves on in-situ burns have primarily investigated the effect of waves on global burn rate, based on burn times and burn residues. While these metrics can be indicative of the performance of a liquid pool fire, they can also be deceptive. In-depth temperature data is needed to completely understand how a wave influences the burning of a liquid pool floating on water. None of these previously mentioned studies have captured the fuel and water temperatures of the burning pool. As well, no studies have evaluated the effect of a wave on burning by incorporating the change in water sublayer behavior into a burning model. This study examines global burn parameters such as burn residues, burn times, global regression rates, and flame heights, as well as temperature data, heat flux gauge data, and directly measured fuel regression rates. We also present a novel approach to collecting temperature data for a fuel layer on a non-static water

surface.

1.1.6 Wavetank Construction

The experimental platforms for this study are wavetanks of differing sizes. Each of the wavetanks used in this study are of generally the same form and function. The wave generator used in each tank is a ‘flapping’ style wave paddle. These types of wave paddles are hinged at the bottom and used to simulate deep-water wave motion [5], [52], [53]. Each wavetank makes use of a wave-absorbing beach to absorb wave energy and prevent wave reflection [54]. Each wavetank has a unique approach to this wave-absorbing beach, dictated by wavetank size and complexity. Two of the wavetanks used in this study were explicitly designed and constructed for these burning experiments. The primary objectives when designing each tank were to provide linear and repeatable wave conditions and to withstand a continued burning environment. App. C contains details of the construction of the two wavetanks built specifically for this study.

1.1.7 Measurement of Wave Velocity

Early in this study, it was hypothesized that the primary mode through which the waves were influencing a fuel burning on water was through increased water sublayer movement. This increased water sublayer movement, especially across the bottom of the fuel, would act to increase convective heat loss from the fuel to the water. Therefore it is important to understand how waves move water, especially the types of waves we would be generating and examining in this study.

For this study, regular and repeatable waves were determined to be more important than waves exactly matching an ocean surface condition. In this way, the different parameters of the wave could be separated, and test conditions could be easily repeated. Ocean waves are generated by the wind blowing over the water’s surface. Ocean conditions typically consist of a distribution of many different wave sizes, speeds, and directions simultaneously [55]. Linear waves are waves of small heights and of equal and regular wave periods and wavelengths, such that their motion can be approximated by linear and wave theory, and that any disturbances are so weak that they can be neglected in the equations for motion [56].

At any fixed position the oscillation of velocity components produced by a wave differs by 90° in their phase, where the horizontal lags behind the vertical component by 90° . These circular particle paths flatten to ellipses when approaching the tank bottom Fig. 1.2.

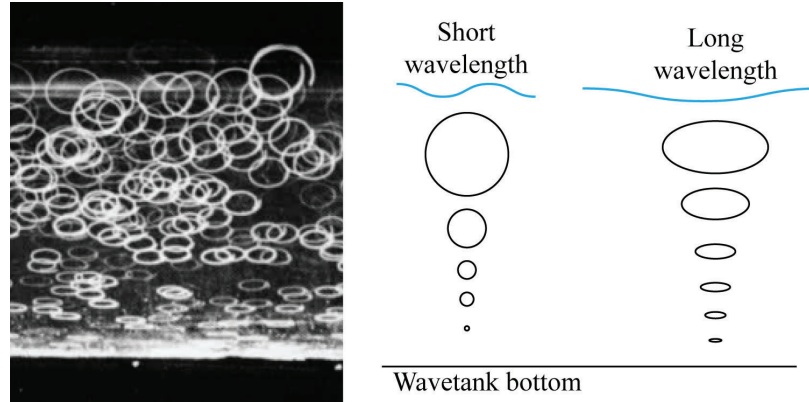


Figure 1.2: *Left*, purely progressive (0% reflection) waves, white reflective particles photographed over one wave period. *Right*, wave paths of a short wavelength wave remain mostly circular, wave paths of long wavelength waves are mostly elliptical.

These paths are assumed to be repeated and regular for the linear equations of wave motion. But as can be seen in Fig. 1.2, even carefully generated waves experience a small net velocity in the direction of wave propagation. Fig. 1.2 shows purely progressive (0% reflection waves) progressing from left to right with $z = 0.22\lambda$, showing the mostly circular particle path traced by white particles suspended in water and photographed over one wave period, from Wallet & Ruellen 1950 [57] adapted from Van Dyke 1982 [58]. This small progressive movement, captured in the difference in position over one wave period, is the Stokes drift. Stokes drift is the difference between the average Lagrangian flow velocity of the fluid parcel and the average Eulerian flow velocity of the fluid at a fixed position [59]–[61]. For this study neither the water velocity components nor Stokes velocity is necessarily of direct interest, the primary component of interest is the water velocity across the bottom of a floating object moving partially along with the waves. However, it is important to understand the velocity components which make up a normally oscillating water wave.

Particle image velocimetry has been conducted in wavetanks for numerous purposes. Powell et al. 1992 used particle image velocimetry to study wave velocities and the formation of beach profiles

due to wave impingement [62]. Other studies have examined deep water breaking waves [63], [64]. Chang and Liu 1998 used particle velocities to study the overturning jets in shallow water breaking waves [65]. Umeyama 2010 used particle image velocimetry (PIV) and particle tracking velocimetry (PTV) to measure velocity fields and distributions of surface waves with and without a current [66]. Jensen et al. 2004 used PIV to measure acceleration in irregular shallow water wave trains, to compare to Stokes theory [67]. Clamond et al. 2004 used PIV to measure velocity fields in irregular steep water waves, to better understand the loads on ships and offshore oil platforms [68]. PIV is used to study many factors in wavetanks, as it is relatively cheap and usually effective at obtaining an accurate measurement. App. A contains details of the PIV equipment used in this study, as well as results obtained from analyzing wave motion. App. C contains extra details of the experimental equipment and codes used in this study.

1.2 Research Objectives

The primary objective of this study is to further the understanding of how a water wave impacts the burning behavior of a floating fuel, with outcomes expected to inform conditions for in-situ burning operations. This research objective is to be obtained through the investigation and answering of four primary research questions:

1. *How does a water wave impact the evaporation of fuel on its surface?*
2. *How does a water wave impact the burning behavior of a floating fuel on its surface?*
3. *What are the controlling non-dimensional parameters that govern the wave characteristics for the heat transfer boundary condition at the fuel-water interface?*
4. *Does the impact of waves on burning scale with burn size?*

This study dedicates a chapter to examining the change in evaporation behavior with a non-stagnant water surface. This is accomplished with a novel method of measuring evaporation time using an infrared camera. This evaporation study was published in the Proceedings of the Arctic Marine Oil Spill Conference [69]. The small, medium, and large scale burning behavior with waves each have been examined in separate wavetanks and have been dedicated their own respective chapters in this work. The small scale was published in Marine Pollution Bulletin and constituted an undergraduate

students MQP report [70], [71]. The medium scale has been accepted pending revisions in Fire Technology and constituted a team of undergraduates' MQP project, and was also published in the Proceedings of the Eastern States of the Combustion Institute Spring Technical Meeting [72]–[74].

Each research question will also need to have an emphasis on the scale being examined. In-situ burn operations are conducted at very large scales, burning thousands of gallons of fuel in each burn. However, for a parametric study, this is unfeasible and impractical. For this study three discrete scales will be examined: small (78.5 cm² burn area), medium (0.5 m² burn area), and large (3.23 m² burn area). The small scale is the easiest and cheapest experiment to operate, with larger scales being progressively more intensive and thus representing less of the total data. The mechanism through which the waves impact burning is evaluated through temperature data at each scale, through heat flux data in the medium scale, and additionally will be measured in the small scale using particle image velocimetry and particle tracking velocimetry.

CHAPTER 2

Transient Burning Behavior of an Oil Slick with Waves ($D = 0.1 \text{ m}$)¹

2.1 Introduction

2.2 Experimental Apparatus

The experimental setup consisted of a 2.4 m long, 0.24 m wide, and 0.28 m tall wave tank filled with fresh water. Two Sony RX10 cameras accomplished video capture. Fig. 2.1a details a sketch of the tank and wave generator setup. The burning test area consisted of a central steel fuel containment ring 10 cm in diameter and 3.5 cm tall, connected to a Styrofoam ring which provided flotation. The Styrofoam ring was 5 cm wide and had an outer diameter of 20 cm. The burn size of 10 cm diameter was chosen partially because of wavetank size limitations, but also to constrain the burn and reduce fuel quantities necessary to conduct the number of anticipated experiments. Fig. 2.1b includes a sketch of the pan and floating ring. A thermocouple array consisting of 26 thermocouples was affixed to the inner stainless-steel burn ring and measured the temperature distribution vertically in the fuel and water layers. Thermocouples were constructed of 36 AWG Type K thermocouple wire with an approximate response time of 0.135 seconds and spaced 1.3 millimeters apart. Fig. 2.1 a, b, and c show detailed sketches of the wavetank and burning ring. Fig. 2.3 shows an image of the wavetank and burning ring during an experiment. Fuel for all experiments was 0.6 cm layers of kerosene. Kerosene for these experiments was assumed to have the following properties: boiling point range ($T_B = 175 - 325^\circ\text{C}$) with an assumed discrete value of (232°C) for this work, liquid specific heat ($C_{p,l} = 1.97 \text{ kJ/kg}\cdot\text{K}$) thermal diffusivity ($\alpha = 8.8 \times 10^{-8} \text{ m}^2/\text{s}$), and thermal conductivity ($k = 0.133\text{W/m}\cdot\text{K}$) [16], [75]. Density was measured at various points before experiments, and an average of $\rho_l = 0.765\text{g/cm}^3$ was calculated for the kerosene fuel. Three repeats of each experimental case were conducted, the averages of which are reported in the results.

Wave dimensions were measured with an Akamina AWP 24-3 wave gauge and an AWP 30 cm

¹Contents of Ch. 2 published in **Marine Pollution Bulletin** as: *A study of thin fuel slick combustion on wavy water* [70]. Also published as MQP Report: *A Study of Burning of a Thin Fuel Slick on Water with Waves* by Julia Cuendet [71].

wave probe head. Waves were measured both with and without the fuel containment ring in place, with no notable change in wave profile being observed with the ring in place. During experiments, the burning ring was placed centered in the tank, and about halfway down the length of the tank. During wave measurement, the wave probe and burning ring were placed in the same location as was used during burning.

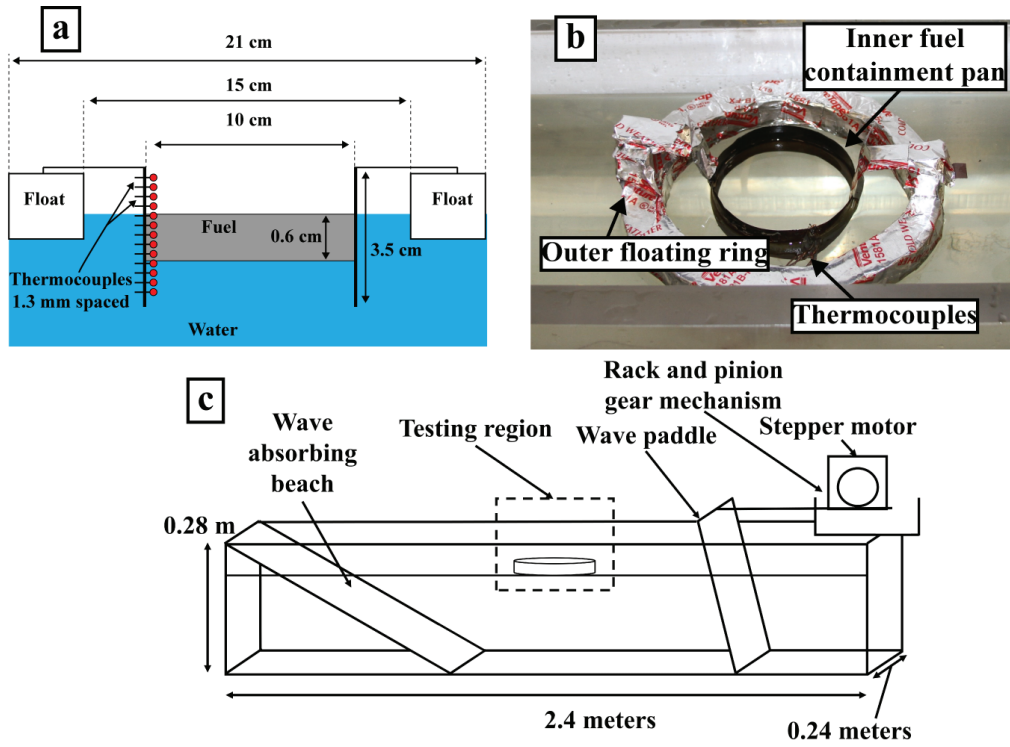


Figure 2.1: (a) Side view sketch of cross-section of fuel pan and floating ring, (b) Top view of fuel pan and floating ring, (c) Sketch of the experimental set-up.

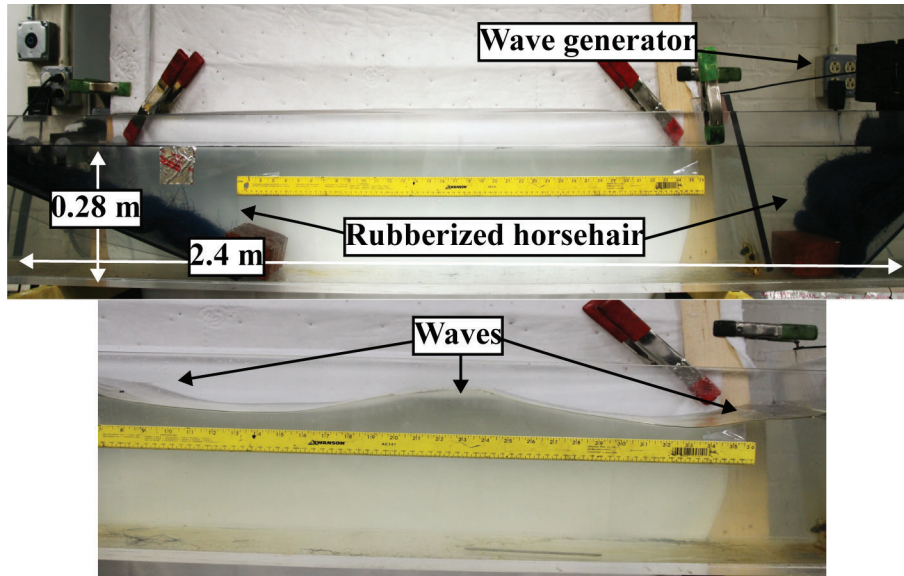


Figure 2.2: Top, side view of wavetank without waves showing wave generator and wave absorbing beach. Wave absorbing rubberized horsehair mat was used both on the beach and behind the wave paddle to suppress disruptive reflections.

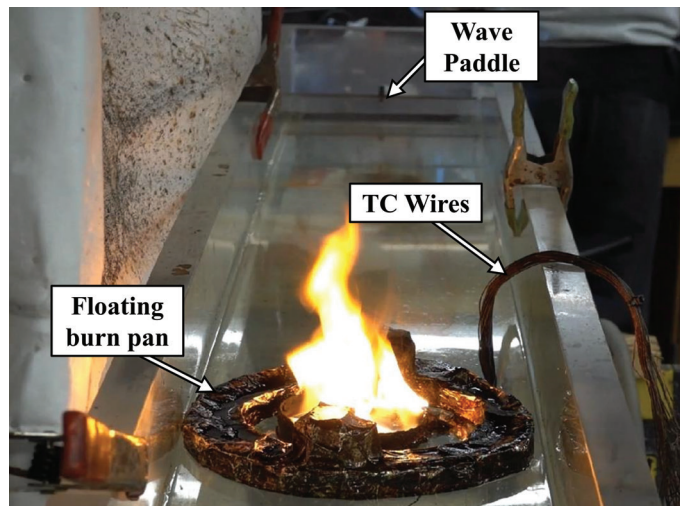


Figure 2.3: Image of the burn pan and floating ring during the experiment.

2.3 Wave Generation

Wave steepness is the primary dimensionless number used to evaluate wave aggressiveness in this study. Steepness is the wave height divided by the wavelength and represents the slope of the leading and trailing edges of the wave. The steepness is calculated using Eqn. 2.1, where S is wave

steepness, λ is wavelength (m), and H is wave height (m) [55]. Typically, the wave steepness is a parameter used to determine if a wave will break, traditionally a steepness value of 1/7 is the threshold for a wave breaking, however, this statement has been an area of continued examination [3], [76], [77].

$$S = \frac{H}{\lambda}, \quad (2.1)$$

The non-dimensional parameter *steepness* incorporates the length scales present in the wave: wave height H and wavelength λ , but also incorporates the wave timescale in the wave period, t_p . This is because for water waves, wavelength can be expressed as a function of the wave period t_p and tank depth z (Eqn. 2.2). Other parameters are the gravitational constant g , the solution for wavelength is obtained by iteration until error between λ_{old} and λ is minimized;

$$\lambda = \frac{gt_p^2}{2\pi} \tanh \frac{2\pi z}{\lambda_{old}}. \quad (2.2)$$

A critical consideration in the construction and design of the wave tank was the generation of the waves used in experiments. Ocean waves are generated by the wind blowing over the water’s surface, first creating small capillary waves, eventually growing into wind waves. It is also important to note that the ocean surface distributes many different wave sizes, speeds, and directions simultaneously [55]. A wave flume also called a linear wave tank, is designed to create discrete, uniform, and repeatable waves to aid in isolating variables during experiments.

For this study, the flapper-paddle style wave generator was chosen both for simulation of deep-water ocean waves and for simplicity of design and construction as compared to other types of wave generators [78]. Critical to wave generation is that the motion that creates the waves is sinusoidal. As the paddle approaches the ‘front’ or ‘back’ of the stroke, its velocity must decrease, and the paddle must have the highest velocity at the ‘midpoint’ of the stroke; its velocity must be sinusoidal over the stroke length. The simplest method to accomplish this is by driving the paddle with a camwheel attached to a motor. This method is simple but effective as the wheel naturally creates

sinusoidal motion for the pushing rod with its circular path. However, this method only allows the wave period to be set with the motor rpm and leaves very coarse control over the wave height by changing the paddle displacement.

For these experiments, complete control over the wave period as well as the wave height was desired. The ideal platform would allow the experimenter to input the wave period and height as desired. The wave generator would then output those waves into the tank for completing experiments. The positional generator built for these experiments consists of the power supply, motor, motor driver, Arduino board, and support platform. A 4 Nm Nema34 closed-loop stepper motor was used as well as a 2-phase hybrid HSS86 servo driver. This application is ideal for a stepper motor as the motor can be directed to move through its steps at a sinusoidal rate, thus emulating the camwheel but with far more control. Complete design description of this small scale wave generator can be found in App. C.2.3.

Waves generated agreed well with the wave height and period input into the program. The wave period was measured to a less than 1% error, and wave heights measured a 3 – 20% error. Errors in wave height were slightly higher in smaller waves (0.5 cm height), where the wave height approached the sensitivity limits of our wave gauge. Table 2.1 shows which waves were selected for the experimental matrix.

Table 2.1: Small scale wave profiles tested.

Wave	Wave Height H (m)	Period t_p (s)	Wavelength λ (m)	Steepness S	Visual (duration=1s)
1	0.003	1	1.18	0.003	
2	0.01	2	2.6	0.004	
3	0.02	2	2.6	0.008	
4	0.01	1	1.18	0.008	
5	0.003	0.4	0.25	0.012	
6	0.005	0.5	0.3882	0.013	
7	0.02	1	1.18	0.017	
8	0.01	0.4	0.25	0.04	
9	0.02	0.4	0.25	0.08	

2.4 Results

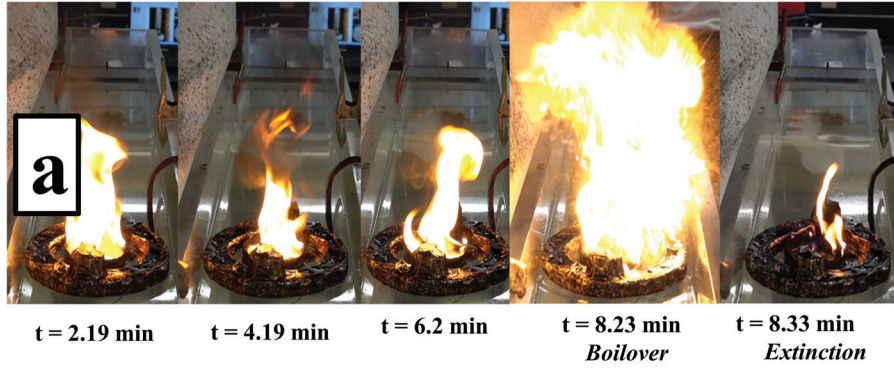
2.4.1 Visual Timeline

Fig. 2.4 shows three distinct burning behaviors observed in these experiments. The first timeline shows the no-wave case, along with its boilover. The second timeline shows wave 2 (Table 2.1), with a 1 cm tall wave with a period of 2 seconds. The third timeline shows wave 9 (Table 2.1), a 2 cm tall wave with a period of 0.4 seconds. These two waves represent “extreme” wave cases, both being tall waves with differing periods.

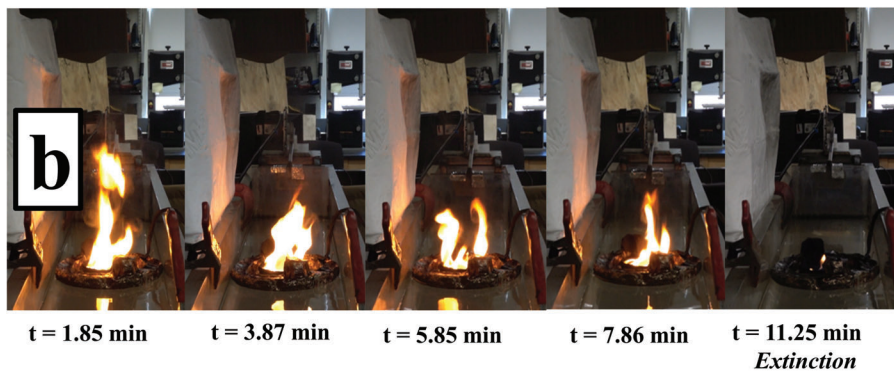
Burning cases with waves showed no boilover and visibly smaller flames (Fig. 2.4a). Between the two wave extremes not only does the case with a lower steepness (Fig. 2.4b) have a larger flame, but it also has a longer total burn time than both the no-wave and high steepness wave case. The flame of the high steepness wave case (Fig. 2.4c) also exhibits a ‘splitting’ behavior, where the flame hugs the side of the burn pan. The wave is moving and mixing the kerosene located in the center of the

pan, causing the flame to have a challenging time propagating in the center. This flame “splitting” behavior was only observed using the highest wave steepness in the experiments (wave 9).

Initial fuel thickness = 0.6 cm, No Wave



Initial fuel thickness = 0.6 cm, Wave 2, Steepness = 0.004



Initial fuel thickness = 0.6 cm, Wave 9, Steepness = 0.080



Figure 2.4: Visual timelines for three different wave profiles: (a) no-wave, (b) wave 2, (c) wave 9.

2.4.2 Average Burn Time

Average burn times tended to increase along with increasing wave steepness as shown in Table 2.2. For all waves except the 2 cm height and 0.4-second period wave (wave 9), the burn time is longer than the no-wave case. This is a combination of fuel ejection from boilover in the no-wave case and cooling action induced by the waves slowing regression rate in the wave cases. As well, the 2 cm height and 0.4-second period wave (wave 9) experienced a lower average burn time due to fuel being visibly carried away from the pan from the start of the experiment. This was the only wave profile where this behavior was observed. It should be noted that this wave has the highest steepness out of all wave profiles evaluated. This observation may also be connected to the flame-splitting behavior observed in the same experiments. If the kerosene is swept underneath the pan, it goes through a heating-cooling process, making it more difficult for the fuel in the center of the pan to retain heat and sustain the flame.

Table 2.2: Small scale average burn times.

Case	Period t_p (s)	Steepness (S)	Total burn time avg. (min)
No-Wave	-	-	8.5
1	1	0.003	9.03
2	2	0.004	10.15
3	2	0.008	10.96
4	1	0.008	10.65
5	0.4	0.012	8.96
6	0.5	0.013	8.93
7	1	0.017	10.73
8	0.4	0.04	10.64
9	0.4	0.08	12.69

2.4.3 Liquid temperature history

Fig. 2.5 shows the temperatures plotted against the depth relative to the fuel/water interface for a no-wave case and for wave 9, considered the worst-case wave as it had the highest steepness amongst all waves tested. When comparing these two cases, it can be observed that waves significantly

impact temperatures at the fuel-water interface. In the no-wave case, as time increases, so do temperatures. However, with the addition of waves, temperatures remain constant over time. The in-depth temperatures for the wave case also approach the ambient water temperature (18°C) at less overall depth than in the no-wave case. The no wave case temperatures are also approximately more linear through the fuel layer, where the wave case temperatures drop rapidly close to the fuel surface. The wave case temperatures also remain more constant than the no wave case, and temperatures actually measure slightly higher at 2.5 minutes than at 5 minutes.

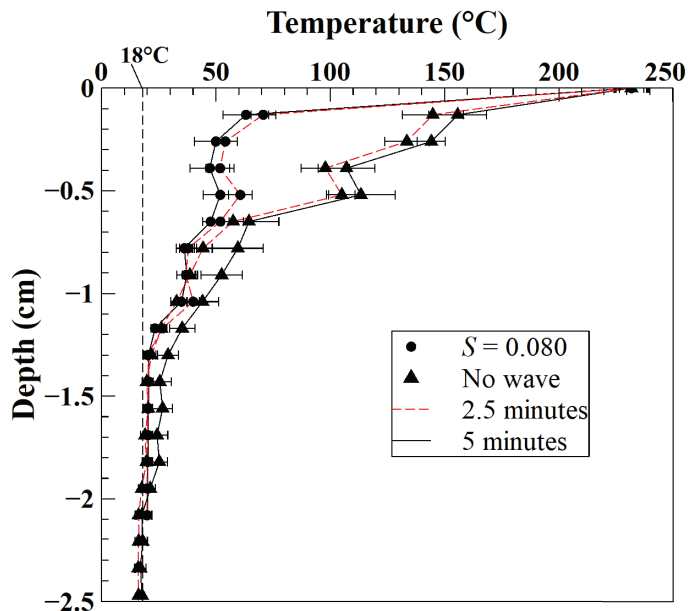


Figure 2.5: Temperature vs. depth plot showing both no-wave and worst-case wave (wave 9, steepness 0.08). Standard deviation for these temperature measurements ranged $2 - 12^\circ\text{C}$ across the three repeats.

For all cases, the surface thermocouple location is obtained by assuming the fuel surface is located where the temperature is close to $T_B = 232^\circ\text{C}$. In some cases, the fuel surface and fuel-water interface locations needed to be linearly interpolated when the surface was found to be between two thermocouple locations. The fuel-water interface temperature was of particular interest as this would be used in determining the increase in convection induced by the waves. For all cases, the fuel thickness over time was approximated by calculating the average global regression rate, as demonstrated in the burning rate model section.

2.5 Interface Temperature Model

Models have been developed previously which examine a burning fuel floating on water. The one-dimensional single-layer conduction models in Table 2.3 and developed by Blinov and Khudyakov, Wu et al., and Garo, rely on the assumption that the thermal diffusivity of the water is approximately equal to the thermal diffusivity of the fuel ($\alpha_w \approx \alpha_F$) [12], [20], [21], [23], [79]. These models also do not present a boundary condition term such that can be evaluated to account for the effect of the wave. The next portion examines some of these models developed to examine the burning of a fuel floating on water. The nomenclature for these models has been left in its original state, descriptions have been added in-text but the nomenclature may not agree with the nomenclature in the rest of this work.

The one-dimensional two-layer conduction model in Table 2.3, developed by Wu et al., Garo, and Torero, provides a more detailed solution by separating the distributions of the fuel and water layers [20], [23], [25], [79]. This model could be used to compare to our experimental data, changing the thermal diffusivity of the water α_w to match experimental regression rates and temperature profiles. This is an applicable approach but would provide no later comparison such as a convective heat transfer coefficient h value would. A calculated h value is desirable to compare to the heat transfer coefficient experiments completed in Sec. A.4.3.

In these models the fuel layer is assumed to have no internal convection, temperatures are assumed to be developed by conduction only. Models are left in their original terminology: vertical coordinate y , initial fuel layer thickness y_0 , location of fuel surface at time $y_s(t)$, thermal conductivity λ , and regression rate r among others. With radiation completely absorbed at the surface $y = y_s(t)$, with the energy balance at the fuel surface expressed as:

$$\dot{q}_s'' = H_v \rho_F r(t) + \dot{q}_c'' \tag{2.3}$$

Where H_v is the heat of vaporization, ρ_F the fuel density, and $r(t)$ the regression rate at time t .

The boundary condition at the free surface is defined as:

$$\dot{q}_c'' = -\lambda_F \frac{\partial T}{\partial y} \Big|_{y=y_s(t)}, \quad (2.4)$$

Where the surface regression rate is expressed as:

$$r(t) = \frac{\partial y_s(t)}{\partial t} = \frac{\dot{m}''}{\rho_F}. \quad (2.5)$$

The contact between the fuel and water sublayer assumes:

$$\dot{q}_c'' = -\lambda_F \frac{\partial T}{\partial y} \Big|_{fuel} = -\lambda_w \frac{\partial T}{\partial y} \Big|_{water}. \quad (2.6)$$

These models are all termed ‘surface absorption models’ as they consider the heat input at the fuel surface and its dictation of the temperature conditions and regression rate. These models also assume a Dirichlet boundary condition, where the surface is assumed to remain at constant temperature T_s ($T = T_s, y = y(t)$), while also not considering the energy balance at interface Eqn. 2.4 or a changing energy balance at the fuel-water interface. The downward propagation of the thermal wave is a portion of this problem with which great consideration has been applied. For thin slicks of fuels with high saturation temperatures, the Dirichlet boundary condition assumption holds well, as heat dissipation through the fuel and regression rate are of the same magnitude and given by $\frac{\alpha}{\delta_i}$. But for fuels of lower saturation temperature, the vaporization rate is much faster in comparison to the heat dissipation through the fuel layer. For experiments in this study, relatively high saturation temperature fuels were used in relatively thin slicks.

Torero and Wu have examined this progressing thermal wave problem with a different approach from the surface boundary condition. Including the regression rate in the calculation for when the fuel-water interface would experience heating from the propagating thermal wave (Eqn. 2.7).

$$t_c = \frac{y_0^2}{\alpha_F + y_0 r}, \quad (2.7)$$

This is accomplished by calculating an equivalent thermal diffusivity α_{EQ} through the two-layer system of fuel and water (Eqn. 2.7):

$$\alpha_{EQ} = \frac{ry_0}{\alpha_F}(\sqrt{\alpha_w} + \sqrt{\alpha_F})^2. \quad (2.8)$$

To approach a solution Garo 2007 considered the water and fuel layers discretely [80]:

$$\frac{\partial T_F}{\partial t} = \alpha_F \frac{\partial^2 T}{\partial y_F^2}, \quad (2.9)$$

$$\frac{\partial T_w}{\partial t} = \alpha_w \frac{\partial^2 T}{\partial y_w^2}. \quad (2.10)$$

Garo neglects radiation and provides a numerical solution based on a study by Ghoshdastidar and Mukhopadhyay 1989, which examined a transient heat transfer model developed for composite fin heat transfer and also obtained a numerical solution [81]. However, none of these studies have examined the fuel-water interface analytically. This study makes an attempt at incorporating the heat loss at the fuel-water interface in the model solution, through calculating a convection coefficient to match experimental interface temperatures.

Table 2.3: Surface Absorption Models from other works, adapted from Hristov 2001 [82].

MODEL	SOLUTION	Reference
<p>One-dimensional single layer conduction model</p> $\frac{\partial T}{\partial t} = \alpha_F \frac{\partial^2 T}{\partial t^2}$ <p>IC: $t = 0 \quad T = T_\infty$</p> <p>BC: $y = y_s(t) \quad T = T_s$ $y \rightarrow \infty \quad T = T_\infty$</p>	<p>Temperature distribution</p> $\frac{T - T_\infty}{T_s - T_\infty} = \exp \left[-\frac{r}{\alpha_F} (y - y_s(t)) \right]$ <p>Assumptions: $\alpha_F = \text{const.}$ $r(t) = r = \text{const.}$ $\alpha_F \approx \alpha_w$</p>	<p>Blinov and Khudyakov [12] Wu et al. [79]</p> <p>Garo et al. [20], [21] Garo and Vantelon [23]</p>
<p>One-dimensional single layer conduction model</p> $\frac{\partial T}{\partial t} = \alpha_F \frac{\partial^2 T}{\partial t^2}$ <p>IC: $t = 0 \quad T = T_\infty$</p> <p>BC: $y = y_s(t) \quad T = T_s$ $y \rightarrow \infty \quad T = T_\infty$</p>	<p>Temperature distribution</p> $\frac{T - T_\infty}{T_s - T_\infty} = \Theta = \exp - \left(\frac{y_0^2}{\alpha_F t_{b0}} \frac{y}{y_0} \right)$ <p>at $t_{B0} \ll t_b$ at small $(y_0^2 / \alpha_F t_b) \propto \Theta(l)$ $\Theta_{bw} = 1 - \exp(\tau_{B0}^2) \text{erfc}(\tau_{B0})$ $\tau_{B0} = \frac{(\lambda_F / \lambda_w)(\alpha t_{B0})^{1/2}}{y_0(1 - t_{B0} \cdot t_b)}$</p>	<p>Blinov and Khudyakov [12]</p> <p>Arai et al. [19]</p>
<p>One-dimensional two layer conduction model</p> $\frac{\partial T}{\partial t} = \alpha_F \frac{\partial^2 T}{\partial t^2} \quad \frac{\partial T}{\partial t} = \alpha_w \frac{\partial^2 T}{\partial t^2}$ <p>IC: $t = 0 \quad T = T_\infty$</p> <p>BC: $y = y_s(t) \quad T = T_s$ $y = 0, \quad -\lambda_F \frac{\partial T}{\partial y} \Big _{y=0-} = -\lambda_w \frac{\partial T}{\partial y} \Big _{y=0+}$ $y \rightarrow \infty \quad T = T_\infty$</p>	<p>Average regression rate (Garo et al., [20], [23].)</p> $r = \frac{1}{H_v \rho_F} \left[\chi \cdot \dot{q}'' - \frac{\alpha_F \lambda_F (T_s - T_\infty)}{y_0 (\sqrt{\alpha_F} + \sqrt{\alpha_w})^2} \right]$ <p>Assumptions: $\alpha_F = \text{const.}$ $r(t) = r = \text{const.}$ $\alpha_F \approx \alpha_w$ and $\alpha_{EQ} = \frac{r y_0}{\alpha_F} (\sqrt{\alpha_F} + \sqrt{\alpha_w})^2$</p>	<p>Wu et al. [79]</p> <p>Garo et al. [20], [21] Garo and Vantelon [23]</p> <p>Torero et al. [25]</p>

To examine how the burn characteristics may change over time, a model was developed to investigate an experimental heat transfer coefficient. This heat transfer coefficient was then compared to experimental values obtained from the lumped capacitance heat transfer experiments detailed in Sec. A.4.3. These heat transfer experiments consisted of assuming a lumped capacitance transient conduction heat transfer condition. Where the temperature of the solid, in this case a solid aluminum sphere, is assumed to be spatially uniform at any time. Thus the change in cooling rate is due only

to a change in the convection coefficient at the solid-liquid boundary of the sphere. For these experiments, the solid aluminum sphere was heated in boiling water, and immersed in the wavetank at various wave conditions. The internal temperature of the sphere was recorded, and an h -value was fit to the experimental curve. The resulting h vs. wave steepness plot is shown in Sec. A.17 and reproduced here in Fig. 2.6. The data labels on this plot are the ratio of elliptical components of the wave motion ($\frac{major}{minor}$), a value of 1 describes perfectly circular motion, with larger values equating to more ‘flat’ ellipse profiles.

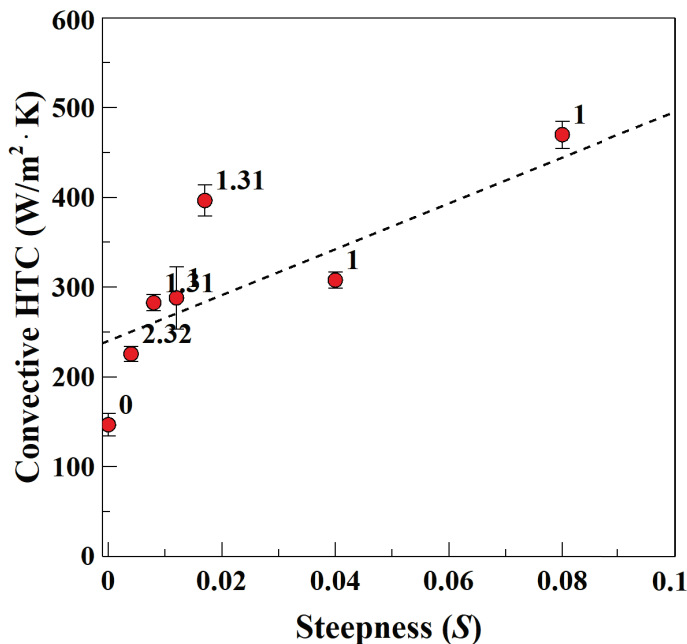


Figure 2.6: Experimentally determined heat transfer coefficient (HTC) from Sec. A.4.3 vs. wave steepness.

The 1D heat conduction equation is considered for the fuel layer Eqn. 2.11

$$\frac{\partial T}{\partial t} = \alpha \frac{\partial^2 T}{\partial y^2}, \quad (2.11)$$

In Eqn. 2.11 T is the temperature through fuel depth y , and α is the thermal diffusivity of the fuel. At the fuel surface ($y = 0$) we can assume a fuel temperature equal to the boiling point of kerosene ($T_B = 232^\circ C$), and at the fuel-water interface ($y = \delta$) a convective boundary condition is assumed,

giving the boundary conditions:

$$\text{At } y = 0, T = T_B = 232^\circ\text{C}, \quad (2.12)$$

$$\text{At } y = \delta, -k_F \frac{dT}{dy} = h(T_\delta - T_\infty), \quad (2.13)$$

Where h is the convective heat transfer coefficient, T_B is the saturation temperature of the fuel, T_δ is the fuel-water interface temperature, and T_∞ is the ambient water temperature. It is acknowledged that approximating the surface temperature T as being constant at T_B is a limited assumption. In reality, the surface temperature changes over the duration of a burn as exact fuel properties slightly change, as found also by Garo et al. 1994 [20]. The surface temperature is also usually slightly less than T_B , defined by thermal equilibrium and obtainable using Clausius-Clapeyron equations. However, the assumption that the surface temperature T is equal to T_B is useful for practical simplification as differences usually do not exceed 2% [83].

$$T = T_B - \frac{h(T_\delta - T_\infty)}{k_F} y, \quad (2.14)$$

Given Eqn. 2.14 at fuel thickness ($y = \delta$), $T_\delta = T_B - \frac{h(T_\delta - T_\infty)}{k_F} \delta$. The temperature at the fuel-water interface T_δ at time step t can be expressed as:

$$T_\delta = \frac{T_B + \frac{h\delta}{k_F} T_\infty}{1 + \frac{h\delta}{k_F}}. \quad (2.15)$$

With Eqn. 2.15 the interface temperature T_δ is a function of the fuel thickness δ , which is itself a function of time. The thickness as a function of time, $\delta(t)$, is approximated using the global regression rate v (Eqn. 2.16). Which is determined by the burn time, and initial and final thicknesses respectively δ_i, δ_f . Global regression rate v is assumed to be constant over the duration of the burn. Although the regression rate will slightly vary over the duration of the burn, especially immediately

post-ignition and pre-boilover, we are only calculating the interface temperature at times during the middle of the burn (150, 240, 360, and 480 seconds) at which points the burn rate should be relatively constant.

$$v = \frac{\delta_i - \delta_f}{\text{burn time}}, \quad (2.16)$$

$$\delta(t) = \delta_i - (v \cdot t). \quad (2.17)$$

This follows that T_δ is a function of δ which is itself a function of time. T_δ is also a function of the heat transfer coefficient h , which is shown to be influenced by wave steepness as shown in Sec. A.4.3. Here the value of h in the model is determined by iteration until the value of T_δ at different time steps matches experimentally measured temperature values with the minimum possible summed errors as calculated with Eqn. 2.18.

$$\varepsilon = \sqrt{\sum_t [T_{\delta,experiment} - T_{\delta,model}]^2} = \sqrt{\sum_t \left[T_{\delta,experiment} - \frac{T_B + \frac{h\delta}{k_F} T_\infty}{1 + \frac{h\delta}{k_F}} \right]^2} \quad (2.18)$$

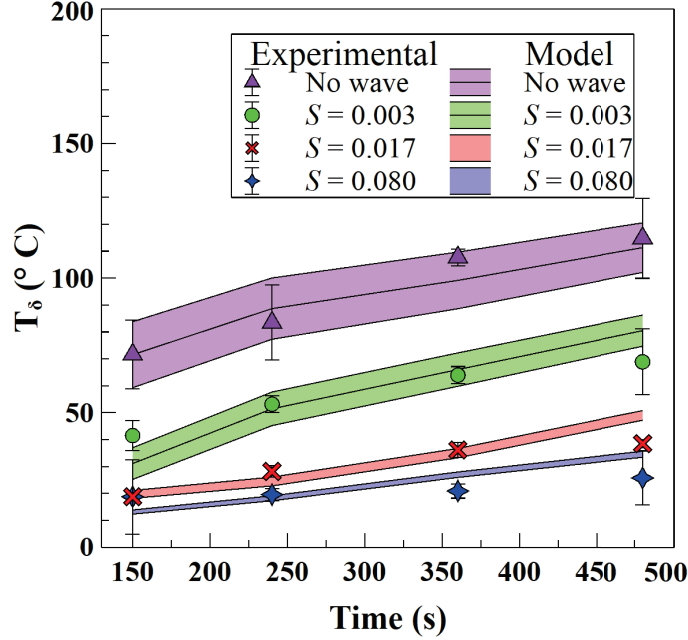


Figure 2.7: Comparison of interface temperature, (T_δ) over the duration of the burn. Shown for the no-wave case and three different steepness waves.

Fig. 2.7 shows the fuel-water interface temperatures over the duration of the experiment, these values are obtained from gathering thermocouple data at the estimated fuel thickness from Eqns. 2.16 & 2.17. The points with error bars on this figure represent experimentally measured interface temperatures, while the lines and shaded error regions represent calculated interface temperatures from the error reduction analysis and Eqn. 2.15. Error bounds for the calculated values represent the standard deviation from the analysis of the repeat cases, not the error between the calculated and experimental values.

Fig. 2.7 shows that the interface temperature steadily decreases with increasing wave steepness, suggesting an increase in heat removal from the fuel layer. It is also noted that the trend of interface temperature vs. time for each individual case flattens with increasing steepness. With no wave the interface temperature noticeably increases with time, eventually leading to boilover as the interface temperature approaches the water superheat temperature associated with boilover of 120 °C as determined by Garo 1999 [23]. However, with increasing steepness the interface temperature profile becomes flatter suggesting the heat transfer coefficient and convective removal of heat at the

interface is maintaining or surpassing the heat reaching the fuel-water interface from combustion. This is supported by the information that none of the wave case interface temperatures reach above 100°C before 8-minutes in the window investigated. This further supports the observed phenomenon of no boilover being observed with any waves in this scale.

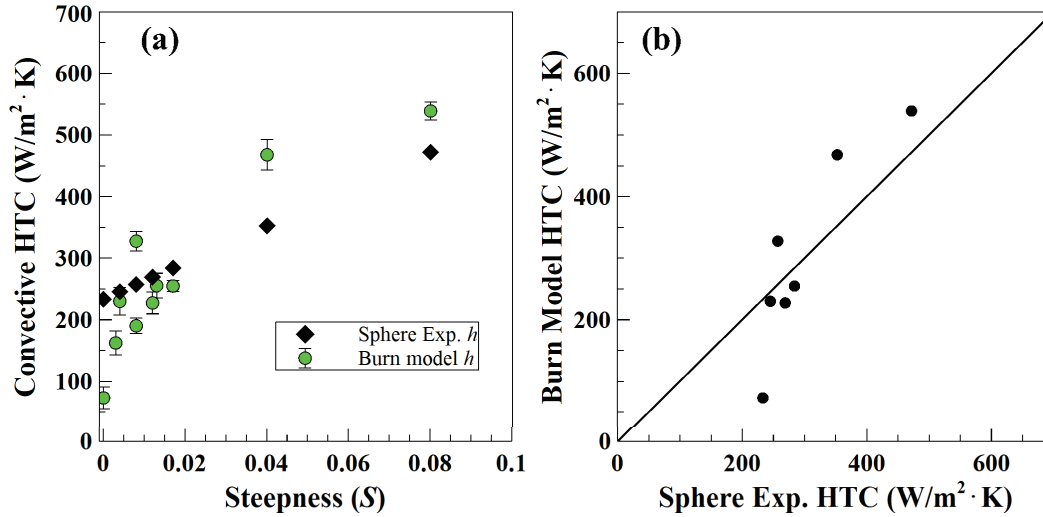


Figure 2.8: (a) Experimental and wave-model heat transfer coefficients as a function of wave steepness. (b) Agreement between burn model heat transfer coefficient and experimentally determined heat transfer coefficient.

Fig. 2.8a shows the h values calculated in this analysis as green dots, these values are calculated from the minimized error analysis above, resulting from best-fit matches to experimental temperature profiles, which is why they are called ‘burn model’ values. The black diamonds on this figure represent heat transfer coefficient values generated by using the linear fit approximation generated in the wave heat transfer sphere experiments in Sec. A.4.3. Fig. 2.8b plots each of these two values against each other to examine their linearity.

It is apparent from Fig. 2.8a that the heat transfer coefficient increases with increasing wave steepness. Examination of the fuel-water interface temperature at this scale further supports this conclusion as the heat transfer coefficient would need to increase to explain the continued reduction in interface temperature with increasing wave steepness. It is also observed that the steepest waves can have a physical effect on the fuel-water interface, sometimes removing fuel at the bottom and

ejecting it out of the pan area. This can impact global regression rate calculations and is a behavior not seen in other waves or at other scales.

2.6 Conclusions

These small scale experiments showed notable trends not previously observed with fuel layers floating on stagnant water. For example, boilover ceases even with the gentlest of waves at this scale of burning. As the steepness of the wave increases, the burning rate decreases linearly. Extremely steep waves (>0.04) tend to be outliers because the fuel is carried away from below by the circulatory motion of the water sub-layer. Temperature measurements using finely spaced thermocouples were used to model interface temperatures and a representative convective heat transfer coefficient using a simple 1-D transient conduction model. As wave steepness increases heat loss from the fuel layer to the water sublayer is enhanced by water movement. Fuel layer mixing and movement is also enhanced, allowing for further heat loss away from the evaporating surface. These two effects combine to reduce the burning rate of the kerosene floating on water. Global regression rate rates and flame heights both show a decrease with increasing wave steepness. Interface temperatures agree with observations that boilover is suppressed with the addition of waves.

Although waves were found to have a significant impact on burning, the small size of these pool fires limits the amount of heat feedback from the flaming region. Pool fires at this scale have a limited fraction of radiative heat feedback, which will increase significantly with pool size. The mechanism by which the waves reduce burning rate is through the waves' thermal interaction with the bottom of the fuel layer, and thus will not scale proportionally with the increasing radiation heat transfer when pool size is increased. In short, the impact of the waves on burning is hypothesized, at this stage, to have a greater effect on smaller scales.

CHAPTER 3

Transient and Steady State Burning Behavior of an Oil Slick with Waves ($D = 0.8 \text{ m}$)²

3.1 Introduction

This chapter investigates the burning behavior of an 80 cm diameter burn under the influence of waves. It will also investigate this behavior both with ‘dynamic’ and ‘constant’ thickness fuel layers. *Dynamic* or ‘transient’ denotes a fuel layer that begins at a selected thickness and thins over the duration of the burn. *Constant* or ‘steady-state’ denotes a fuel layer that during the burn has fuel added to it at the same rate of burning, such that the fuel thickness is the same over a portion of the burn. The previous chapter on small scale experiments examined only the behavior of transient fuel layer thickness. As such, transient experiments were conducted at the medium scale as well to have comparative data between the 10 cm and 80 cm scale. Steady-state fuel thickness was desirable to investigate for several reasons. First, under steady conditions, the temperature profiles were hypothesized to approach constant values. This is especially important for obtaining consistent temperature data, which will become useful for an energy balance formulation later. Constant fuel layer thickness also allows for the investigation of wave behavior and the resulting heat transfer coefficient, as well as their impact on the different fuel thicknesses when the balance of heat within the fuel layer has reached equilibrium. Finally, maintaining the fuel layer thickness allows for the direct measurement of the burning rate, a parameter that is not directly measurable in the transient fuel layer cases.

3.2 Experimental Apparatus

For the medium-scale study, a wavetank (Fig. 3.1) was designed and built specifically to withstand the harsh environment of burn experiments. This wave tank had to be modular for storage purposes, able to work under intense heat and flames, and provide repeatable wave conditions for experiments.

A final size was determined as 3.66 m (12 ft) long, 1.83 m (6 ft) wide, and 0.91 m (3 ft) tall, with a

²Contents of Ch. 3 currently accepted with revisions in **Fire Technology** as: *Burning behavior of liquid fuel on wavy water*[72]. Transient fuel layers also included in proceedings of the Eastern States Section of the Combustion Institute Spring Technical Meeting [74]. Construction of wavetank published as MQP report: *FPE Wave Tank* [73].

static water depth of 0.61 m (2 ft). At these dimensions, the wavetank holds 4 m³ (1077 gallons) of water. The kerosene fuel used in these experiments has a boiling point range ($T_B = 175 - 325^\circ\text{C}$) with an assumed value of $T_B = 232^\circ\text{C}$, liquid specific heat $C_{p,l} = 1.97\text{kJ/kg}\cdot\text{K}$, thermal diffusivity $\alpha = 8.8 \times 10^{-8} \text{ m}^2/\text{s}$, and thermal conductivity $k = 0.133 \text{ W/m}\cdot\text{K}$ [16], [75], [84]. Kerosene was chosen as fuel for these experiments for its optical clarity, making monitoring fuel thickness with the underwater camera easier, and for its more homogeneous composition than crude oil. Kerosene was also chosen as the results from the dynamic thickness experiments could be directly compared to experiments in the small scale Ch. 2 which also used kerosene fuel.

The flume of the wavetank was constructed of 1/8" (3.175 mm) mild steel sheets and rests on top of a steel I-beam frame which provides the structural support for the large weight of water. To aid in withstanding the intense heat, a deluge system was built which pumps water out of the tank and sprays it against the inside walls of the flume. Water from the tank could not be discarded down conventional drains after burn experiments, as it was considered hazardous waste. To overcome this challenge, water from the wavetank was filtered and stored in large 1 m³ (275-gallon) intermediate bulk containers (IBC) (Fig. 3.2a). This allowed for the consistent use of clean water in the wave tank, especially important for the visibility required for the underwater camera. The underwater camera used was an Eyoyo underwater fishing camera. This camera in conjunction with an RCA USB capture card, allowed for underwater video recording directly to a computer.

Two important wavetank components were wave generation and wave absorption. Wave absorption in this tank was accomplished with a 1:6 sloped beach made of expanded metal and covered in a semi-porous plasticized horsehair mat as shown in Fig. 3.1.

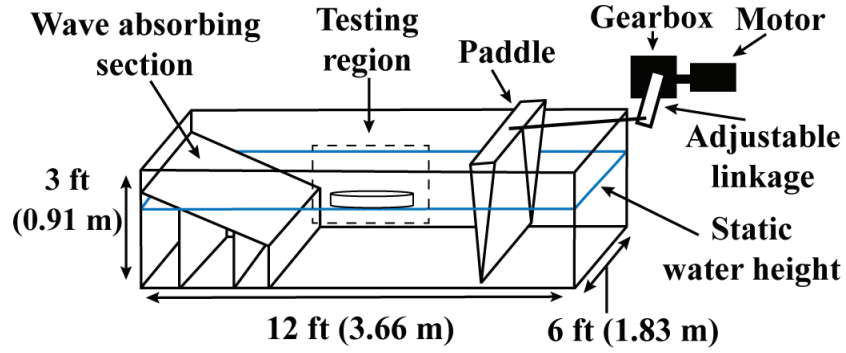


Figure 3.1: Schematic of wavetank used for testing.

Important for the medium-scale study was the generation of linear waves. Linear waves are waves that are discrete, uniform, and repeatable in shape and size. Linear wave generation requires a sinusoidal wave paddle velocity, such that the paddle slows as it reaches its maximum and minimum displacement. To achieve this, a custom wave generator was built making use of a 3hp 3-phase AC induction motor, 30:1 gearbox, and variable frequency drive to control motor speed (Fig. 3.2d). An adjustable linkage and rotating tie-rod facilitate the conversion of the rotational shaft motion into sinusoidal linear paddle motion while allowing for the creation of different paddle displacements and motor speeds to create different wave profiles.

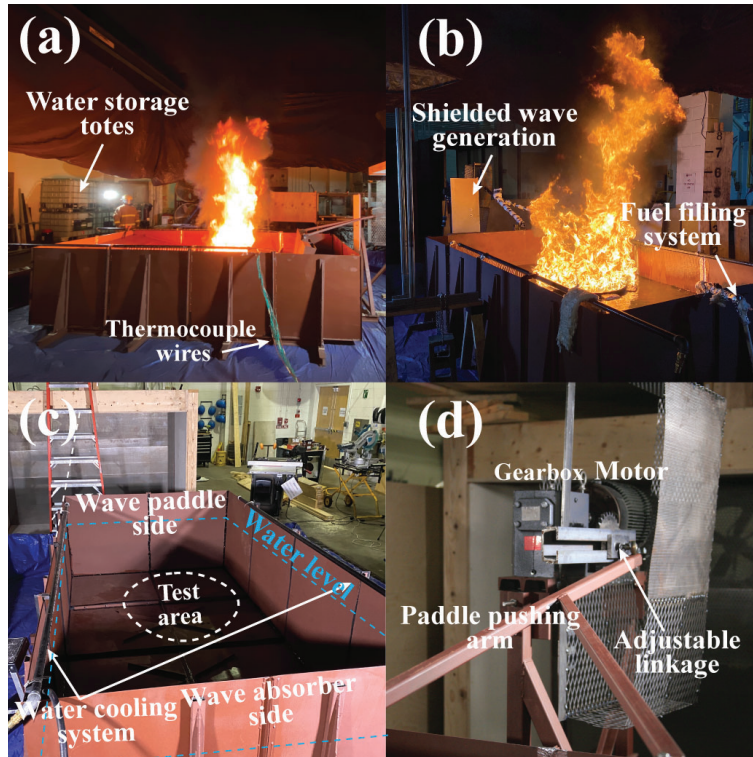


Figure 3.2: (a) Side view of wavetank during testing. (b) Looking towards the wave generation paddle during a burn test with waves. (c) Empty wave flume before installing wave generation mechanism, wave paddle, and wave absorbing section. (d) Wave generation mechanism attached to the paddle pushing arm.

Another challenge for these experiments was designing a way to contain the fuel, while still allowing interaction with the wavy water. This was accomplished by constructing a floating fuel ring that contained the fuel to a known diameter and supported the instrumentation used for the experiments. The burn ring was constructed from a 15 cm wide 16 gauge (1.6 mm) thick strip of mild steel, formed into an 80 cm diameter ring using a slip-roll and welded with a small overlap. Supports constructed of 1/8" (3.175 mm) diameter mild steel rod were welded in place across the center of the pan, both as supporting members for instrumentation and to help the pan hold its shape (Fig. 3.3). Markings were made along the inside of the pan at a 0.5 cm spacing and were used to help monitor and maintain fuel level thickness (Fig. 3.4b). The pan was floated by 8 balsa wood floats measuring 3" x 3" x 6" (7.62 cm x 7.62 cm x 15.24 cm). These balsa wood floats were covered in reflective aluminum tape with one layer of 1/2" (1.27 cm) thick fiberglass insulation taped to the top of the float.

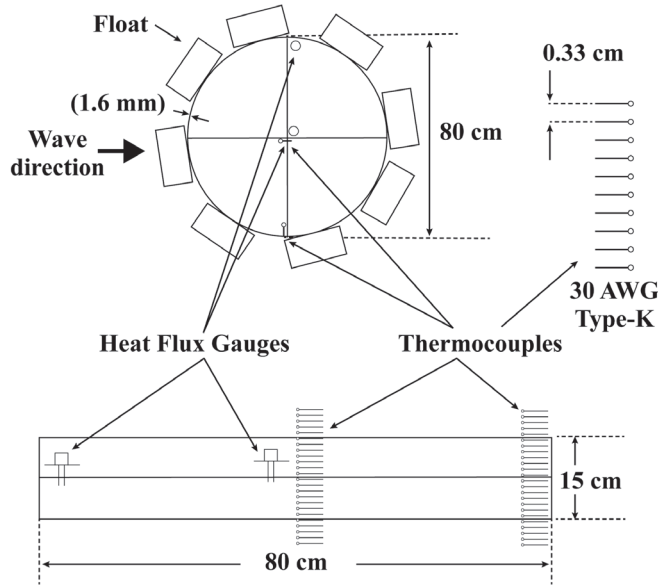


Figure 3.3: *Top*, top-down schematic of the fuel containment pan used in the experiments. *Bottom*, side view of fuel pan showing radial positions of thermocouples and heat flux gauges.

Temperature measurement was accomplished using two thermocouple arrays, one placed at the center of the ring, and one at the edge of the ring. Temperature data acquisition was accomplished with a National Instruments PXIe-1075 chassis and NI PXIe-4353 thermocouple modules. Each array was constructed of 24 Type-K 30 AWG thermocouples in ceramic tubes (Fig. 3.4a). Custom thermocouple arrays were made such that the thermocouples were all spaced at exactly 0.33 cm apart, the total array providing 7.92 cm of gas, fuel, and water temperatures. Two water-cooled Gardon-style heat flux gauges were also supported by the floating pan; one near the center ($r/D = 0.06$), and the second 5 cm away from the pan wall ($r/D = 0.44$) (Fig. 3.4c). Maintaining a constant fuel layer thickness was important for this study, as we needed to examine the burning behavior changes due to waves under steady-state conditions. To achieve this, a fuel filling system was constructed which supplied fuel evenly to the underside of the burning pool with an adjustable and recordable flow rate. The fuel filling ring (Fig. 3.4d) was constructed of 1/2" (12.7 mm) diameter vinyl in a 60 cm diameter circle and drilled with small 1/16" (1.57 mm) holes. An Omega FTB602 infrared electro-optical pulse output flowmeter and custom-made Arduino flow display and recorder were used to monitor and record the fuel flow rate during experiments. The fuel pump used was

a 12 VDC Holley Red Electric marine-style fuel pump. The fuel flow rate was controlled with an easy-set precision flow adjustment needle-type flow valve, with a fuel bleed overflow loop back to a fuel reservoir to prevent the deterioration of pump performance due to pressure buildup at low flow rates.

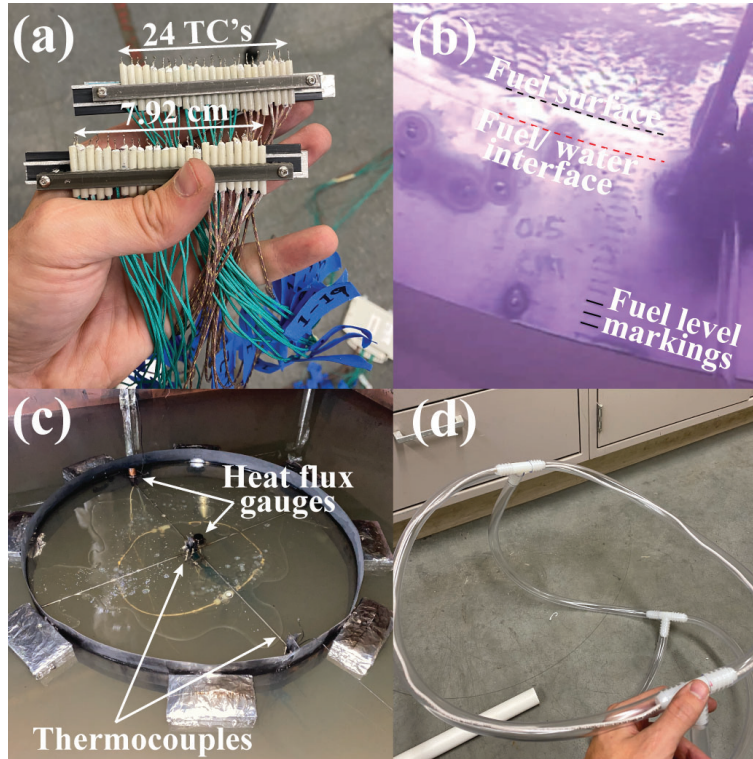


Figure 3.4: (a) Thermocouple arrays used for measuring gas, fuel, and water temperatures. (b) View from underwater camera showing measurement lines used for maintaining fuel thickness, the bottom of kerosene layer is differentiable from water and partially marked with a red dashed line. (c) Floating burn ring in the wavetank, fuel filling apparatus visible below the water surface. (d) Fuel filling ring during construction.

Fig. 3.5b shows the fuel layer in reference to the pan wall for the 3 thicknesses tested. For the dynamic fuel layer thicknesses only a fuel thickness of 2 cm was tested, but constantly maintained fuel layers were tested at 1, 2, and 3 cm thicknesses. In the constant fuel layer thickness experiments, the fuel level was maintained by balancing the regression rate of burning, with the fuel supplied by the pump. The flowmeter reported a flow rate in mm/min with an update rate of 1 Hz. Based on the transient burning experiments which had been conducted earlier, ballpark data on the

global regression rate was already available. Starting fuel filling with the known global regression rate allowed us to prevent drastically over or under-filling the experiment during the first trial. Each constant fuel layer experiment was repeated immediately, such that the same experiment was operated 3 times in succession. This also contributed to enhanced accuracy as the individual in charge of fuel filling gained experience with each individual case. The fuel level was maintained by manually monitoring the underwater camera and placing markings on the screen for where the fuel level should be maintained. For the baseline cases, this was easiest as the fuel was not undulating. With the addition of waves, ‘high’ and ‘low’ markers were placed on the fuel undulation points, and fuel was added to maintain these markings.

It should be noted that the exact position of the kerosene in reference to the pan lip is a function of the difference in density between the kerosene and water as shown in Eqn. 3.3 and therefore will change slightly as the fuel and water rise in temperature and their densities slightly change.

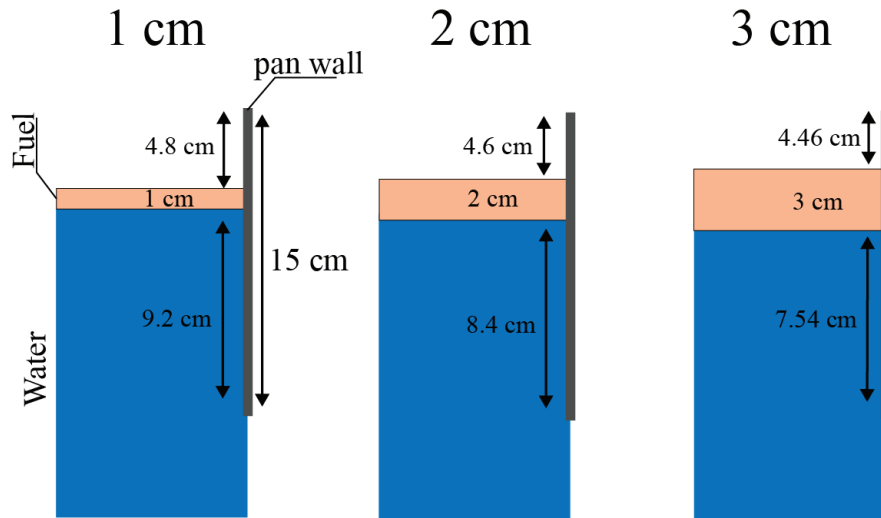


Figure 3.5: Position of the fuel layer relative to the pan wall for the three thickness cases examined in this section: 1 cm, 2 cm & 3 cm.

The difference in density of the kerosene and water drives the height at which the kerosene will float in the water. The floating kerosene will displace a mass of water volume equal to its own mass in order to float. The volume of each is approximated to be a cylinder ($V = \pi r^2 \delta$), with δ as the fuel

layer thickness, or water height. Since the radius of both pools is equal, all of the terms in Eqn. 3.2 cancel leaving just the height and density remaining:

$$\text{mass of water} = \text{mass of kerosene fuel}, \quad (3.1)$$

$$\pi r^2 \delta_w \cdot \rho_w = \pi r^2 \delta_F \cdot \rho_F, \quad (3.2)$$

$$\delta_w \cdot \rho_w = \delta_F \cdot \rho_F. \quad (3.3)$$

Eqn. 3.3 shows the height of water that the kerosene will displace in order to float on its surface. In this way, we can see that the displacement in height is proportional to the difference in density of the two liquids. This equation is used to calculate the position of the fuel layer relative to the floating pan in Fig. 3.5.

The two water-cooled Gardon-style heat flux gauges were both individually calibrated using a cone calorimeter prior to testing. Fig. 3.6 shows the resulting calibration fit from both heat flux gauges, showing good linear agreement between the ideal heat flux output from the cone heating element, and the measured heat flux from the experimental heat flux gauges.

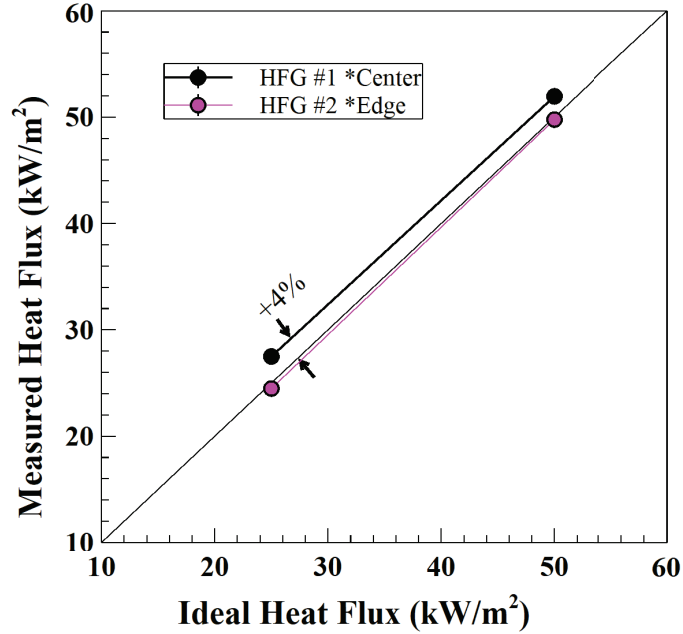


Figure 3.6: Ideal vs. measured heat flux for the two heat flux gauges used during burn experiments.

To parameterize how well the wavetank performed at producing linear waves, each wave profile was measured and compared to theoretical conditions. In the small scale a more extensive study of wave motion was completed and is presented in App. A. An extensive PIV study was not possible in this tank without severe modification to either the PIV setup or the wavetank itself. As such an Akamina AWP 24-3 wave gauge and AWP 30 cm wave probe head were used to measure the water surface location over time. Fig. 3.7a shows the ideal wave profile as the dark blue line by plotting water surface location as a function of time. The wave profile measured by the wave gauge is shown with the red-shaded region. It is observed that the experimental wave maintains the proper period and overall displacement but does deviate from the ideal at certain points over the wave cycle. However, these deviations repeat with each cycle and do not amplify over the duration of the experiments.

Plotting the experimental water heights versus the ideal water heights shows the linearity between the ideal and measured waves (Fig. 3.7b). The R^2 between the ideal and measured waves was also calculated and can be found in Table 3.1. Three of the four waves had an R^2 above 0.96, with one wave having a value of 0.86. Wave steepness will be used in this study to evaluate the effect of the

wave on the burning pool. Wave steepness is calculated in the same fashion as for the small scale with Eqn. 2.1.

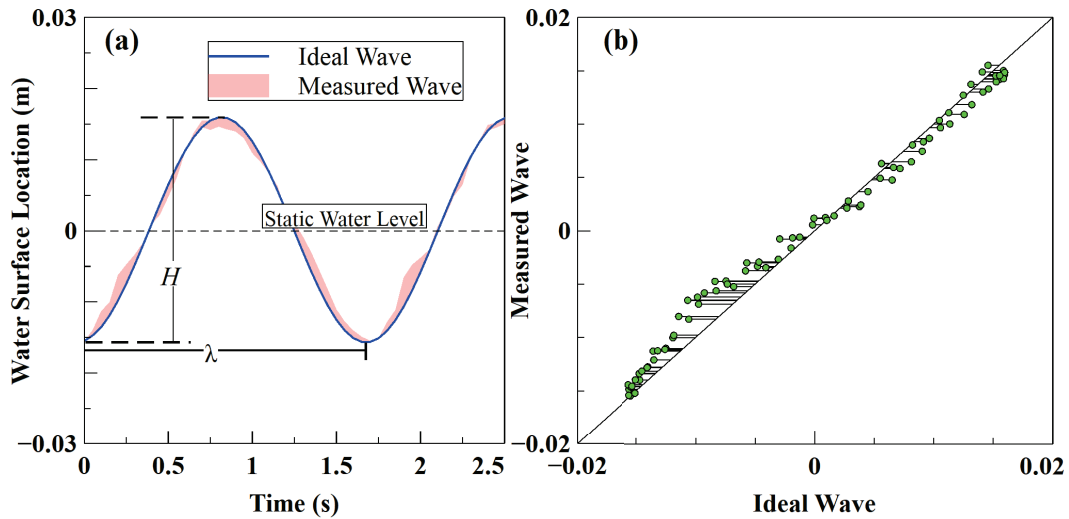


Figure 3.7: (a) Ideal wave profile shown with measured wave profile in experimental apparatus ($S = 0.008$) (b) Ideal wave heights vs. their corresponding measured wave heights.

Table 3.1: Medium scale wave profiles tested.

Wave Height H (m)	Wavelength λ (m)	Period t_p (s)	Steepness S	R^2	Dynamic (D) Steady (S) Both (B)	4-second Profile
0.014	8.28	3.5	0.0017	0.951	D	
0.03	3	7	0.0043	0.922	D	
0.031	3.89	1.82	0.008	0.989	B	
0.055	5.71	2.5	0.0096	0.86	B	
0.057	3.73	1.76	0.0153	0.963	S	
0.032	1.83	1.1	0.0174	0.989	B	

Current U.S. Coast Guard and American Petroleum Institute guidelines state that the sea state condition must be below a Beaufort level of 3 for in-situ burn operations, and that ideal conditions for ISB are under a Beaufort Sea state of 1 [1], [2]. In Ch. 2, 0.1 m kerosene burns were examined in the small-scale wavetank with wave steepness ranging from $S = 0.003 - 0.08$. This chapter focuses on the range of steepness more likely to be associated with in-situ burning operations, centering around a Beaufort Sea state of 1. The Beaufort scale empirically correlates wind speed to sea conditions, usually wave height. The steepness for the waves on the Beaufort scale was calculated assuming that the waves follow standard ocean distributions for corresponding wavelengths and periods, such as those from Trujillo & Thurman 2001 [3]. Assuming waves in each sea state have a wavelength consistent with that of an ‘average’ wave for its wave height, the steepness for a Beaufort scale of 1 would be about 0.015. As such, waves up to a steepness of approximately 0.015 were selected for this study. Beaufort scales of 2 and 3 would have steepness values of 0.024 and 0.03 respectively.

3.3 Results - Dynamic Fuel Layer Thickness

Results reported in this section are from kerosene burning experiments where a set amount of fuel was added to the burning ring and then ignited. As such the fuel layer thinned over the duration of the experiment, with very little quasi-steady state period. These experiments are named ‘dynamic’ as the fuel layer changes in thickness over the duration of the burn, in contrast to the constant thickness experiments later in Section 3.4. The initial fuel layer thickness for the dynamic fuel layer experiments was 2 cm.

Comparison of the results from this section with the results from the small scale is especially key as this bridges the behavior from the small scale to the medium scale. We see that both scales experience similar reductions in the burning rate at 35% and 27% in Table 3.2 with the thin fuel layers.

Table 3.2: Comparison of burn parameters and results between small and medium scales.

	Small (D = 0.1 m)	Medium (D = 0.8 m)
Fuel	kerosene	kerosene
Burn Area	78.54 cm ²	0.5 m ²
Steepness	0 - 0.08	0 - 0.017
Boilover	No wave only	All waves
\dot{m}'' % red.	35%	27%
Fuel layer thickness	transient	transient and steady
δ_i	0.6 cm	1, 2 & 3 cm

3.3.1 Time to Boilover & Boilover Duration

The timelines for these dynamic thickness burns are shown in Fig. 3.8. Blue bars represent normal burning and red bars represent boilover burning. It was observed during experiments, and from video analysis, that cases with waves took longer to reach boilover with identical initial fuel layer thickness compared to no wave cases. When these cases did reach boilover, the boilover was typically less intense and did not last as long as no wave cases.

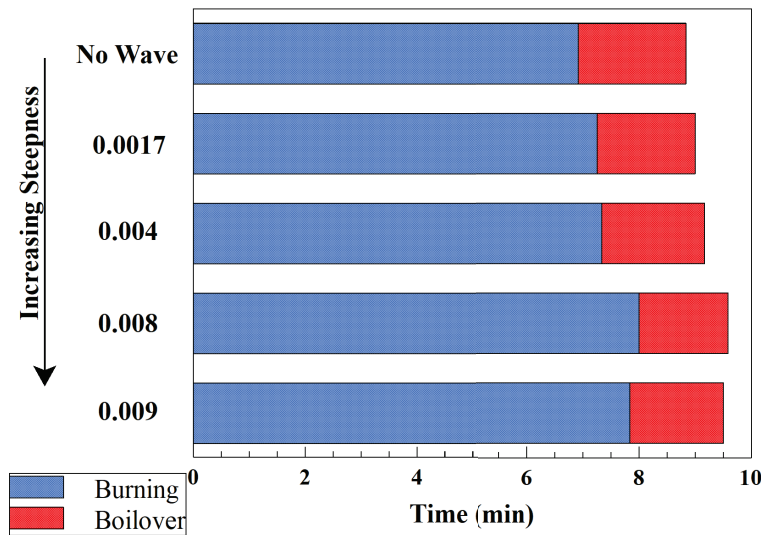


Figure 3.8: Timelines of the dynamic burn experiments with 2 cm fuel layers of kerosene. Blue portions show burning and red portions show boilover.

Fig. 3.9 and Fig. 3.10 plot the data shown in Fig. 3.8 vs. wave steepness. Each of these cases is a

single experiment; thus, no error bars are present for any points. Fig. 3.9 shows that time to boilover increases linearly with wave steepness. This increasing time to boilover is an expected result: as the regression rate drops, the time increases for the interface to reach the temperature required to change the water phase from liquid to steam. Garo et al. 2007 [80] provides a calculation for time to boilover, if the regression rate and thermal penetration rate are assumed to be constant. This is similar to the regression rate estimate used in Sec. 2.5 in Eqn. 2.16. The equation used in Garo et al. 2007 is adapted in Eqn. 3.4 for the nomenclature used in this work; δ_i initial thickness, v regression rate, v_p thermal penetration rate, and t_B time to boilover.

$$t_B = \frac{\delta_i}{v + v_p}. \quad (3.4)$$

It follows that if the regression rate v is estimated by initial thickness δ_i , final thickness δ_F , and time to boilover t_B as represented in Eqn. 2.16, then some of these terms cancel leaving Eqn. 3.6 as remaining. This shows thermal penetration rate can be expressed as a function of the final thickness δ_F , and time to boilover t_B .

$$t_B = \frac{\delta_i}{\frac{\delta_i - \delta_F}{t_B} + v_p}, \quad (3.5)$$

$$v_p = \frac{\delta_F}{t_B}. \quad (3.6)$$

As the thermal penetration rate for these experiments was not able to be captured, a thermal penetration rate of 1 mm/s (60 mm/min) was assumed for calculating a potential time to boilover for comparison to experimental data. This value was in the range of the highest values investigated in Garo et al. 2007 [80]. The dotted line running across all steepness values at 430 seconds represents this calculation. The dotted line at approximately 550 seconds represents the time to boilover calculation if the thermal penetration rate is zero. These two lines represent a continuum of times at which boilover are possible when the thermal penetration rate is changing.

It should also be noted that in the small scale, boilover was only observed in the no-wave case; no cases with waves underwent boilover in the small scale. However, in the medium scale, every case

demonstrated boilover, even cases with the steepest waves. This is believed to be due to the much higher available supply of heat from the fire, in contrast to the heat loss to the water sublayer which is only scaling as a function of the burn area.

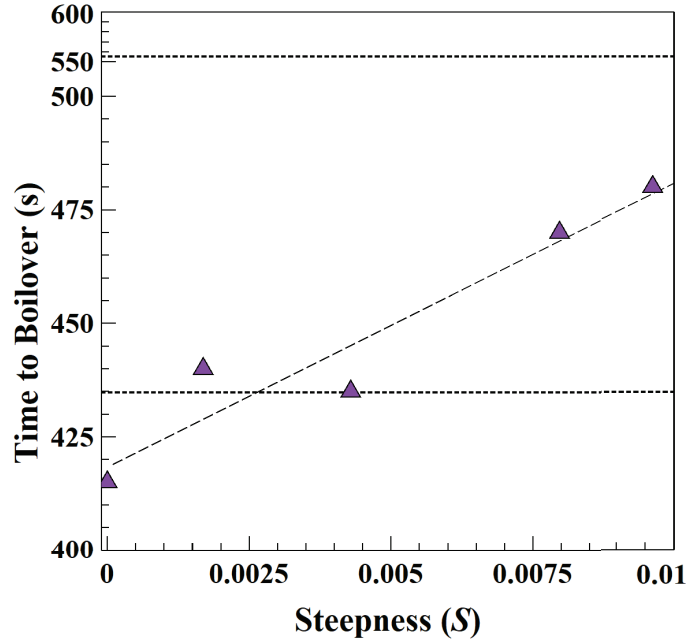


Figure 3.9: Time to boilover vs. wave steepness. Burns took longer to reach boilover with increasing steepness waves.

Fig. 3.10 shows the duration of these boilover events vs. wave steepness, indicating that as wave steepness increases the boilover duration decreases. This suggests that as the steepness increases, the fuel remaining at the onset of boilover is less than that remaining in the no wave case. Meaning that although the regression rate has lowered with the wave, since the burn has continued slightly proportionally longer, there is less fuel remaining at boilover.

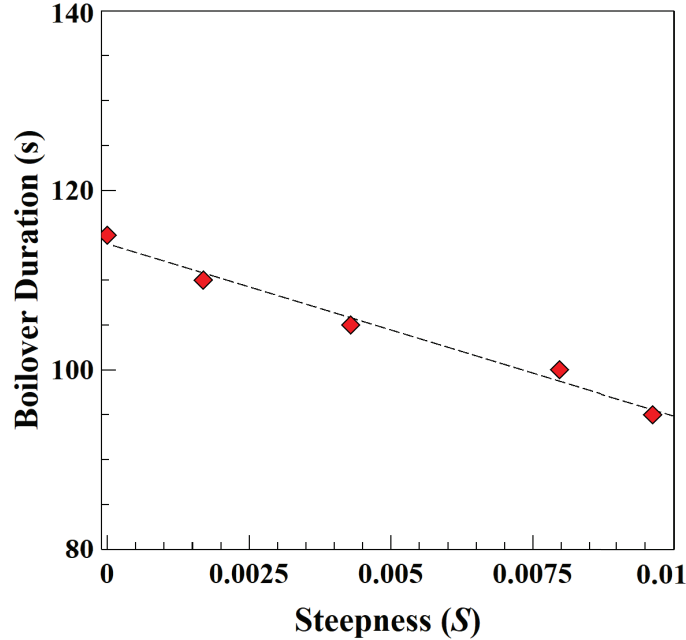


Figure 3.10: Boilover duration plotted vs. wave steepness for dynamic fuel layer experiments.

The increase in time to boilover and boilover duration for the dynamic fuel layers demonstrates that boilover is a complex phenomenon related to fuel thickness, fuel regression rate, and water sublayer cooling. Garo et al. 1999 & 2007 note that boilover occurs at a water sublayer temperature of approximately 120°C [23], a superheat temperature for water. This is a known phenomenon, as a liquid not in contact with a gas phase will need to approach a ‘limit of super heat’ temperature in order for bubble nucleation to begin [23]. In the case of a burning fuel floating on water, the temperature of the fuel-water interface, and thus the time to boilover, is a function of numerous factors including heat feedback from the flame, heat loss to the water, fuel thickness, and fuel and water thermal diffusivity. Experiments in the small scale may have been just past a threshold where water sublayer cooling exceeded available heat from the flame, and thus prevented boilover from ever occurring.

3.3.2 Global Regression Rate

The global regression rate for these experiments was calculated similarly to in other sections. However this time with the addition of the underwater camera, the fuel thickness at boilover was more

precisely known. With waves, the thickness at boilover decreased from the fuel remaining at boilover in the baseline case. As such the global regression rate could be adjusted slightly to account for this small amount of remaining fuel at boilover and was approximated by Eqn. 3.7. The initial fuel thickness for these experiments was 2 cm.

$$\text{Global regression rate} = \frac{\text{Initial thickness} - \text{Thickness at boilover}}{\text{Time to boilover}}. \quad (3.7)$$

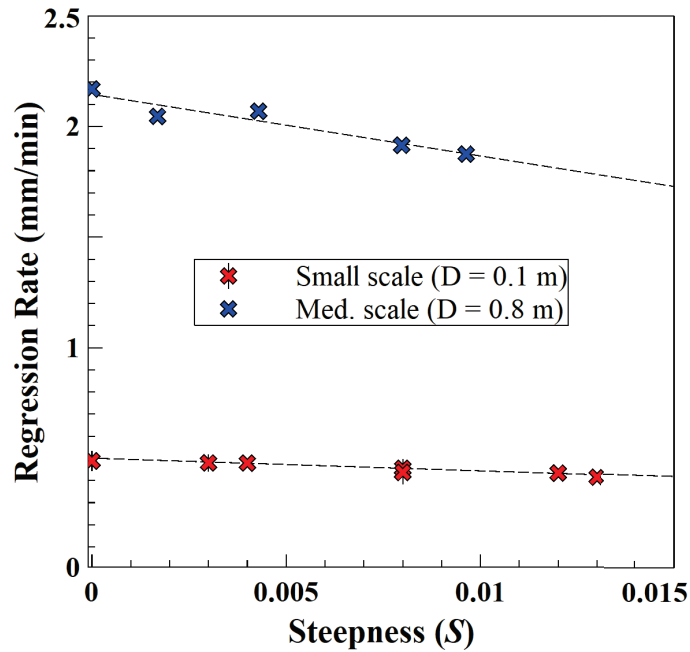


Figure 3.11: Global regression rate calculated from Eqn. 3.7 plotted vs. wave steepness S for both the medium and small scales. Showing a decrease in global regression rates with waves steepness.

The global regression rate follows the same trend as the small scale with increasing wave steepness corresponding to a decreasing regression rate. Though we could observe the fuel layer for these dynamic fuel layer thickness experiments through the underwater camera, we had no direct measurement of the fuel thickness remaining at any given time. We can observe also the temperature profiles taken during the experiment such as in Fig. 3.12. These temperature profiles were taken for the no wave and highest steepness ($S = 0.009$) wave used in the dynamic fuel layer experiments.

Both of these temperature profiles were obtained from an average of 30 seconds of temperature data taken from 5 minutes and 7 minutes post-ignition. These temperature profiles show similar behavior to what was observed in the small scale. The no-wave case maintains higher in-depth temperatures than the case with the wave. The case with the wave maintains the same or very similar fuel surface temperature but reaches ambient temperatures at a much shallower depth than the case without waves. These trends continue into the 7-minute temperature profiles where the no-wave in-depth temperatures remain higher than the wave case. The wave case temperatures, while lower, also remain more constant than the no wave case, suggesting a suppression of the internal migrating thermal wave.

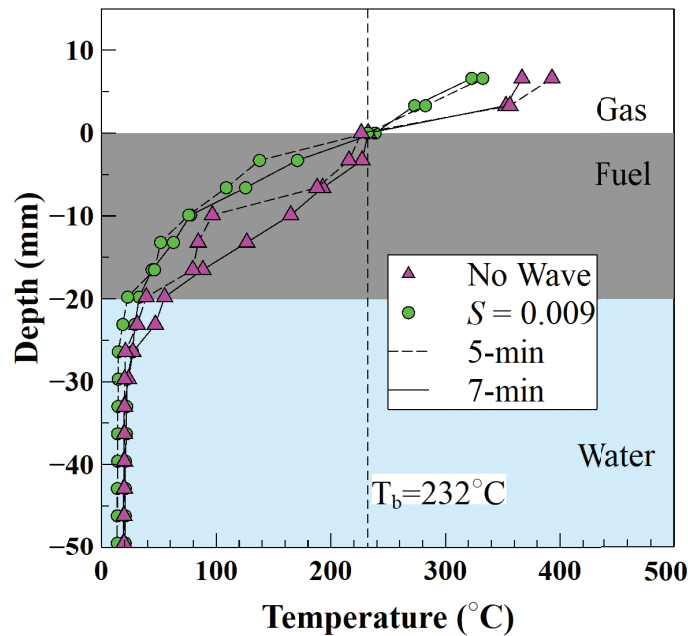


Figure 3.12: In-depth temperature profiles for the dynamic fuel layer thickness case without wave and with $S = 0.009$ wave, data from 5 & 7 minutes post-ignition. Gray region shows the initial fuel thickness of 2 cm.

3.3.3 Interface Temperature Model

A model was developed similar to Sec. 2.5 which examined the interface temperature as a function of regression rate and time to calculate a convective heat transfer coefficient. Here the 1D heat transfer equation, boundary conditions, solution, and error function are represented for clarity.

$$\frac{\partial T}{\partial t} = \alpha \frac{\partial^2 T}{\partial y^2}, \quad (3.8)$$

At the fuel surface ($y = 0$) we can assume a fuel temperature equal to the boiling point of kerosene ($T_B = 232^\circ\text{C}$), and at the fuel-water interface ($y = \delta$) a convective boundary condition is assumed, giving the boundary conditions:

$$\text{At } y = 0, T = T_B = 232^\circ\text{C}, \quad (3.9)$$

$$\text{At } y = \delta, -k_F \frac{dT}{dy} = h(T_\delta - T_\infty), \quad (3.10)$$

Where h is the convective heat transfer coefficient, T_B is the saturation temperature of the fuel, T_δ is the fuel-water interface temperature, and T_∞ is the ambient water temperature. It is acknowledged that approximating the surface temperature T as being constant at T_B is a limited assumption. In reality, the surface temperature changes over the duration of a burn as exact fuel properties slightly change, as found also by Garo et al. 1994 [20]. The surface temperature is also usually slightly less than T_B , defined by thermal equilibrium and obtainable using Clausius-Clapeyron equations. However, the assumption that the surface temperature T is equal to T_B is useful for practical simplification as differences usually do not exceed 2% [83]. The solution for Eqn. 3.11 is then given as:

$$T = T_B - \frac{h(T_\delta - T_\infty)}{k_F} y, \quad (3.11)$$

Given Eqn. 3.11 at fuel thickness ($y = \delta$), $T_\delta = T_B - \frac{h(T_\delta - T_\infty)}{k_F} \delta$. The temperature at the fuel-water interface T_δ at time step t can be expressed as:

$$T_\delta = \frac{T_B + \frac{h\delta}{k_F} T_\infty}{1 + \frac{h\delta}{k_F}}. \quad (3.12)$$

With Eqn. 3.12 the interface temperature T_δ is a function of the fuel thickness δ , which is itself a function of time. The thickness as a function of time, $\delta(t)$, is approximated using the global regression rate v , Eqn. 3.13. Which is determined by the burn time, and initial and final thicknesses respectively δ_i, δ_f . Global regression rate v is assumed to be constant over the duration of the burn. Although the regression rate will slightly vary over the duration of the burn, especially immediately post-ignition and pre-boilover, we are only calculating the interface temperature at times over the duration of the experiment (180, 240, 300, 360, 420, and 480 seconds) to investigate the interface temperature over the duration of the dynamic thickness experiments.

$$v = \frac{\delta_i - \delta_f}{\text{burn time}}, \quad (3.13)$$

$$\delta(t) = \delta_i - (v \cdot t). \quad (3.14)$$

It follows that T_δ is a function of δ which is itself a function of time. T_δ is also a function of the heat transfer coefficient h , which is shown to be influenced by wave steepness as shown in Sec. A.4.3. Here the value of h in the model is determined by iteration until the value of T_δ at different time steps matches experimentally measured temperature values with the minimum possible summed errors as calculated with Eqn. 3.15:

$$\varepsilon = \sqrt{\sum_t [T_{\delta,experiment} - T_{\delta,model}]^2} = \sqrt{\sum_t \left[T_{\delta,experiment} - \frac{T_B + \frac{h\delta}{k_F} T_\infty}{1 + \frac{h\delta}{k_F}} \right]^2}. \quad (3.15)$$

Fig. 3.13 shows the best-fit interface temperatures calculated for the chosen timesteps as lines and the measured thermocouple data as the points. The experimentally measured range of boilover times is also shown as the flat dotted line with points. Both the measured and model data show an increasing interface temperature over the duration of the experiment leading to eventual boilover (boilover temperatures excluded from interface figures). This is expected: as the fuel layer thins and the experiment progresses the interface gradually approaches boilover temperatures. Notably, with each wave, the temperature profile seems to flatten slightly, suggesting less active heat penetration

or more heat loss at the fuel-water interface.

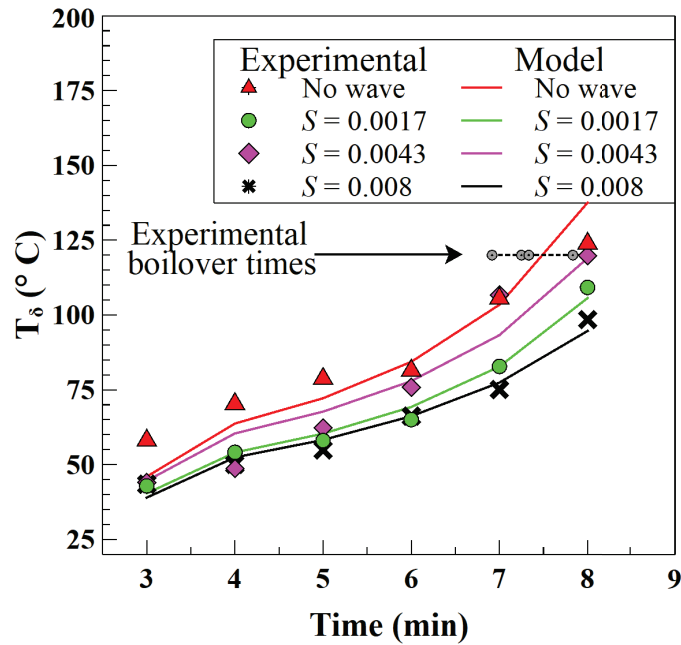


Figure 3.13: Comparison of interface temperature (T_δ) over the duration of the burn for the medium scale dynamic fuel layers. Shown for the no-wave case and three different steepness waves.

Comparing Fig. 3.13 with Fig. 2.7, the first observation is the more rapid rise in T_δ , especially approaching boilover times. In Fig. 2.7 only the baseline case approached boilover later in the experiments, an observation consistent with the lack of boilover in wave cases. All fuel-water interface values remain under 120°C until very close to the measured boilover times. The points at which the model and measured interface temperatures cross 120°C is relatively close to the measured time to boilover from these experiments. This suggests that boilover is happening somewhere between 100 and 120°C, but maybe not at exactly a constant 120°C. This deviation could also be due to an error in the estimation of fuel thickness, an imprecise thermocouple location, or an error in the global regression rate. Error in the global regression rate would also ‘accumulate’ such that estimation for instantaneous fuel thickness towards the end of the experiment could be more erroneous than one taken at the beginning of the experiment.

Also noticeable from Fig. 3.13 is the distance between each line and its corresponding set of points.

As the steepness increases the vertical separation between each line seems to increase proportionally, suggesting a relatively linear correlation between wave steepness and the change in behavior at the fuel-water interface. Fig. 3.14a plots the calculated heat transfer coefficients (HTC) from this analysis vs. wave steepness. Also present on this plot are the values calculated from a linear fit of the experimental data from Sec. A.4.3, shown as the black dots. These black dots represent the anticipated HTC values from the wave investigations. Fig. 3.14b shows the comparison of expected values from the wave investigation, vs. the experimental values calculated in this section.

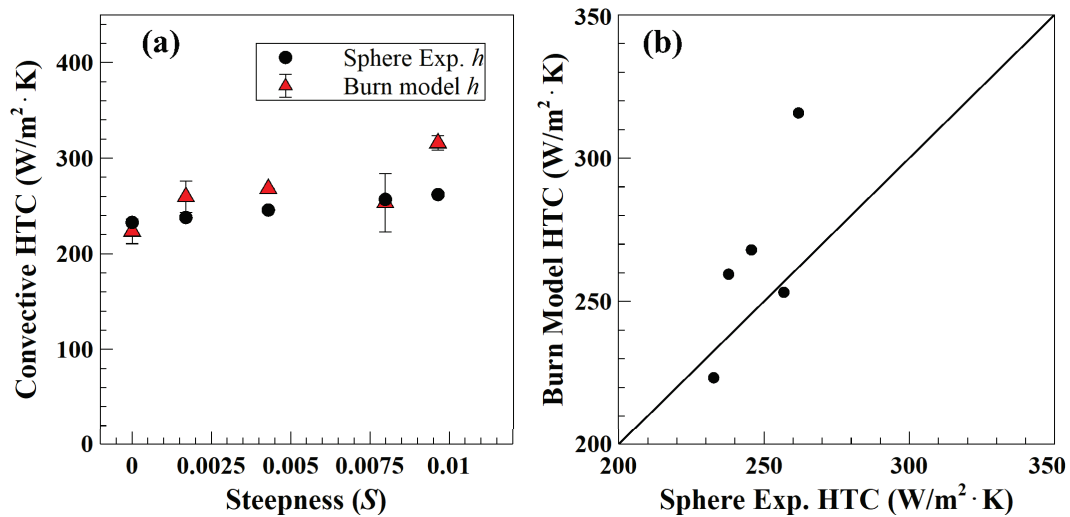


Figure 3.14: (a) Heat transfer coefficients calculated from the dynamic fuel thickness experiments examined, black dots show the linear fit values obtained from Sec. A.4.3. (b) Agreement between burn model heat transfer coefficient and experimentally determined heat transfer coefficient.

Heat transfer values calculated from experimental regression rate and temperature data agree relatively well with anticipated values determined from the wave study work in Sec. A.4.3, suggesting that the heat removal rate at the fuel-water interface is tied to wave steepness. This is likely a connection between the distance that the water sublayer is moving (tied to the wave height H) and the timescale over which it is moving (tied to the wave period t_p , which defines the wavelength λ). Comparison between these values in Fig. 3.14b shows good agreement for these dynamic fuel layer experiments. This demonstrates that even though the values of regression rate change drastically with scale (small scale 0.5 mm/min, med scale 2 mm/min), the value of heat transfer coefficient

remains constant across similar steepness waves. This indicates that the heat transfer coefficient is independent of pool size, and related solely to the wave and its behavior.

3.4 Results - Constant Fuel Layer Thickness

Results from the small and medium dynamic thickness experiments have demonstrated a relatively constant value of heat transfer coefficient for the two scales thus far. As a next step, fuel layers of constantly maintained thickness were evaluated. Temperature profiles obtained in the small and medium scales so far have been used to evaluate a heat transfer coefficient relating to fuel thickness and interface temperature. However, these fuel layers have simultaneously been experiencing a thinning and heating effect, making this analysis more sensitive to thermocouple location and selection. With a constant fuel thickness, the interface temperature should reach equilibrium where the feedback loop is composed of heat input from the flame, heat loss to fuel sensible and latent heats, and heat loss to the water sublayer. Observation of flattening temperature profiles and constant interface temperatures will provide more supporting data that the heat transfer coefficient is a function of only wave parameters. This also provides the first opportunity in this study to measure the regression rate of a fuel floating on water, accomplished by recording the amount of fuel required to maintain the constant fuel layer thickness.

3.4.1 Flowmeter Regression Rate

Fig. 3.15 shows the regression rate obtained from the flowmeter vs. the wave steepness for the 3 different thicknesses. The regression rate is measured using the quantity of fuel that was needed to maintain a constant fuel thickness throughout the steady state portion of the experiment. This data was obtained from a 1-minute average of recorded flowmeter rates for the steady state region of burning. The error bars represent the standard deviation from the 3 repeats of each case. The 3 cm data does not have an error bar as only a single run was conducted for these cases. Flowmeter values did not vary significantly during steady state, as only small changes were made if the fuel layer was seen to be thinning or thickening.

The highest regression rates at any respective steepness were seen with the 3 cm thickness tests. Decreasing the fuel layer caused a decrease in the regression rate, as seen with the baseline case.

Increasing the wave steepness was then seen to also decrease the regression rate. When observing the reduction in thickness from 2 cm to 1 cm, the steepest wave at 2 cm reduced the regression rate as much as reducing the thickness to 1 cm, although reducing the thickness from 3 cm to 2 cm showed a much smaller reduction in the baseline regression rate. Across all thicknesses, waves were observed to reduce the regression rate to varying degrees.

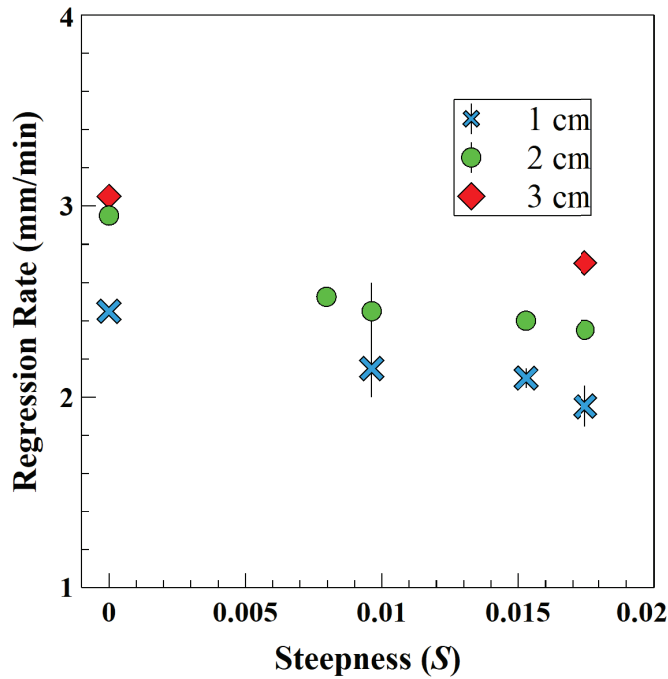


Figure 3.15: Experimental regression rate from flowmeter data vs. wave steepness for the 3 thicknesses. 1 cm thickness case as blue crosses, 2 cm as green dots, and 3 cm as red diamonds.

3.4.2 Flame Height and Flame Heat Flux

Flame heights for each experiment were evaluated from video captured during using an image scaling MATLAB code and frames taken from video footage documenting the experiments. Specifics on the MATLAB code used are available in App. C.3.5. Video was captured with a Sony RX10 camera capturing 1440 by 1080 resolution images at 30 fps, taken from approximately 20 ft (6.1 m) behind the wavetank beach, and approximately 3 ft (0.91 m) above the water surface. This MATLAB operation first obtains color images from video frames and converts these to gray-scale. The image is then binarized by replacing the pixel greyscale values to 1 or 0 based on a threshold value. Otsu's

method [85] is used to determine the global threshold value, evaluated to be between 0.3 – 0.6 for different cases in this study. The variance in threshold is required due to changes in camera exposure during flame capture. Before ignition the camera auto-exposes to the relatively dark lab background, upon ignition the flame is overexposed and very bright, and after a few moments the camera automatically adjusts to properly expose the flame and plume region. If the grayscale pixel value is equal to or above the threshold value, a value of 1 is given to that pixel. Using this binarized image data the summation of the binary values at each pixel height is evaluated, starting from the fuel base. When the summation reaches zero this indicates the tip of the flame. The method also suggests that only the continuous flame height is calculated and does not account for flamelets leaving the continuous flame zone. An individual flame height is taken at a rate of 1 measurement per second over the duration of the burn.

Fig. 3.16 shows flame heights for the no wave and wave with $S = 0.017$, over the duration of the experiment. The wave with $S = 0.017$ is shown because this wave profile showed the maximum reduction in burning rate across all waves and is henceforth termed the ‘worst-case’ wave from these experiments. The points on Fig. 3.16 are obtained from an average of 30 seconds of flame height data. The shaded regions show 90% confidence intervals, obtained from the standard deviation also calculated for each 30 second averaging window. A ‘median’ wave, $S = 0.009$ is also shown for some context to the additional waves’ behavior. It should be noted that the total duration of experiments differed as the experimental method was refined, hence the difference in total burn time. A steady state region can be observed in the flame height data from about 2 minutes to 4 minutes for both experiments. During this region, fresh fuel was being fed into the burn. After the fuel replenishment is cut off a slight dip in flame height is observed, and shortly after a large increase is also observed which correlates with boilover. Most notable is that the worst-case wave has an overall shorter flame height than the no wave case at almost all times during the experiment.

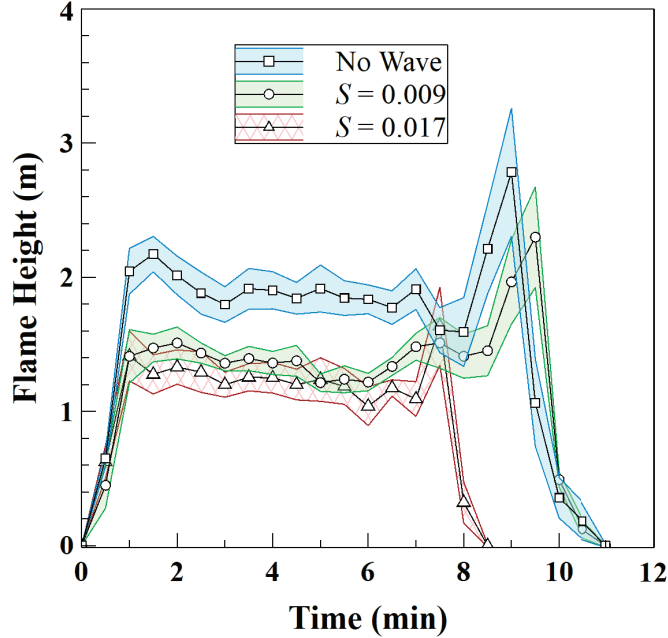


Figure 3.16: Flame height vs. time for the no wave case (squares), and two waves from this study: $S = 0.009$ (circles) and $S = 0.017$ (triangles), data from 1 cm thickness cases. Shaded regions show 90% confidence intervals of the flame oscillations.

Fig. 3.17 shows time-averaged flame images for three cases: baseline, $S = 0.009$, and $S = 0.017$ waves. These images were created by taking one frame from video footage every 30 seconds during the burn and compositing these frames over each other to create a single averaged frame that represents the flame over the course of the burn. Each case for which these images were created had similar duration (Baseline = 7.5 minutes, ($S = 0.017$) = 6.5 minutes). The boilover portions of each experiment were excluded from these average flame images.

Fig. 3.17 shows that the baseline flame is much taller than the wave case flames, and demonstrates a more narrow and tapered flame shape. The flame shape is typical of a gravity-driven buoyant plume expected from a pool fire of this shape and size. The wave cases, however, present a shorter flame, which appears less cone-shaped and less tapered at the base, remaining wider higher up in the intermittent flame zone. The flame also appears less bright and less intense at the base close to the pan edge. The flame height reduces from 1.8 m in the baseline case to 1.4 m with the steepest wave ($S = 0.017$), a reduction of 22%. The flame base width was measured approximately 10 cm

above the edge of the pan. Flame width with the steepest wave measured 91 cm, and in the baseline, case measured 75 cm, a 20% increase with the wave. Flame heights and widths were measured from time-averaged images like Fig. 3.17, with image data taken only from the steady state period of burning.

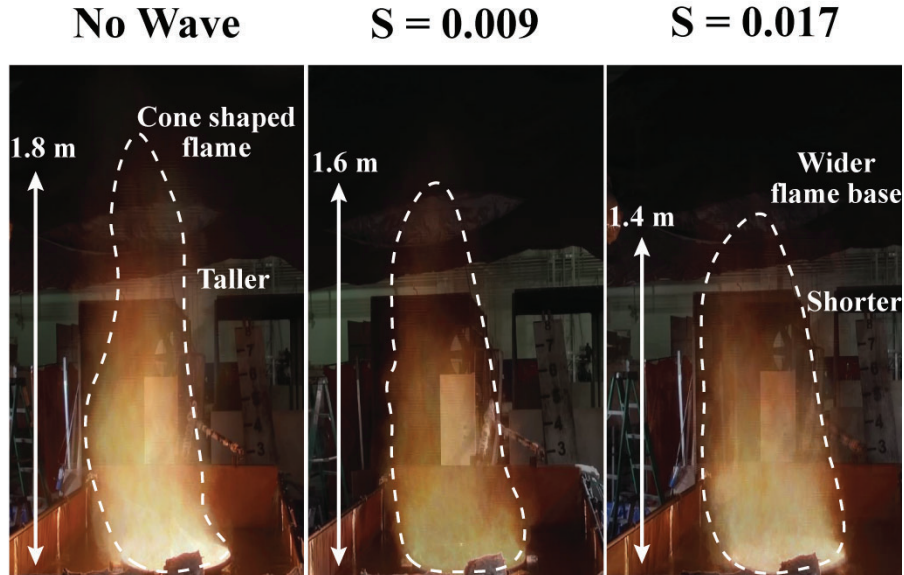


Figure 3.17: *Left* No wave, *middle* moderate wave ($S = 0.009$), and *right* worst-case wave ($S = 0.017$), displaying different flame behavior with and without the waves, different flame shapes being indicators of the different heat feedback distributions across the radius of the pool. Images taken every 30 seconds during burn, boilover excluded.

Table 3.3 and Fig. 3.18 show measured heat flux as a function of the normalized radial position (radius/ diameter [r/D]) for the 1 cm thickness experiments. Heat fluxes were experimentally measured by data obtained from the water-cooled Gardon-style heat flux gauges. Data represents 1-minute averages taken during the steady state period of burning, while fresh fuel was being supplied. It is observed that cases with waves have reduced heat feedback to the fuel layer close to the center line ($r/D = 0.06$). The baseline case has significantly higher center-line heat feedback and very similar edge-area heat feedback as the low-steepness wave cases. Further increasing of wave steepness has less of an effect on the center-line heat feedback but the edge-area heat feedback continues to decrease with further increasing steepness. These heat fluxes are further analyzed in

Section 3.5 to obtain an overall energy balance during steady-state burning.

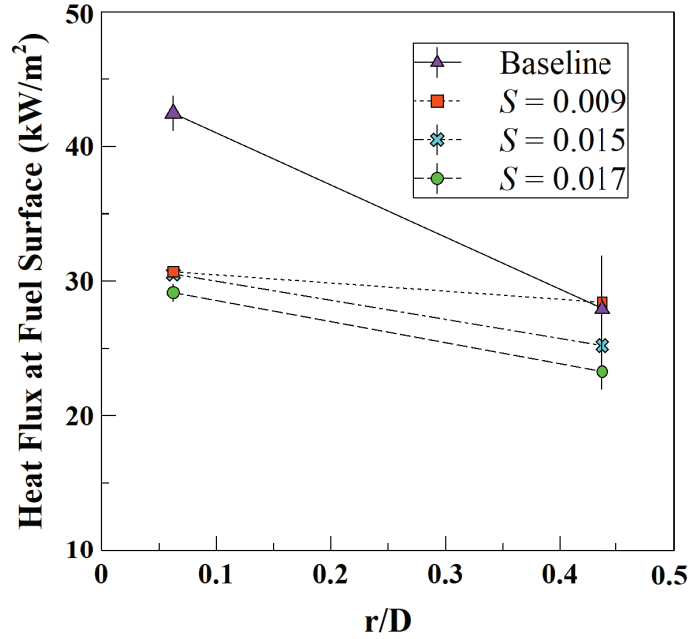


Figure 3.18: Heat flux vs. normalized position for 1 cm thickness tests. Values are obtained from steady-state regions of experiments and averaged over repeat cases.

Fig. 3.19 show an additional plot of heat flux vs. normalized radial position for the 2 cm thickness cases. The trend of decreasing heat flux with increasing wave steepness holds. However, the significantly reduced center line heat flux values seen in the 1 cm case are no longer observed. Center line values have reduced, but not enough to match the edge heat flux values.

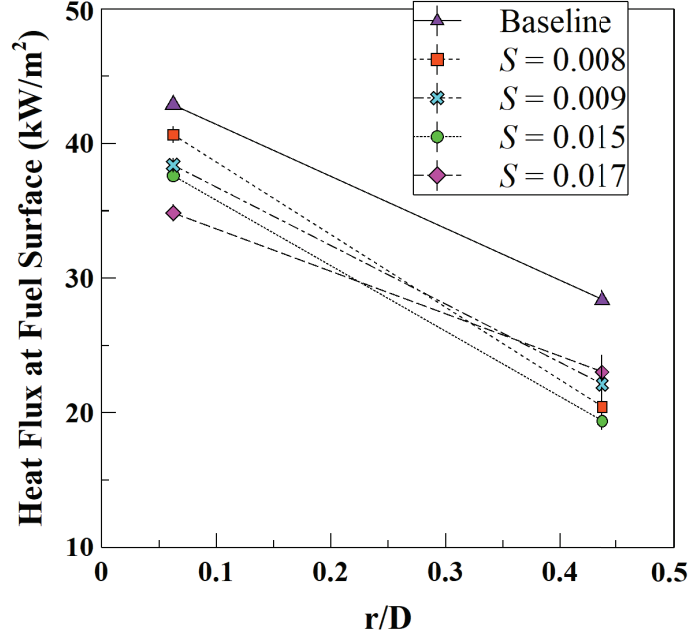


Figure 3.19: Heat flux vs. normalized position for 2 cm thickness tests. Values are obtained from steady-state regions of experiments and averaged over repeat cases.

Table 3.3: Heat flux vs. normalized position for 1 cm thickness tests. Values obtained from steady-state regions of experiments and averaged over repeat cases.

Steepness (S)	Heat Flux at Fuel Surface (kW/m^2)	
	Center ($r/D = 0.06$)	Edge ($r/D = 0.44$)
Baseline	42.5 + 3%	27.9 + 4%
0.0096	30.8 + 1%	27.2 + 3%
0.0153	30.5 + 1%	25.2 + 7%
0.0174	29.1 + 3%	23.3 + 12%

This change in center-line heat flux is assumed to be a direct result of the overall lowering burn rate of the cases with waves, in turn, caused by increased heat loss to the water sublayer. Less evaporating fuel leads directly to a lower heat release rate, which in turn corresponds to less heat measured at the fuel surface. This also then contributes to the lowering of mass flux of the fuel, and lowering the heat release rate, until this negative feedback loop reaches equilibrium. This change in behavior is also observed in the averaged flame photographs, where the no-wave flame is noticeably

taller, suggesting a longer diffusion length as a result of the higher amount of fuel evaporating into the burning region.

These heat flux values compare well with literature as shown in Fig. 3.20, although the literature on larger diameter kerosene fires with heat flux measured by radial position is limited. Bouhafid et al. 1991 tested 15 cm diameter kerosene fires with data presented in Fig. 3.20 [86]. Other studies included examined Toluene fuel burning heat flux, including Hamins et al. 1994, and Kim et al. 2019 [87], [88].

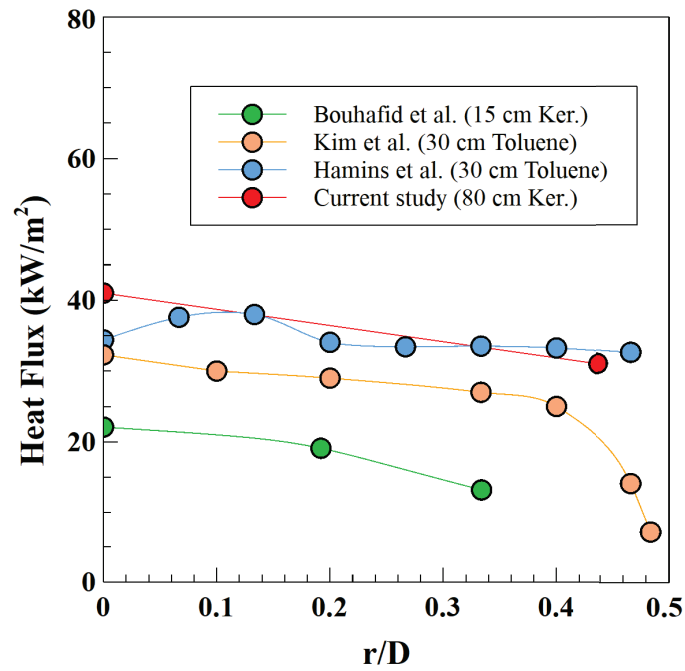


Figure 3.20: Heat flux vs. radial position for the no wave case compared to similar fires where data is available in literature.

Torero et al. 2003 provides a correlation for heat feedback to the fuel as a fraction of heat release rate presented in Eqn. 3.16 [25]. This relation is used to calculate the heat feedback fraction χ required to sustain the heat flux measured by the heat flux gauges in this experiment and presented in Fig. 3.20. For this experiment the average of the center and edge values is used. A flame temperature T_f of 1100 K is assumed for these calculations [25],

$$\dot{q}_s'' = \chi \frac{4\rho_\infty C_p (T_\infty g(T_f - T_\infty))^{1/2} d^{1/2}}{\pi}. \quad (3.16)$$

In similar studies, Chang 2022 and Farahani 2013 determined values for χ of 5.25×10^{-3} and 5×10^{-3} respectively [89], [90]. Chang 2020 additionally calculated values for \dot{q}_s'' of $3 - 4 \text{ kW/m}^2$ at a pool diameter of 10 cm. The 0.8 m in this study corresponds to an order of magnitude increase in heat feedback from the flame (\dot{q}_s''), with a value of χ calculated from Eqn. 3.16 to match the measured heat flux of $\chi = 1.6 \times 10^{-2}$, roughly double the heat feedback fraction measured by Farahani and Chang [89], [90]. Assuming similar conditions between Chang's 10 cm experiments and the 10 cm experiments examined in Ch. 2 of this work would offer an explanation as to the change in boilover behavior of the scales. In this work, at the small scale, boilover is only observed in the no wave case, whereas in the medium scale boilover is observed in every case, even with waves. This can be attributed to the order of magnitude increase in heat feedback, as measured by the heat flux gauges, as well as to the increase in total heat release rate feedback fraction.

3.4.3 Temperatures

Fig. 3.21 shows a temperature vs. time plot for a select few thermocouples of the no-wave case. Two thermocouples are from the gas phase, one at the fuel surface, three in the fuel layer, and one far down in the water sublayer. This chart makes evident that there is a period at the beginning of the burn, for about 300 seconds, where the fuel layer is still heating and has not reached equilibrium. From 300 s to 400 s the fuel is still being fed and steady-state burning has been reached. When the fuel feed has been shut off the fuel layer begins to thin, and this is evident from the rising temperatures leading to boilover.

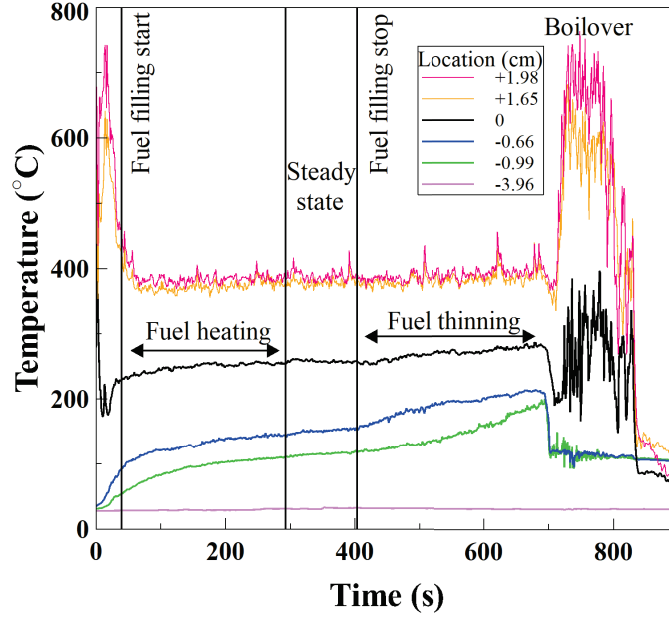


Figure 3.21: Temperature vs. time for the 2 cm thickness no wave case, showing regions of fuel heating, and steady-state burning. A clear period of fuel layer thinning is visible after fuel feeding is shut off.

Figs. 3.22 - 3.24 show temperature profiles for the baseline and worst-case wave measured during the steady state period of each experiment. This data was obtained from 30-second averages of the centerline thermocouple array data from a single experiment for each case. The two cases plotted in Fig. 3.23 are the 2 cm thickness cases for baseline and worst-case wave ($S = 0.017$), where Figs. 3.22 & 3.24 show the same cases for the 1 cm thickness and 3 cm thickness. The gray layer represents the kerosene fuel layer, and the blue shaded area represents the water sublayer location for these cases. The assumed boiling point ($T_B = 232^\circ\text{C}$) is shown with the vertical dashed line. Both the baseline and worst-wave case show good agreement between the measured and the assumed boiling point at the surface location.

During the fuel feeding period, little to no change was observed in the surface temperature for either the baseline or wave cases. Temperatures towards the bottom of the fuel layer show that wave cases reach an ambient temperature at shallower depths, suggesting higher amounts of heat loss to the water sublayer below. Fuel temperatures for the wave cases are in general cooler than

their non-wave counterparts. At the fuel-water interface, the wave cases also demonstrated higher gradients and overall cooler temperatures. Temperatures deeper in the water sublayer show almost no difference between baseline cases and wave cases.

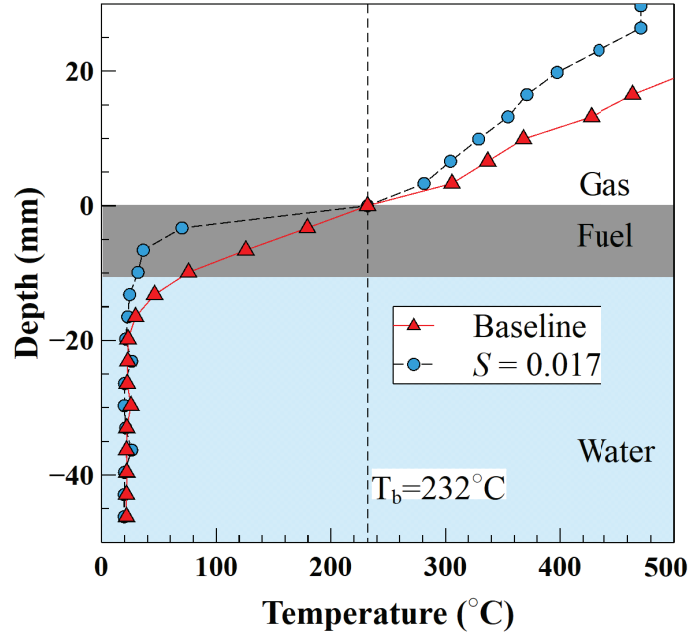


Figure 3.22: Temperature vs. depth for baseline and highest steepness wave case at 1 cm fuel thickness. Wave case demonstrates overall lower temperatures in the fuel layer, with nearly identical surface temperatures. Temperature data taken from a 1-minute average at 4-minutes post ignition.

Between the 1 cm and 2 cm cases, the difference in the interface temperature is evident, especially for the baseline cases. The temperature profile for the 1 and 2 cm cases remains similar across the same depth region. However, due to the thinner fuel layer in the 1 cm case, the interface temperature is much higher when the fuel layer is much thinner. This supports the hypothesis that thinner fuels have a higher heat loss to the water sublayer than thicker fuel layers, especially with the presence of waves.

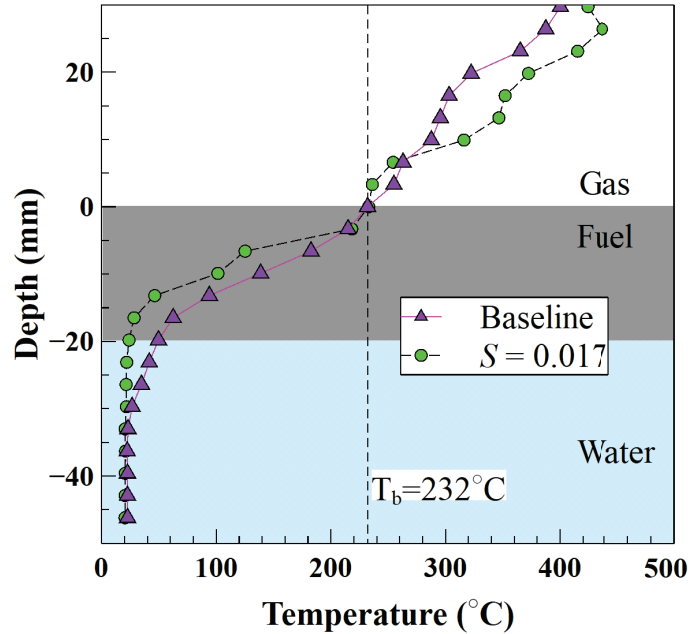


Figure 3.23: Temperature vs. depth for baseline and highest steepness wave case at 2 cm fuel thickness.

The 3 cm case shows a similar temperature profile to the 1 and 2 cm cases. Now with the thickest fuel layer, the temperature profile has almost reached ambient at the fuel-water interface. Suggesting that a wavy boundary condition on this surface will have less of an influence than on thinner fuels. This is hypothesized to be due both to the increase in fuel depth providing more ‘insulation’ with its lower thermal conductivity, from the moving water sublayer. Additionally, thicker fuels could be dampening the motion of the waves, having an effect on the physical movement of the water. Across these experiments, when wave steepness is used to examine the changes in burning behavior, it is assumed that all of the waves move the fuel physically to the same degree, that assumption may break down for thicker fuel layers, and especially those fuels of much higher viscosity.

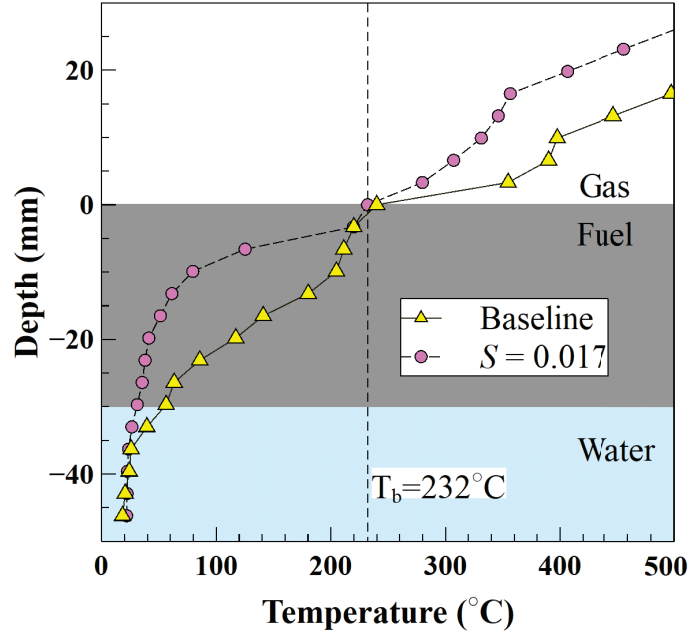


Figure 3.24: Temperature vs. depth for baseline and highest steepness wave case at 3 cm fuel thickness.

These temperature profiles across the 3 steady-state fuel layer thicknesses were all obtained at least 4-minutes post-ignition. Manually examining the fuel-water interface supports the hypothesis that thicker fuel layers should experience less of a change in burning behavior than thinner fuels. Thicker fuels have a more ‘insulated’ effect from the wave-imposed boundary condition, where more heat remains in the fuel layer and is therefore available as sensible or latent heat to support burning. Thinner fuels have higher fuel-water interface temperatures, suggesting that more heat is lost to the water sublayer through convection enhanced by the wave.

3.5 Burning Rate Formulation

Following Williams [91] the energy balance for the fuel layer:

$$\dot{Q}_s = \dot{Q}_{evap} + \dot{Q}_{sens} + \dot{Q}_{loss,water}, \quad (3.17)$$

Where \dot{Q}_s is the heat feedback from the flame which is absorbed by the fuel surface, \dot{Q}_{evap} is the

heat used to vaporize the fuel, \dot{Q}_{sens} is the sensible heat used to raise the temperature of the fuel from ambient to the boiling point T_B , and $\dot{Q}_{loss,water}$ is the heat lost from the fuel layer to the water sublayer. This heat balance is expressed schematically in Fig. 3.25.

The instrumentation for these experiments was selected such that each of these components could be measured experimentally to determine if and to what degree waves had an impact on each. The non-measured components are \dot{Q}_{evap} and \dot{Q}_{sens} which together would contain the \dot{m} to be calculated from the other experimentally determined values, Eqn. 3.18 follows where $C_{p,l}$ is the fuel specific heat, L_F is the latent heat of vaporization of the fuel, and \dot{m} is the mass loss rate:

$$\dot{Q}_{evap} + \dot{Q}_{sens} = \dot{m} \cdot L_F + \dot{m}C_{p,l}(T_B - T_\infty). \quad (3.18)$$

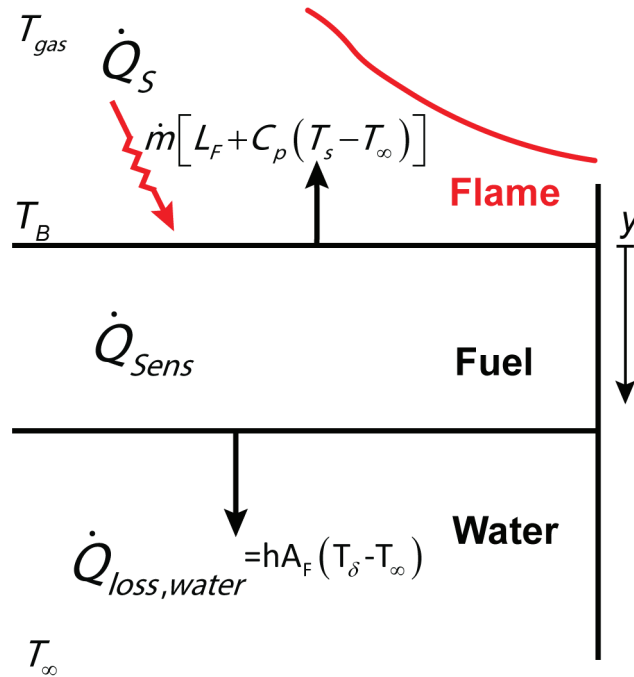


Figure 3.25: Diagram of energy balance under consideration. \dot{Q}_s is the heat input, \dot{Q}_{sens} is the heat used to raise the temperature of the replenished fuel from ambient to T_B , and $\dot{Q}_{loss,water}$ is the heat lost from the fuel to the water sublayer.

Heat feedback into the fuel layer \dot{Q}_s is determined from the heat flux gauge measurements taken

near the surface of the fuel. To represent the radial heat flux distribution across the surface, a Gaussian function is fit to the two heat flux measurement points. This Gaussian equation $\dot{q}''(r)$, now representing heat flux as a function of radial position, is then integrated over the area of the pool to determine total heat feedback to the fuel surface, Eqn. 3.19:

$$\dot{Q}_s = 2\pi \int_0^r \dot{q}''(r) r dr. \quad (3.19)$$

Heat loss to the water sublayer, $\dot{Q}_{loss,water}$, is calculated as convection across the bottom of the fuel layer, where the convective coefficient is obtained from a best-fit method to experimental temperature profiles, considering 1-dimensional conduction through the fuel layer. This method is similar to that used in Sec. 2.5 but here the fuel layer thickness is not a function of time, as the fuel layer was held at constant thickness during the experiment. This heat transfer coefficient is later compared to values obtained from the lumped capacitance heat transfer experiments detailed in Sec. A.4.3, as well as used to calculate a regression rate in conjunction with the heat flux data also acquired at the same time. The 1D heat conduction equation is considered for the fuel layer Eqn. 2.11:

$$\frac{\partial T}{\partial t} = \alpha \frac{\partial^2 T}{\partial y^2}, \quad (3.20)$$

In Eqn. 3.20 T is the temperature through fuel depth y , and α is the thermal diffusivity of the fuel. At the fuel surface ($y = 0$) we can assume a fuel temperature equal to the boiling point of kerosene ($T_B = 232^\circ C$), and at the fuel-water interface ($y = \delta$) heat loss is assumed to be purely convective, giving the boundary conditions:

$$\text{At } y = 0, T_B = 232^\circ C, \quad (3.21)$$

$$\text{At } y = \delta, -k \frac{dT}{dy} = h(T_\delta - T_\infty), \quad (3.22)$$

Where h is the convective heat transfer coefficient, T_B is the saturation temperature of the fuel, T_δ is the fuel-water interface temperature, and T_∞ is the ambient water temperature. The solution for these boundary conditions is given as:

$$T = T_B - \frac{h(T_\delta - T_\infty)}{k}y, \quad (3.23)$$

Given Eqn. 3.23 at fuel thickness ($y = \delta$), $T_\delta = T_B - \frac{h(T_\delta - T_\infty)}{k}\delta$. The temperature at the interface T_δ at time step t can be expressed as:

$$T_\delta = \frac{T_B + \frac{h\delta}{k}T_\infty}{1 + \frac{h\delta}{k}}. \quad (3.24)$$

With Eqn. 3.24 the interface temperature T_δ is a function of the fuel thickness δ , which for these experiments was held constant at 1 cm, 2 cm, and 3 cm. With thickness δ constant, T_δ is now a function of time and the constant known thickness. T_δ is also a function of the heat transfer coefficient h , which is shown to be influenced by wave steepness as shown in Sec. A.4.3. Here, similar to Sec. 2.5, the value of h in the model is determined by iteration until the value of T_δ at different time steps matches experimentally measured temperature values with the minimum possible summed errors as calculated with Eqn. 3.25.

$$\varepsilon = \sqrt{\sum_t [T_{\delta,experiment} - T_{\delta,model}]^2} = \sqrt{\sum_t \left[T_{\delta,experiment} - \frac{T_B + \frac{h\delta}{k}T_\infty}{1 + \frac{h\delta}{k}} \right]^2}, \quad (3.25)$$

These heat transfer coefficients are calculated for steady-state periods post ignition, then plotted vs. time in Figs. 3.26, 3.27, & 3.28. The lines on these figures represent the best-fit interface temperatures that are generated by the model. These temperatures are flat lines because the fuel layer thickness is not changing with time. Previously these values were a function of fuel layer thickness and heat transfer coefficient. With fuel layer thickness now constant the heat transfer coefficient is driving the interface temperature, and therefore the interface values are constant as we

are finding an average h value that satisfies the experiment over a select few timesteps. The points on these figures are the experimentally obtained temperature values from thermocouple data.

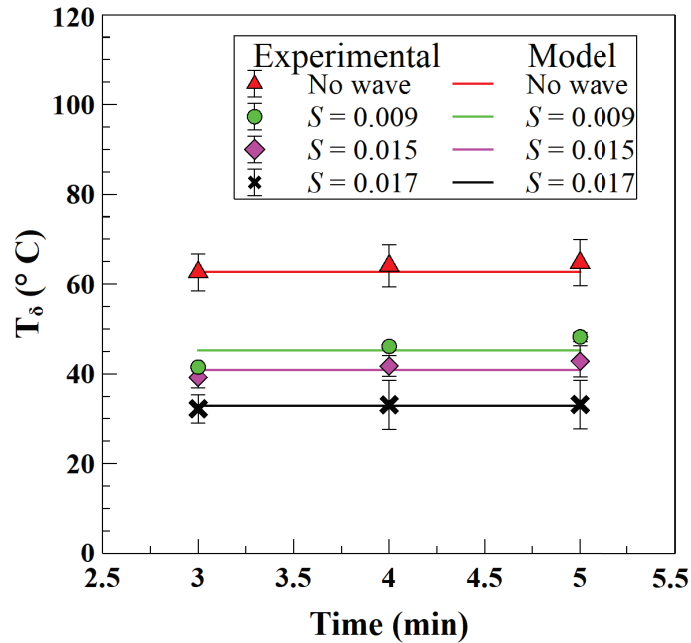


Figure 3.26: 1 cm fuel thickness fuel-water interface temperatures. Lines calculated from model, points obtained from experimental thermocouple data.

Also evident is the distance between the lines and points, representing the interface temperatures. Between the 1 cm and 2 cm cases we can observe that the 1 cm case has a larger difference between interface temperatures captured at different wave conditions. This suggests that the wave condition has a more dramatic effect at smaller fuel-layer thicknesses. Although for the 2 cm case it should be noted that the baseline case remains significantly above any of the wave cases, while the wave cases all have more similar interface temperatures. However, this distance between baseline and the first wave case is also larger at the thinnest case than at the other fuel thicknesses.

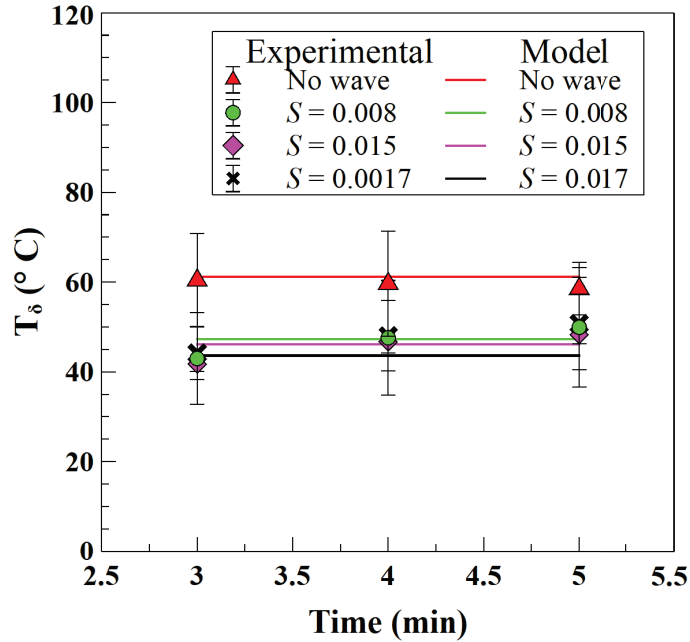


Figure 3.27: 2 cm fuel thickness fuel-water interface temperatures. Lines calculated from model, points obtained from experimental thermocouple data.

This behavior is also observed between the 2 cm and 3 cm cases. Here the difference in interface temperature between the no wave and wave case again narrows for the 3 cm fuel thickness. Although no other waves were tested at the 3 cm thickness, this was the highest steepness wave tested at the other thicknesses. These observations all support the hypothesis that thicker fuels act as more ‘insulation’ for the fuel layer from the convective boundary condition. Thus more heat is retained in the fuel layer for sensible and latent heats, which directly translates into higher mass loss rates and burning behavior.

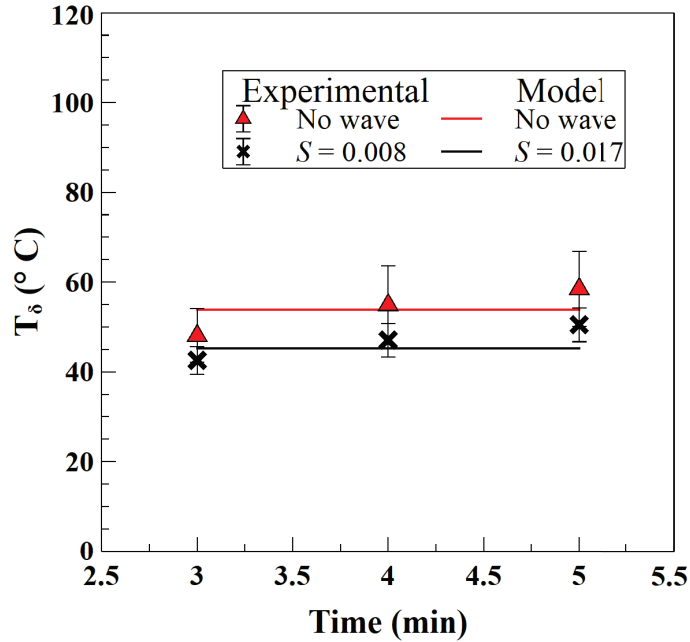


Figure 3.28: 3 cm fuel thickness fuel-water interface temperatures. Lines calculated from model, points obtained from experimental thermocouple data.

The calculated values of h are then plotted vs. wave steepness in Fig. 3.29a where the black dots are the linear approximation representing the sphere heat transfer experimental values obtained in Sec. A.4.3. The yellow points represent 1 cm fuel thickness, red 2 cm, and green 3 cm. Noticeable is that 1 and 2 cm fuel thicknesses both have higher maximums than the 3 cm fuel thickness case. Although this case only has one data point at a steepness of 0.017, so the trend is hard to observe. Fig. 3.29b shows the experimental heat transfer coefficient values from Sec. A.4.3 on the x-axis compared with their respective best-fit values from the temperature-based model developed in this section.

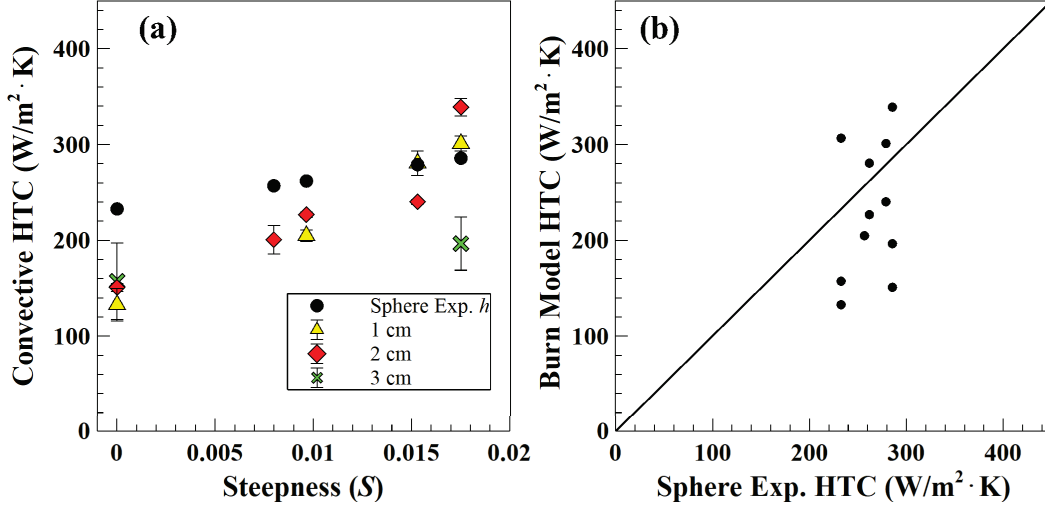


Figure 3.29: (a) Heat transfer coefficients calculated from each fuel thickness examined in this section, black dots show the linear fit values obtained from Sec. A.4.3. (b) Agreement between burn model heat transfer coefficient and experimentally determined heat transfer coefficient.

$\dot{Q}_{loss,water}$ is then calculated as a function of the interface temperature T_δ , heat transfer coefficient h , ambient water temperature T_∞ , and burning area A_F as in Eqn. 3.26

$$\dot{Q}_{loss,water} = hA_F(T_\delta - T_\infty), \quad (3.26)$$

The values for \dot{Q}_s and $\dot{Q}_{loss,water}$ are then used to calculate a mass loss rate \dot{m} (kg/s) in Eqn. 3.27. The Regression rate v in mm/min is calculated using \dot{m} from Eqn. 3.27 as $v = \frac{\dot{m}}{A_F \cdot \rho_l} \cdot 6 \times 10^4$,

$$\dot{m}[L_F + C_{p,l}(T_B - T_\infty)] = \dot{Q}_s - \dot{Q}_{loss,water}. \quad (3.27)$$

Fig. 3.30 shows each component from the calculations grouped by steepness, with the different shading in the bars representing the different thicknesses tested. Heat feedback from the flame \dot{Q}_s terms are in red, heat loss to the water sublayer $\dot{Q}_{loss,water}$ terms are in blue, and calculated regression rates are denoted by the crosses above each set of bars, with values plotted from the

secondary axis. Examining the baseline case the heat feedback to the fuel is seen to increase with increasing fuel layer thickness, as well heat loss to the water is observed to slightly decrease, with calculated regression rates also increasing with thickness. As steepness increases heat feedback to the fuel is also seen to decrease, the bars representing 2 cm heat feedback are seen to decrease from left to right with increasing steepness. As well heat loss to the water can be seen increasing with increasing wave steepness, although within each group the heat loss decreases with increasing thickness. Examining the highest steepness case ($S = 0.017$) for example we see the highest heat loss to the water of any case with the 1 cm thickness, but as fuel layer thickness increases this heat loss to the water decreases, and the 3 cm thickness case experiences a heat loss similar to the 2 cm cases at ($S = 0.0096$ & 0.015).

This demonstrates that the magnitude of heat lost to the water as a result of the wave is dependent both on the steepness of the wave, as well as on the thickness of the fuel it is interacting with. This is consistent with previous studies such as Garo et al. 2007 [80] which demonstrated maximum fuel regression rates were dependent on pool diameter as well as on initial fuel layer thickness, especially for very thin fuel layers which saw lower regression rates that increased and plateaued as initial fuel layer thickness increased. In the case of current experiments, it is hypothesized that the thicker fuels act as more ‘insulation’ between the hot upper layers close to the boiling point of the fuel and the cooler layers at the bottom interacting with the water sublayer. With thicker fuels more energy goes towards the fuel sensible heat, preheating the fuel before it vaporizes. With thinner fuels much of this heat is lost directly through the fuel and warms the water sublayer, which never undergoes evaporation.

It is also likely that in-depth radiation absorption plays a role in the difference between thinner and thicker fuels. Thicker fuels would act more optically opaque to impinging radiation than thinner fuels, and thus more energy would be available for sensible and latent heat than in thinner fuel cases. However, for this study in-depth radiation is not explicitly separated from total heat feedback to the fuel. Thus, this discrepancy is lumped into our heat feedback term \dot{Q}_s .

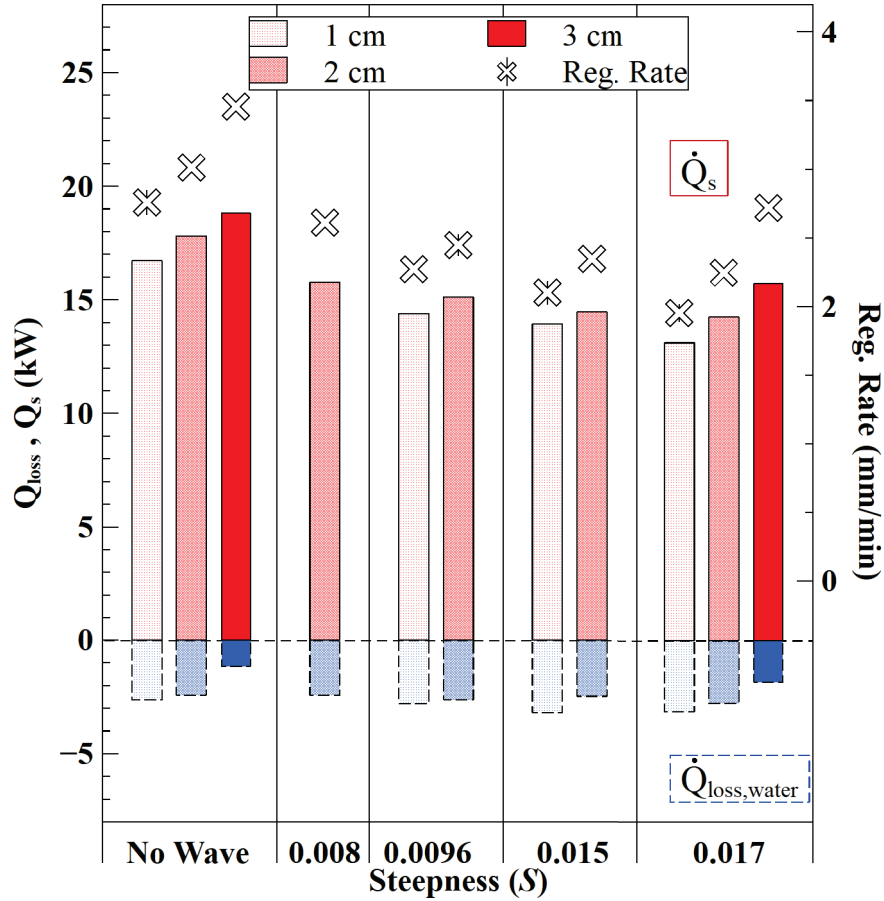


Figure 3.30: Experimentally measured \dot{Q}_s in red, and $\dot{Q}_{loss,water}$ in blue. Increasing thickness demonstrated both an increase in heat return to the fuel layer, and a decrease in heat loss. Calculated regression rates are black-and-white crosses on the secondary y-axis. Bars are grouped by wave steepness, and shaded by fuel thickness.

Fig. 3.31 shows the calculated vs. experimental regression rate. There is good agreement between experimental and calculated values, with the energy balance method slightly overpredicting the regression rate. Several factors are likely contributing to the overprediction of regression rates when using the energy balance method. First, conductive losses through the metal pan wall are not accounted for. This loss is likely relatively small but would lower the overall energy available for latent and sensible heat. It is also likely that for thinner fuels, in-depth radiation absorption would play a more important role. The heat flux gauges are assumed to measure all incident radiation heat feedback due to their high absorptivity black coating. A thinner fuel would be more optically

transparent to this incident radiation, absorbing less than the heat flux gauge. Accounting for this slight change would also correct the energy balance regression rate.

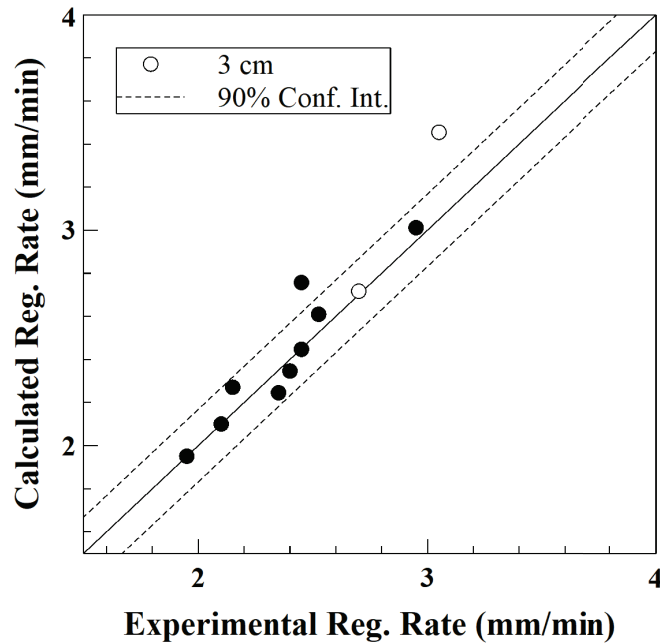


Figure 3.31: Calculated vs. experimental regression rates show relatively good agreement between the two values, with a tendency for the energy balance to over predict the regression rate.

Fig. 3.32 shows a schematic of the burn behavior as observed and measured in the results of these experiments. The no-wave burns demonstrate a more gravity driven plume, with the rate of fresh air entrainment at the base of the flame determined by the buoyant rise of combustion products. Additionally heat loss to the water in the no wave cases is dominated by the thermal diffusivity of the fuel and water. The burn case with waves shows a shorter and more uniform flame across the radius of the pool with an overall lower and more even heat feedback to the fuel layer. Heat loss to the water in the wave cases is dominated by the movement of water across the bottom of the fuel as well as internal mixing in the fuel layer caused by the waves. For thicker fuel layers (>3 cm) the internal mixing at the fuel-water interface does not influence the burning rate as compared to thinner fuels (~ 1 cm). Additionally, side to side and up and down movement induced by the waves increases the air entrainment at the base of the flame, widening and shortening the flame further. The waves

impact both the losses at the fuel-water interface as well as the air entrainment at the fuel-air interface. The current experiments are performed over a steepness range of $S = 0.008 - 0.017$ or one order of magnitude range. This range is comparable to conditions in the Beaufort Sea state of 1 which is a current guideline-recommended range for ISB operations. During this range the current study shows that the burning rate reduces with wave steepness linearly.

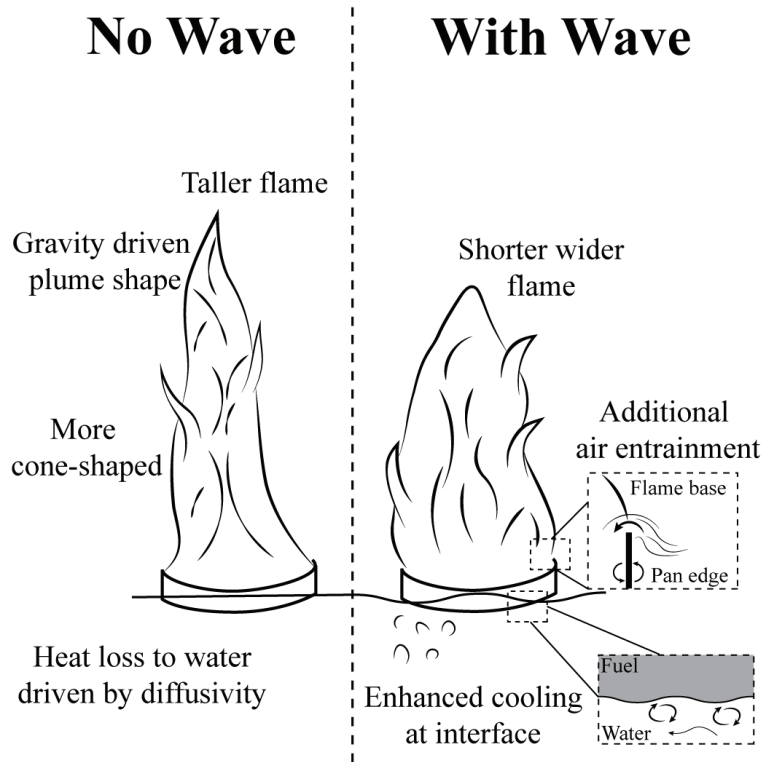


Figure 3.32: Schematic of altered flame and burn behavior with the addition of waves. *Left*, no wave case demonstrating a more gravity-driven plume. *Right*, wave case demonstrating a shorter flame and lower burn rate.

3.6 Conclusions

The burning behavior of kerosene fuel was studied with 80 cm diameter pool fires on a static and wavy water surface. A modular wavetank was constructed for experiments that could withstand burning and be disassembled for storage. Waves produced for this study ranged from 3.1 – 5.7 cm in height H , 1.83 – 5.71 m in length λ , with periods t_p from 1.1 – 2.5 seconds. A floating fuel containment ring allowed for control of the pool diameter and served as a platform for mounting thermocouple arrays and heat flux gauges for heat transfer data acquisition. A subsurface fuel

monitoring and filling system maintained a constant fuel layer thickness through a steady state portion of the experiments.

Experiments show a non-static water surface condition (waves) does influence burning. A decrease in flame height with waves is observed across all cases. A change in flame shape is also observed, with wave cases having shorter and wider flames and non-wave cases having taller and more cone-shaped flames. The change in flame shape accompanied a change in fuel surface heat feedback measured by heat flux gauges. Non-wave cases demonstrated higher centerline heat feedback than wave cases. Increasing wave steepness resulted in an associated reduction in total heat flux. Wave cases also measured lower in-depth temperatures in both the fuel and water layers, indicating an increase in heat loss and an increase in internal mixing.

An energy balance analysis was conducted using the heat flux gauge, thermocouple, and flowmeter data. Reasonable calculations for regression rate could be made using the heat flux gauge data for heat feedback and thermocouple data for heat loss. Comparisons with experimental flowmeter data were made and demonstrated good agreement, with calculated regression rates slightly over predicting experimental regression rates.

It is observed throughout the study that waves have a negative impact on a burning fuel floating on water. With 1 cm thick fuel layers the regression rate was reduced by a maximum of 27%, for 2 cm layers a maximum of 19%, and for 3 cm layers a maximum of 12%, for the constantly maintained fuel thickness cases. It is hypothesized that as fuel layer thickness increases the efficiency of heat extraction due to wave action is reduced, with thicker fuels being more ‘insulated’ from the moving water sublayer. This allows for more heat to be retained for sensible and latent heat rather than being lost to the water sublayer. Whether waves will continue to have this impact at larger scales is somewhat unknown. Previous studies with larger pool fires have noted the effect of waves at these scales. However, studies have yet to measure extensively the modes by which waves are reducing or impacting those burns.

CHAPTER 4

Burning Behavior of an Oil Slick with Waves ($D = 2$ m)³

4.1 Introduction

4.2 Experimental Apparatus

The wave tank used for testing is owned and operated by the U.S. Army Corps of Engineers Cold Regions Research and Engineering Laboratory (CRREL) in Hanover, New Hampshire (Fig. 4.1). The above-ground wave tank was positioned outdoors on a concrete pad for testing. These experiments were conducted from 9/21/2020 – 10/2/2020, average ambient temperatures ranged from 10°C to 22°C with one day of rain during which these experiments were not conducted. The primary wave flume measured 13.7 m long \times 2.4 m wide \times 2.25 m tall and during testing was filled to a water depth of about 2 m (Fig. 4.2). Hoover Offshore Oil Pipeline System (HOOPS) crude oil was used as fuel for these experiments with an initial thickness of 8 cm, crude oil density was measured to be $\rho_l = 784$ kg/m³, and is assumed to have the properties: $T_B = 180^\circ\text{C}$, $L_F = 250$ kJ/kg, and $k = 0.133$ W/m·K. Waves are generated by a computer-controlled wave board, and passive wave absorption at both ends reduces wave reflections. An American Fireboom was used to create a 1.9 m \times 1.7 m square floating burn area. Over 2200 kg of salt was used to achieve a salinity of 30 parts per thousand in the wave tank, mimicking ocean salinity. Observation video cameras were placed on a small hill located 15 m from the beach end of the wave tank. The wave generation mechanism can create waves up to 0.6 m high, with periods t_p ranging from 1.7 to 3.3 seconds.

³Contents of Ch. 4 currently under review for the **14th International Symposium on Fire Safety Science** under the title *Burning Capability of the Flame Refluxer under the influence of Waves*. Experiments presented in Ch. 4 were also part of a larger test program presented in the Final Report for BSEE Contract No. 140E0118R0007 *Advancing the Maturity of the Flame Refluxer Technology* [92].

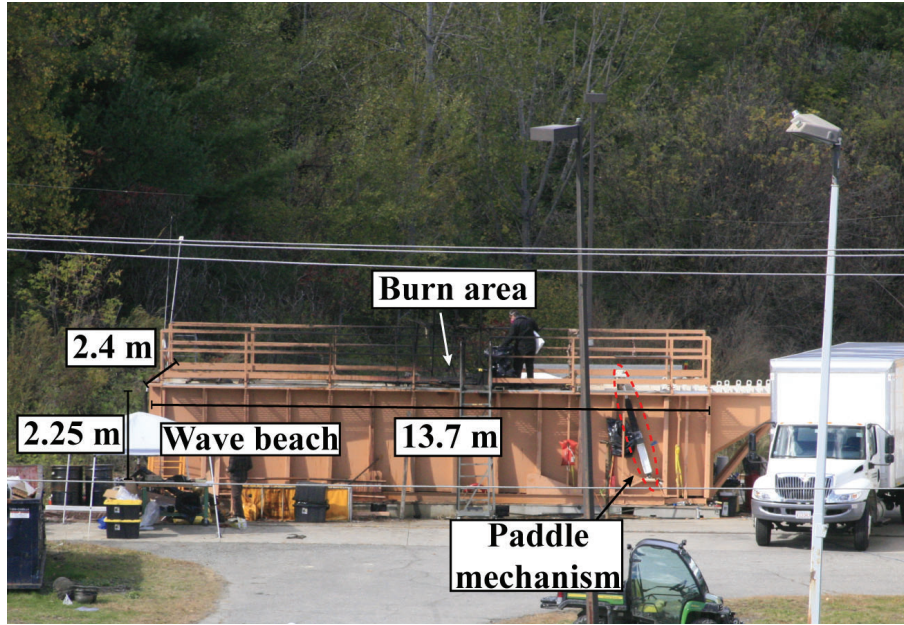


Figure 4.1: Overview of the wave tank used for these burn experiments at the U.S. Army Cold Regions Research and Engineering Laboratory facility.

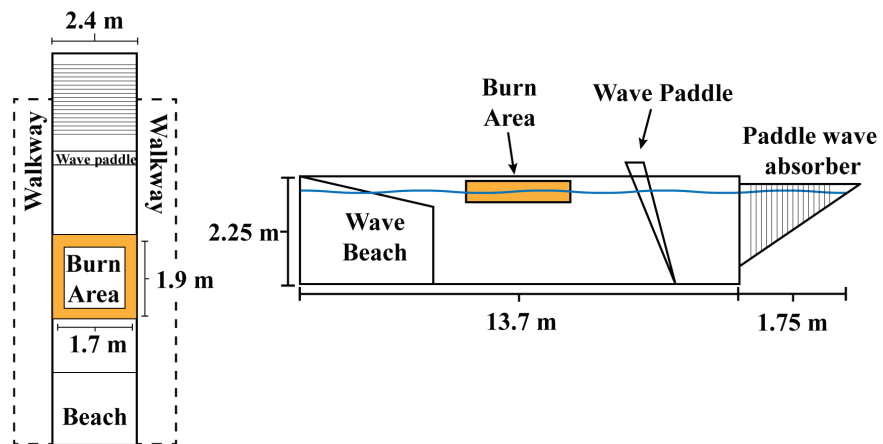


Figure 4.2: Schematic showing dimensions of the CRREL wave tank used in this study.



Figure 4.3: Top-down view of wavetank site during a burn, showing linear distances to key locations.

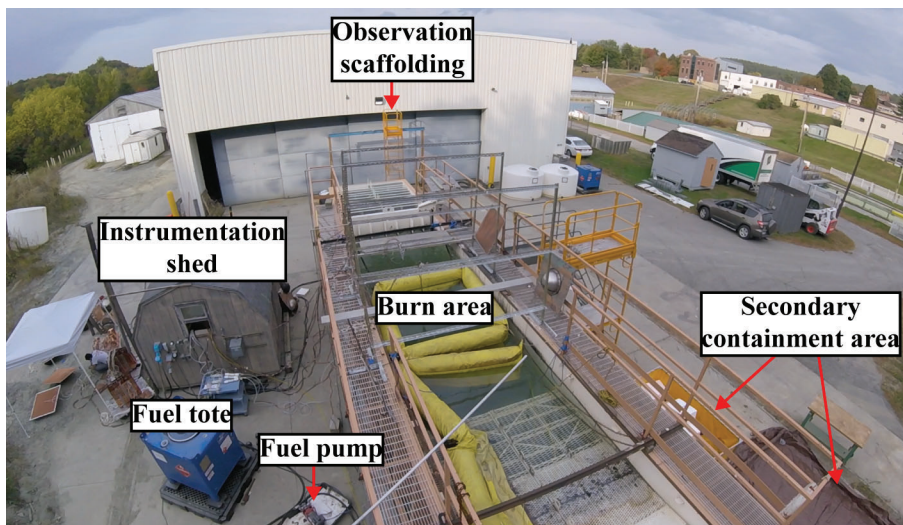


Figure 4.4: View of fully prepared testing location before experiments, showing fuel containment boom and other testing apparatus.

Fig. 4.5 shows a schematic of the grid-type FR used during these experiments. The FR consists of a 90 cm x 90 cm 'blanket' composed of a mat of 1 cm thick copper wool (0.0127 cm wire diameter) and 0.2 cm layer of kapok fiber sandwiched between two pieces of copper mesh (0.058 cm wire diameter, 0.13 cm gap). On top of this blanket is an interlocked series of copper sheeting creating a grid shape 50 cm tall, with four internal chimneys, and 3 exposed fins on each side (Fig. 4.5). Two

of these grid FRs were placed inside of the floating burn area for these tests. These prototypes were self-floating.

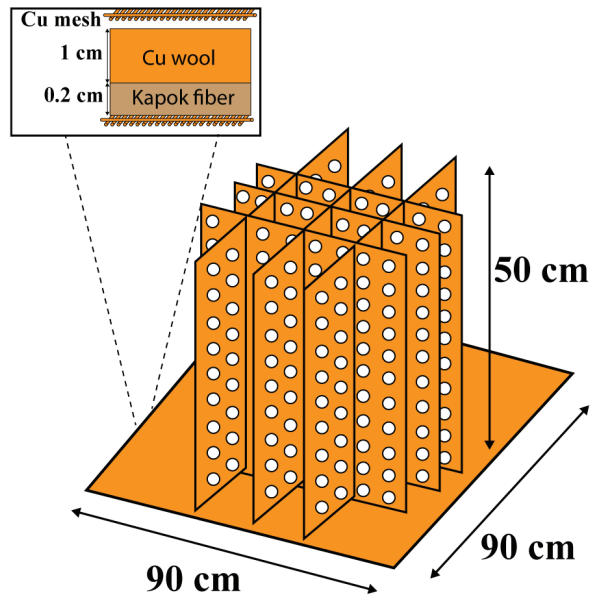


Figure 4.5: *Left*, grid-style FRs inside of the containment boom in the wave tank. *Right*, schematic of grid FR showing major dimensions.

Two thermocouple (TC) arrays were used to collect temperature data during the experiments. Fig. 4.6 shows each thermocouple array containing 31 18AWG Type-K thermocouples spaced 0.5 cm apart vertically. One TC array was mounted to each FR, such that it moved along with the water surface. One TC array was placed near the center of the burning pool, and the other near the edge, as seen in Fig. 4.6. These thermocouples were sampled for all cases at a rate of 1 Hz.

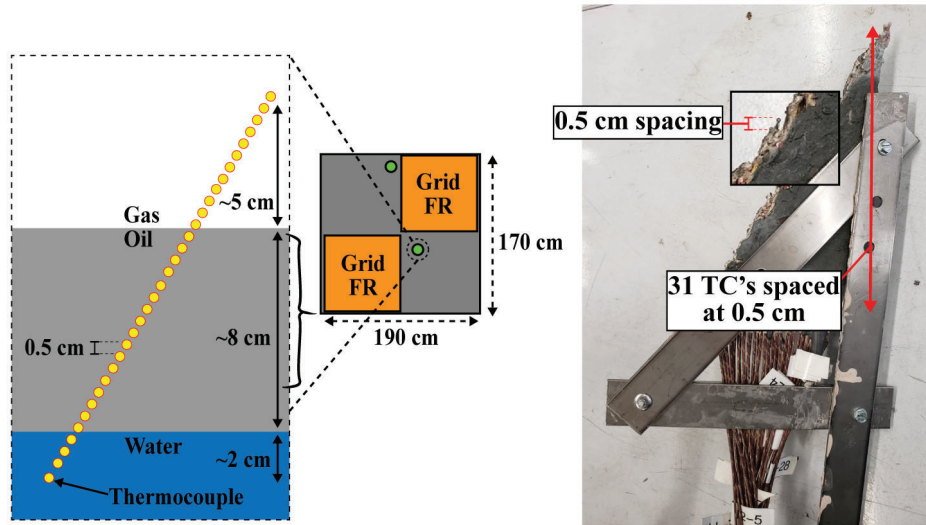


Figure 4.6: Primary instrumentation for these experiments was the thermocouples. *Left*, TC locations in the burning pool, one center and one edge location. *Right*, thermocouple tree showing the number and spacing of TCs.

An Akamina AWP 24-3 wave height gauge with a 1 m dual-sensing wire wave probe head was used to precisely measure the wave heights and periods for each wave used for experiments. Fig. 4.7 shows an example of the data collected from the wave gauge. Ideally, waves for testing would be linear, such that the wave profile is sinusoidal in shape, and where the wave peak and trough are equally spaced above and below the static water line. The non-linear wave shape is believed to be caused by wave reflections induced by the large floating American Fireboom placed in the wave tank. While this does not represent an ideal testing condition, it does represent a real-use scenario.

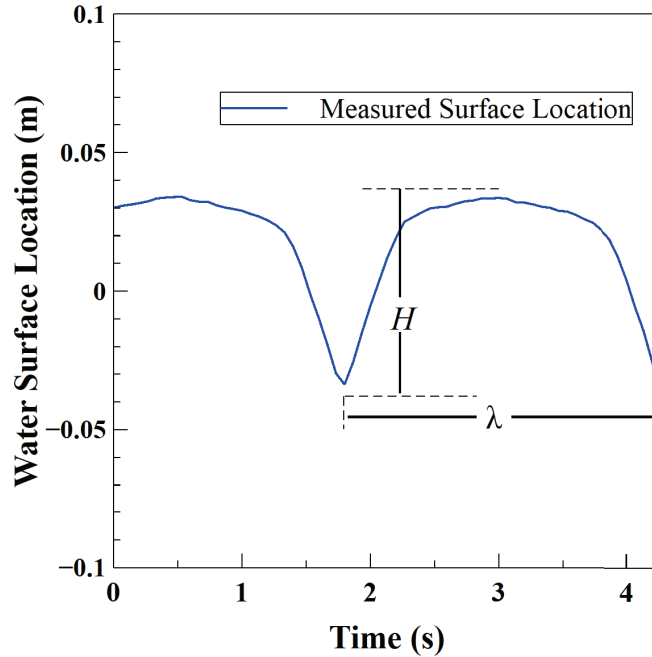


Figure 4.7: Water surface location vs. time showing one of the waves tested. The non-linear profile is due to reflections inside the burn area from the heavy oil containment boom.

Table 4.1 lists the parameters of the two waves which were selected for investigation at this scale in addition to the no-wave case. Wave 1 has a height of 0.07 m and a period of 2.5 seconds; with a shorter period and smaller height, this wave is the slightly ‘choppier’ of the two. Wave two has a height of 0.14 m and a period of 4 seconds, making this a longer more swell-type wave. The steepness of each wave is also presented and is calculated as before from Eqn. 2.1.

Table 4.1: Large Scale Wave Profiles Tested.

Name	Wave Height H (m)	Wavelength λ (m)	Period t_p (s)	Steepness S
No Wave	-	-	-	-
Wave 1	0.07	8.6	2.5	0.008
Wave 2	0.14	15.9	4	0.009

4.3 Results

4.3.1 Flame Height & Smoke Color Intensity

Fig. 4.8 shows image collages for the burning timelines of the no-wave and wave 2 cases. These image timelines are up until the first foaming behavior that the no-wave case experienced at 20 minutes. Evident from the image comparisons is the increase in flame height over time with the no-wave case. As the FR heats up and the burn reaches optimal performance, the flame height increases to a maximum of about 4.8 m. The wave case flame height also does increase throughout the burn, but only from an initial 1.5 m to a maximum of 4 m, indicating a loss in burning performance with the addition of the wave. This is especially evident in Fig. 4.9 showing the flame heights vs. time measured from the video. Fig. 4.9 (left) shows the flame heights over time for the grid with no wave and the grid with wave 1, showing a distinct reduction in flame height with the wave. This reduction is especially present from 2 to 10 minutes post ignition. Flame heights are extracted from calibrated binarized images of the flames every 30 seconds during video obtained of the burns. Values for the bar graph on Fig. 4.9 (right) are obtained by averaging the flame heights from 5 – 15 minutes post ignition, with error bars representing standard deviations of these values.

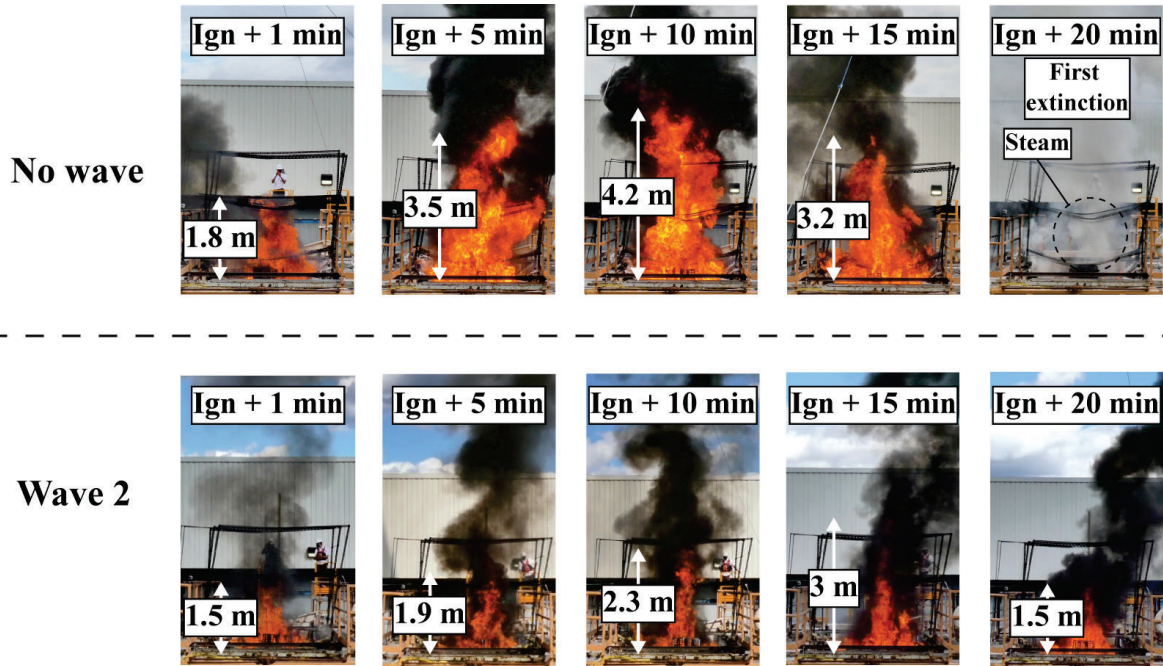


Figure 4.8: Images from the first 20 minutes of burning, for the no-wave case *top* and wave 2 case *bottom*.

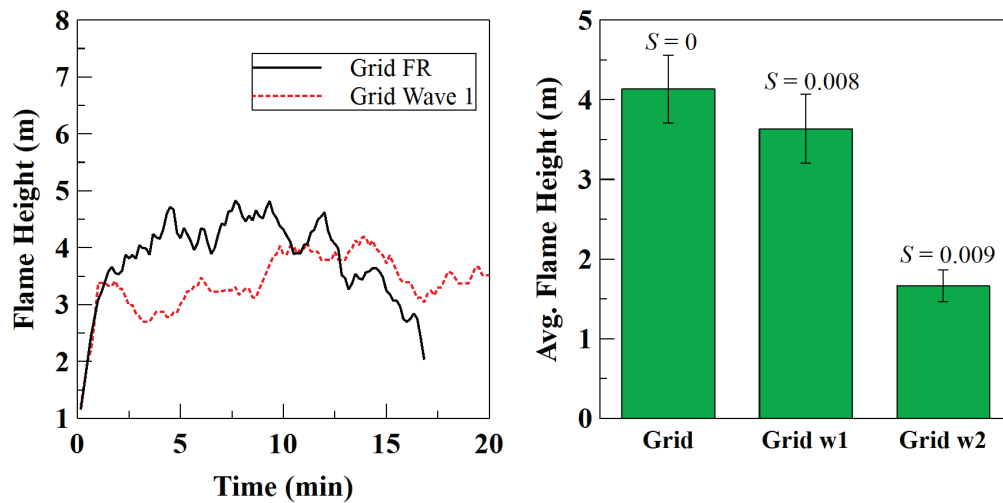


Figure 4.9: *Left*, flame height vs. time for the grid Flame Refluxer with no wave and with the wave showing the decrease in flame height with the presence of the wave, indicating a decrease in burn performance with the wave. *Right*, flame height averages from 5 – 15 minutes during the burn experiment, error bars display standard deviation in the dataset.

Table 4.2 shows the average flame heights from 5 – 15 minutes post ignition for the 3 cases, as

well as the global regression rate. The global regression rate is calculated in the same fashion as Eqn. 2.16. But is essentially the total fuel consumed, divided by the total burn time. Also evident is the white steam after the extinction of the no-wave case at 20 minutes past ignition.

Table 4.2: Regression rates and flame heights of 3 experiments, flame heights are averages of data taken from 5 – 15 minutes post ignition.

Name	Flame Height (m)	Reg. Rate v (mm/min)
No Wave	4.1 + 0.42	1.8
Wave 1	3.6 + 0.43	1.5
Wave 2	1.7 + 0.19	1.4

4.3.2 Temperatures

Fig. 4.10 shows temperatures vs. depth for the no-wave, wave 1, and wave 2 cases. This temperature data was obtained from 5, 10 and 15 minutes post-ignition and represents an average of 30 seconds of data. Standard deviations of temperature ranged from 1°C to 10°C for liquid temperature points. For the wave cases, no temperature data is available further than 5 cm below the surface, for these experiments the TC arrays were mounted higher on the FRs. The development of a clear thermal front is apparent in the no-wave case, with temperatures becoming stagnant at about 150°C and this thermal front moves downwards towards the water. However, during wave experiments, only the surface temperatures reach above 150°C, while in-depth temperatures gradually slope towards the ambient at approximately 15°C. It can also be observed that the steeper wave case has a more pronounced reduced temperature profile than the slightly less steep wave case.

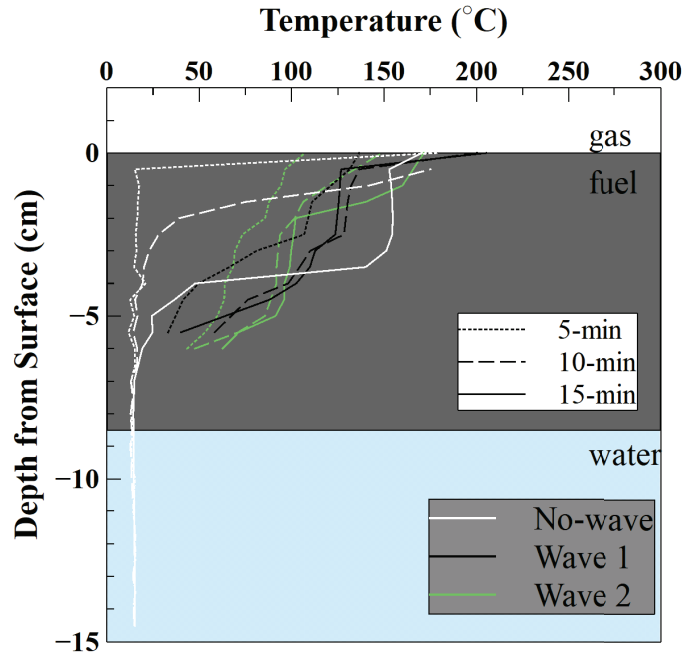


Figure 4.10: Temperature vs. depth plot for the grid without waves (white) and with waves (green and black). Without waves show a progressive temperature development throughout the experiment. Cases with waves show a much steadier linear temperature gradient through the depth of the fuel over the experiment.

Fig. 4.11 (left) shows the temperature data for the grid FR with no wave, plotted vs. time post-ignition. Most apparent on this chart are the large rises and falls of temperature starting at 20 minutes post ignition. During this experiment a series of extinctions and reignitions occurred, during which the oil layer experienced a dramatic foaming event resulting in extinction. Each line on this graph represents a thermocouple, separated 0.5 cm vertically from its neighbors. Also observable, especially in the first 20 minutes, is the regular interval of the rising of these lines one after another. This indicated the presence of a downward propagating thermal wave, which was being measured by the thermocouples. An estimate for fuel thickness at the first foaming event was made, and based on this estimate it was found that foaming occurred at an interface temperature of about 120°C. This is consistent with previous research that identified slightly superheated interface temperatures at the onset of boilover, such as Garo et al. 2007 and Laboureur et al. 2013 [24], [80]. Therefore, a threshold temperature of 120°C was decided upon for tracking the downward

propagating thermal wave. The boxes in Fig. 4.11 (left) represent the periods for which the thermal penetration rate is investigated, with the top of the box representing the threshold temperature.

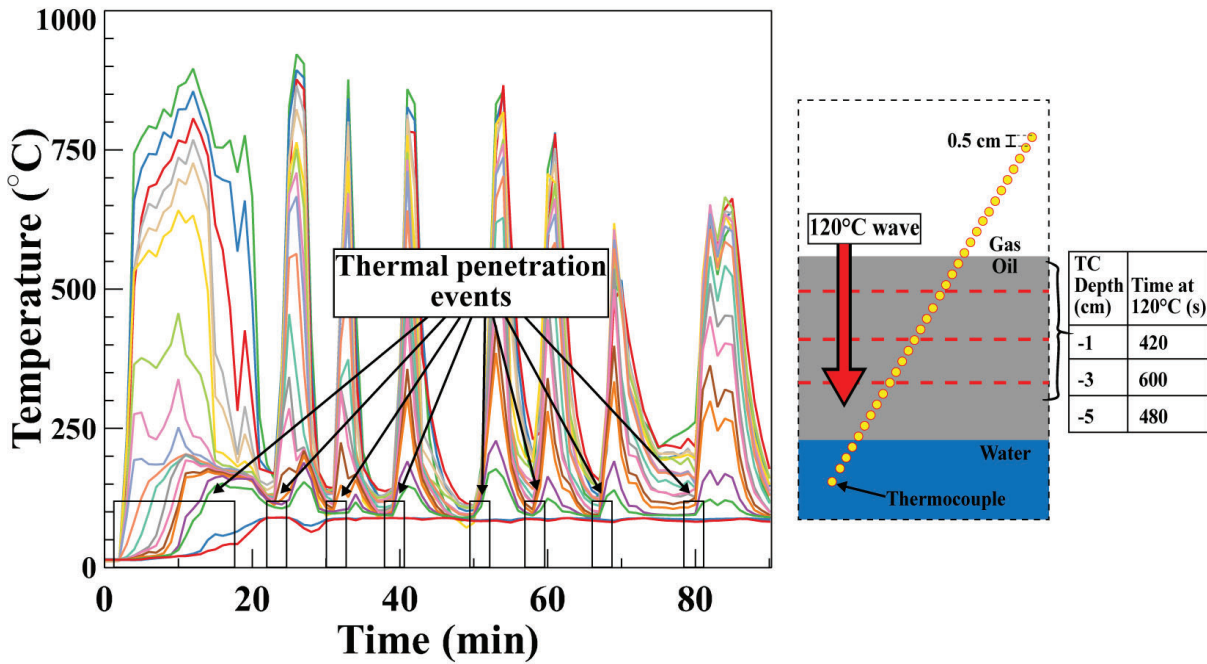


Figure 4.11: *Left*, temperature vs. time plot for a burn experiment, regions outlined in red indicate thermal penetration events of interest. *Right*, thermocouple diagram showing descending thermal front heating TCs at different times.

4.3.3 Thermal Penetration Rate

To conduct this analysis each thermocouple is examined discretely, and the time at which it exceeds 120°C is tabulated. The TC's depth from the surface and the time at which its recorded temperature exceeds 120°C are then plotted along with the other thermocouples and their depths and times. This is shown as an example for the grid with no wave in Fig. 4.12 (left). The linear slope of this plot is the thermal penetration rate in mm per minute. Eqn. 4.1 shows the linear fit used to extract thermal penetration rate, where t_i is the time to the threshold temperature (120°C) and y_i is the TC depth from the surface in mm, \bar{t} and \bar{y} are the averages of all time and depth points respectively. This analysis is conducted for both the center and outer thermocouple arrays where data is available, and for the wave cases. The bar chart, Fig. 4.12 (right), shows only the first thermal penetration rate for the no-wave case, as foaming and extinction did not occur for the wave cases. The chart of

depth from surface vs. TC time. Fig. 4.12 (left) demonstrates the consistency and linearity of the thermal penetration rate. While the right demonstrates that the wave has a measurable slowing effect on the thermal penetration rate, which increases with increasing wave steepness.

$$\text{thermal penetration rate} = \frac{\sum_{i=1}^n (t_i - \bar{t})(y_i - \bar{y})}{\sum_{i=1}^n (t_i - \bar{t})^2}. \quad (4.1)$$

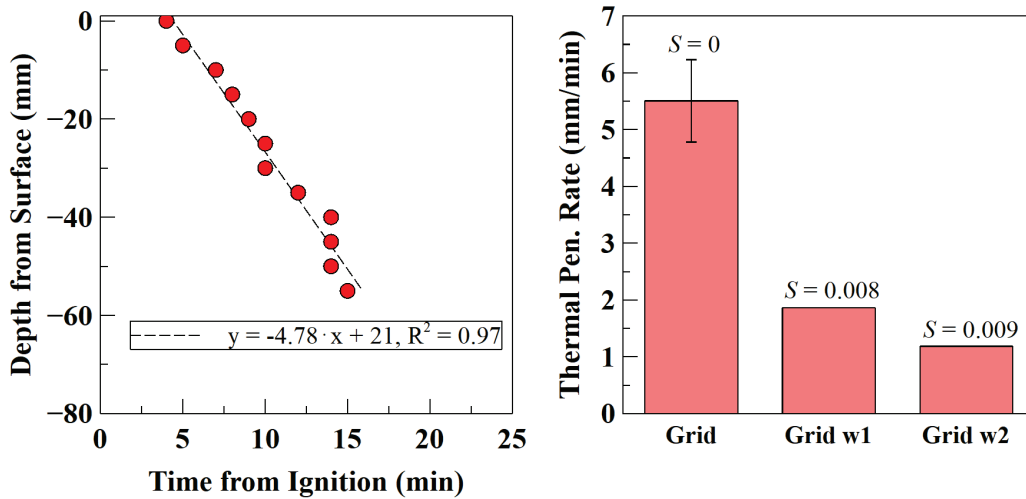


Figure 4.12: *Left*, depth from surface vs. time from ignition for the grid with no wave, points are plotted for the time at which the thermocouple at that depth rises above 120°C. The slope of this line is the thermal penetration rate in mm/min. *Right*, thermal penetration rates for the grid FR at stagnant water, wave 1, and wave 2. Demonstrating a clear decrease in thermal penetration rate with increasing wave steepness.

4.4 Burning Rate Formulation

Fig. 4.12 shows that the examined waves have a measurable effect on the thermal conditions in the fuel during burning. A simple model is then examined for the burning behavior, to quantify a regression rate produced by a thermal energy balance in the fuel layer. Using the same method as in Sec. 2.5 the heat transfer coefficient at the fuel-water interface is calculated from experimentally obtained temperature profiles from examining a 1-dimensional heat conduction equation, Eqn. 4.2.

$$\frac{\partial T}{\partial t} = \alpha \frac{\partial^2 T}{\partial y^2}, \quad (4.2)$$

The boundary conditions and solution for this equation are detailed in Sec. 2.5 but the analytical solution for the interface temperature T_δ is represented as Eqn. 4.3, where T_B is the fuel saturation point, h is the convection coefficient, T_∞ is the ambient water temperature, and δ is the fuel thickness as estimated by the global regression rate.

$$T_\delta = \frac{T_B + \frac{h\delta}{k}T_\infty}{1 + \frac{h\delta}{k}}. \quad (4.3)$$

With Eqn. 4.3 the interface temperature T_δ is a function of the fuel thickness δ , which is itself a function of time. The thickness as a function of time, $\delta(t)$, is approximated using the global regression rate v , Eqn. 4.4. Which is determined by the burn time, and initial and final thicknesses respectively δ_i , δ_f .

$$v = \frac{\delta_i - \delta_f}{\text{burn time}}, \quad (4.4)$$

$$\delta(t) = \delta_i - (v \cdot t). \quad (4.5)$$

This follows that T_δ is a function of δ which is itself a function of time. T_δ is also a function of the heat transfer coefficient h , which is shown to be influenced by wave steepness as shown in Sec. A.4.3. Here the value of h in the model is determined by iteration until the value of T_δ at different time steps matches experimentally measured temperature values with the minimum possible summed errors as calculated with Eqn. 4.6:

$$\varepsilon = \sqrt{\sum_t [T_{\delta,experiment} - T_{\delta,model}]^2} = \sqrt{\sum_t \left[T_{\delta,experiment} - \frac{T_B + \frac{h\delta}{k}T_\infty}{1 + \frac{h\delta}{k}} \right]^2}. \quad (4.6)$$

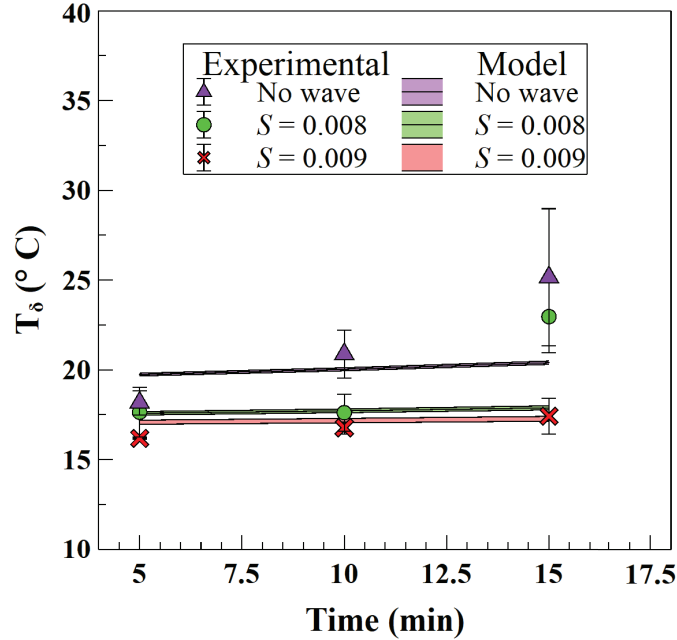


Figure 4.13: Interface temperature T_δ over time, point represent experimentally measured data, lines represent model best-fit interface temperatures from Eqn. 4.3

Fig. 4.13 shows the interface temperatures over the duration of the experiment for the large scale. The values are obtained from gathering thermocouple data at the estimated fuel thickness from Eqns. 4.4 & 4.5. The points with error bars (triangles, circles, and crosses) on this figure represent experimentally measured interface temperatures for the different wave cases. While the lines and shaded error regions represent calculated interface temperatures from the error reduction analysis and Eqn. 4.3. Error bounds for the calculated values represent the standard deviation from the analysis of the inner and outer thermocouple arrays, not the error between the calculated and experimental values.

From Fig. 4.13 it is observed that interface temperature decreases with increasing wave steepness, although due to the thickness of fuel used the change is less drastic than seen in the thin layers used at the small scale. It is also noted that the trend of interface temperature vs. time for each individual case flattens with increasing steepness. With no wave the interface temperature noticeably increases with time, eventually leading to water boiling at the interface causing foaming.

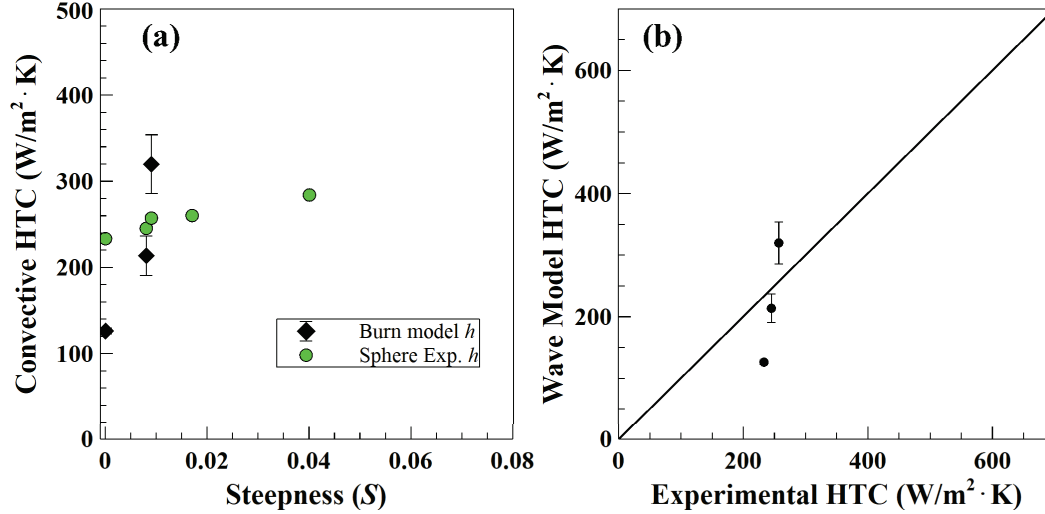


Figure 4.14: (a) Experimental and wave-model heat transfer coefficients vs. wave steepness. (b) Agreement between burn model heat transfer coefficient and experimentally determined heat transfer coefficient.

Fig. 4.14(a) shows the h values calculated in this analysis as green dots, these values are calculated from the minimized error analysis above, resulting from best-fit matches to experimental temperature profiles, which is why they are called ‘experimental’ values. The black diamonds on this figure represent heat transfer coefficient values generated by using the linear fit approximation generated in the wave heat transfer sphere experiments in Sec. A.4.3, Fig. 2.8(b) plots each of these two values against each other to examine their linearity.

It is apparent from Fig. 4.14(a) that the calculated heat transfer coefficient increases with increasing wave steepness. This was hypothesized to be true due to the reduction in burning rate, change in temperature profile, and suppression of boilover. However, examination of the interface temperature further supports this conclusion as the heat transfer coefficient would need to increase to explain the continued reduction in interface temperature with increasing wave steepness. In the large-scale experiments, this is also supported by the measurement of a reduction in the thermal penetration rate, a parameter only able to be measured at this stage due to the significant fuel thicknesses used.

4.5 Conclusions

This study presents new results from 1.7 m x 1.9 m burn experiments conducted in a large-scale

wave tank with Flame RefluxerTM technology. Burn experiments were conducted with HOOPS crude oil layers 8 cm thick, with two waves and a no-wave condition. The burn experiment without waves exhibited unique foaming behavior which led to the extinction of the burn, and later re-ignition once the foaming subsided, foaming was not observed with the wave cases. A method for calculating the thermal penetration rate from thermocouple data is presented. The thermal penetration rate is measured to decrease with the presence of waves. A simple energy balance model is presented to quantify the effect of the wave. This model demonstrates waves do have an increased cooling effect with wave steepness, causing higher heat loss to the water sublayer than in the no-wave case. The decrease in thermal penetration rate also coincides with an increase in wave steepness.

CHAPTER 5

Conclusions

5.1 Summary

In this study the influence of waves on a burning fuel floating on water is investigated. Three burning sizes are used to investigate the effect of scaling on the impact of a wave on burning. Small scale (10 cm diameter) experiments were conducted with dynamic fuel layers of kerosene fuel with an initial thickness δ_i of 0.6 cm. Medium scale (80 cm diameter) experiments were conducted with dynamic kerosene fuel layers ($\delta_i = 2$ cm), and fuel layers maintained at a constant thickness ($\delta_i = 1, 2$ & 3 cm). Large scale experiments were conducted with crude oil with approximately 2 m diameter pools, and dynamic fuel layers with initial thickness $\delta_i = 8$ cm.

In all scales, surface water waves are observed to reduce the burning of a fuel floating on water. This reduction is measured in global burn rate reduction, flame height reduction, change in boilover behavior, and lower fuel temperatures. At the small scale the global regression rate is calculated with initial and final fuel thickness, and time to boilover data. In medium scale dynamic fuel thickness experiments the fuel regression rate is also calculated with initial thickness, thickness at boilover (from underwater camera), and time to boilover data. The medium scale experiments with constant fuel layer thickness have a measured regression rate obtained from flowmeter data required to keep the fuel at a constant thickness. In the large scale global regression rate is obtained with initial fuel thickness, fuel residue, and burn time data. Normalized regression rates are calculated by dividing the regression rate of each case by the regression rate of the no wave case. Fig. 5.1 shows the normalized regression rates vs. wave steepness for all of these cases. Across the experiments examined in this work waves decreased the fuel regression rate proportionally across the three scales. Also shown on Fig. 5.1 are tests conducted in the large scale with 25% water emulsions and HOOPS crude oil.

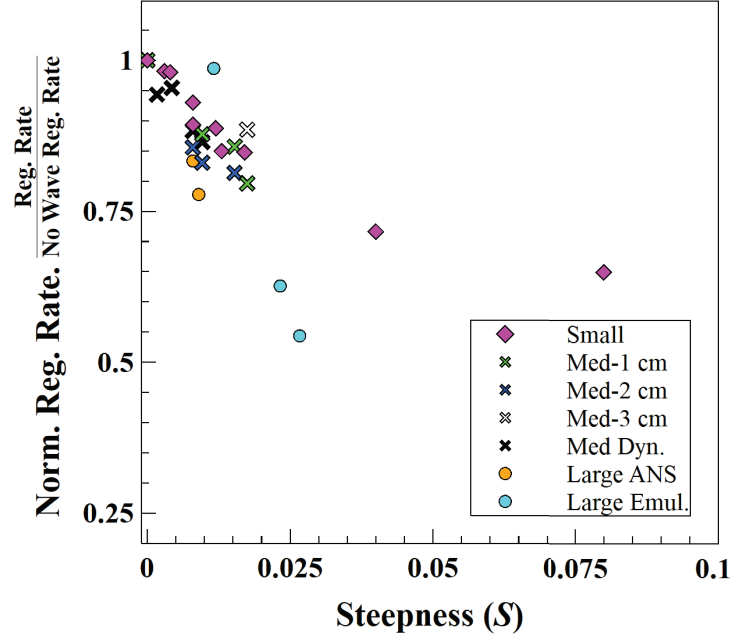


Figure 5.1: Normalized regression rate for the 3 different scales vs. wave steepness.

The non-dimensional parameter, wave steepness, was correlated to a reduction in burning behavior associated with waves. The wave steepness is defined in Eqn. 5.2 and is the wavelength divided by the wave height. For linear water waves of regular period and wavelength, with a known water depth; the wavelength λ is calculated with the dispersion equation (Eqn. 5.1). Where the wavelength is an iterative solution depending only on the period t_p and the tank depth z [4], [5].

$$\lambda = \frac{gt_p^2}{2\pi} \tanh \frac{2\pi z}{\lambda_{old}}, \quad (5.1)$$

In this way the wave steepness (Eqn. 2) captures both the magnitude and frequency of the wave motions. The distance of the motion is the wave height, which for deep water waves horizontal motions are approximately equal to vertical motions. As well the frequency of oscillations is captured in the wavelength, as the wavelength is purely a function of the wave period as shown in Eqn. 1,

$$S = \frac{H}{\lambda}. \quad (5.2)$$

At each scale a 1D heat transfer model is examined and used to calculate a convective heat transfer coefficient based on mass loss rate and fuel-water interface temperature. The calculated heat transfer coefficient at each scale increases with increasing wave steepness, as shown in Fig. 5.2.

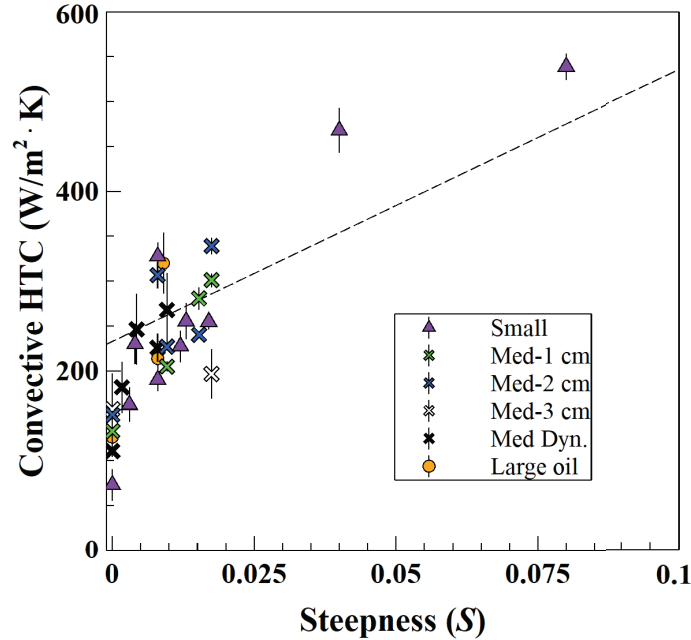


Figure 5.2: Heat transfer coefficient (HTC) vs. wave steepness. Heat transfer coefficient is the calculated value from each phase. Dashed line is from linear fit to sphere experiments data from Sec. A.4.3.

Fig. 5.2 shows that the heat transfer coefficient, regardless of scale, demonstrates relatively the same magnitude. And is a function of the wave steepness H/λ which represents both the distance and frequency of the oscillating flow. While the magnitude of total heat loss to the water sublayer will scale with pool diameter, this loss is proportional to the scaling of the incident heat flux with pool diameter. Agreeing relatively well with maximum regression rates predicted by Blinov and Khudyakov 1961 based on pool diameter [12].

As a final step a linear fit is applied to the sphere experiments heat transfer coefficient. Fig. 5.3 shows the sphere experiments h values as the red dots, along with the heat transfer coefficients calculated from the burning models throughout this study. This linear fit is then used to calculate values for h for the medium scale constantly replenished fuel layers. This is the only set of experiments where

the heat feedback to the pool was measured reliably. The h values and interface temperatures are then used to calculate the heat loss to the water. The regression rate is then recalculated with the new values for heat loss to the water sublayer and compared to the regression rates calculated with their discrete burn model h values (Fig. 5.4).

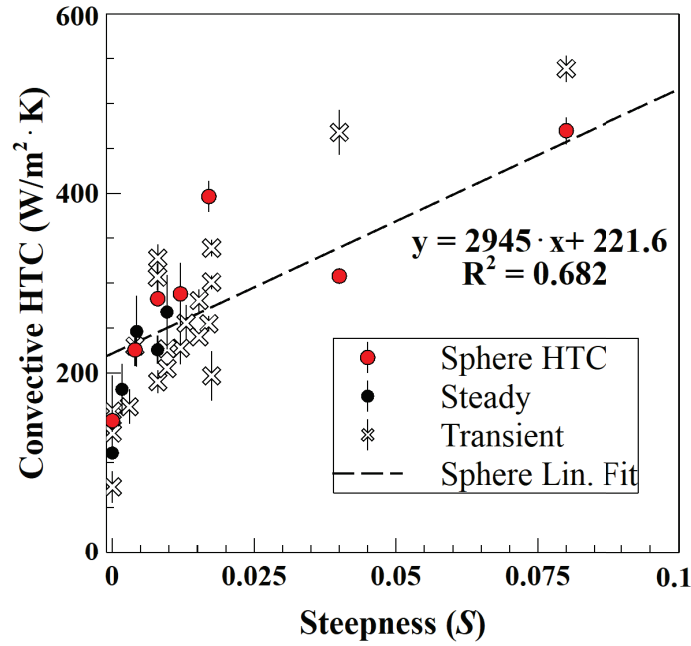


Figure 5.3: Heat transfer coefficient determined from burning models and from sphere experiments data.

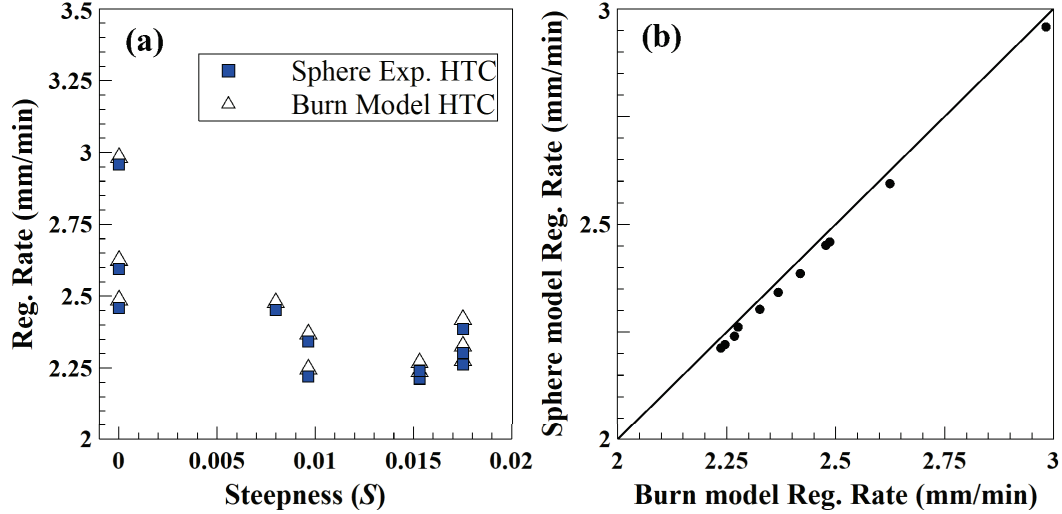


Figure 5.4: (a) Regression rate determined from medium scale burning model with discrete h values calculated for each case (triangles) and regression rates determined from the sphere linear fit approximation (blue squares). (b) Regression rates from the medium scale, x-axis calculated from linear fit to sphere experimental HTC data, y-axis calculated from burning model HTC as presented in Ch. 3.5.

Fig. 5.4 demonstrates that it is not necessarily required to complete burning experiments to espouse the effect of a wave, or increased heat transfer coefficient h , on burning. If one could make some assumptions about the change in heat feedback supplied to the fuel layer, the changes in water sublayer cooling could be modeled with relative accuracy from a linear approximation from non-burning experiments.

5.2 Future Works

This work investigates the burning behavior of a fuel floating on wavy water, with additional work on an evaporating fuel, investigation of wave behavior, and an experiment to investigate the heat transfer coefficient induced by waves. The author acknowledges the difficulty and limitations in making measurements of burning behavior, especially that of floating fuel on water. There is much room past this work for future investigations of fuels floating on wavy water, especially due to the lack of existing work on this topic.

The first and most prominent potential avenue for future research is to incorporate different and more realistic wave profiles. All of the waves examined in this work had a sinusoidal profile and

were as regular and linear as possible. In reality, the most regular periodic water waves have a trochoidal profile, otherwise known as a Gerstner wave [60], [93]. There are also additional wave profiles that are described by their own respective approaches to water wave theory, such as Stokes waves and cnoidal waves (Fig. 5.5).

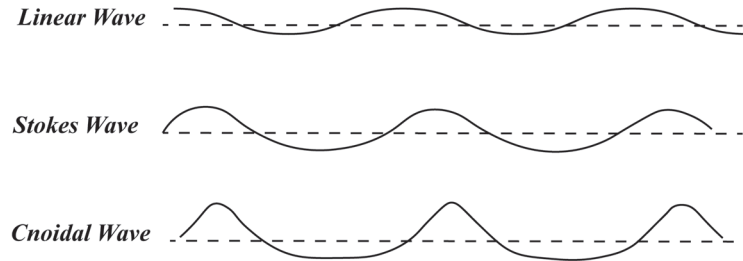


Figure 5.5: Various wave profiles defined by differing wave theory, compared with the linear sinusoidal wave examined in this work.

As well, at any one moment, an ocean surface is composed of a distribution of many waves of differing parameters [55]. Fig. 5.6b shows one of these distributions for wave heights measured during Hurricane Andrew in 1992 [94]. Fig. 5.6a shows the irregular water surface location also measured during Hurricane Andrew. Incorporating a water surface condition more analogous to a real ocean surface condition would serve to further the understanding of a wavy surface on burning.

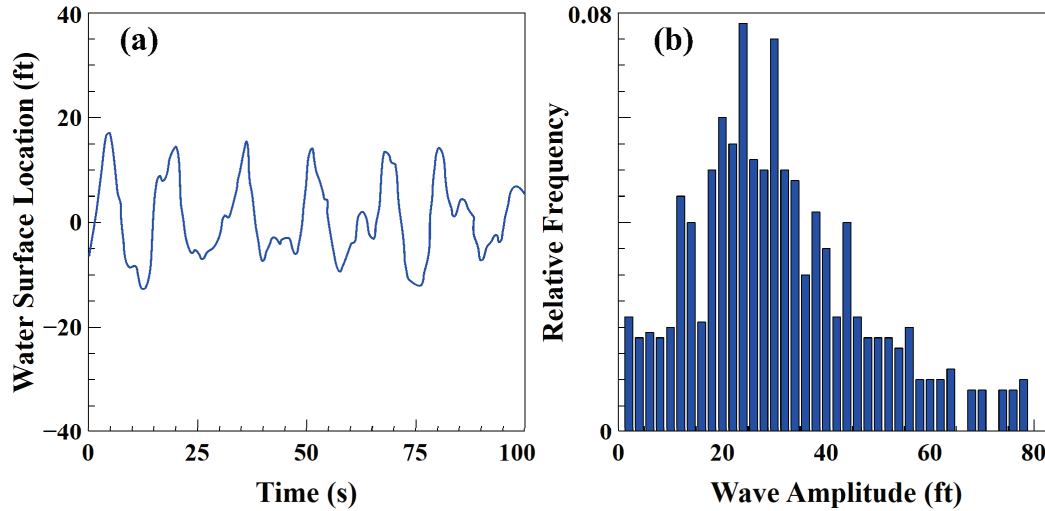


Figure 5.6: (a) Irregular water surface location measured during Hurricane Andrew, in contrast to the regular sinusoidal wave profiles examined in this study. (b) Distribution of ocean wave heights observed during Hurricane Andrew 1992. Data from both plots adapted from Judge 2019 [94].

Additionally, the evaporation study in App. B of this work shows promise for expansion into future work. Only n-Pentane was examined in the evaporation study, which has a lower saturation temperature than water. Expanding into different fuels would further expand the understanding of both the effect of the fuel saturation point and also the convective heat transfer as related to the wave parameters.

Finally, the understanding of the impact waves of a fuel burning on water would benefit from additional experimental backing. Particularly additional experiments could expand the range of wave steepness tested at the different scales. This could be problematic as even in the ranges of steepness in this study, some waves were too aggressive and caused fuel to slosh out of the burn containment pan.

BIBLIOGRAPHY

- [1] U. S. Coast Guard, *U.S. Coast Guard Oil Spill Response Offshore In-situ Burn Operations Manual*, Mar. 2003.
- [2] API, *In Situ Burning: A Decision Maker's Guide*, Report 125. American Petroleum Institute, Oct. 2016.
- [3] A. P. Trujillo and H. V. Thurman, "Essentials of Oceanography (7th. Edition)," 2001.
- [4] T. H. Havelock, "Forced surface-waves on water," *The London, Edinburgh, and Dublin Philosophical Magazine and Journal of Science*, vol. 8, no. 51, pp. 569–576, Oct. 1929, ISSN: 1941-5982. DOI: 10.1080/14786441008564913.
- [5] F. Biesel and F. Suquet, "Laboratory Wave Generating Apparatus," *La Houille Blanche*, vol. 2, 4, 1951.
- [6] D. Schmidt Etkin, *Analysis of Oil Spill Trends in the United States and Worldwide*. International Oil Spill Conference Proceedings, 2001, pp. 1291–1300. DOI: <https://doi.org/10.7901/2169-3358-2001-2-1291>.
- [7] S. B. Joye, "Deepwater Horizon, 5 years on," *Science*, vol. 349, no. 6248, pp. 592–593, Aug. 2015, ISSN: 10959203. DOI: 10.1126/science.aab4133. [Online]. Available: <https://www.science.org/doi/abs/10.1126/science.aab4133>.
- [8] S. Venn-Watson, K. M. Colegrove, J. Litz, *et al.*, "Adrenal Gland and Lung Lesions in Gulf of Mexico Common Bottlenose Dolphins (*Tursiops truncatus*) Found Dead following the Deepwater Horizon Oil Spill," *PLoS ONE*, vol. 10, no. 5, e0126538, May 2015, ISSN: 1932-6203. DOI: 10.1371/JOURNAL.PONE.0126538.
- [9] U. S. Coast Guard, *On Scene Coordinator report, Deepwater Horizon oil spill, submitted to the National Response Team*, 0. [Online]. Available: <https://repository.library.noaa.gov/view/noaa/283>.
- [10] A. A. Allen and R. J. Ferek, *Advantages and Disadvantages of Burning Spilled Oil*. International Oil Spill Conference Proceedings, Mar. 1993, vol. 1993, pp. 765–772. DOI: 10.7901/2169-3358-1993-1-765.
- [11] N. Barnea, "Health and Safety Aspects of In-situ Burning of Oil," National Oceanic and Atmospheric Administration, Seattle, WA, Tech. Rep., 2017. [Online]. Available: <https://response.restoration.noaa.gov/sites/default/files/health-safety-ISB.pdf>.
- [12] V. I. Blinov and G. N. Khudyakov, "Diffusion burning of liquids," Akademii Nauk SSSR, Moscow, Tech. Rep., 1961.
- [13] H. C. Hottel, "Certain laws governing the diffusive burning of liquids-A review," *Fire Res. Abs., Rev.*, vol. 1, pp. 41–44, 1959. [Online]. Available: <https://ci.nii.ac.jp/naid/10018472697/en/>.
- [14] A. T. Modak and P. A. Croce, "Plastic pool fires," *Combustion and Flame*, vol. 30, pp. 251–265, Jan. 1977, ISSN: 0010-2180. DOI: 10.1016/0010-2180(77)90074-8.
- [15] N. Iqbal and J. Quintiere, "Flame Heat Fluxes in PMMA Pool Fires," *Journal of Fire Protection Engineering*, vol. 6, no. 4, pp. 153–162, Nov. 2016, ISSN: 10423915. DOI: 10.1177/104239159400600402.
- [16] J. G. Quintiere, *Fundamentals of Fire Phenomena*. Chichester: John Wiley, 2006, ISBN: 978-0-470-09113-5.

- [17] T. A. Brzustowski and E. M. Twardus, *A study of the burning of a slick of crude oil on water*. Symp. (Int.) Combust., Jan. 1982, vol. 19, pp. 847–854. DOI: 10.1016/S0082-0784(82)80260-9.
- [18] S. E. Petty, “Combustion of crude oil on water,” *Fire Safety Journal*, vol. 5, no. 2, pp. 123–134, 1983, ISSN: 03797112. DOI: 10.1016/0379-7112(83)90005-X.
- [19] M. Arai, K. Saito, and R. A. Altenkirch, “A Study of Boilover in Liquid Pool Fires Supported on Water Part I: Effects of a Water Sublayer on Pool Fires,” *Combustion Science and Technology*, vol. 71, no. 1-3, pp. 25–40, May 1990, ISSN: 1563521X. DOI: 10.1080/00102209008951622.
- [20] J. P. Garo, J. P. Vantelon, and A. C. Fernandez-Pello, *Boilover burning of oil spilled on water*. Symp. (Int.) Combust., 1994, vol. 25, pp. 1481–1488. DOI: [https://doi.org/10.1016/S0082-0784\(06\)80792-7](https://doi.org/10.1016/S0082-0784(06)80792-7). [Online]. Available: <http://www.sciencedirect.com/science/article/pii/S0082078406807927>.
- [21] J. P. Garo, J. P. Vantelon, and A. C. Fernande-Pello, *Effect of the fuel boiling point on the boilover burning of liquid fuels spilled on water*. Symp. (Int.) Combust., 1996, vol. 26, pp. 1461–1467. DOI: [https://doi.org/10.1016/S0082-0784\(96\)80367-5](https://doi.org/10.1016/S0082-0784(96)80367-5). [Online]. Available: <http://www.sciencedirect.com/science/article/pii/S0082078496803675>.
- [22] J. P. Garo, J. P. Vantelon, and H. Koseki, “Thin-layer boilover: Prediction of its onset and intensity,” *Combustion Science and Technology*, vol. 178, no. 7, pp. 1217–1235, Jul. 2006, ISSN: 00102202. DOI: 10.1080/00102200500296846.
- [23] J. P. Garo and J. P. Vantelon, “Thin Layer Boilover of Pure or Multicomponent Fuels,” in *Prevention of Hazardous Fires and Explosions*, Springer Netherlands, 1999, pp. 167–182. DOI: 10.1007/978-94-011-4712-5{_}13.
- [24] D. Laboureur, L. Aprin, A. Osmont, J. M. Buchlin, and P. Rambaud, “Small scale thin-layer boilover experiments: Physical understanding and modeling of the water sub-layer boiling and the flame enlargement,” *Journal of Loss Prevention in the Process Industries*, vol. 26, no. 6, pp. 1380–1389, 2013, ISSN: 0950-4230. DOI: <https://doi.org/10.1016/j.jlp.2013.08.016>. [Online]. Available: <http://www.sciencedirect.com/science/article/pii/S095042301300171X>.
- [25] J. L. Torero, S. M. Olenick, J. P. Garo, and J. P. Vantelon, “Determination of the Burning Characteristics of a Slick of Oil on Water,” *Spill Science & Technology Bulletin*, vol. 8, no. 4, pp. 379–390, 2003, ISSN: 1353-2561. DOI: [https://doi.org/10.1016/S1353-2561\(03\)00071-9](https://doi.org/10.1016/S1353-2561(03)00071-9). [Online]. Available: <http://www.sciencedirect.com/science/article/pii/S1353256103000719>.
- [26] A. Y. Walavalkar, “Combustion of Water-in-oil Emulsions of Diesel and Fresh and Weathered Crude oils floating on Water,” Ph.D. dissertation, Pennsylvania State University, Aug. 2001.
- [27] L. Van Gelderen, “In-Situ Burning of Crude Oil on Water A study on the fire dynamics and fire chemistry in an Arctic context,” Ph.D. dissertation, Technical University Denmark, Jan. 2017, ISBN: 9788778774644. [Online]. Available: www.byg.dtu.dk.
- [28] Y. Chen, J. Fang, X. Zhang, *et al.*, “Pool fire dynamics: Principles, models and recent advances,” *Progress in Energy and Combustion Science*, vol. 95, p. 101070, Mar. 2023, ISSN: 0360-1285. DOI: 10.1016/J.PECS.2022.101070.
- [29] L. Chang and A. S. Rangwala, “Experimental study of crude oil slick burning on a turbulent water surface,” *Combustion and Flame*, vol. 241, p. 112119, Jul. 2022, ISSN: 0010-2180. DOI: 10.1016/J.COMBUSTFLAME.2022.112119.
- [30] M. E. Lepara and G. Debono, “Investigating waste oil disposal by direct incineration,” *Journal of the Air Pollution Control Association*, vol. 27, no. 2, pp. 144–146,
- [31] C. H. Thompson, G. W. Dawson, and J. L. Goodier, “Combustion: An Oil Spill Mitigation Tool,” U.S. Department of Energy, Tech. Rep. DOI: <https://doi.org/10.2172/5826420>.

- [32] A. Freiburger and J. M. Byers, *Burning agents for oil spill cleanup*. International Oil Spill Conference, 1971, pp. 245–251.
- [33] R. P. LaBelle, J. A. Galt, E. J. Tennyson, and K. B. McGrattan, “The 1993 oil spill of Tampa Bay, a scenario for burning?” *Spill Science & Technology Bulletin*, vol. 1, no. 1, pp. 5–9, Sep. 1994, ISSN: 1353-2561. DOI: 10.1016/1353-2561(94)90003-5.
- [34] J. Lindstedt-Siva, “The need for experimental oil spills,” *Spill Science & Technology Bulletin*, vol. 1, no. 2, pp. 97–100, Dec. 1994, ISSN: 1353-2561. DOI: 10.1016/1353-2561(94)90018-3.
- [35] I. Buist and J. McCourt, “The Efficacy of In situ Burning for Alaskan Risk Oils,” *Final Report, SL Ross Environmental Research, Ltd*, 1998.
- [36] J. M. Shaw, “A microscopic view of oil slick break-up and emulsion formation in breaking waves,” *Spill science & technology bulletin*, vol. 8, no. 5-6, pp. 491–501, 2003, ISSN: 1353-2561.
- [37] R. J. B. Bouweester and R. B. Wallace, *The break-up of an oil film due to wind-wave action*. Proceedings of the 8th Arctic and Marine Oil Spill Program Technical Seminar, 1985, pp. 14–25.
- [38] D. Botrus, E. Wickley-Olsen, R. Weggel, *et al.*, *Wave tank to simulate the movement of oil under breaking waves*. Proceedings of the 31st Arctic and Marine Oil Spill Program Technical Seminar, 2008, pp. 153–168.
- [39] R. L. Reisbig, “Oil Spill Drift Caused by the Coupled Effects of Wind and Waves, AD0777702,” Rolla, Tech. Rep., 1973. [Online]. Available: <https://apps.dtic.mil/sti/pdfs/AD0777702.pdf>.
- [40] R. Belore, *Wave tank tests to determine the effectiveness of Corexit 9500 dispersant on Hibernia crude oil under cold water conditions*. Proceedings of the 25th Arctic and Marine Oil Spill Program Technical Seminar, 2002, pp. 735–740.
- [41] Q. Lin, I. A. Mendelssohn, N. P. Bryner, and W. D. Walton, “In-situ burning of oil in coastal marshes. 1. Vegetation recovery and soil temperature as a function of water depth, oil type, and marsh type,” *Environmental science & technology*, vol. 39, no. 6, pp. 1848–1854, 2005, ISSN: 0013-936X.
- [42] Q. Lin, I. A. Mendelssohn, K. Carney, S. M. Miles, N. P. Bryner, and W. D. Walton, “In-Situ Burning of Oil in Coastal Marshes. 2. Oil Spill Cleanup Efficiency as a Function of Oil Type, Marsh Type, and Water Depth,” *Environmental Science & Technology*, vol. 39, no. 6, pp. 1855–1860, 2005. DOI: 10.1021/es0490626. [Online]. Available: <https://pubs.acs.org/sharingguidelines>.
- [43] D. E. Fritz, “In situ burning of spilled oil in freshwater inland regions of the United States,” *Spill Science & Technology Bulletin*, vol. 8, no. 4, pp. 331–335, 2003, ISSN: 1353-2561.
- [44] C. Bech, P. Sveum, and I. Buist, *The effect of wind, ice and waves on the in-situ burning of emulsions and aged oils*. Proceedings of the 16th Arctic and Marine Oil Spill Program Technical Seminar, 1993.
- [45] J. McCourt, I. Buist, and J. Mullin, *Laboratory testing to determine operational parameters for in situ burning of six US outer continental shelf crude oils*. Proceedings of the 21st Arctic and Marine Oil Spill Program Technical Seminar, 1998, vol. 2, pp. 623–632.
- [46] I. Buist, J. McCourt, J. Mullin, *et al.*, *Mid-Scale Tests of In Situ Burning in a New Wave Tank at Prudhoe Bay, AK*. Environment Canada, Ottawa, ON: Proceedings of the 21st Arctic and Marine Oil Spill Program Technical Seminar, 1998, pp. 599–622.
- [47] I. Buist, J. McCourt, and J. Morrison, *Enhancing the In-Situ Burning of Five Alaskan Oils and Emulsions*. Allen Press, Apr. 1997, vol. 1997, pp. 121–129. DOI: 10.7901/2169-3358-1997-1-121.

- [48] I. Buist, L. Majors, K. Linderman, D. Dickins, J. Mullin, and C. Owens, *Tests to determine the limits to in situ burning of thin oil slicks in brash and frazil ice*. Environment Canada, Ottawa: Proceedings of the 26th Arctic and Marine Oil Spill Program Technical Seminar, 2003, pp. 629–648.
- [49] I. Buist, S. Potter, T. Nedwed, and J. Mullin, “Herding surfactants to contract and thicken oil spills in pack ice for in situ burning,” *Cold Regions Science and Technology*, vol. 67, no. 1-2, pp. 3–23, Jun. 2011, ISSN: 0165232X. DOI: 10.1016/J.COLDREGIONS.2011.02.004.
- [50] J. Brandvik, K. R. Sørheim, I. Singasaas, and M. Reed, “Short state-of-the-art report on oil spills in ice-infested waters SINTEFA06148,” SINTEF Materials and Chemistry. Marine Environmental Technology., Tech. Rep., 2006.
- [51] J. Aurell, A. Holder, B. Gullett, *et al.*, “Analysis of emissions and residue from methods to improve efficiency of at-sea, in situ oil spill burns,” *Marine Pollution Bulletin*, vol. 173, Dec. 2021, ISSN: 18793363. DOI: 10.1016/J.MARPOLBUL.2021.113016.
- [52] National Engineering Science Company, “Design of Wave Tanks,” U.S. Army Engineer Waterways Experiment Station, Pasadena, Ca, Tech. Rep., 1962. DOI: DA-22-079-CIVENG-62-46. [Online]. Available: <https://ntrl.ntis.gov/NTRL/dashboard/searchResults/titleDetail/ADA054080.xhtml>.
- [53] M. H. Patel and P. A. Ionnaou, “Comparative Performance Study of Paddle- and Wedge-Type Wave Generators,” Ph.D. dissertation, May 1980. DOI: 10.2514/3.63181. [Online]. Available: <https://arc.aiaa.org/doi/10.2514/3.63181>.
- [54] J. Milgram, “Compliant water wave absorbers.,” Jan. 1965.
- [55] P. Webb, *Introduction to Oceanography*. [Online]. Available: <https://rwu.pressbooks.pub/webboceanography/>.
- [56] J. Lighthill, *Waves in Fluids*. Cambridge university press, 2001, ISBN: 0521010454.
- [57] A. Wallet and F. Ruellan, “Trajectories of particles within a partial clapotis,” *Houille Blanche*, vol. 5, pp. 483–489, 1950.
- [58] M. Van Dyke, *An album of fluid motion*. Parabolic Press Stanford, 1982, vol. 176, ISBN: 9780915760039.
- [59] A. D. Craik, “Georgy Gabriel Stokes on Water Wave Theory,” *Annual Review of Fluid Mechanics*, vol. 37, pp. 23–42, Jan. 2005, ISSN: 00664189. DOI: 10.1146/ANNUREV.FLUID.37.061903.175836.
- [60] G. G. Stokes, “On the Theory of Oscillatory Waves,” *Transactions of the Cambridge Philosophical Society*, vol. VIII, p. 441, 1847.
- [61] D. G. Andrews and M. E. McIntyre, “An exact theory of nonlinear waves on a Lagrangian-mean flow,” *Journal of Fluid Mechanics*, vol. 89, no. 4, pp. 609–646, 1978, ISSN: 14697645. DOI: 10.1017/S0022112078002773.
- [62] K. A. Powell, P. A. Quinn, and C. A. Greated, “The Formation of Shingle Beach Profiles due to Wave Impact, and the Measurement of the Wave Velocities using Particle Image Velocimetry.,” in *Proc. 23rd Int. Conf. on Coastal Eng., ASCE*, 1992.
- [63] D. Skyner, “A comparison of numerical predictions and experimental measurements of the internal kinematics of a deep-water plunging wave,” *Journal of Fluid Mechanics*, vol. 315, pp. 51–64, 1996, ISSN: 1469-7645.
- [64] M. Perlin, J. He, and L. P. Bernal, “An experimental study of deep water plunging breakers,” *Physics of fluids*, vol. 8, no. 9, pp. 2365–2374, 1996, ISSN: 1070-6631.

- [65] K.-A. Chang and P. L.-F. Liu, “Velocity, acceleration and vorticity under a breaking wave,” *Physics of Fluids*, vol. 10, no. 1, pp. 327–329, 1998, ISSN: 1070-6631.
- [66] M. Umeyama, “Coupled PIV and PTV Measurements of Particle Velocities and Trajectories for Surface Waves Following a Steady Current,” *Journal of Waterway, Port, Coastal, and Ocean Engineering*, vol. 137, no. 2, pp. 85–94, Jun. 2010, ISSN: 0733-950X. DOI: 10.1061/(ASCE)WW.1943-5460.0000067.
- [67] A. Jensen, M. Huseby, D. Clamond, G. Pedersen, and J. Grue, “PIV Measurements of Accelerations in Water Waves,” *Advances in Coastal and Ocean Engineering*, vol. 9, p. 279, 2004, ISSN: 0219-4880.
- [68] D. Clamond, J. Grue, M. Huseby, and A. Jensen, “PIV Measurements of the Velocity Field in Steep Water Wave Events,” 2004.
- [69] N. G. Sauer, A. Saar, H.-H. Ho, S. Nair, L. Zabilansky, and A. S. Rangwala, *Evaporation Behavior of a Volatile Fuel in Waves*. Environment Canada, Ottawa: Proceedings of the 44th Arctic and Marine Oil Spill Program Technical Seminar, 2022.
- [70] N. G. Sauer, J. M. Cuendet, and A. S. Rangwala, “A study of thin fuel slick combustion on wavy water,” *Marine Pollution Bulletin*, vol. 182, p. 113 932, Sep. 2022, ISSN: 0025-326X. DOI: 10.1016/J.MARPOLBUL.2022.113932. [Online]. Available: <https://linkinghub.elsevier.com/retrieve/pii/S0025326X22006142>.
- [71] J. M. Cuendet, “A Study of Burning of a Thin Fuel Slick on Water with Waves,” Tech. Rep., 2021. [Online]. Available: <https://digital.wpi.edu/show/2r36v155t>.
- [72] N. G. Sauer and A. S. Rangwala, “Burning behavior of a liquid fuel on wavy water,” *Fire Technology*,
- [73] A. C. Saar, D. J. Leary, C. Kulczyk, N. G. Sauer, and A. S. Rangwala, “F20 FPE Wave Tank,” Tech. Rep., 2021. [Online]. Available: <https://digital.wpi.edu/show/rr172094z>.
- [74] N. G. Sauer, H.-H. Ho, S. Nair, L. Zabilansky, and A. S. Rangwala, *A study of Kerosene Pool Burning on Wavy Water*. Orlando, FL: Eastern States Section of the Combustion Institute Spring Technical Meeting, 2022.
- [75] Inchem, *Inchem ICSC 0663 - Kerosene*. [Online]. Available: <https://inchem.org/documents/icsc/icsc/eics0663.htm>.
- [76] J. H. Michell, “The highest waves in water,” *The London, Edinburgh, and Dublin Philosophical Magazine and Journal of Science*, vol. 36, no. 222, pp. 430–437, Nov. 1893, ISSN: 1941-5982. DOI: 10.1080/14786449308620499. [Online]. Available: <https://zenodo.org/record/1431203>.
- [77] A. Toffoli, A. Babanin, M. Onorato, and T. Waseda, “Maximum steepness of oceanic waves: Field and laboratory,” *Geophysical Research Letters*, vol. 37, no. 5, Mar. 2010, ISSN: 00948276. DOI: 10.1029/2009GL041771.
- [78] E. R. Chappell, “Theory and design of a wave generator for a short flume,” eng, Ph.D. dissertation, 1969. [Online]. Available: <https://open.library.ubc.ca/collections/831/items/1.0050588>.
- [79] N. Wu, G. Kolb, and J. L. Torero, “Piloted ignition of a slick of oil on a water sublayer: The effect of weathering,” in *Symposium (International) on Combustion*, vol. 27, Elsevier, Jan. 1998, pp. 2783–2790. DOI: 10.1016/S0082-0784(98)80135-5.
- [80] J. P. Garo, H. Koseki, J. P. Vantelon, and C. Fernandez-Pello, “Combustion of liquid fuels floating on water,” *Thermal Science*, vol. 11, no. 2, pp. 119–140, 2007, ISSN: 03549836. DOI: 10.2298/TSCI0702119G.

- [81] P. S. Ghoshdastidar and A. Mukhopadhyay, “Transient heat transfer from a straight composite fin: a numerical solution by ADI,” *International communications in heat and mass transfer*, vol. 16, no. 2, pp. 257–265, 1989, ISSN: 0735-1933.
- [82] J. Hristov, “Burning of a Slick of Fuel on Water, Qualitative Analysis of the Heat Transfer Model and the Pre-boilover Time on the Basis of Data Available,” *Transport Phenomena in Two Phase Flow*, 2001.
- [83] S. R. Turns and D. C. Haworth, *An introduction to combustion : concepts and applications*, p. 749, ISBN: 9781260477696.
- [84] D. W. Green, R. H. Perry, and D. Maloney, *Perry’s Chemical Engineers’ Handbook (8th rev. ed.)* 7th. 2004, ISBN: 0071542086. DOI: 10.1036/0071511245.
- [85] N. Otsu, “A threshold selection method from gray-level histograms,” *IEEE transactions on systems, man, and cybernetics*, vol. 9, no. 1, pp. 62–66, 1979, ISSN: 0018-9472.
- [86] A. Bouhafid and J. Vantelon, “Radiative Heat Flux and Energy Balance at the Surface of a Small Scale Kerosene Pool Fire,” *Dynamics of Deflagrations and Reactive Systems: Heterogeneous Combustion*, pp. 297–313, Jan. 1991. DOI: 10.2514/5.9781600866050.0297.0313.
- [87] A. Hamins, J. Fischer, M. E. Klassen, J. P. Gore, and T. Kashiwagi, “Heat feedback to the fuel surface in pool fires,” *Combustion Science and Technology*, vol. 97, no. 1-3, pp. 37–62, Apr. 1994, ISSN: 1563521X. DOI: 10.1080/00102209408935367. [Online]. Available: <https://www.tandfonline.com/doi/abs/10.1080/00102209408935367>.
- [88] S. Chan Kim, K. Y. Lee, and A. Hamins, “Energy balance in medium-scale methanol, ethanol, and acetone pool fires,” *Fire Safety Journal*, vol. 107, pp. 44–53, Jul. 2019, ISSN: 03797112. DOI: 10.1016/j.firesaf.2019.01.004.
- [89] L. Chang, “Influence of Turbulence on Fuel Slick Fires with an Immersed Conductive Object,” Ph.D. dissertation, Sep. 2021. [Online]. Available: <https://digitalwpi.wpi.edu/concern/etds/xw42nb83h?locale=en>.
- [90] H. F. Farahani, “A Study on Burning of Crude Oil in Ice Cavities Repository Citation,” Tech. Rep., 2013. [Online]. Available: <https://digitalcommons.wpi.edu/etd-theses/501>.
- [91] F. A. Williams, “Heat transfer in fires: thermophysics, social aspects, economic impact.,” in ser. *Advances in thermal engineering*, 1, P. Blackshear, Ed., International Centre for Heat and Mass Transfer, 1974, pp. 170–190, ISBN: 0470077808.
- [92] A. Rangwala, K. Arsava, N. G. Sauer, *et al.*, *Advancing the Maturity of the Flame Refluxer Technology*, Washington, DC, USA, 2021. [Online]. Available: <https://ntrl.ntis.gov/NTRL/>.
- [93] A. D. Craik, “The Origins of Water Wave Theory,” *Annual Review of Fluid Mechanics*, vol. 36, pp. 1–28, Jan. 2004, ISSN: 00664189. DOI: 10.1146/ANNUREV.FLUID.36.050802.122118. [Online]. Available: <https://www.annualreviews.org/doi/abs/10.1146/annurev.fluid.36.050802.122118>.
- [94] C. Q. Judge, “Seakeeping and Maneuvering,” in *USNA EN455*, 2019, ch. 3, The Inp. [Online]. Available: https://www.usna.edu/NAOE/_files/documents/Courses/EN455/AY20_Notes/EN455CourseNotesAY20_Chapter3.pdf.
- [95] M. Raffel, C. E. Willert, F. Scarano, C. J. Kähler, S. T. Wereley, and J. Kompenhans, “Particle Image Velocimetry,” 2018. DOI: 10.1007/978-3-319-68852-7. [Online]. Available: <https://link.springer.com/10.1007/978-3-319-68852-7>.
- [96] S. Scharnowski, M. Bross, and C. J. Kähler, “Accurate turbulence level estimations using PIV/PTV,” *Experiments in Fluids*, vol. 60, no. 1, pp. 1–12, Jan. 2019, ISSN: 07234864. DOI:

- 10.1007/S00348-018-2646-5. [Online]. Available: <https://link.springer.com/article/10.1007/s00348-018-2646-5>.
- [97] R. D. Keane and R. J. Adrian, "Optimization of particle image velocimeters. I. Double pulsed systems," *Measurement Science and Technology*, vol. 1, no. 11, p. 1202, Nov. 1990, ISSN: 0957-0233. DOI: 10.1088/0957-0233/1/11/013. [Online]. Available: <https://iopscience.iop.org/article/10.1088/0957-0233/1/11/013>.
- [98] R. D. Keane and R. J. Adrian, "Optimization of particle image velocimeters: II. Multiple pulsed systems," *Measurement Science and Technology*, vol. 2, no. 10, p. 963, Oct. 1991, ISSN: 0957-0233. DOI: 10.1088/0957-0233/2/10/013. [Online]. Available: <https://iopscience.iop.org/article/10.1088/0957-0233/2/10/013>.
- [99] W. Thielicke and E. J. Stamhuis, *Affordable and Accurate Digital Particle Image Velocimetry in MATLAB, J. Open Res. Softw. 2 (2014)*.
- [100] W. Thielicke and R. Sonntag, "Particle Image Velocimetry for MATLAB: Accuracy and enhanced algorithms in PIVlab," *Journal of Open Research Software*, vol. 9, no. 1, 2021, ISSN: 2049-9647.
- [101] J. Kravtchenko and L. Santon, "The Parasite Phenomenon In a Tcave Canal," *Coastal Engineering Proceedings*, vol. 1, no. 5, p. 6, Jan. 1954. DOI: 10.9753/icce.v5.6. [Online]. Available: <https://icce-ojs-tamu.tdl.org/icce/index.php/icce/article/view/2004>.

APPENDIX A

Wave Turbulence

A.1 Purpose

Particle image velocimetry (PIV) and particle tracking were used to investigate the wave-based boundary condition, for a cold-flow non-burning state. Waves were hypothesized to increase water movement across the bottom of the fuel layer but a measurement was needed to confirm as well as quantify this water movement, to be associated with a reduction in burning. The wavetank, see-through pan, PIV setup, and particle tracking image generation are described in the following sections.

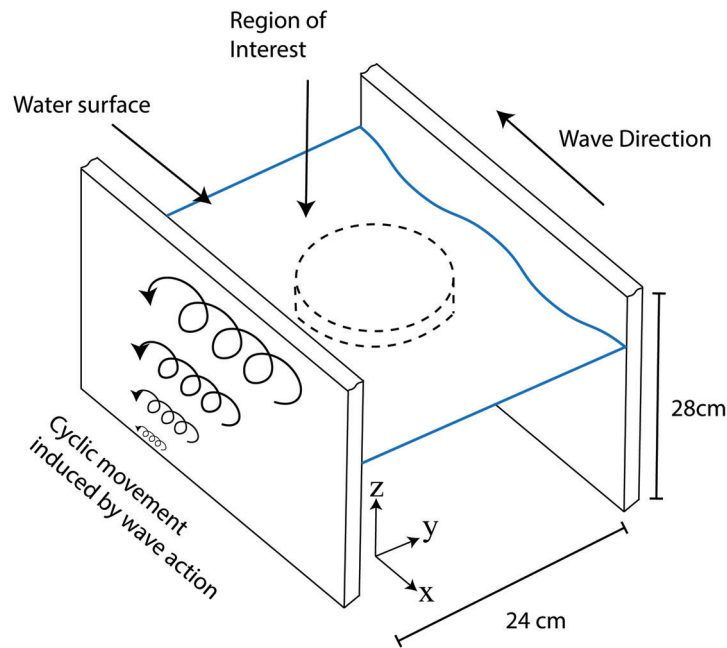


Figure A.1: Sketch of wavetank showing planes of interest and approximate size and location of the footprint of the floating ring for burn experiments denoting the measurement region of interest.

A.2 Experimental Setup

A.2.1 Wavetank and Pan

The wavetank used for this study is the same used for a later small scale burning Sec. 2, as such further details about the experimental setup can be found in Sec. 2.2. This wavetank is 2.4 m long, 0.24 m wide, and 0.28 m tall and filled with fresh water, a sketch is shown in Fig. A.2

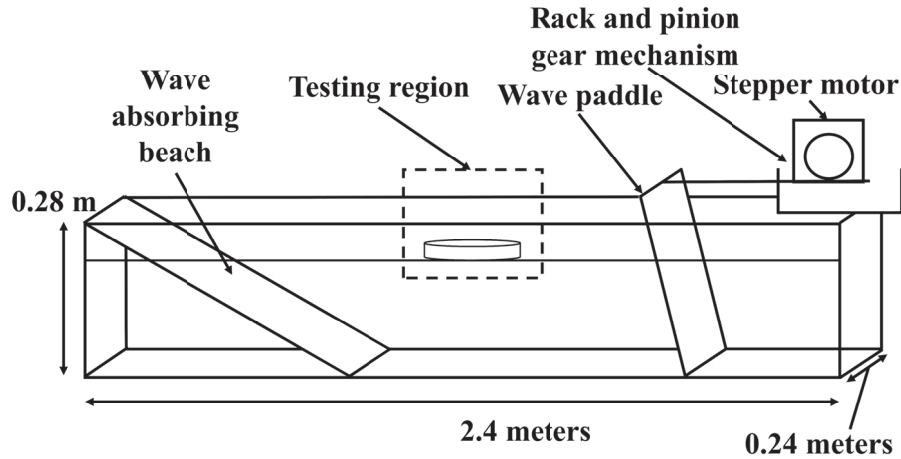


Figure A.2: Image of the pan with the laser sheet at the edge, used for capturing information about vortices generated due to the pan lip.

The pan used for this portion of the study was made of borosilicate glass 10 cm in diameter and a total height of 4 cm. The glass pan was supported by a styrofoam ring 20 cm in diameter and 3 cm tall. Two pieces of string tethered the styrofoam ring to the wavetank walls. The amount of pan-edge below the waterline was adjusted by securing the pan to different positions on the styrofoam ring with aluminum tape.

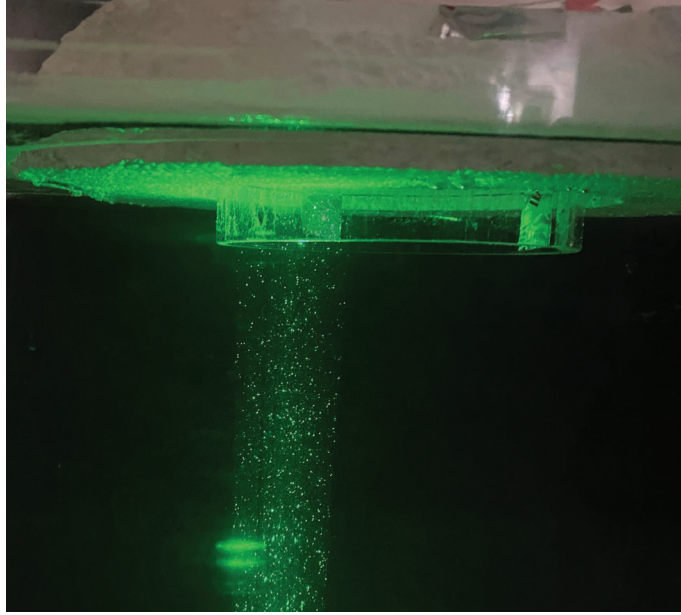


Figure A.3: Image of the pan with the laser sheet at the edge, used for capturing information about vortices generated due to the pan lip.

Additional images of the wavetank and some of the setup components are shown in Fig. A.6, the pan and floating ring are shown as well.

A.2.2 Wave Tank Preparation

Specific preparations were made to the small scale wavetank to facilitate more accurate PIV measurements being made easier. Any metal or porous surfaces in the wavetank were either replaced with stainless-steel components or coated in plastic. This was done to prevent rusting and the resulting clouding of the water which would obscure the optical clarity needed for the cameras. The water could be replaced, but the PIV particles are costly and replacing the water would require re-seeding. The bottom surface of the wavetank as well as the wavetank walls, were then sanded and polished to provide the laser and high-speed camera the clearest paths. A black cloth was then suspended behind the wavetank, which served to provide a uniform dark background and as well could be re-positioned to dampen ambient light reflection causing glare in the high-speed camera.

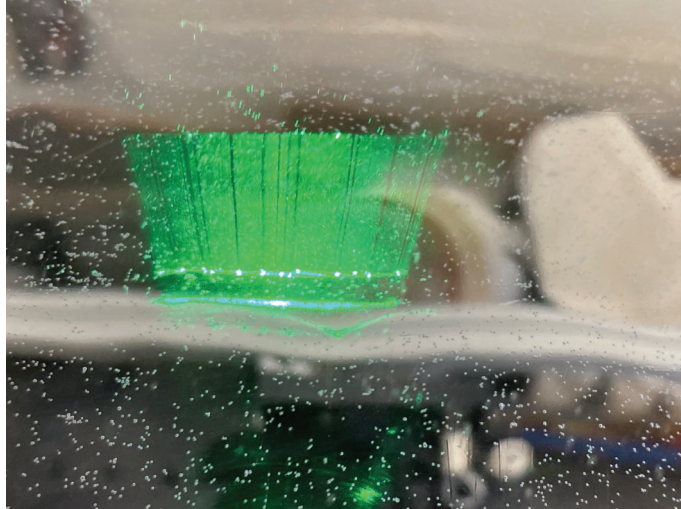


Figure A.4: Polished surfaces on the bottom of the wavetank where the laser enters from the bottom.

An important component of PIV and more importantly particle tracking is that the plane of motion of the particles is aligned with the plane of motion of the laser as much as possible. Since the wavetank should have very little side-to-side water movement, the plane of the laser could be aligned to be parallel to the tank walls to align particle motion with the laser sheet. First, the wavetank was leveled such that a level reference could be used to ensure the laser sheet was orthogonal to the bottom of the wavetank. This ensured that the laser sheet was not tilted in relation to the wavetank, which would cause particles to only be illuminated by the sheet for a short distance as they traversed in and out of the plane. The distance from each edge of the laser sheet to the tank wall was then measured to ensure the laser sheet was parallel to the walls of the tank.

A.2.3 Particle Image Velocimetry

The PIV setup generally consists of a laser, optics to generate a light sheet, high-speed camera, seeding particles, and a post-processing scheme. PIV generally works like flash photography. A high-speed camera captures video or individual images of a precise investigation area, and a laser or other bright light source illuminates this area in 2 dimensions. In very high-speed applications the laser can be precisely timed to ‘straddle’ two camera frames, such that it illuminates the end of one frame and the beginning of the next. This creates a very small time difference between two frames,

generally the interframe time of the camera being used. Anticipated velocities in the wavetank were very low <1 m/s, and thus did not require a synchronization unit between the laser and high-speed camera as frame straddling was not required. A Photron FASTCAM SA1.1 with 80mm Nikkor F2.8 lens was used to capture images at 500 fps. A Thorlabs NPL52B Nanosecond Pulsed Laser was used as the laser light source. This laser outputs pulses with adjustable lengths of $5\text{ ns} \pm 1\text{ ns}$ to $39\text{ ns} \pm 3\text{ ns}$, at a frequency of 1, 5, or 10 MHz, for these experiments 10 MHz and 39 ns was used. At these settings, each camera frame would capture about 20,000 laser pulses. Due to the slow speeds being measured the motion blur on particles was minimal and could be reduced further by increasing the camera frame rate for particularly fast wave action. The optics configuration consisted of a plano-concave cylindrical lens, and a plano-convex spherical lens, resulting in a sheet of light that expands in height but converges in thickness Fig. A.5.

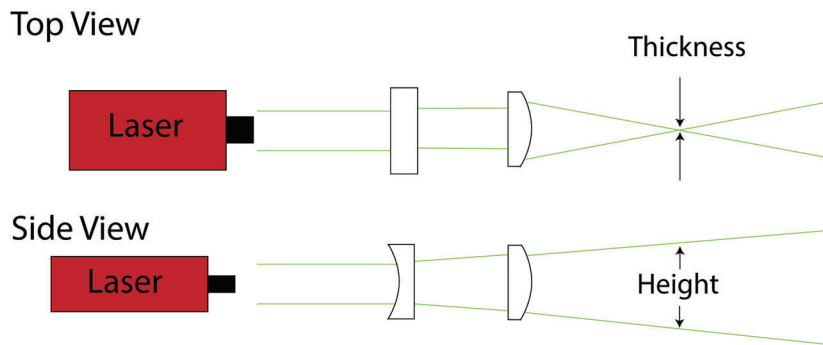


Figure A.5: Laser sheet optics used in PIV investigation.

Dantec silver-coated hollow glass spheres of size $D_p = 10\ \mu\text{m}$ were chosen as seeding particles and the timescales of the flow velocity and particles were calculated to ensure appropriateness for the flow being measured. Larger particles are better for image capture because they scatter more light, making them brighter and easier to pick up on low-light high-speed video. But smaller particles are optimal for flow tracing because they have less inertia, and will follow small changes in velocity more naturally with the flow. Eqn. A.1 shows the particle response time τ_p (s/m) given in [95]. A maximum velocity of 1 m/s was anticipated for measurement in the small wavetank, therefore 1 m/s is used for τ_w the characteristic time scale of the flow (s/m). The ratio of particle response

time to flow characteristic time scale is the particle Stokes number Eqn. A.2. Particle diameter D_p (m), particle density ρ_p (kg/m³), and fluid dynamic viscosity μ_w (kg/m·s) are also present. A Stokes number value below 10^{-1} is an acceptable range for flow tracing accuracy. Stokes for these conditions was calculated to be 5.5×10^{-8} , well below the threshold for accurate velocity fluctuation accuracy:

$$\tau_p = \frac{\rho_p D_p^2}{18\mu_w}, \quad (\text{A.1})$$

$$St = \frac{\tau_p}{\tau_w}. \quad (\text{A.2})$$

The laser and optics configuration were mounted underneath the tank, and a 2-inch mirror directed the laser sheet up into the wavetank from below Fig. A.6. At the investigation zone, the beam measured 38 mm across. The camera captured an area approximately 50 mm across with a resolution of 1024×1024 pixels. However, a region of interest of only $15 \text{ mm} \times 15 \text{ mm}$ ($300 \text{ px} \times 300 \text{ px}$) was used. Subsequent interrogation areas of 128 px, 32 px, and 16 px were used for 3 total passes with a 50% overlap and tracer displacement was approximately 0.02 mm between frames. This followed the traditional “1/4” rule of a maximum in-plane motion of one-quarter of the linear dimension of the interrogation window [95]–[98]. The number of particles was counted using a Matlab script and the particle density was calculated to be 9.4 for the largest interrogation window, within the minimum threshold of 5 to 10 suggested by Raffel et al. [95]. Image post-processing, velocity validation, and data export were accomplished with PIVlab [99], [100].

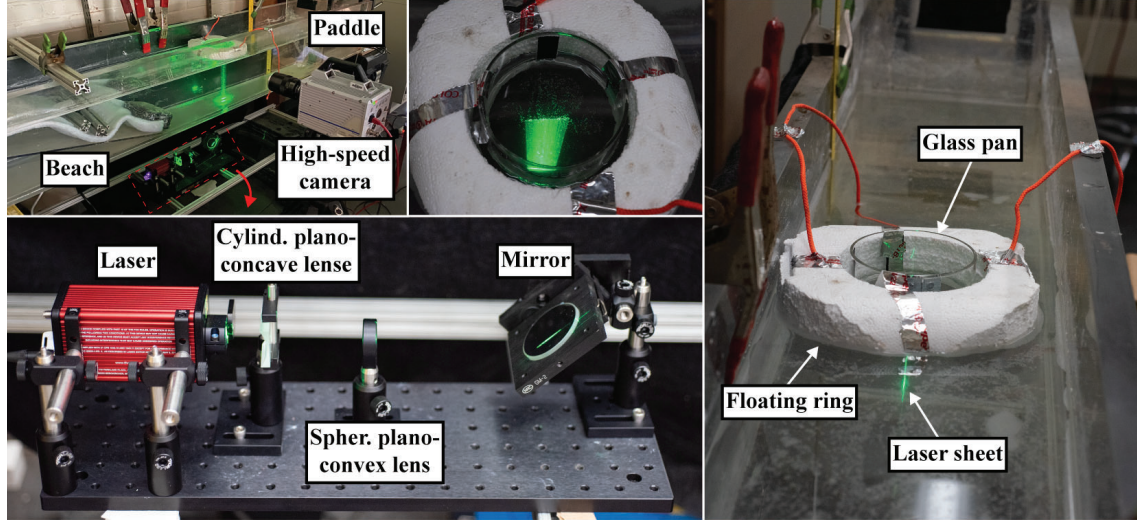


Figure A.6: Image of PIV setup in use in small wavetank, laser and optics configuration visible at the bottom, laser sheet visible center.

With relatively low velocities expected in the wavetank, very low interframe times were not expected to be needed for acquiring appropriate PIV images. As such the relatively low-power Thorlabs NPL-52B laser was adequate for this investigation, and frame straddling or syncing the laser with the highspeed camera was not required. For all cases a framerate of 500 fps was used, and when analyzing in PIVlab every 2nd frame was used for a majority of the cases in order to reduce processing time and load.

A.2.4 Particle Tracking

Particle tracking was also used in this section to examine some of the wave paths, especially those without the pan in place. To produce these particle path images a DSLR camera was used with the shutter speed set to one wave period t_p or slightly over one wave period. The PIV laser and laser particles were used to create the particle paths. In this way the diameter of the particle path could be measured using a scaling factor, and duration of the particle path were known to be the shutter speed on the camera. This was a faster method for measuring particle paths when the paths were simpler and more regular. This method also gives a good visual representation of the behavior of the water under a wave. A Nikon d810 36.3 MP DSLR camera with 60mm f/2.8D Micro Nikkor macro lens was used to acquire the wave path images.

A.2.5 Heat Transfer Coefficient

A series of experiments were conducted to examine an experimentally determined heat transfer coefficient being induced by waves. These experiments define a convective heat transfer coefficient correlation as a function of wave steepness that will be referenced later in this work. The waves examined in these experiments are the same waves examined in the PIV wave motion study in Table A.1.

These experiments involved submerging a small solid metal sphere with an embedded thermocouple and measuring the temperature decay of the solid sphere. For these experiments, a solid sphere of 2017 aluminum 1.27 cm in diameter was used. A small hole approximately 3/32" was drilled halfway into the sphere, and a 36AWG thermocouple wire, with bead diameter approximately 0.5 mm, was inserted with thermally conductive and electrically insulating paste. The hole was sealed and the thermocouple was secured to the sphere with a small amount of cyanoacrylate glue. This thermocouple was sampled at 2Hz over the duration of each experiment.

The sphere was hung from a piece of 80-20 extruded aluminum, so its height in the water bath and height in the wavetank were consistent across trials. The sphere was heated in a boiling water bath (100°C) until its temperature stabilized, the sphere was then transferred quickly to the wavetank. During data analysis, the first 2 - 3 seconds of temperature data are discarded as this was during this transfer period. Three trials of each experimental condition were conducted.

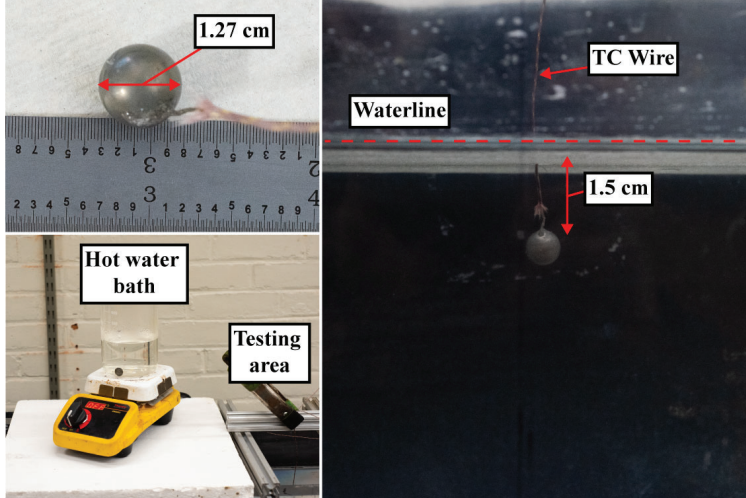


Figure A.7: *Clockwise from top-right*, sphere suspended from TC wire as configured during experiments, hot-plate and beaker used for hot-water bath, 2017 aluminum sphere with thermocouple wire protruding.

Analysis of this temperature data was made under the assumption of the sphere acting in a thermally thin condition. The lumped capacitance method is used to iterate an h value such that a calculated non-dimensional temperature vs. time curve matches the experimental temperature vs. time curve.

A.3 Experimental Matrix/ Waves Examined

Table A.1 shows the waves selected for examination with the PIV and particle tracking setups. These waves are primarily selected from the waves also examined in the small scale burning section from Table 2.1 with an emphasis placed on achieving the full range of steepness for both wave selections.

Table A.1: Waves examined in the PIV section.

Wave Period τ_p (s)	Wavelength λ (m)	Wave Height H (m)	Steepness S (H/λ)
2	2.6	0.01	0.004
1	1.18	0.01	0.008
0.4	0.25	0.003	0.012
1	1.18	0.02	0.017
0.4	0.25	0.01	0.04

These waves were also compared to the medium and large scale waves tested in their respective sections to ensure the range of steepness's for all burning experiments was captured during this small scale investigation of the wave behavior.

A.4 Results

In this section, the measured wave motions are presented for their behavior with and without the pan. Measured wave motions are also compared to wave theory-predicted motions where appropriate.

A.4.1 Wave Motion without Pan

For linear water waves of regular period and wavelength, with a known water depth; the wavelength λ is traditionally calculated with a form of the dispersion equation Eqn. A.3. Where the wavelength is an iterative solution depending only on the period t_p and the tank depth z [4], [5].

$$\lambda = \frac{gt_p^2}{2\pi} \tanh \frac{2\pi z}{\lambda_{old}}, \quad (\text{A.3})$$

Circular Paths

Sinusoidal deep-water waves can be approximated as having particle paths that follow perfectly circular motions. Following a path with radius:

$$r = \omega^{-1} k \Phi_0 e^{ky}. \quad (\text{A.4})$$

Where ω is the angular velocity, y is the distance below the surface with the tank bottom at $y = -z$. Other variables include the wavenumber k , the wave period t_p , and the wavelength λ . Φ_z is the dependence of a waves amplitude and motions on the distance z below the surface, with Φ_0 being a constant for this value at the water surface. For these calculations Φ_0 is found by iteration until the vertical component of motion is equal to the measured wave height. Angular velocity and wavenumber can be expressed as:

$$\omega = 2\pi t_p, \quad (\text{A.5})$$

$$k = 2\pi/\lambda, \quad (\text{A.6})$$

This approximation of particle motion as perfect circles with radius equal to Eqn. A.4 only holds for cases where the water depth z is much greater than the wavelength, Lighthill defines this limit as ($z < 0.07\lambda$) [56]. In our case the most applicable wave compared to our tank depth is the period 0.4 s wave ($\lambda = 0.25$ m). Fig. A.8 shows three distinct period 0.4 s waves, showing that for each the motion is approximately circular through the depth of the tank. While at the surface and close below the surface each wave has a distinct path diameter approximately the same as the wave height. For waves where the λ is larger, the wave path is approximated as an ellipsoid with major axis Eqn. A.7, and minor axis Eqn. A.8.

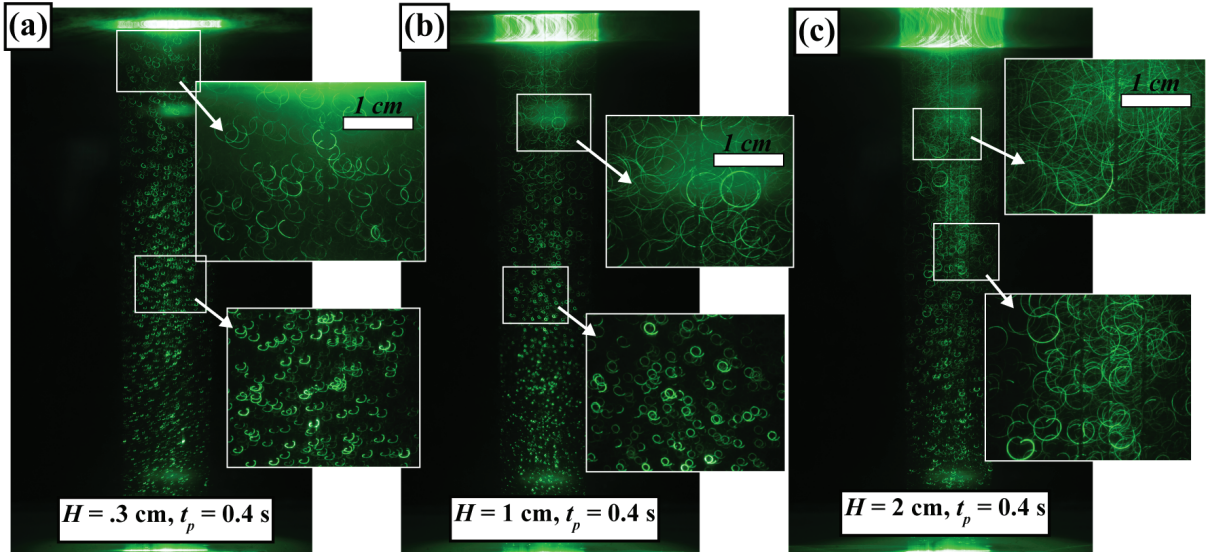


Figure A.8: Images taken with (shutter speed = $1 \cdot t_p$), paths are traced by PIV particles. Wave shown all have a period of 0.4s and mostly circular paths.

Fig. A.9 below shows the Eqn. A.4 path radius vs. z , showing a decreasing orbital path size with depth towards h , this is shown for the 0.4 s period wave only, as this is the closest wave we made to being able to approximate with a perfectly circular path.

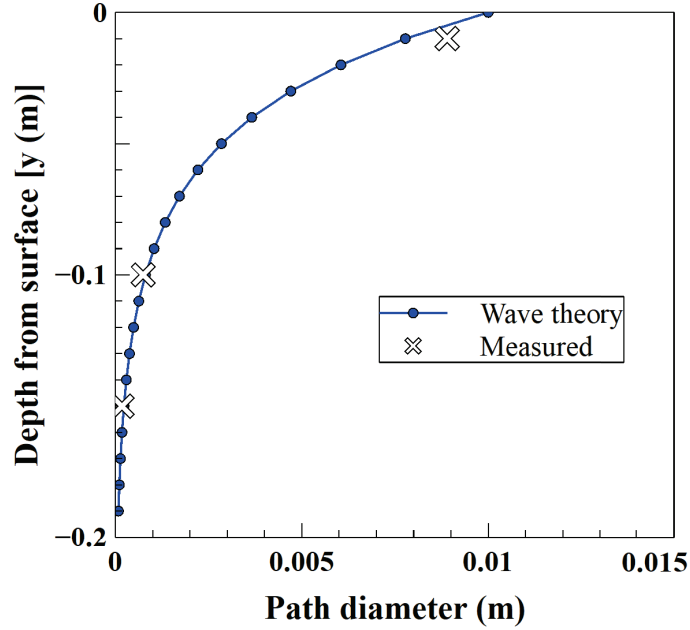


Figure A.9: Calculated wave path radius vs. Depth from surface for the $t_p = 0.4$ s wave.

Elliptical Paths

For cases where the wavelength is greater in proportion to the tank depth ($z < 0.07\lambda$), according to Lighthill [56]. As the depth increases the paths collapse into flatter and flatter ellipses, where the horizontal and vertical components of motion are separated and can be approximated by Eqn. A.7, and minor axis Eqn. A.8.

$$2a = \omega^{-1}k\Phi_0 \cosh [k(y + z)], \quad (\text{A.7})$$

$$2b = \omega^{-1}k\Phi_0 \sinh [k(y + z)], \quad (\text{A.8})$$

$$\frac{x^2}{a^2} + \frac{y^2}{b^2} = 1. \quad (\text{A.9})$$

From these two equations it is evident that as y approaches $-z$, the major axis Eqn. A.7 decreases much less in proportion to the minor axis Eqn. A.8, meaning the ellipsoid will flatten as y approaches $-z$. This contrasts with Eqn. A.4 where the path stays circular but shrinks in radius as y approaches

—z.

Fig. A.10a shows the horizontal (major) and vertical (minor) ellipses components for the longer period waves plotted vs. depth towards z , which in our case is 0.19 m. Lines on Fig. A.10b are the ratio between major and minor ($\frac{major}{minor}$), showing that for small waves and near the surface, the two values are close to identical (ratio = 1), but as the depth increases the minor axis shrinks faster than the major, causing a flatter and flatter path, and a larger ratio between the two values. The period 1 s and 2 s waves from Table A.1 are plotted on this chart. To see if these calculated paths matched the experimental paths, images of the wavetank with PIV laser and particles in place were taken. The shutter speed was controlled so that the shutter was open for 1 wave period allowed the capturing of images with traced wave paths. Fig. A.11 shows these wave paths with circles and ellipses traced to approximate the visual paths. Scaled measurements are then made for the paths and the results are plotted on Fig. A.10a & b as crosses signifying experimental measurements.

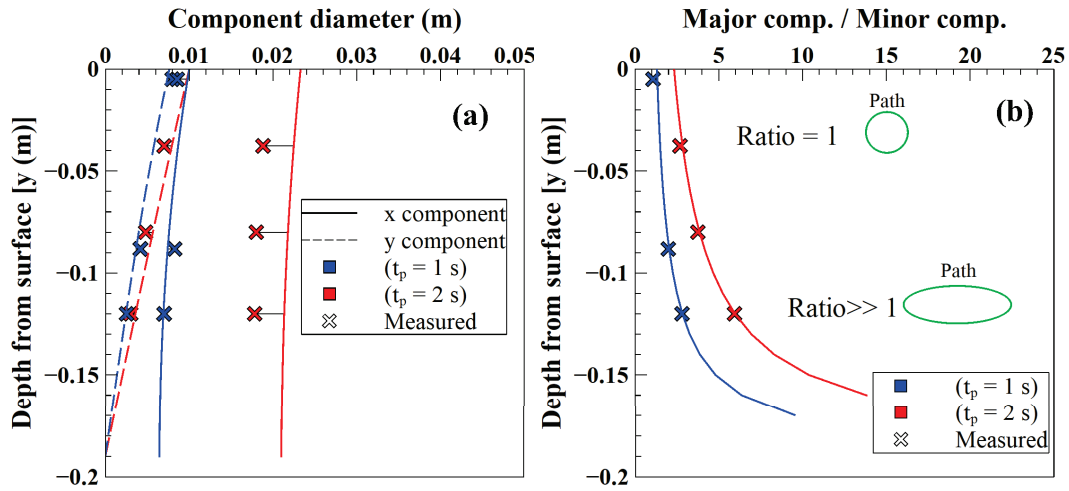


Figure A.10: (a) Component radius vs. depth from surface for $t_p = 1$ s and $t_p = 2$ s waves, crosses signify measurements from images. Solid lines generated from Eqn. A.7, dashed lines generated from Eqn. A.8. (b) Ratio of major component to minor component ($\frac{major}{minor}$) of ellipse plotted vs. depth from surface, showing a flattening ellipse with depth towards bottom.

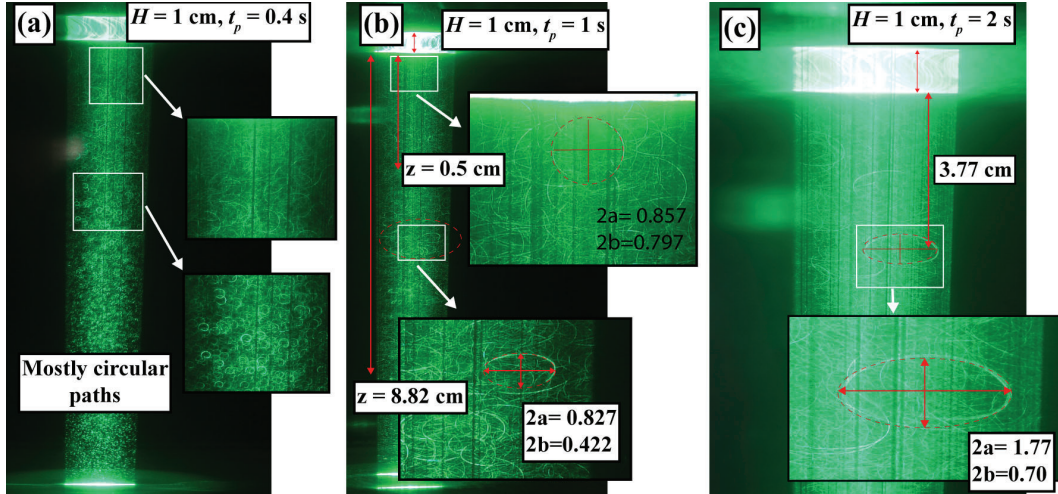


Figure A.11: Images taken with (shutter speed = $1 \cdot t_p$), paths are traced by PIV particles and measured using a pixel scaling then compared to calculated values.

There is good agreement between experimental and theoretical wave paths. The more reliable way to predict wave motion in our tank is the elliptical paths as defined in Eqn. A.7 & A.8. Although the circular path approximation Eqn. A.4 still holds for waves of very short wavelength in our tank.

A.4.2 Wave Motion with Pan

The Nusselt correlation for fluctuating flow heat transfer requires an amplitude and period of fluctuations. Where the amplitude is the forward and back displacement of the fluid. The section above demonstrated traditional equations for wave motion, especially for that of the ellipse, could predict the wave motion in our wavetank reasonably well. However, what is more important is predicting the motion for when the burn pan is in place. First, we will use PIV to quantify the forward and back displacement inside of the pan area. PIV measurements were acquired very close to the water surface through a glass-walled pan. Fig. A.3 shows a picture of the ring in place with the laser sheet examining a portion.

Fig. A.12 shows the u velocity component as a function of time for the $t_p = 1$ s, $H = 1$ cm wave from Table A.1. The solid lines represent measured values from PIV analysis, and the dashed line represents the ideal velocity vs. time curve which would represent that wave. The total horizontal displacement inside of the pan would be the area under each velocity vs. time curve. If the area

under one curve is larger than the other that suggests a progressive velocity down the tank in that direction. We will denote the positive displacement over one wave period u_+ , and the negative total displacement over one period u_- . If the positive u_+ and negative u_- displacements are equal, that suggests a non-progressive motion; i.e a particle that starts at location (x,y) will return exactly to (x,y) after one wave period.

Also evident from Fig. A.12 is that for the wave period $t_p = 1$ s we would expect the u velocity to cross from positive to negative at exactly $(\frac{1}{2} \cdot t_p)$, however for this wave it crosses slightly later at 0.568 s, then back again to positive completing the wave cycle at exactly 1 s. This is consistent with other waves, crossing from positive to negative displacement happens slightly before or after $(\frac{1}{2} \cdot t_p)$, but the cycle completes at almost exactly t_p this is shown for the wave ($t_p = 2$ s, $H = 1$ cm) and ($t_p = 0.4$ s, $H = 0.3$ cm) in Figs. A.13 & A.14.

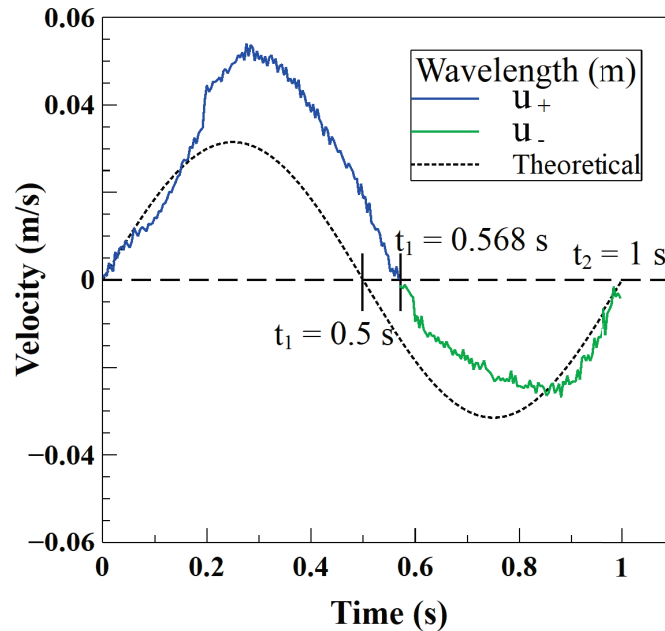


Figure A.12: Horizontal (u) velocity component inside of the pan vs. time for $t_p = 1$ s, $H = 1$ cm wave from Table A.1.

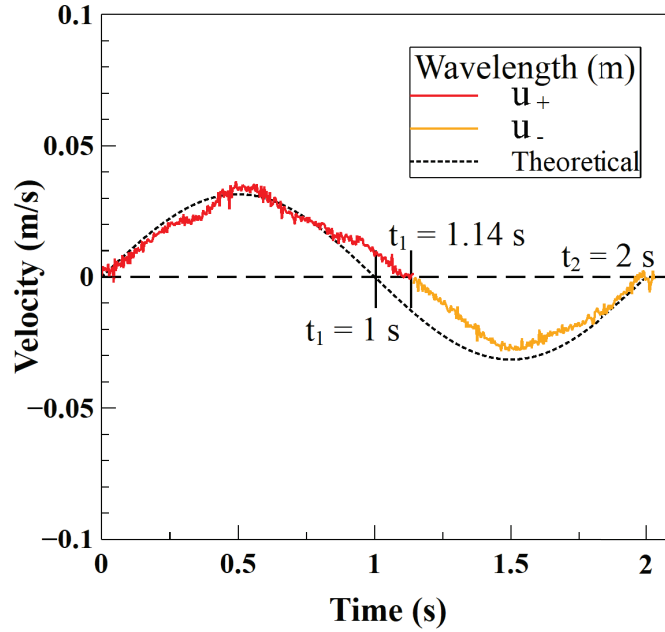


Figure A.13: Horizontal (u) velocity component inside of the pan vs. time for $t_p = 2$ s, $H = 1$ cm wave from Table A.1.

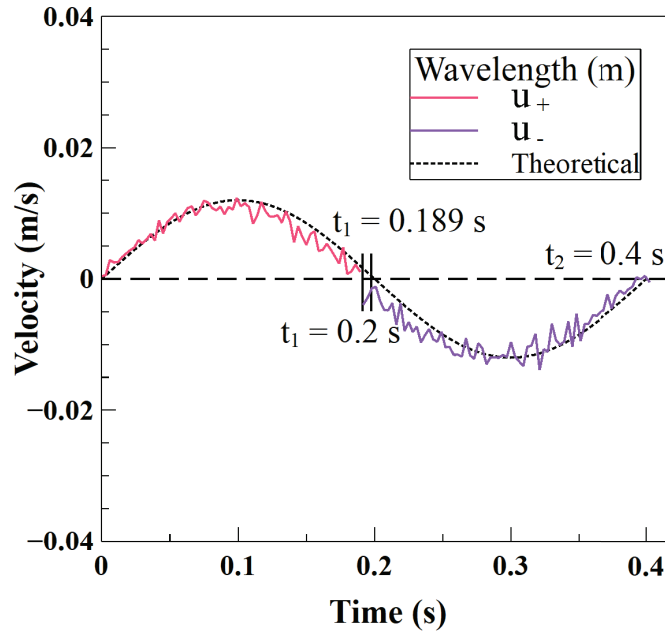


Figure A.14: Horizontal (u) velocity component inside of the pan vs. time for $t_p = 0.4$ s, $H = 0.3$ cm wave from Table A.1.

The total displacement of the positive and negative components of the u velocity are comparable to

the major component of the elliptical path as discussed earlier. To obtain the total displacements (u_+ , u_-) for each wave a 4th order polynomial Eqn. A.10 is fit to the positive and negative velocity curves obtained from PIV analysis. This polynomial is then integrated over the time duration for each section Eqn. A.11 & Eqn. A.12,

$$u(t)_{+,-} = at^4 + bt^3 + ct^2 + dt + e, \quad (\text{A.10})$$

$$u_+ = \int_0^{t_1} u(t)_+ dt, \quad (\text{A.11})$$

$$u_- = \int_{t_1}^{t_2} u(t)_- dt. \quad (\text{A.12})$$

This calculation is shown as an example with coefficients for the $t_p = 1$ s period wave from Table A.1, whose velocity profile u is shown in Fig. A.12,

$$u(t)_+ = 6.5t^4 - 8t^3 + 2.6t^2 - 0.075t + 0.004, \quad (\text{A.13})$$

$$u(t)_- = 6.7t^4 - 20t^3 + 22.6t^2 - 11.5t + 2.2, \quad (\text{A.14})$$

$$u_+ = \int_0^{0.568} u(t)_+ dt = 0.016 \text{ m}, \quad (\text{A.15})$$

$$u_- = \int_{0.568}^1 u(t)_- dt = 0.007 \text{ m}. \quad (\text{A.16})$$

It is immediately evident that one displacement is larger than the other, suggesting a residual forward velocity in the wavetank equal to the difference in total displacements. It is also apparent that the larger of the two velocities is also larger than the major axis of the elliptical path predicted from Eqn. A.7. This is hypothesized to be due to the introduction of an eddy at the bottom of the pan wall, with a frequency determined by the wave period and a size correlated to the wave height. This is discussed further in Sec. A.4.4. Fig. A.15 shows the predicted vs. measured particle displacements in the u direction.

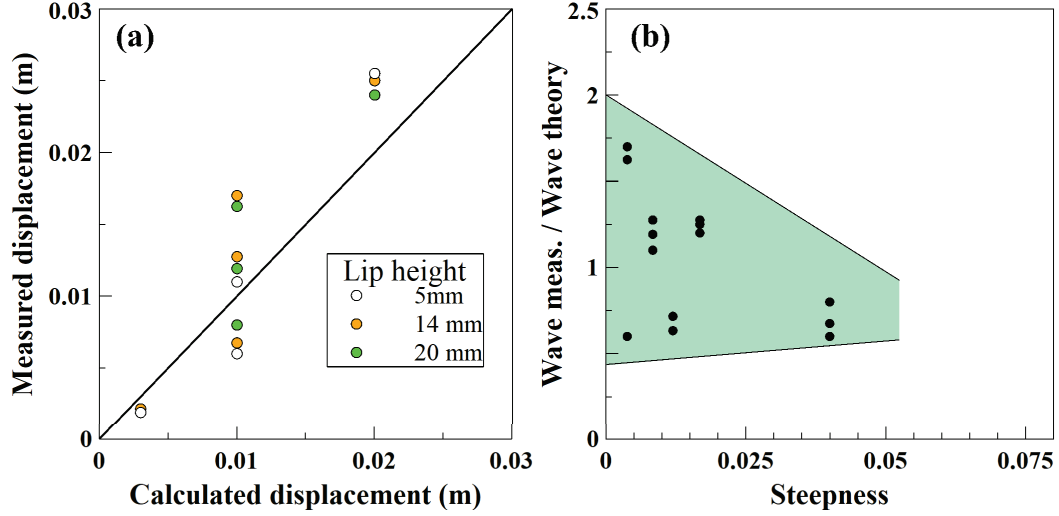


Figure A.15: (a) Wave theory horizontal displacement vs. PIV measured horizontal displacement inside of the floating pan. (b) Ratio of measured displacement to calculated displacement vs. wave steepness.

A.4.3 Experimental Heat Transfer Coefficient

A set of experiments were also conducted to experimentally determine a convective heat transfer coefficient with the addition of waves. These experiments entailed plunging a heated, thermally thin sphere into the wavetank under different wave conditions. The sphere is solid 2017 aluminum with thermal conductivity $k = 200 \text{ W/m}\cdot\text{K}$, and is validated as being thermally thin in Eqs. A.17 - A.18.

$$Bi = \frac{hL}{k}, \quad (\text{A.17})$$

Assuming the properties: $h = 100 \text{ W/m}^2\cdot\text{K}$, $k = 200 \text{ W/m}\cdot\text{K}$, $L = r = 0.00635 \text{ m}$.

$$Bi = \frac{100 \cdot 0.00635}{200} = .0032 \ll 0.1. \quad (\text{A.18})$$

Assuming lumped capacitance the heat transfer the energy balance becomes a relation between the energy lost to cooling and the energy stored in the material. Where h is the convection coefficient ($\text{W/m}^2\cdot\text{K}$), A_s is surface area in m^2 , T is the temperature in Kelvin, m is mass in kg, t is time, and

C_p is material specific heat in J/kg·K.

$$-hA_s(T - T_\infty) = mC_p \frac{dT}{dt}, \quad (\text{A.19})$$

Which becomes the solution:

$$\frac{T - T_\infty}{T_i - T_\infty} = \exp \left[- \left(\frac{hA_s}{mC_p} \right) t \right]. \quad (\text{A.20})$$

The analytical solution Eqn. A.20 can be solved over a series of timesteps to obtain a calculated temperature profile. This calculated temperature profile is then compared to the experimental temperature profile and the Pearson correlation coefficient (R) Eqn. A.21 is used to calculate the R^2 between the experimental and calculated values, measuring the linearity between the two curves. The h value is then iterated using Excel solver until the R^2 is the maximum possible value, i.e. until the two curves have as linear of a relationship as possible.

$$R = \frac{\sum(x_i - \bar{x})(y_i - \bar{y})}{\sqrt{\sum(x_i - \bar{x})^2(y_i - \bar{y})^2}}. \quad (\text{A.21})$$

Fig. A.16 shows an example of this curve fitting. Where the red line is the experimental data obtained from plunging the heated sphere into the wavetank. The black dotted lines are the curve generated from the lumped capacitance analysis Eqn. A.20, with convection coefficient h iterated to find the best-fit solution. This curve-fit is shown for a no wave case and a wave case to show the difference in cooling rate imposed by the wave boundary condition.

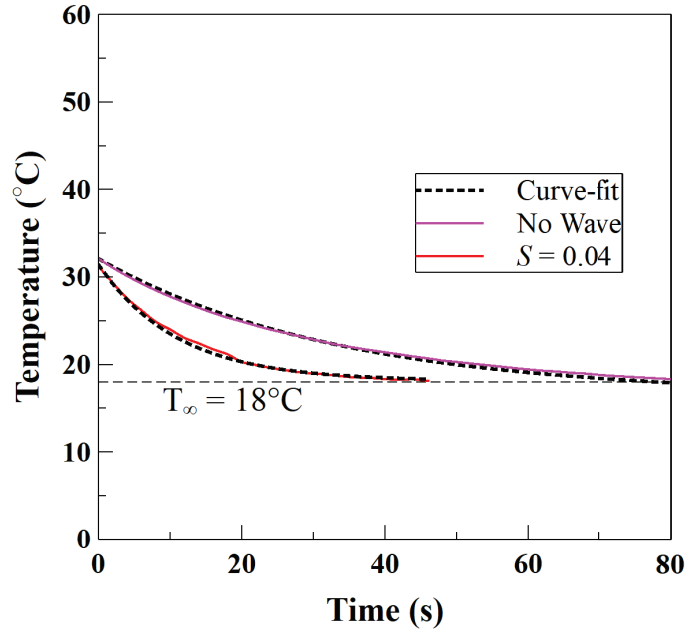


Figure A.16: Experimental and calculated temperature vs. time curves for the convective cooling of the aluminum sphere. Calculated curve obtained from Eqn. A.20.

These experimental convection coefficient curves were fit for 3 repeats of each wave and for the 5 waves examined in this chapter from Table A.1. These values were then plotted vs. wave steepness to obtain Fig. A.17. A linear fit is approximated for the data points and will be used for correlations further in this work. The number labels on each data point are the calculated ratio of major component, to minor component ($\frac{major}{minor}$) imposed by the wave. Expressing the no-wave condition as having a zero for this ratio is not exactly correct as this condition has no movement at all and thus no components to compare. These values are the major to minor components as calculated from the wave theory expressions in Sec. A.4.1.

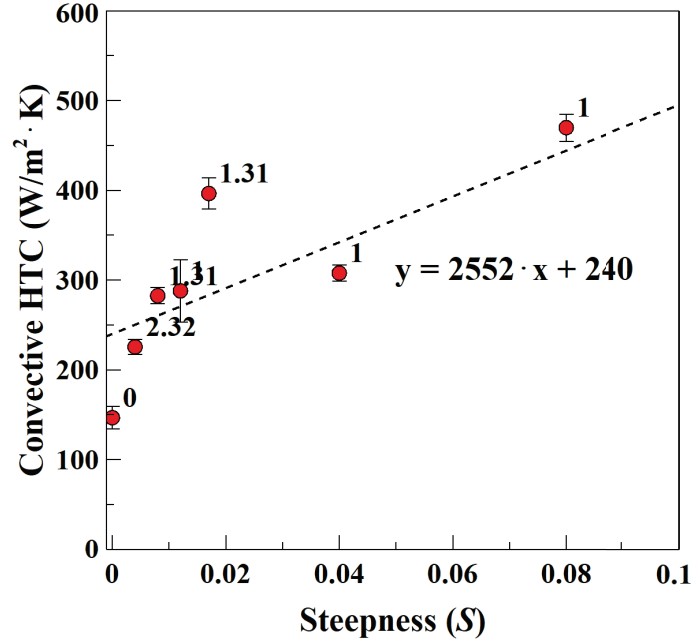


Figure A.17: Experimentally determined heat transfer coefficient (HTC) from sphere experiments versus wave steepness. Showing an increase in heat transfer coefficient with increasing wave steepness.

Fig. A.17 shows that imposing the wave on a surface undergoing cooling increases the rate of heat transfer between the surface and the surrounding fluid. Fig. A.17 shows that this heat transfer coefficient also continues increasing with increasing wave steepness. There also exists a relationship that as the ratio of major to minor components of wave motion approaches 1 the convective coefficient also rises. Although this is likely due to high steepness waves also having low periods, which dictates a smaller wavelength and therefore more circular motion at the surface by necessity.

With the effect of wave motion quantified the effect of the pan was then examined using the same lumped capacitance heat transfer experiments (Fig. A.18). Three different configurations were tested in these experiments. The first is the ‘pan’ which denotes measurements taken in the center of the pan, with the pan centered in the wavetank. Next the ‘1/2’ case denotes experiments conducted halfway between the wall and the center of the wavetank, with no pan in place. Finally, the ‘3/4’ denotes measurements taken 3/4 of the distance from the center of the wavetank to the wall. The original heat transfer values are also included in Fig. A.18 as black dots, for comparison of how the

measured heat transfer coefficient changed with these differing experiments.

The value of the heat transfer coefficient was measured to be very similar between the different cases, values with the pan are only slightly elevated from the original values measured in the center of the tank with no pan. Values measured closer to the wall only begin to decay very close to the wall at the 3/4 measurement point, this is assumed to be due to boundary layer effects at the tank wall. Consistent with the PIV measurements is that for the low steepness waves the pan seems to be increasing the heat transfer coefficient, this is assumed to be through a slight increase in water velocity. Although this behavior seems to be slightly unpredictable it does seem that shorter or steeper waves seem to have an opposite relationship with the pan. With overall wave displacement and heat transfer coefficient experiencing reductions rather than enhancements with the addition of the pan.

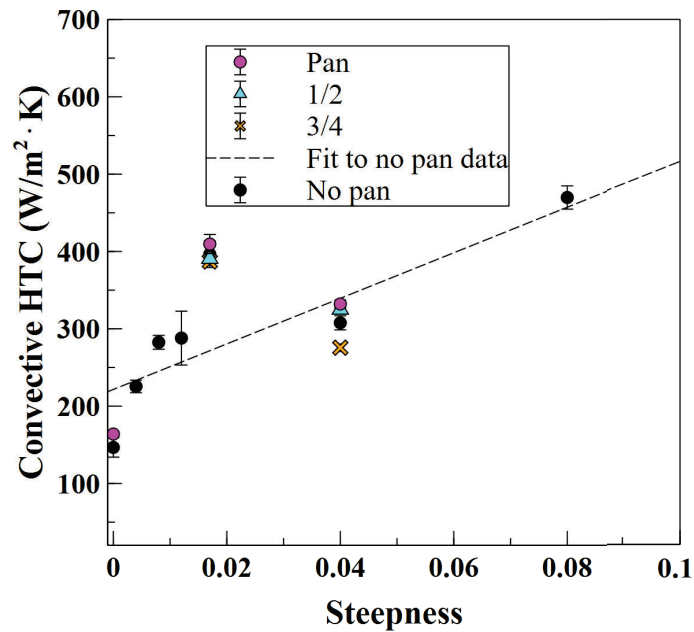


Figure A.18: Experimentally determined heat transfer coefficient (HTC) from the sphere experiment with different conditions. Pan indicates with the pan in place, measured in the center. 1/2 indicates measuring across the width of the tank, 1/2 from the edge of the tank to the center. 3/4 indicates a measurement 3/4 of the distance from the center to the wall of the wavetank.

A.4.4 Vortices Induced at Pan Edge

The change in wave motion with and without the pan in place is hypothesized to be due to the generation of vortices on the leading and trailing edges of the pan. These vortices have a frequency determined by the wave period and a size correlated to the wave height. Fig. A.19 shows the vortex on the leading edge (beach side) of the pan, with a colormap associated with the vortex intensity. The top photo strip shows the wave with $H = 1$ cm and $t_p = 0.4$ s, and the bottom photo strip shows the $H = 1$ cm and $t_p = 2$ s wave from Table A.1. The top and bottom images in each strip of Fig. A.19 are taken from a fraction of the wave period (t/t_p). A small difference in vortex size is observed, most obvious in the third (middle) frame. This size difference is expected to be inversely associated with wave steepness and wave height (top $S = 0.04$, bottom $S = 0.004$) as the motion of the bottom of the pan wall is determined by the motion of the float on the surface which supports the pan. However, the frequency of this vortex appears to be directly tied to the wave period, even with these two very different periods the vortex lasts the same duration as a fraction of the wave period.

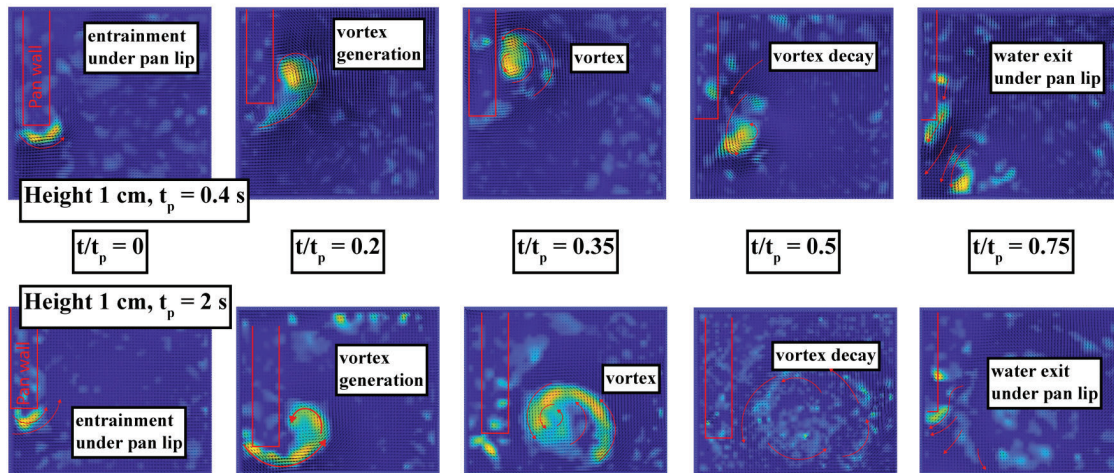


Figure A.19: PIV images taken next to pan wall, colormap shows vortex intensity. Period 0.4 s and 2 s wave are shown, with images taken at time intervals of fractions of the total wave period. Shows vortex generation and decay on the edge of the pan with a frequency equal to the wave period.

The generation of these vortices is theorized to have some effect on the water movement inside of

the pan and therefore underneath the fuel layer. This is also theorized to explain the difference between wave theory displacement values and the measured wave displacement values with the pan in place. This remains an area requiring further investigation in future works.

A.5 Conclusions

These experimental results of the heat transfer coefficient trend with waves are consistent with what one would expect given the information about waves. As wave steepness (H/λ) increases either the wave displacement will need to increase, or the frequency of the oscillations will need to increase (same as wave period t_p decreasing). Frequency of oscillations induced by the wave is the inverse of the wave period, and the wave period directly dictates the wavelength as shown in Eqn. A.3. Experimental results with and without the pan in place corroborate this theory, as the heat transfer coefficient was matched to the cooling rate of a lumped capacitance system. Finally experimentally determined heat transfer coefficients with the pan in place agreed with PIV measurements that sometimes the fuel containment pan would increase water sublayer movement, and sometimes it would dampen water sublayer movement. This is theorized to be due to the generation of vortexes on the leading and trailing edges of the pan. Vortexes were observed being generated at the same frequency as the wave motion, but varied in size and intensity with different waves (Fig. A.19). The author would like to note that this is an area that would benefit from future study.

APPENDIX B

Evaporation Study⁴

B.1 Experimental Apparatus

The wavetank used in this evaporation study is the same wavetank used for the medium scale burning experiments in Ch. 3, the details of the wavetank and experimental apparatus are available in Sec. 3.2. The evaporation experiments were conducted in the large wavetank with the fuel contained in small plastic floating rings. These small rings were 5.08 cm in diameter and 3-D printed using PLA plastic, shown in Fig. B.2. The rings are kept small in comparison to the waves generated in our medium scale wavetank intentionally to facilitate more accurate measurements over the small evaporation area as well as to regulate the volumes of the n-Pentane fuel needed for experimentation. The schematic of the wavetank used shown in Fig. B.1.

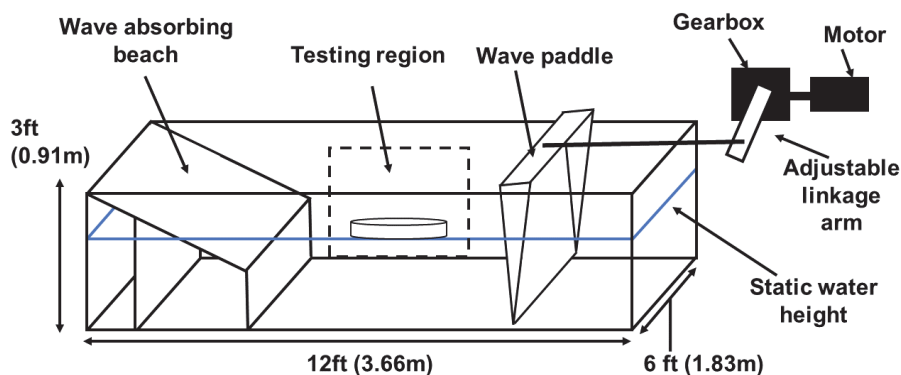


Figure B.1: Dimensioned wavetank schematic of the wavetank used for these experiments.

Fuel selected for these experiments was n-Pentane due to its insolubility in water and high volatility. The density of n-Pentane used in these experiments was measured and found to be ($\rho_l = 626\text{kg/m}^3$). Other important properties include latent heat of gasification ($\Delta h_{fg} = -2034\text{ kJ/kg}$), boiling point

⁴Contents of App. B published in **Arctic Marine Oil Spill Proceedings** as: *Evaporation Behavior of a Volatile Fuel in Waves* [69].

($T_B = 309\text{K}$), and the molecular weight of the fuel ($MW_F = 72.148 \text{ kg/mol}$). The initial thickness of the n-Pentane was 4 mm, fuel was placed in the ring by use of a precise syringe.

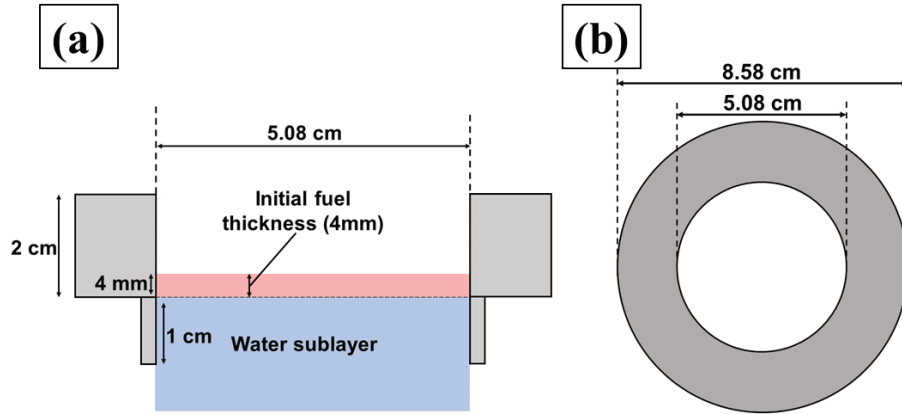


Figure B.2: (a) Side view of 5.08 cm diameter evaporation plastic ring (b) Top view of small evaporation ring.

Monitoring the fuel in the plastic rings was accomplished with the use of a FLIR T335 camera, using a novel method discussed further in this work. A constant wind of about 1.4 m/s was induced with a fan pointed toward the water surface at the beach end of the wavetank, opposite the paddle. Wind measurements were taken at various points 2 cm above the water surface using an OMEGA Model HHF143 rotating vane anemometer. Wind measurements are shown in Fig. B.3 showing good consistency across the water surface. Initially, an arrangement of five small 5.08 cm rings spaced evenly in a cross pattern over the center of the wavetank was used. No significant difference was observed in repeat cases in the evaporation rates of the multiple small rings, and so for further experiments, only a single small ring was used. As such these results may be treated as representative of larger fuel areas, while not an exact reconstruction.

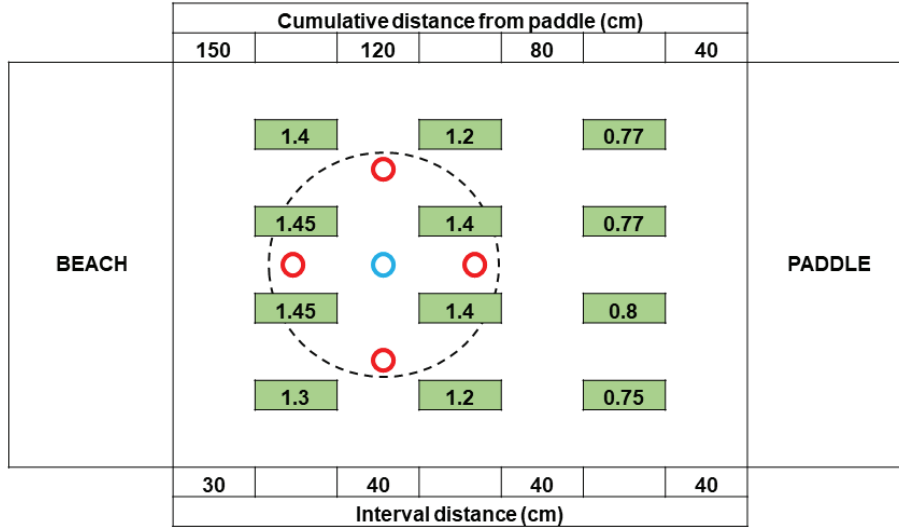


Figure B.3: Wind speed measurements taken inside of the wavetank measured in m/s with a rotating vane anemometer. Initial layout of 5 evaporation locations is shown in red with final chosen location shown in light blue. Dashed line denotes an 80cm circle.

Six different wave profiles were selected for evaluation with evaporating fuel. The objective of the selected waves was to represent a range of wave sizes and wave periods. Wave heights range from 1.4 – 5.7 cm and wave periods range from 1.1 – 3.5 seconds and are shown in Fig. B.1. Data on the water surface position was also collected with an Akamina AWP-24 wave gauge at various positions in the wavetank to ensure relatively linear wave profiles with limited reflections. This data was used to generate the 4 second wave profiles seen in Table B.1.

Table B.1: Evaporation study wave profiles.

Case	Wave Height H (cm)	Wavelength λ (m)	Period t_p (s)	Steepness (S)	Visual (duration = 4s)
No Wave	-	-	-	0	-
Wave 1	3.1	3.89	1.82	0.00797	
Wave 2	5.5	5.71	2.5	0.00963	
Wave 3	1.4	8.28	3.5	0.00169	
Wave 4	3.2	1.83	1.1	0.01749	
Wave 5	3	7	3	0.00429	
Wave 6	5.7	3.73	1.76	0.01526	

B.2 Results & Analysis

Due to the low surface temperature of the evaporating Pentane, the time at which the fuel has evaporated can be obtained using the infrared images obtained from the FLIR camera. An image processing technique was developed to extract the evaporation times of the various cases. These times, along with the initial fuel thickness and fuel residue estimations were used to calculate the global regression rate as well as develop an evaporation model. The first step in image processing was to motion stabilize the moving fuel ring and crop the video to show just the fuel surface. The frames-per-second of the video was also reduced from 30 fps to 10 fps to increase processing speed. Pre-processed video is shown in a screenshot in Fig. B.4a, and a processed screenshot is shown in Fig. B.4b.

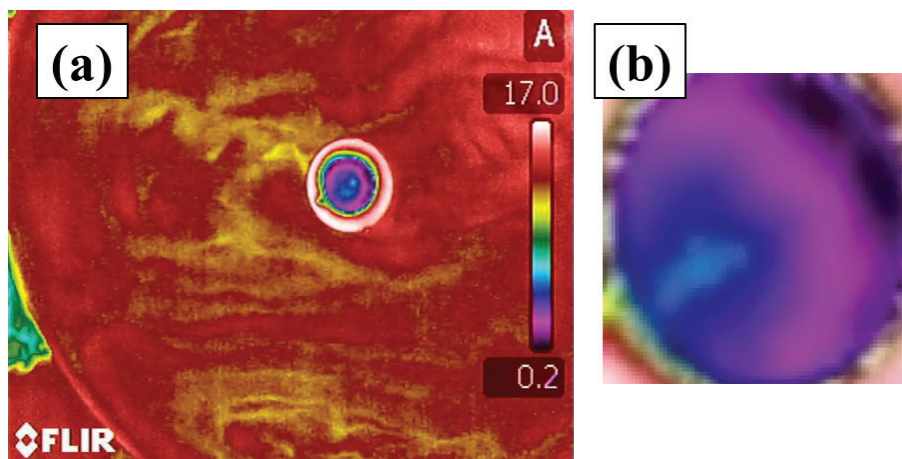


Figure B.4: (a) Raw video footage obtained from FLIR showing the uncentered fuel ring units show degrees Celsius (b) Cropped and stabilized video footage showing just the center of the fuel ring and the cold n-Pentane undergoing evaporation.

A MATLAB script was then used to analyze these cropped video files. Processing involved finding the average red, blue, and green (RGB) channel values for each frame and plotting the averages versus the frame number. An example of this plot is provided in Fig. B.5. As the water underneath the evaporating fuel is exposed the RGB levels change. This is due to the higher temperature water showing up mostly in the red channel, while the cooler Pentane primarily shows up in the green and blue channels. Screenshots showing the various surface conditions are provided along with the average RGB values. A threshold value of an average blue channel intensity of 130 was used to determine the time at which the fuel had evaporated. It may also be a viable method to see when the RGB channels converge just before again diverging to evaluate the evaporation time.

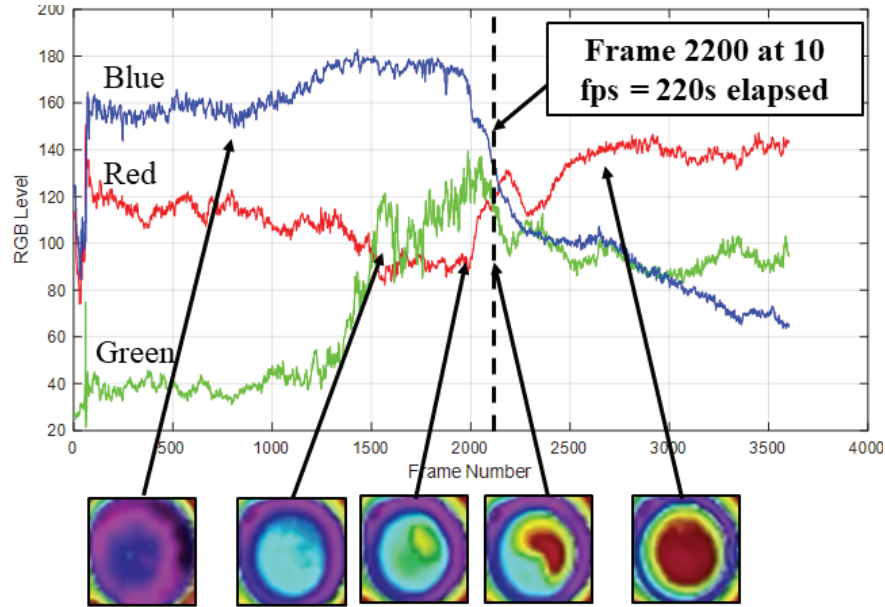


Figure B.5: Mean RGB level plotted vs. frame number for a no wave case.

As the fuel continues to evaporate a small amount remains stuck to the walls of the plastic ring via surface tension. Since we are interested in evaporation just up until the water is visible, the volume of this remaining fuel was estimated and subtracted from the initial volume to find the total volume evaporated. The evaporation rate was then determined from the amount of fuel evaporated over the time duration obtained from the averaged RGB values Fig. B.1. These evaporation rates were then plotted vs. wave steepness (S) Eqn. B.2. Table B.1 shows the waves used in these experiments along with their calculated steepness values.

$$Evaporation\ Rate = \frac{Initial\ Thickness - Final\ Thickness}{Evaporation\ Time}, \quad (B.1)$$

$$S = \frac{H}{\lambda}. \quad (B.2)$$

The regression rate vs. steepness plot in Fig. B.6 shows the clear trend between an increasing wave steepness and an increased evaporation rate. An increasing steepness can be correlated with a more ‘aggressive’ wave. Steepness represents the slope of the leading and trailing edge of the wave peak. Therefore, as wave steepness increases, the wave jostles the floating ring up and down more

aggressively and causes more water movement across the bottom of the fuel.

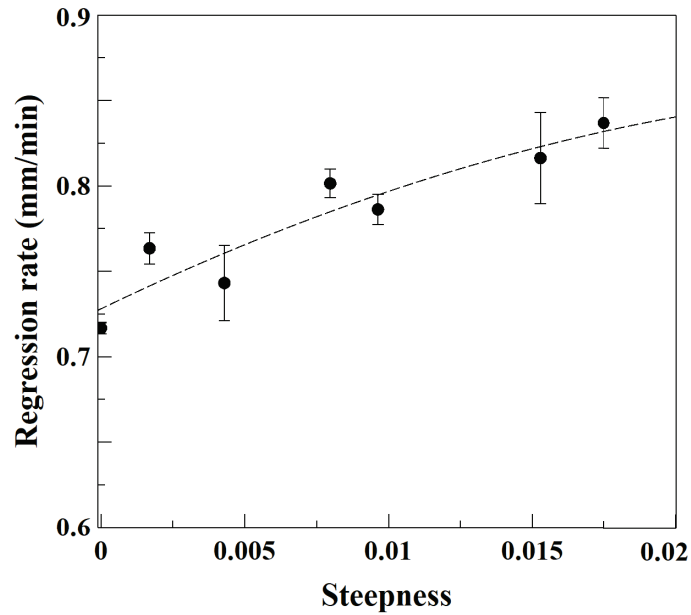


Figure B.6: Regression rate vs. steepness for the evaporation of n-Pentane with waves.

Additionally, a model was then developed to analyze the evaporating fuel with waves. A coordinate direction (y) is defined in the following equations and it denotes the vertical coordinate direction (in depth), with s being the fuel surface location at ($y = 0$). The energy balance is demonstrated in Fig. B.7 where a one-dimensional model is assumed for heat and mass transfer at fuel-air interface Eqn .B.3, and heat transfer at the fuel-water interface. The heat from the water sublayer is assumed to be from convection.

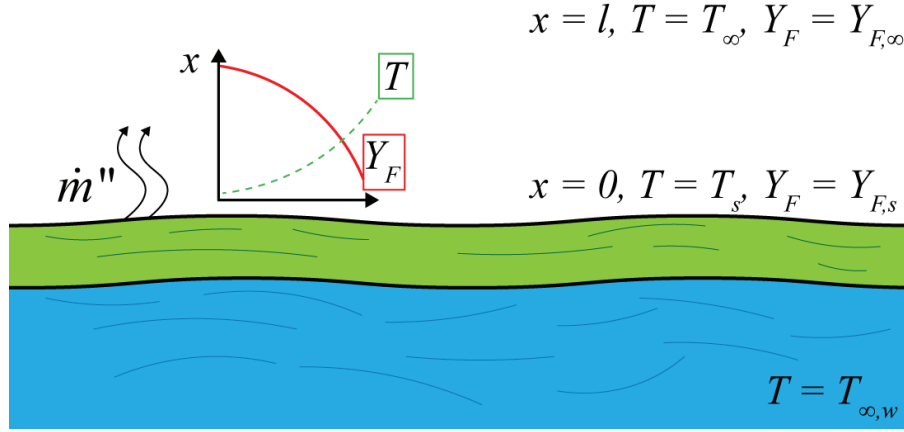


Figure B.7: Model parameters and boundary conditions

The energy equation in cartesian coordinates is expressed as shown in Eqn. B.3.

$$k_g \frac{dT}{dy} \Big|_+ - k_F \frac{dT}{dy} \Big|_- = \dot{m}'' h_{fg}, \quad (\text{B.3})$$

Here, \dot{m}'' represents the evaporative mass flux, ($C_{p,g} = 1.66\text{kJ/kg}\cdot\text{K}$) is the specific heat of the gas phase, T is the temperature, and ($k_g = 0.026\text{W/m}\cdot\text{K}$) is the thermal conductivity of the gas phase. The second-order differential equation is solved using the boundary conditions: ($x = 0, T = T_s$) and ($x = l, T = T_\infty$). This model uses a boundary layer thickness l . Thus, integrating Eqn. B.3 gives the equation:

$$k_g \frac{\frac{C_{p,g} \dot{m}'' (T_\infty - T_s) e^{-\frac{C_{p,g} \dot{m}'' l}{k_g}}}{1 - e^{-\frac{C_{p,g} \dot{m}'' l}{k_g}}} + h_w (T_{\infty,w} - T_s) = \dot{m}'' h_{fg}, \quad (\text{B.4})$$

From the solution to this energy balance in Eqn. B.4 the unknowns are convection induced at the fuel-water interface h_w , surface temperature T_s , and boundary layer thickness l . The boundary layer thickness can then be considered as a function of the Reynolds number:

$$l_x = \frac{5x}{\sqrt{\text{Re}_x}}, \quad (\text{B.5})$$

The diffusion length is integrated over the evaporating pool diameter to find the spatial average of

the boundary layer thickness.

$$\frac{1}{D} \int_0^D l_x dx, \quad (\text{B.6})$$

Giving the resulting average diffusion length as:

$$l_{avg} = \frac{10D}{3\sqrt{\text{Re}_D}}. \quad (\text{B.7})$$

The thermal boundary layer thickness l_T is then calculated as a function of the average boundary layer thickness and the Prandtl number.

$$l_T = \frac{l_{avg}}{\text{Pr}^{1/3}}, \quad (\text{B.8})$$

Similarly, the concentration boundary layer thickness is calculated as a function of the average diffusion length l_{avg} and the Lewis number Le ,

$$l_D = \frac{l_{avg}}{Le^{1/3}}. \quad (\text{B.9})$$

The fuel mass fraction at the fuel-air interface can be approximated using the mass fraction gradient at the surface $\left. \frac{dY_F}{dx} \right|_s$ and can then be evaluated using Eqn. B.10.

$$\left. \frac{dY_F}{dx} \right|_s = \frac{\dot{m}''(1 - Y_{F,s})}{\rho_g D} \simeq \frac{Y_{F,s}}{l_D}. \quad (\text{B.10})$$

In Eqn. B.10 the fuel concentration gradient $\left. \frac{dY_F}{dx} \right|_s$ is also presented as an approximation of the surface mass fraction $Y_{F,s}$ divide by the diffusion length l_D :

$$\left. \frac{dY_F}{dx} \right|_s = \frac{Y_{F,s}}{l_D}. \quad (\text{B.11})$$

Where the mass fraction at the surface $Y_{F,s}$ and mole fraction at the surface $X_{F,s}$ are calculated using Clausius Clapeyron equation as shown in Eqn. B.12 & B.13. The mass fraction at the interface is evaluated using Eqn. B.12 as a function of the mole fraction, molecular weight of the fuel $MW_F =$

72.15 g/mol and air $MW_{air} = 28.97$ g/mol and the ideal gas constant $R_u = 8.314$ J/mol·K. The mole fraction at the surface $X_{F,s}$ is evaluated in Eqn. B.13 where T_B is the saturation temperature of the fuel, h_{fg} is the enthalpy of vaporization, and T_s is the unknown surface temperature;

$$Y_{F,s} = \frac{X_{F,s}MW_F}{X_{F,s}MW_F + (1 - X_{F,s})MW_{air}}, \quad (\text{B.12})$$

$$X_{F,s} = \exp \left[-\frac{\Delta h_{fg}}{R_u/MW_F} \left(\frac{1}{T_s} - \frac{1}{T_B} \right) \right]. \quad (\text{B.13})$$

With two methods for calculating fuel concentration gradient $\left. \frac{dY_F}{dx} \right|_s$ the surface temperature T_s is determined by iteration until the error between the two calculated fuel concentration gradients is minimized.

Fig. B.8 shows the surface temperature plotted vs. steepness. Calculated surface temperatures range from slightly above 282 K to just above 284.5 K, a range of about 2.5 degrees Kelvin. Also observable is the relationship between increasing wave steepness and increasing surface temperature. Showing that as wave steepness increases the anticipated fuel surface temperature is also increasing. This increase in surface temperature is driven by increased convection at the fuel-water interface. However, in burning cases, the fuel layer is hotter and transfers heat to the water sublayer. In evaporation cases, the fuel layer is colder, and heat is flowing from the warmer water sublayer into the colder fuel layer.

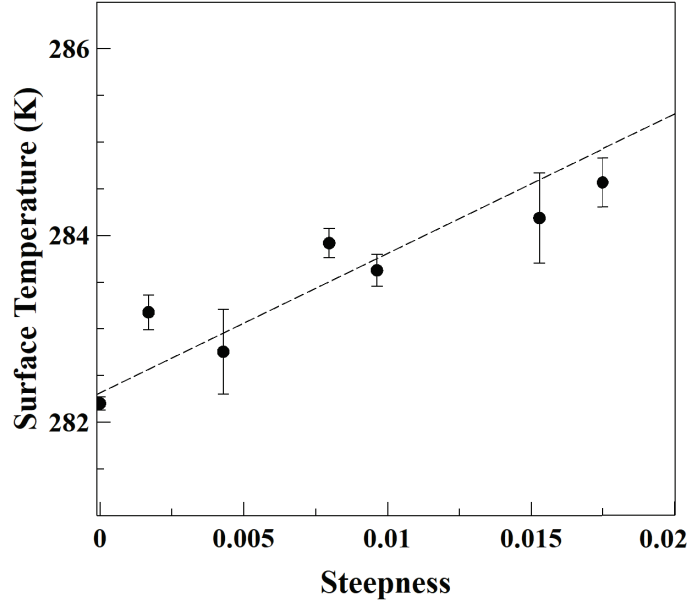


Figure B.8: Calculated surface temperature vs. wave steepness. Surface temperature is predicted to rise with increasing wave steepness.

With T_s then known the final remaining unknown variable is the heat transfer coefficient at the fuel-water interface h_w , which is embedded in the term $-k_F \left. \frac{dT}{dy} \right|_-$ and presented as $h_w(T_{\infty,w} - T_s)$. The sum of all terms in Eqn. B.3 should be zero, such that the two energy terms can account for the observed mass flux \dot{m}'' . In this way the h_w term is solved iteratively until the calculated mass flux matches the experimental mass flux. The convective heat transfer coefficient is calculated for each case and plotted vs. wave steepness in Fig. B.9a. The triangles on Fig. B.9a represent the h_w values calculated from the experimental evaporation data in this chapter, while the circles represent data points calculated from the linear fit generated in Sec. A.4.3. Fig. B.9b are these two sets of points plotted against each other, with the evaporation experiments on the x-axis and the sphere experimental fit on the y-axis. Fig. B.9b shows how well the linear fit to the sphere experiments agrees with the calculations from this evaporation section.

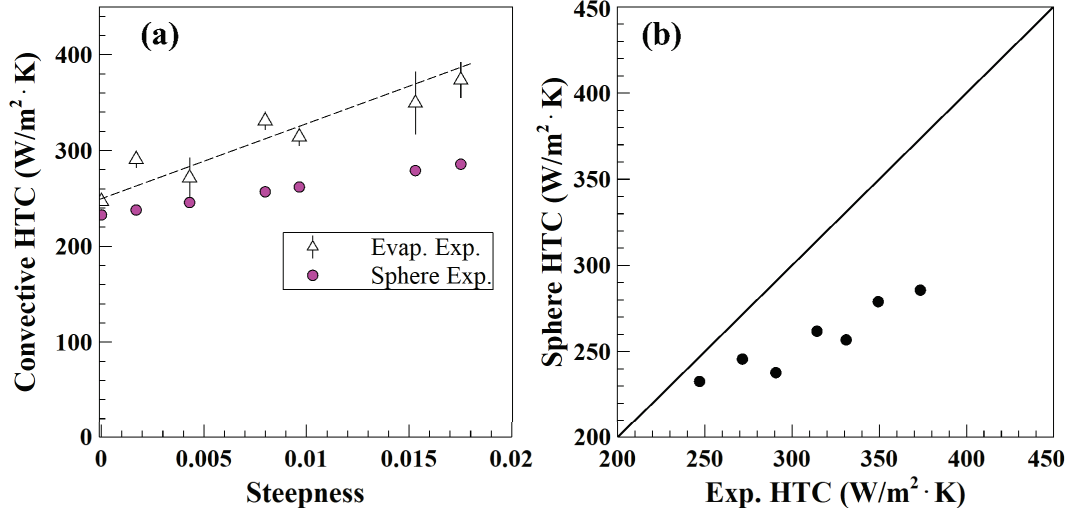


Figure B.9: (a) Convective heat transfer coefficient vs. wave steepness, triangles calculated in this section. (b) Convective heat transfer coefficient (HTC) values calculated in this section plotted vs. HTC from the sphere experiments Sec. A.4.3

Waves improve the mass loss rate of the evaporating fuel via a slight increase in surface temperature, an increase in the fuel concentration gradient, and enhanced heating of the cold fuel from the water sublayer. First, any mechanism by which fuel is transported away from the interface faster will increase the fuel concentration gradient $\left. \frac{dY_F}{dx} \right|_s$ and further increase the mass loss rate. The no-wave case reaches ambient concentrations (0%) a greater height over the fuel than the wavy case. This indicates that the air boundary layer over the baseline case becomes saturated with fuel vapor, reducing the evaporation rate. The addition of waves induces up and down undulations as well as slight side-to-side movements of the fuel slick. These movements create areas of low and high concentrations in the fuel-air boundary layer, effectively mixing fresh air into the saturated fuel-air mixture. Waves also induce an enhancement of the convective heat transfer coefficient at the fuel-water interface, a proposition supported by experimental data in App. A.4.3. For fuels colder than ambient this enhanced heat transfer coefficient serves to add more heat to the evaporating fuel, which in turn enhances the mass loss rate. Without waves, the evaporation rate is purely driven by the diffusion of the fuel concentration gradient. Waves induce a mixing behavior, transporting the fuel vapor away from the surface more quickly.

B.3 Conclusions

Studies on the evaporation of oils and fuels have indicated the significant impact that the evaporation rate can have on fuel residues in the environment. This study focused on the impact of waves on the evaporation rate of a highly volatile fuel floating on water. A novel method utilizing an infrared camera was developed for determining the evaporation time of a volatile fuel under wavy conditions. This method proved reliable in providing accurate evaporation times, where a load cell or other method is not viable. Results indicate that the evaporation rate increases with increasing wave steepness. A model developed indicates that predicted surface temperatures also increase slightly. Further, the model indicates that the fuel concentration gradient at the surface increases with waves and that the heat transfer coefficient at the fuel-water interface increases with waves. Supporting the hypothesis that wave motion helps to move fuel vapors away from the fuel surface faster and thus increases evaporation. As well as that the wave action produces an enhanced heat transfer coefficient across the fuel-water interface. Resulting wave heat transfer coefficient values h agree well with results both from burning experiments and from the heat transfer experiments conducted in App. A.4.3.

APPENDIX C

Experimental Equipment/ Codes

C.1 Wave Turbulence

C.1.1 PIV Particle Count Code

This code is written for MATLAB and counts the number of particles (dots) in an image. This code was written by Nate Sauer.

```
1 clc;
2 I = imread('count1.png');
3 gray = rgb2gray(I);
4 binaryImage = gray > 110;
5 imshow(binaryImage);
6 figure; imshow(I);
7 [labeledImage, numberOfCircles] = bwlabel(binaryImage);
8 numberOfCircles
```

C.1.2 PIV Frames and Laser Visualization Code

This code is written for MATLAB and provides a visualization of the camera framerate and laser pulse output timing. This code also counts the number of laser pulses per camera frame. This code was written by Nate Sauer.

```
1 clear;
2 clf(figure(1));
3 clf(figure(2));
4
5 %-----Camera settings
6 shutter=1900;           %shutter duration microseconds
7 framerate=500.0000;    %camera framerate fps
```

```

8 t=-1:1:10^-6;           %range to generate data over 1s=10^-6
j=10000;                 %x-axis range for figure 1
10 s=num2str(shutter);    %converting shutter to characters for filenaming
p=num2str( framerate);   %converting framerate ...
12 %-----laser settings
pulsew=.039;            %pulse width
14 mega=10;              %laser MHz

16 %-----camera section%-----
f=framerate/1000000;    %frequency adjustment
18 frame=(1/framerate)*10^-6;
shutperc=(shutter/frame)*100;
20 sq=0.5+(0.5*square((2*pi*f*t),shutperc));
%-----%laser section%-----
22 lasfreq=mega*10^-6;   %convert to Hz
l=lasfreq/1000000;      %freq adjustment
24 n = shutter;          %range to generate laser pulses over, set to generate
                        over one frame for visualization
b=0:.01:n;               %generates pulses for underneath the shutter square wave
26 las=(1/lasfreq)*10^-6;
lasperc=(pulsew/las)*100;
28
sq2=0.75*(0.5+(0.5*(square((2*pi*l*b),lasperc))));
30 for i=1:n
    numberOfPulses=nnz(diff(sq2 > .7) > 0) %counts pulses, make sure threshold is
                        below what the laser square wave will exceed
32 end
gap=(frame-shutter);
34
k=shutter+50;
36 z=shutter-50;

38 figure(1);
plot(b,sq2,'green','linewidth',0.1); %plots laser pulse lines
40 hold on;

```

```

plot(t,sq,'black','linewidth',2);           %plots framerate lines
42 xlabel('Time \muS');
set(gca,'YTick', []);
44 xlim([-2 j]);                             %X-AXIS LIMITS FIG 1
ylim([-0.005 1.5]);                         %Y-AXIS LIMITS FIG 1
46 dim=[0.25, .7, 0.1, 0.1]
str=sprintf('%.2f',numberOfPulses);
48 annotation('textbox',dim,'String',str,'FitBoxToText','on');
text(z-1500,1.1,'Pulses per camera frame');
50 hold off;

52 figure(2);
plot(b,sq2,'green','linewidth',0.1);       %plots laser pulse lines
54 hold on;
plot(t,sq,'black','linewidth',2);         %plots framerate lines
56 xlabel('Time \muS');
set(gca,'YTick', [])
58 xlim([1850 1950]);
ylim([-0.005 1.5]);
60 dim=[0.25, .7, 0.1, 0.1]
str=sprintf('%.2f',numberOfPulses);
62 annotation('textbox',dim,'String',str,'FitBoxToText','on');
text(1860,1.1,'1Mhz = 1 Pulse per \muS');
64 hold off;

66 exportgraphics(figure(1),['frames',p,'fps',s,'micS'],'.png','Resolution',500)
exportgraphics(figure(2),['laseerpulse',p,'fps',s,'micS'],'.png','Resolution',500)

```

C.2 Small Scale

This section contains the materials needed to begin operating the small-scale wavetank. It also contains a design overview, operation guidelines, and procedures for operating the small-scale wave-tank.

C.2.1 Overview

As of 2/17/21 a new positionally controlled wave generator was installed on the wavetank. Prior to this data all waves had been generated with a cam and pusher arm style of wave generator. This method is simple, and while effective offers a limited range of wave sizes and periods. The current wave generator offers a much wider range of wave parameters, as well as the ability to change between waves much faster. This section will focus on explaining the basics of this method, as well as how to operate the system.

The wave generator consists of 3 main components the power supply, motor, motor driver, Arduino board, and platform. The user will also need a laptop and some software to run the wavetank. The power supply is a 500W 70V switch power supply typically used for CNC router tables. The motor is a 4Nm Nema34 closed loop stepper motor, which was purchased as a package with a 2 phase hybrid HSS86 servo driver. The Arduino is an Arduino MEGA 2560. The power supply, motor driver, and Arduino are mounted to an aluminum shield and are located away from the tank. The stepper motor and motor platform are located on the tank.

C.2.2 Flume Construction

The flume of the wave tank is constructed of 2.54 cm acrylic glued together at the edges. A 1:6 sloped beach covered with a rubberized horsehair mat acts as the wave absorber at the end of the tank opposite the wave generator. Typically, the wave tank is filled with water to a depth of 18 cm. At this depth the tank is holding about 27.5 gallons of water, the water alone weighs 230 lbs.

The beach is constructed of an acrylic sheet, and held in place using two bricks, one placed vertically under the rear to create the slope. Another brick is placed horizontally across the front of the beach to both prevent the horsehair from floating, as well as to prevent the beach from sliding forward.

The wave paddle is secured to the floor of the tank using a semi-flexible glue such as silicon caulk or RTV. This joint does decay over time and will need to be replaced, but this method prevents the need from drilling holes in the bottom of the tank which present their own complications.

C.2.3 Wave Generator Design and Construction

Design of the Arduino program started with knowing that the inputs would be wave period and wave height, and the resulting output would be motor step and direction commands. The flow of data is illustrated in Fig. C.1.

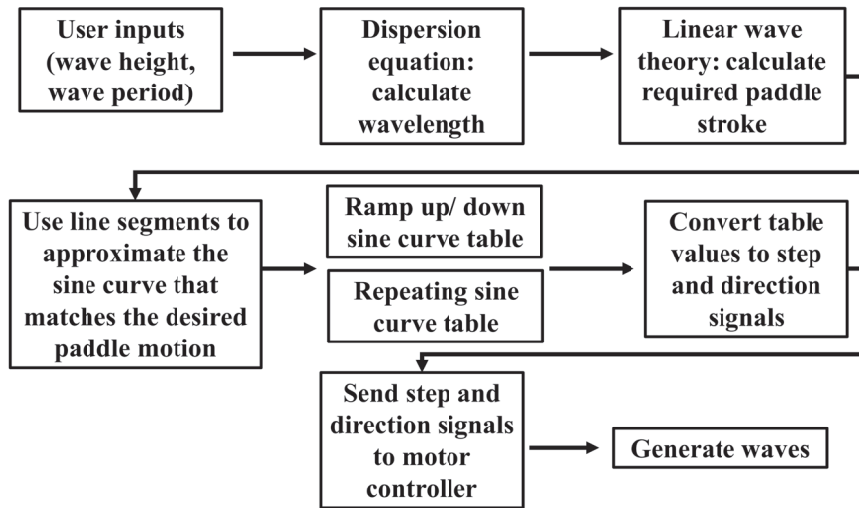


Figure C.1: The flow of data from the user input to the output signals to the motor.

To obtain the paddle's positions, the first step is to calculate how far the paddle needs to move back and forth (stroke length, K') to create the desired wave. Calculating this information from the desired wave parameters requires the use of the water wave dispersion equation as well as linear wave theory developed by Havelock [4], Biesel and Suquet [5], and Kravtchenko and Santon [101] and summarized in Design of Wave Tanks [52]. The dispersion equation C.1 is used to calculate the wavelength of a wave with the period τ , height H , and tank depth d known.

$$\lambda = \frac{g\tau^2}{2\pi} \tanh\left(\frac{2\pi d}{\lambda_{old}}\right), \quad (\text{C.1})$$

Linear paddle motion is then calculated with:

$$m = \frac{2\pi}{\lambda}, \quad (\text{C.2})$$

$$K' = 2 \frac{\sinh(md)(1 - \cosh(md) + md \sinh(md))}{md[\sinh(md) \cosh(md) + md]}, \quad (\text{C.3})$$

$$H = \eta(K')2z. \quad (\text{C.4})$$

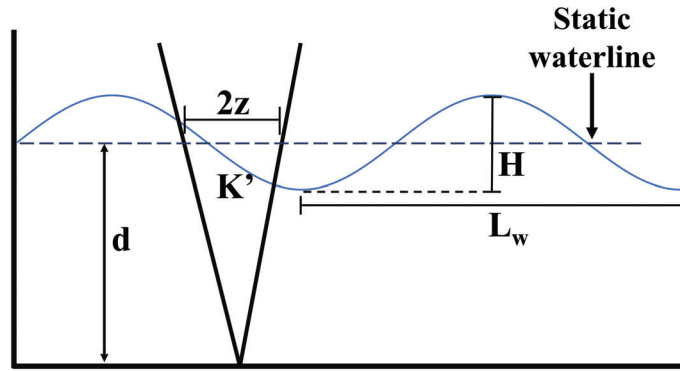


Figure C.2: Variables used when calculating stroke length.

Fig. C.2 shows the variables referenced in the dispersion relation. Using the wave height to calculate K' , $2z$ is solved for the stroke required at the free surface to create the wave. The paddle velocity is then calculated by moving the correct distance ($2z$) throughout the wave period. Each motor step is then fit to a sinusoidal velocity profile. The motor step and direction commands are then sent to the controller, which operates the motor and generates the waves.

Fig. C.3 shows the hardware and electronics used to make the wave generator, including the motor platform, pusher arm, wave paddle, and rack and pinion gears. The rack gear is permanently affixed to the top of the pusher arm. The rack gear runs through a PTFE-slotted block and is held against the pinion gear via a hinged spring-loaded plate. This allows the pusher arm to always ride against the pinion gear no matter the angle of the pusher arm, and the PTFE block acts as both a guide and a smooth-running surface while being much simpler and more resistant to corrosion than rolling bearings.

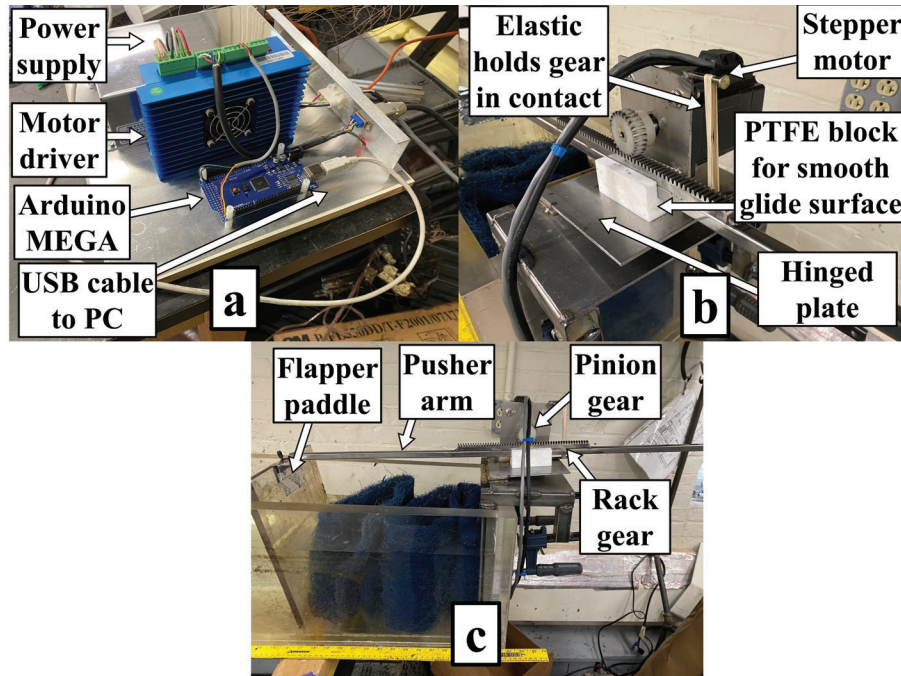


Figure C.3: (a) Stepper motor controller hardware, (b) Stepper motor and gear configuration, (c) Wide view of stepper motor and wave paddle.

Basic Operation

Described simply the user inputs the desired wave height and period, the Arduino then calculates several wave parameters ending in the needed paddle stroke. The program then translates this linear paddle stroke into sinusoidal forward and back motion, and finally the motor steps needed to perform this action. The Arduino then sends these motor steps to the motor driver, which actuates the motor and generates waves.

Operation Checklist

This will serve as a basic step-by-step on how to turn on the wave tank and begin making waves.

1. Turn on laptop/ pc that will be used to control Arduino
 - (a) Be sure to have Teraterm installed
2. Plug Arduino into computer via usb
3. Plug orange power supply cord into wall
4. Teraterm operation

- (a) Open Teraterm (may need to do as admin)
- (b) Select SERIAL: USB-COM that the Arduino is plugged into.
- (c) SETUP > Serial Port
 - i. COMx, 9600, 8-bit, none, 1-bit, none
- (d) SETUP > Terminal
 - i. Receive: LF, Send: LF
- (e) If needed EDIT > Clear screen
 - i. If the terminal and serial port are not setup correctly the command window will become jumbled when commands are sent/ received.

5. **VERY IMPORTANT**

- (a) An impossible wave or improper value (say inputting a 0 into the wave period) will lock up the motor. The entire system must be reset to resume making waves.
- (b) If an improper or impossible value is entered into the program you can always press the reset button on the Arduino and the user inputs will start over. In this way you can prevent a mistake from locking up the motor and requiring a restart.
- (c) Reset procedure on motor lockup
 - i. Unplug the orange power cable from the wall, wait 30 seconds.
 - ii. Plug the cable back into the wall
 - iii. Press the reset button on the Arduino
 - iv. Fresh user input line should appear in Teraterm.

6. Generating waves

- (a) To generate waves simply input the desired wave height in centimeters followed by the desired period in seconds.
- (b) The program will begin ramping up to generate waves
- (c) Once the program is generating the full profile waves the terminal will read "Output Running . . ."
- (d) The waves can then be stopped at any point by pressing the enter key.

7. Emergency stopping

- (a) The waves can be stopped at any point by pushing down on the lever that holds the gear against the motor.
- (b) Should the input wave be too large the motor will run off either end of the gear, this is fine and does not hurt any components but once the program is stopped the motor must be re-centered.

8. Additional notes

- (a) Wave absorbing material (blue rubberized horsehair mat) should be added to both the beach and behind the paddle to reduce reflections.
- (b) The tape holding the pushing arm to the paddle may need to be replaced/ reinforced occasionally.
- (c) Some wave profiles can generate a standing cross wave (especially those that have fast periods, sub 0.5 seconds.
 - i. This is a complex phenomenon but should be avoided if possible.
 - ii. Example of this seen here: <https://www.youtube.com/watch?v=IQoKzO-0eTI> .
- (d) Editing the program
 - i. Several parameters in the Arduino program may need to be edited over time to optimize performance of the wave generator. These primarily include tank depth and efficiency.
 - ii. The user will need to download Arduino IDE to edit the program.
 - A. Open the code file
 - B. Tools > Board > Arduino MEGA
 - C. Tools > Port > Comx if needed
 - D. Edit code as needed
 - E. Sketch > Upload to upload new code to board
 - F. Tools > Serial monitor to test (same as teraterm)

C.2.4 Small Wavemaker Arduino Code

This code is written for Arduino IDE and operates the small wavetank wave generator in the logic path shown in Fig. C.1. This code was written by Jeff and Nate Sauer.

```

1 //*****
// Wave tank motor control program
3 //
// In this program we are controlling a stepper motor which drives the paddle in a
// wave tank.
5 // First we obtain console input for the wave height (in feet) and wave period (in
// seconds).
// Then we use the dispersion equation to calculate the paddle motion. Next we
// create two tables
7 // of line segments which approximate the motion of the paddle. The first table is
// the repeating
// table that maintains a constant amplitude sinusoid for as long as required. The
// second table
9 // is the startup waveform which gradually builds up the sinusoidal paddle amplitude
// . The second
// table is also used in reverse when stopping the motion of the paddle. These
// tables of segments
11 // are then used to create step and direction signals for the stepping motor
// controller. After the
// start sequence is finished and repeating motion is established, hitting <ENTER>
// will initiate
13 // the stop sequence and return the paddle to top-dead-center. The program then goes
// back to the
// beginning and prompts for new console input.
15 //
// Initial creation by Jeff & Nate Sauer      01/03/2021
17 // Added crude stop on <Enter> keypress      01/05/2021
// Added precision stop by reversing startup  01/06/2021
19 // Cut back on segments, changed count+1
// to rounding, improved console printing     02/03/2021
21 //*****

23 #include <arduino.h>
#include <math.h>

```

```

25 const int pulse_pin = 22;           // Use pin 22 for the motor step pulse
    output signal
27 const int direction_pin = 24;      // Use pin 24 for the motor direction
    output signal
const float tank_depth = 16.5;       // Water depth in cm
29 const float gear_ratio = 1000.0/11.969; // Motor steps per cm of travel
const int num_of_segs = 32;          // Number of line segments per wave period
31 const int quadrant_segs = 8;       // Number of segments in one quadrant =
    num_of_segs/4
float height;                         // User input wave height
33 float period;                      // User input wave period
float paddle_amplitude;               // paddle motion returned from the
    dispersion equations
35 int seg_count;
int pulse_count;
37 unsigned long time_of_last_pulse;

39 struct line_seg_struct             // Declare a structure for the array of line segments
    {
    // Each linear segment in the table contains...
41 int directn;                      // a direction bit (NOTE – Don't use the reserved word '
    direction')
int count;                            // the number of pulses in the segment
43 unsigned long interval;           // and the time interval between pulses (in microseconds
    )
    };
45 line_seg_struct repeating_seg[num_of_segs]; // Instantiate an array for the
    repeating waveform
line_seg_struct startup_seg[num_of_segs*3]; // Instantiate an array for three
    cycles of startup waveform
47
void setup()
49 {
Serial.begin(9600);                   // Initialize the RS-232 channel
51 digitalWrite(direction_pin, LOW); // Initialize the direction output pin

```

```

pinMode(direction_pin , OUTPUT);
53 digitalWrite(pulse_pin , LOW);      // Initialize the pulse output pin.
pinMode(pulse_pin , OUTPUT);
55 }

57 void loop()
{
59 height = get_console_input("Input the wave height (cm) = ");    // These two
    subroutine calls take care
period = get_console_input("Input the wave period (s) = ");    // of reading in the
    console data.
61
paddle_amplitude = dispersion_calculations(height , period);    // The dispersion
    subroutine returns two_e
63 paddle_amplitude = paddle_amplitude*gear_ratio/2.0;    // Here we scale two_e
    for the drive mechanism

65 // In this section the array of line segments for the repeating waveform are
    calculated and stored using the
// number of segments, wave amplitude, and wave period passed in from above. First
    define some useful local variables.
67
unsigned long  time_per_seg;
69 float angle_inc;
float old_point;
71 float new_point;
float delta;
73 int i;

75 time_per_seg = period*1000000.0/(float)num_of_segs;
angle_inc = 2.0*PI/(float)num_of_segs;
77 old_point = 0;
i = 0;
79
Serial.println();

```

```

81 Serial.println("Calculating the segments in the first quadrant...");
Serial.println();
83 Serial.println("Segment Delta   Count   Time");
Serial.println("-----");
85
while(i<quadrant_segs) // We calculate only one quadrant and then copy to the
    others. This insures a net
87 // zero drift of the waveform by matching the number of
    positive and negative pulses.
{
89 new_point = paddle_amplitude*sin(angle_inc*(float)(i+1)); // This equation
    defines the waveshape... SINE for now
    delta = new_point - old_point;
91
    repeating_seg[i].directn = 1;
93    repeating_seg[i].count = (delta + 0.5); // The (delta + 0.5) rounds to the nearest
        step
    if(repeating_seg[i].count < 1)
95        { repeating_seg[i].count = 1; } // Insure at least one point in the segment
    repeating_seg[i].interval = time_per_seg/delta;
97
    Serial.print(i);
99    Serial.print('\t');
    Serial.print(delta,2);
101    Serial.print('\t');
    Serial.print(repeating_seg[i].count);
103    Serial.print('\t');
    Serial.println(repeating_seg[i].interval);
105
    repeating_seg[2*quadrant_segs-i-1].directn = 0;
107    repeating_seg[2*quadrant_segs-i-1].count = repeating_seg[i].count;
    repeating_seg[2*quadrant_segs-i-1].interval = repeating_seg[i].interval;
109
    repeating_seg[2*quadrant_segs+i].directn = 0;
111    repeating_seg[2*quadrant_segs+i].count = repeating_seg[i].count;

```

```

repeating_seg[2*quadrant_segs+i].interval = repeating_seg[i].interval;
113
repeating_seg[num_of_segs-i-1].directn = 1;
115 repeating_seg[num_of_segs-i-1].count = repeating_seg[i].count;
repeating_seg[num_of_segs-i-1].interval = repeating_seg[i].interval;
117
old_point = new_point;
119 i += 1;
}
121
// In this section the array of line segments for the startup waveform are
calculated and stored.
123 // The calculations ramp the amplitude up slowly over three waveform periods until
the repeating
// amplitude is attained. Otherwise the calculations are exactly as in the last
section.
125
old_point = 0;
127 i = 0;

129 while(i<num_of_segs*3)
{
131 new_point = paddle_amplitude * sin(angle_inc*(i+1));
delta = (new_point - old_point)*(float)(i+1)/(float)(num_of_segs*3); // Here we
multiply the delta
133 // by a linear ramp function.

if(delta < 0)
135 {
startup_seg[i].directn = 0;
137 startup_seg[i].count = (int)(-1.0*delta + 1.0);
startup_seg[i].interval = (unsigned long)time_per_seg/(-1.0*delta);
139 }
else
141 {
startup_seg[i].directn = 1;

```

```

143     startup_seg[i].count = (int)(delta + 1.0);
        startup_seg[i].interval = (unsigned long)time_per_seg/delta;
145     }

147     old_point = new_point;
        i += 1;
149     }

151     // In this section, the array of startup segments is used to generate direction and
        pulse signals
        // to the step motor driver. When the startup waveform is complete, we drop into the
        repeating section below.

153
        seg_count = 0;
155     pulse_count = 0;
        digitalWrite(direction_pin, startup_seg[0].directn);
157     time_of_last_pulse = micros();
        Serial.println();
159     Serial.println("Starting output");
        Serial.println();
161     while(seg_count < num_of_segs*3)
        {
163         if(micros()-time_of_last_pulse > startup_seg[seg_count].interval) // then its time
            to put out a pulse
            {
165             digitalWrite(pulse_pin, HIGH);

167             pulse_count += 1;
            time_of_last_pulse = time_of_last_pulse + startup_seg[seg_count].interval;
169
            digitalWrite(pulse_pin, LOW);
171
            if(pulse_count == startup_seg[seg_count].count) // then go to the next line
            segment
173             {

```

```

    pulse_count = 0;
175    seg_count += 1;
        digitalWrite(direction_pin, startup_seg[seg_count].directn);
177    }
    }
179 }

181 // Here we are preparing to drop into the loop with the appropriate variables re-
    initialized
Serial.println("Output running....");
183 Serial.println();
Serial.println("Hit <Enter> key to stop");
185 Serial.println();

187 seg_count = 0;
    pulse_count = 0;
189 digitalWrite(direction_pin, repeating_seg[0].directn);
    time_of_last_pulse = micros();
191
    // In this section, the array of repeating segments is used to generate direction
        and pulse signals
193 // to the step motor driver. When the last segment has completed, the waveform wraps
        around to
    // the first segment and repeats forever.
195
while(1)
197 {
    if(micros()-time_of_last_pulse > repeating_seg[seg_count].interval) // then its
        time to put out a pulse
199    {
        digitalWrite(pulse_pin, HIGH);
201
        pulse_count += 1;
203    time_of_last_pulse = time_of_last_pulse + repeating_seg[seg_count].interval;

```

```

205     digitalWrite(pulse_pin, LOW);

207     if(pulse_count == repeating_seg[seg_count].count) // then go to the next line
segment
        {
209         pulse_count = 0;
            seg_count += 1;
211         if(seg_count == num_of_segs) // then at the end of the waveform so
loop back to start
            { seg_count = 0; }
213         if(seg_count == 2*quadrant_segs) // then just finished the first half of
the waveform, so
            { // time to check for a key press to stop
the waveform
215             if (Serial.available() > 0) // Check to see if a key was pressed
                {
217                 Serial.read(); // If so, clear the input
buffer
                    Serial.println("Stopping waveform..."); // Print the stop message
219                     Serial.println();

221                     // In this section, the array of startup segments is used in reverse (
and in the
                        // opposite direction from startup) to decelerate the paddle to a stop
at top dead
223                         // center. When the stop waveform is complete, we break back to the
beginning of
                            // the program.

225
                                seg_count = num_of_segs*3-1;
227                                pulse_count = 0;
                                    if(startup_seg[seg_count].directn > 0) // Here we are flipping the
polarity of the direction
229                                        { digitalWrite(direction_pin, LOW);}
                                            else

```

```

231         { digitalWrite(direction_pin , HIGH);}
time_of_last_pulse = micros();
233     while(seg_count >=0)
        {
235         if(micros()-time_of_last_pulse > startup_seg[seg_count].interval) //
then its time to put out a pulse
            {
237             digitalWrite(pulse_pin , HIGH);

239             pulse_count += 1;
time_of_last_pulse = time_of_last_pulse + startup_seg[seg_count].
interval;

241             digitalWrite(pulse_pin , LOW);

243             if(pulse_count == startup_seg[seg_count].count) // then go to the
next line segment
                {
245                 pulse_count = 0;
247                 seg_count -= 1;
                    if(startup_seg[seg_count].directn > 0) // Flipping the polarity
of the direction
249                     { digitalWrite(direction_pin , LOW);} // for each new
segment
                        else
251                             { digitalWrite(direction_pin , HIGH);}
                                }
253                            }
                                }
255                    break;
                        }
257                }
digitalWrite(direction_pin , repeating_seg[seg_count].directn);
259    }
}

```

```

261     }
    }
263
float get_console_input(String text)
265     {
    String in_string;
267     char read_byte;
    float answer;
269
    read_byte = "";           // Clear input buffers
271     in_string = "";

    Serial.print(text);
    while(read_byte != '\n')
275     {                       // Read in characters until a linefeed occurs
        if (Serial.available() > 0)
277         {
            read_byte = Serial.read();
279             Serial.print(read_byte);
            in_string += read_byte;
281         }
        }
283     in_string.trim();
    return(in_string.toFloat()); // Convert the string to a floating point number
    and return
285 }

287
float dispersion_calculations(float h, float p)
289     {
    const float twoPI = 2.0*PI;
291     const float gravity = 980.665; // Units are centimeters per second squared
    const float efficiency = 0.7;
293     int count;
    float oldWaveLength;

```

```

295 float newWaveLength;
    float error;
297 float md;
    float kprime;
299 float two_e;

301 Serial.println();
    Serial.println("Iterating the wave length...");
303 Serial.println();
    Serial.println("Step      Old Length      New Length      Error");
305 Serial.println("-----");
    count = 0;
307 oldWaveLength = 100.;
    error = 100.0;
309
    while(abs(error)>0.0001)
311 {
        count += 1;
313 newWaveLength = gravity*p*p/twoPI*tanh(twoPI*tank_depth/oldWaveLength);
        error = newWaveLength - oldWaveLength;
315 Serial.print(count);
        Serial.print('\t');
317 Serial.print(oldWaveLength,6);
        Serial.print('\t');
319 Serial.print(newWaveLength,6);
        Serial.print('\t');
321 Serial.println(error,6);
        oldWaveLength = (oldWaveLength + newWaveLength)/2;
323 }
    Serial.println();
325 Serial.print("Length = ");
    Serial.println(newWaveLength,6);
327
    md = twoPI*tank_depth/newWaveLength;
329 Serial.print("md      = ");

```

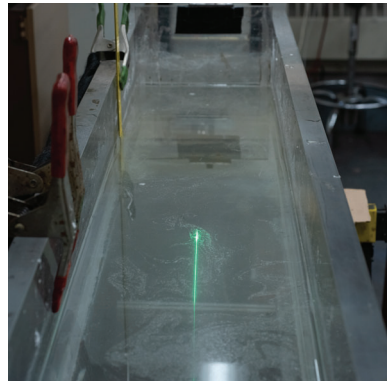
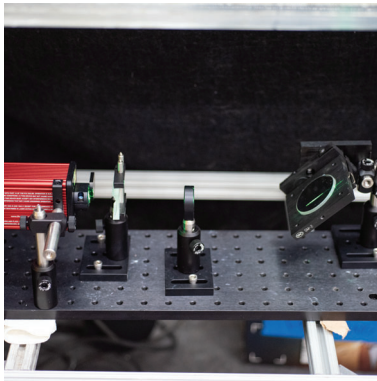
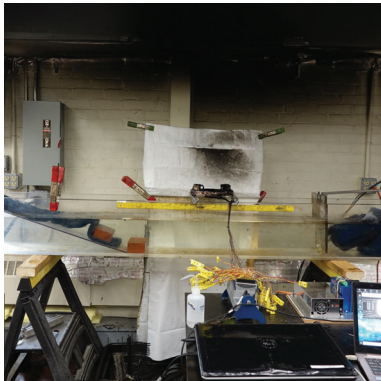
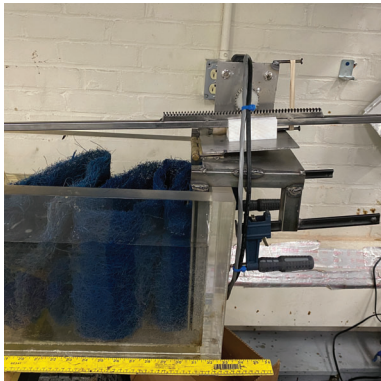
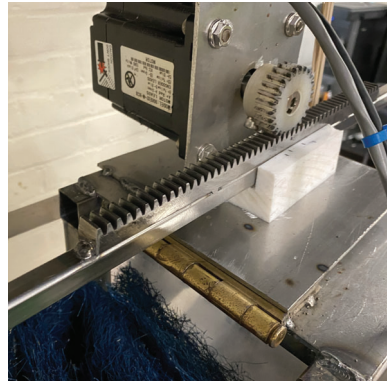
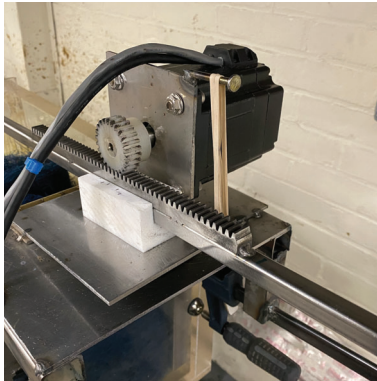
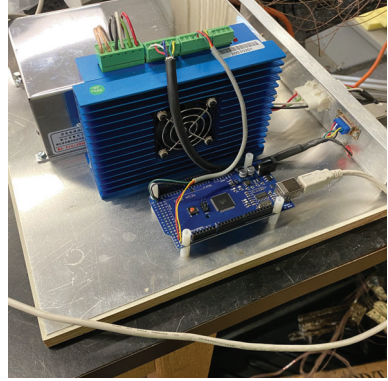
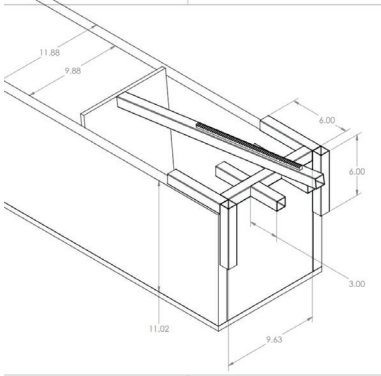
```

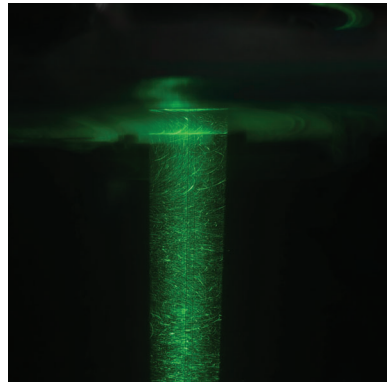
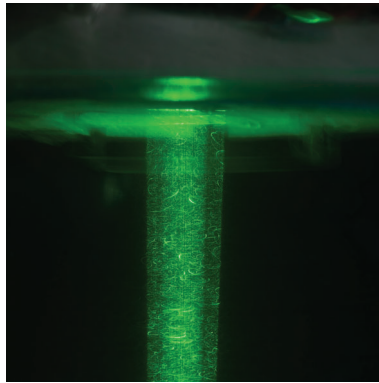
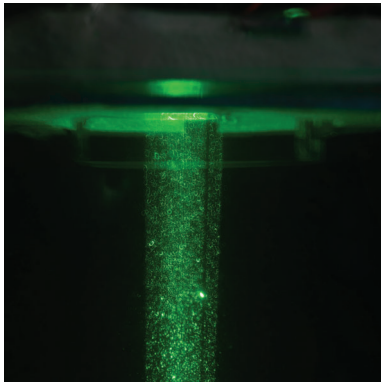
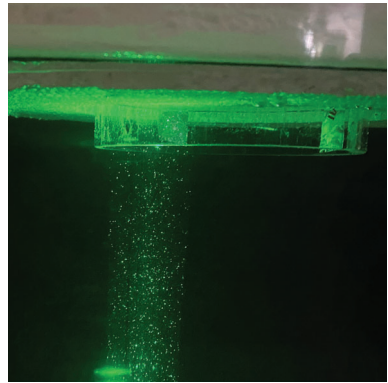
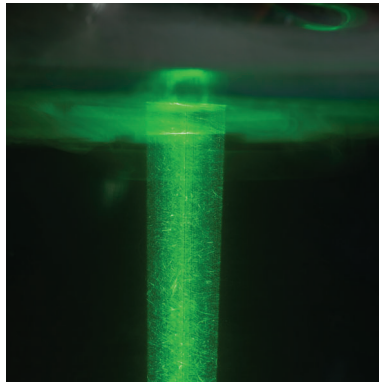
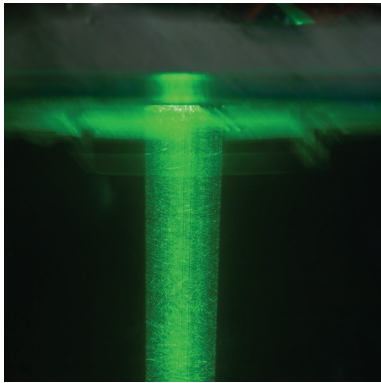
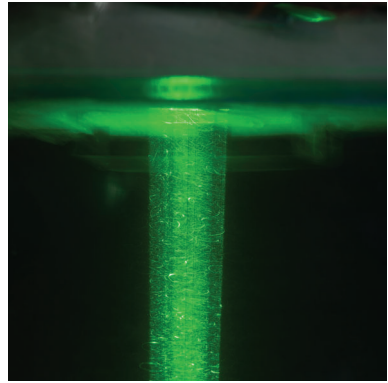
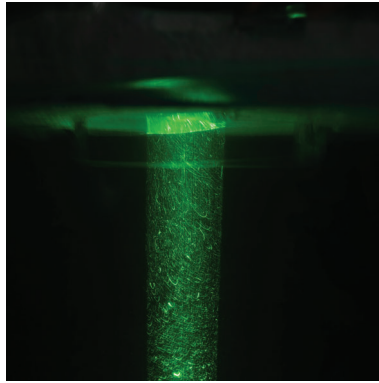
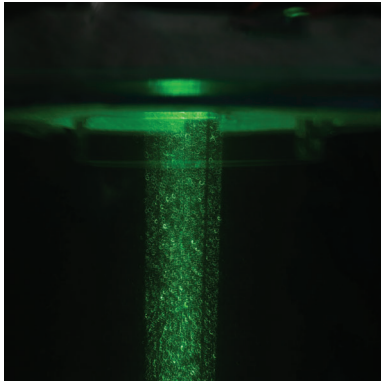
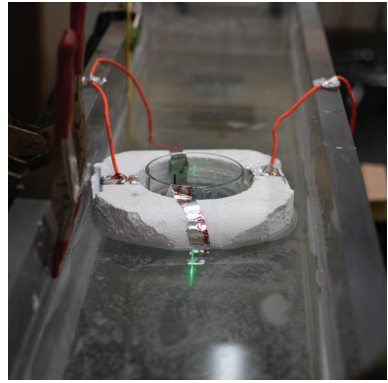
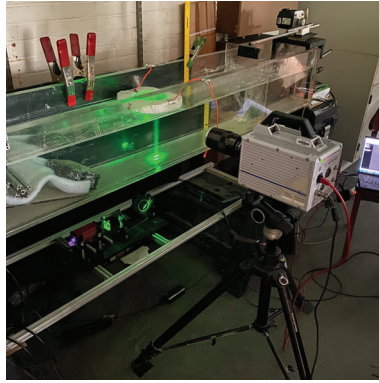
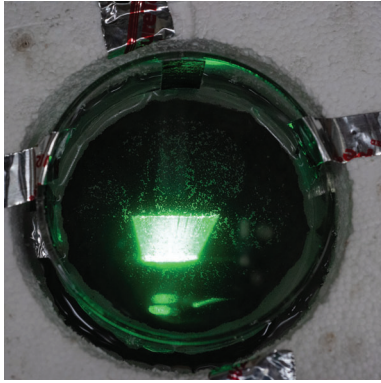
Serial.println(md,6);
331
kprime = 2.0*((sinh(md))*(1.0-(cosh(md))+md*sinh(md))) / (md*((sinh(md))*(cosh(md)
)))+md));
333 Serial.print("kprime = ");
Serial.println(kprime,6);
335
two_e = h/efficiency/kprime;
337 Serial.print("2 x e = ");
Serial.println(two_e,6);
339 Serial.println();
return(two_e);
341 }

```

C.2.5 Wavetank Construction Photos

This section presents further photos of the small scale wavetank as well as some extra photos of the PIV setup and some wave motion photos.





C.3 Medium Scale

C.3.1 Wave Generator Design Graphs

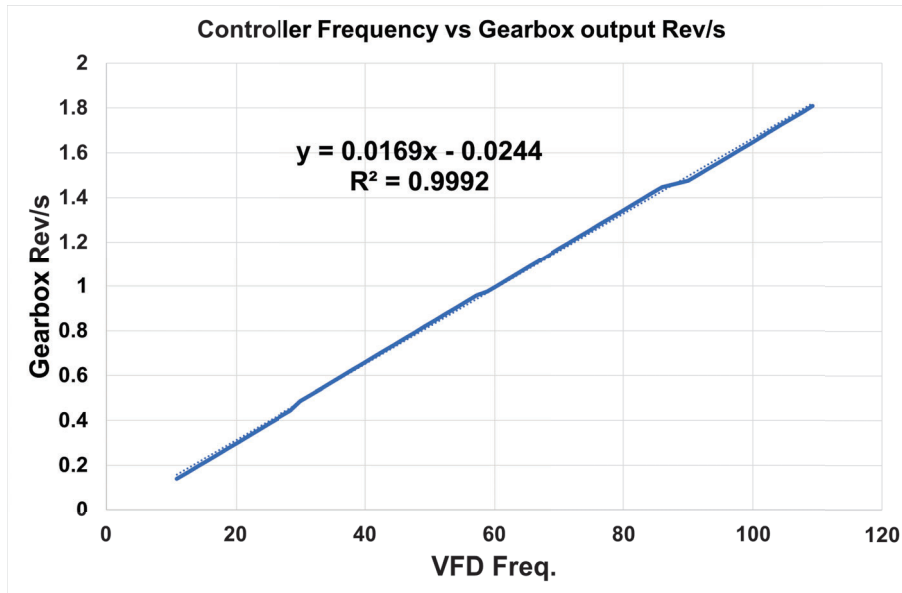


Figure C.4: VFD controller frequency vs. gearbox output in revolution per second.

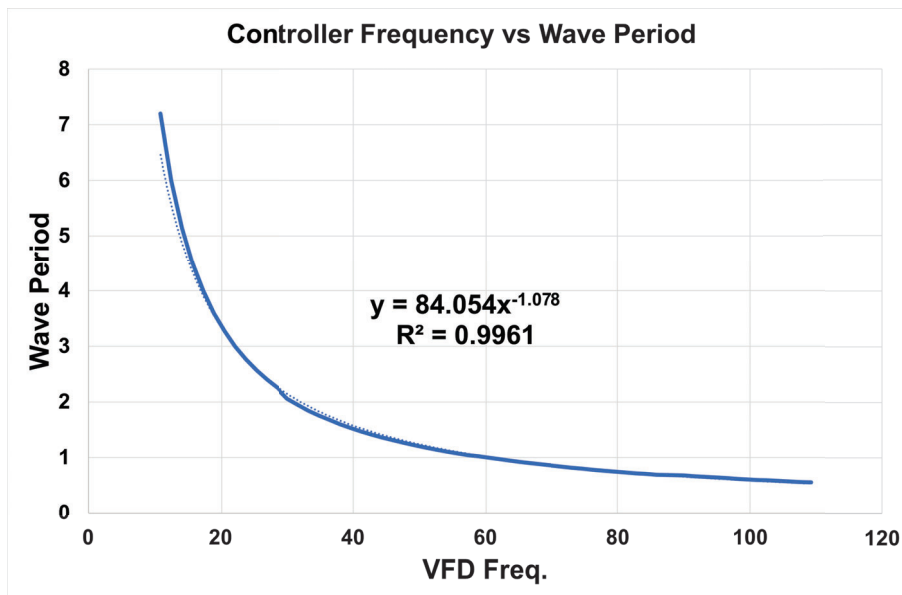


Figure C.5: Controller frequency vs. output wave period.

C.3.2 Wavetank Assembly and Operation Checklists

Initial Wavetank Assembly

1. Place down tarp in testing area (long side parallel to hood control room)
2. Place frames down on floor (frames are lettered and numbered)
3. Place flume sections on top of frames
 - (a) Start with paddle end (needs to slide over bolts)
4. Apply gaskets between flume sections
 - (a) Strip off old gasket, wrap gasket down and under corners if needed
5. Bolt flume sections together
 - (a) Start from paddle end
 - (b) Drill holes in gasket for bolts, 3/8 bit
 - (c) Use spud wrench to line up bolts to get started
 - (d) Start bolts by hand, then use impact driver and wrench to tighten
6. Put beach top into tank
 - (a) Should slide over bolts that are mounted inside on brackets
7. Wave generator
 - (a) Move wave generator assembly with furniture dollies
 - (b) Remove wooden boards from bottom with lags
 - (c) Bolt generator to back frame section (3/8 bolts)
 - (d) Use wooden moving boards to shim back stabilizer arms
8. Install paddle in tank
 - (a) Check for pillow blocks on the pivot rod at the bottom of paddle
 - (b) Min 3 persons carry paddle to position next to tank
 - (c) Make sure bolts in tank are Teflon taped, gasketed, and heavily Teflon greased
 - (d) Move gantry into position, wrap lifting strap under paddle
 - (e) Use gantry to lift paddle and slide into position over tank
 - i. **ALWAYS KEEP HANDS/ ARMS/ BODYPARTS OUT OF GAPS**
 - (f) Slowly lower paddle onto bolts

- (g) Apply gasket to top of bolts and tighten down with nuts and washer
- (h) Place pusher arm onto tie-rod bolts on generator and paddle
- 9. Deluge
 - (a) Place deluge pipes into position and secure with hose clamps
- 10. Secondary containment
 - (a) Setup secondary containment walls, ONLY once all heavy things are in place

Testing day – Morning Prep

1. Filling tank
 - (a) Use small pump for bottom totes with filter
 - (b) Once 2-3 people are present use big pump for top totes
2. Check underwater camera
 - (a) Clean if necessary
3. Check pan
 - (a) Floats
 - (b) Thermocouples
4. Turn on all DAQs/ computers
5. Turn on FLIR
6. Repair any instrumentation if required
7. Water clarity
 - (a) Run small pump and filter circulating if necessary
 - (b) Continue to clean water surface with absorbents if necessary
8. Hook up wave generator to power

Testing day – Afternoon Breakdown

1. Draining tank
 - (a) Use small pump for bottom totes with filter
 - (b) Use use big pump for top totes
 - (c) If water is very dirty just use small pump so all water is filtered
2. Check underwater camera

- (a) Clean if necessary
- 3. Check Pan
 - (a) Floats
 - (b) Thermocouples
- 4. Turn off all DAQs/ computers
- 5. Turn off FLIR
- 6. Repair any instrumentation if required
- 7. Clean inside of tank if necessary
- 8. Put away tools/ equipment and pickup space
- 9. Disconnect wave generator from power
- 10. Ensure all data is saved to combustion drive file path

Emergency Shutdown Procedure

- 1. Snuffing/ smothering device
 - (a) Attempted in Fall 2021 with limited success
 - (b) Potential for pushing fuel out of pan & is heavy/ cumbersome
- 2. Snuffing blanket/ cover
 - (a) Roll of fiberglass or similar insulation pre-cut to width of tank, kept rolled up at the deluge end of wavetank
 - (b) Can be used to quickly extinguish, likely in conjunction with other options
- 3. CO2 fire extinguishers
 - (a) Should be effective against our pool size especially with the tank walls holding some of the heavier CO2 contained
 - (b) Last resort measure
 - (c) Consumable
- 4. Deluge cooling
 - (a) Should be implemented no matter which other method is used
 - (b) Can serve to cool the hot metal pan walls easing in extinguishing

Procedure

1. Call is made that experiment needs to be terminated for safety reasons
2. Turn off fuel feed pump and fuel feed cutoff valve
3. Turn of wave generator
4. Turn deluge pipes towards burning pool
 - (a) Steps 3 & 4 take place about 5ft away from the tank, and slightly further from the burning pool
5. Implementation of snuffing blanket and/or CO2 extinguishers

*Note: The wavetank will easily survive the entire surface being on fire for a limited duration (2-3 minutes). This can occur without compromising water retention abilities and without damaging critical experimental components (wave generator electronics etc). If personnel safety is in jeopardy the wavetank can be left until the remaining fuel has burned off and will very likely still be useable without needing repair.

C.3.3 Additional Data

This section contains some extra data from the medium scale that was omitted from the main section for brevity and or clarity purposes.

This first set of plots shows the averaging scheme mentioned in the large scale appendix C.4.2 applied to some of the wavy data in the medium scale. Showing that temperatures began as highly fluctuating, with data taken at a rate of 1 Hz. But that trends could be extrapolated with an averaging scheme applied.

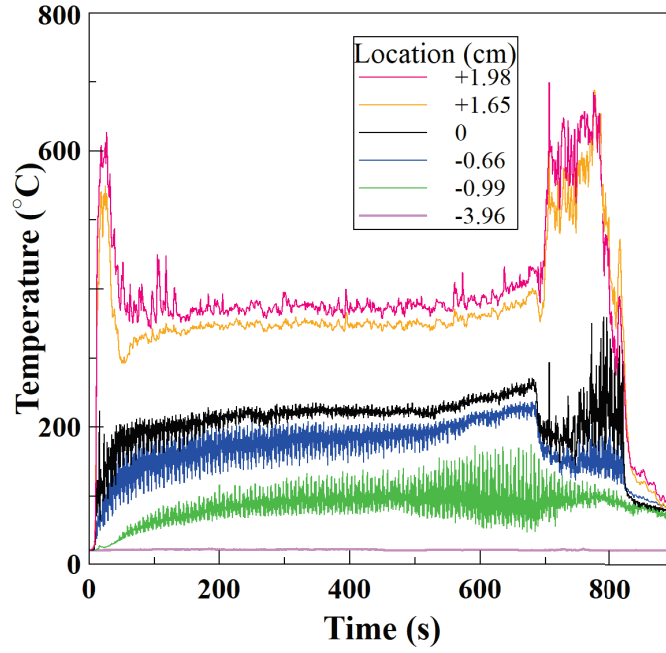


Figure C.6: In-depth fuel temperature profile information taken during the wave case in the medium scale, showing temperature fluctuations with the wave.

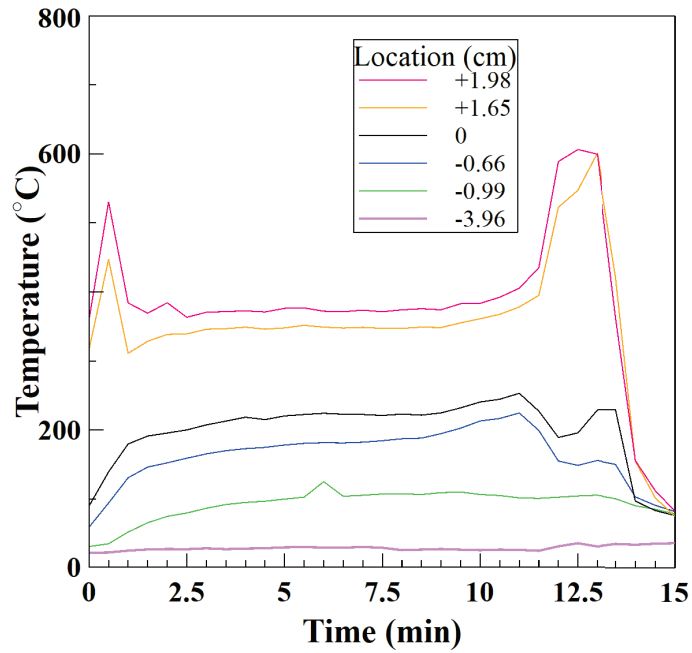


Figure C.7: In-depth fuel temperature data taken with the wave, now with the 1-minute moving average applied.

C.3.4 Flowmeter Arduino Code

This code is written for Arduino IDE and counts the output pulses from a square wave pulse flowmeter. This code was written by Jeff and Nate Sauer.

```
//
2 // This sketch counts pulses from an OMEGA flowmeter and logs the data to an SD card
// while also printing the data to an LCD screen.
4 //
// The program starts by first attempting to initialize the SD card, reporting
    success
6 // or failure. Failure at this point usually means a missing or unformatted SD card.
// If the SD card initializes, then the program tries to open the file "data.csv".
8 // If "data.csv" does not exist on the SD card, then it is created and opened at
    this
// time. If "data.csv" already exists, then the existing file is opened and new data
10 // is appended to the existng data already in the file.
//
12 // Next, the program waits for a button push to start collecting data. Data is
// collected at a user programable interval and simultaneously displayed on an LCD
14 // display and written to the file on the SD card.
//
16 // Data collection continues until the button is pressed a second time, which
    trggers
// the program to close the data file and terminate.
18 //
// Shield connections are as follows:
20 //
// +-----+
22 // |      Screw Shield 1.0      |
// |                               |
24 // |                               |
// |                               |
26 // |                               |
// | X GND                        |
```

```

28 // | X GND SWITCH COM X |
// | X +9V TO FLOW METER SWITCH NC X |
30 // | X PULSES FROM FLOW METER |
// | | |
32 // | X +5V TO LCD SCREEN |
// | X GND |
34 // | X SDA TO LCD SCREEN |
// | X SCL TO LCD SCREEN |
36 // +-----+
//
38 // Version 3.00 April 16, 2022 by Jeff Sauer and Nate Sauer
// Version 3.01 April 23, 2022 Changed START/STOP button to normally closed
40 // Version 3.02 April 24, 2022 Added startup delay

42 #include <Wire.h>
#include <SPI.h>
44 #include <SD.h>
#include <LiquidCrystal_I2C.h>
46 #include <util/atomic.h> // for temporarily blocking interrupts

48 const bool CLOSED = 0; // Normally closed switch polarity
const bool OPEN = 1; // Normally closed switch open circuit and pulled
up
50 const int switch_common = 7; // D7 connects the switch common
const int switch_NC = 6; // D6 connects to the switch normally open
52 LiquidCrystal_I2C lcd(0x27,20,4); // Set the LCD hardware address to 0x27

54 File myFile;
String myfilename = "data.csv"; // This hard-codes the filename on the SD card
56
const unsigned long interval = 1000; // This constant (in milliseconds) sets
the logging interval
58 const float liters_per_pulse = 1.0/8000.0; // Flow sensor dependent (FTB602 gives
8000 pulse per liter)

```

```

60 const float readings_per_minute = 60000.0/(float)interval;    // 60,000 since "
    interval" is in milliseconds

62 float flow_rate;
    float total_liters;
64 float previous_liters;
    const float panarea = 4656.63;        //pan area in cm^2
66 float regrate;        //regression rate in mm/min calculated later for
    printing

68 unsigned long milliseconds;
    unsigned long start_time;
70 unsigned long next_time;

72 volatile unsigned long pulse_count;
    unsigned long copy_of_pulse_count;
74 unsigned long previous_pulse_count;

76
void pulsecounter() // This is the Interrupt service routine to count pulses on
    DIN2
78 {
    pulse_count +=1;
80 }

82
void setup()
84 {
    pinMode(switch_common, OUTPUT);
86 digitalWrite(switch_common, LOW); // Ground one side of the switch
    pinMode(switch_NC, INPUT_PULLUP); // Pull-up the normally closed side of the
        switch
88
    delay(3000);
90 lcd.init(); // Initialize the LCD screen

```

```

lcd.backlight();
92
lcd.setCursor(0,0);
94 lcd.print("OMEGA Version 3.02");
delay(5000);
96
lcd.setCursor(0,0);
98 lcd.print("Initializing SD card");
delay(3000);
100
if (!SD.begin(10)) // Hardware chip select on pin 10
102 {
    lcd.setCursor(0,1);
104 lcd.print("SD initalize failed");
    lcd.setCursor(0,2);
106 lcd.print("Program STOPPED");
    while(1); // Trap here
108 }

110 lcd.setCursor(0,1);
    lcd.print("SD card initialized");
112 delay(3000);

114 myFile = SD.open(myfilename, FILE_WRITE); // Try opening the file for WRITING.

116 if (myFile) // If the file opened okay, print a success message.
    {
118 lcd.setCursor(0,2);
        lcd.print("DATA.CSV opened");
120 delay(3000);
    }
122 else
    {
124 lcd.setCursor(0,2);
        lcd.print("DATA.CSV open failed");

```

```

126  lcd.setCursor(0,3);
    lcd.print("Program STOPPED");
128  while(1);
    }
130
    lcd.clear();
132  lcd.setCursor(0,1);
    lcd.print("  Push Button to  ");
134  lcd.setCursor(0,2);
    lcd.print(" START logging data ");
136
while(digitalRead(switch_NC)== CLOSED)
138  {
    // Waiting here for START switch to go OPEN
140  }

142  myFile.println("Time(sec), Rate(L/min), Total(L), Rate(mm/min), Pulses"); // Write a
    header into the output file

144  lcd.clear();
    lcd.setCursor(0,0);
146  lcd.print("Time  L/min  TotalL");
    lcd.setCursor(0,2);
148  lcd.print("mm/min");
    lcd.setCursor(8,3);
150  lcd.print("Push to STOP");

152  attachInterrupt(digitalPinToInterrupt(2), pulsecounter, RISING); // Turn on the
    interrupt

154  previous_pulse_count = 0;
    start_time = millis(); // Zero the timer here before we drop into the loop
156  next_time = start_time + interval; // Calculate the next timer value to look for

158  while(1) //In this section we wait for the logging interval, then log the data.

```

```

{
160 if (millis() - start_time > 5000) // Wait 5 seconds before looking for the
STOP button
{
162 if (digitalRead(switch_NC) == OPEN) // True if STOP button is being pushed
{
164 myfile.close();
lcd.setCursor(0,0);
166 lcd.print(" ");
lcd.setCursor(0,1);
168 lcd.print("Closing DATA.CSV ");
lcd.setCursor(0,2);
170 lcd.print(" ");
lcd.setCursor(0,3);
172 lcd.print(" ");

174 delay(4000);
lcd.setCursor(0,1);
176 lcd.print(" Program STOPPED ");
while(1);
178 }
}
180 if (millis() > next_time) // Time to record some data
{
182 milliseconds = millis() - start_time;

184 ATOMIC_BLOCK(ATOMIC_RESTORESTATE) // Macro that blocks interrupts from splitting
this instruction
{
186 copy_of_pulse_count = pulse_count;
}

188
total_liters = liters_per_pulse * (float)copy_of_pulse_count;
190 previous_liters = liters_per_pulse * (float)previous_pulse_count;
flow_rate = (total_liters - previous_liters)*readings_per_minute;

```

```

192     regrate = flow_rate*(1000)*(1/panarea)*(10/1);
194
196     myFile.print(String(milliseconds/1000));
198     myFile.print(", ");
200     lcd.setCursor(0,1);
202     lcd.print(String(milliseconds/1000));
204
206     myFile.print(String(flow_rate,2));
208     myFile.print(", ");
210     lcd.setCursor(8,1);
212     lcd.print(String(flow_rate,2));
214
216     myFile.print(String(total_liters,2));
218     myFile.print(", ");
220     lcd.setCursor(16,1);
222     lcd.print(String(total_liters,2));
224
226     myFile.print(String(regrate,2));
228     myFile.print(", ");
230     lcd.setCursor(0,3);
232     lcd.print(String(regrate,2));
234
236     myFile.println(String(copy_of_pulse_count));
238
240     next_time = next_time + interval;
242     previous_pulse_count = copy_of_pulse_count;
244     }
246 }
248 void loop()
250 {
252 }

```

C.3.5 Flame Height MATLAB Code

This code is written for MATLAB and determines the flame height over a period of frames which are obtained from video. This code was written by Sharanya Nair, with small changes by Nate Sauer.

```
1 clear all;
2 n=1;
3 maxg=300;
4 for k=0:30:510
5     check=0;
6     img=imread(['img_',num2str(k,'%05d'),' .png']);
7     img=rgb2gray(img);
8     %img=imbinarize(img);
9     img=im2double(img);
10
11    sum=0;
12    dim=size(img);
13    max(n)=0;
14    for i=dim(1):-1:1
15        sum=0;
16        for j=1:1:dim(2)
17            sum=sum+img(i,j);
18        end
19        a(i,1,n)=i;
20        a(i,2,n)=sum;
21
22        if(max(n)<sum)           %finding maximum summation
23            max(n)=sum;
24            maxi=i;
25        end
26
27        if(sum<(max(n)*0.25))  %0.25 is obtained by fine tuning
28            flhtp(n)=dim(1)-i;
29            check =1;
```

```

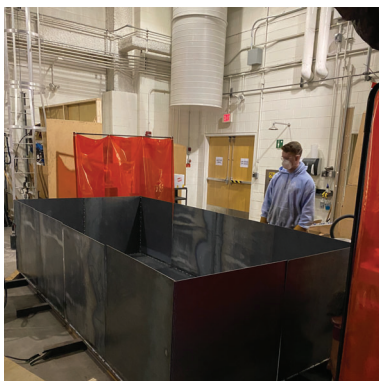
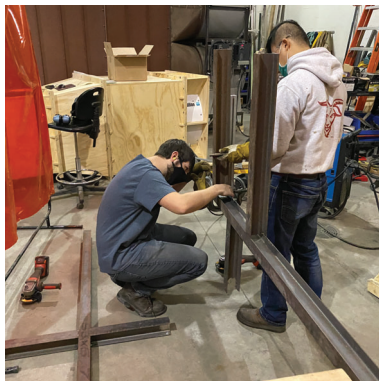
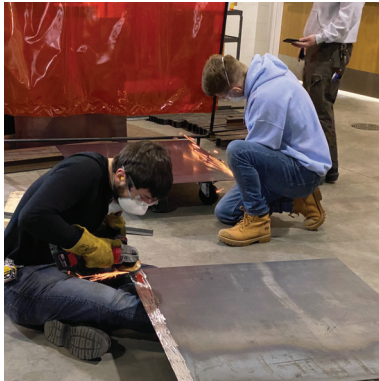
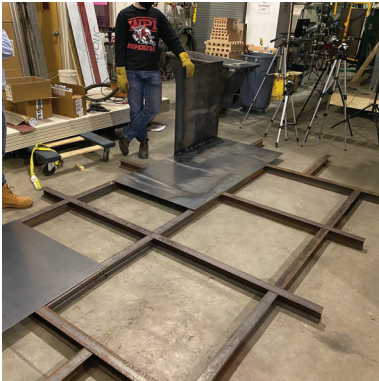
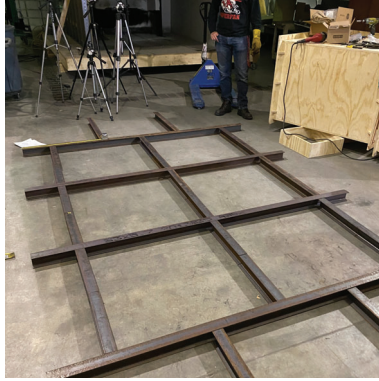
    if(maxg < max(n))
31         maxg = max(n);
    end
33     break;
    end
35
    end
37     if(check==0)
        flhtp(n)=dim(1)-i;
39     end
    if(check==1 && max(n) < 0.7 * maxg)    %checks for no flame images
41         flhtp(n)=0;
    end
43     n=n+1;
end
45
length=0.77;
47 no_of_pixel=250; %obtain pixels for known distance
m_per_pixel=length/no_of_pixel;
49     flhtm= flhtp*m_per_pixel;    %flame height in m
    flhtm=flhtm';

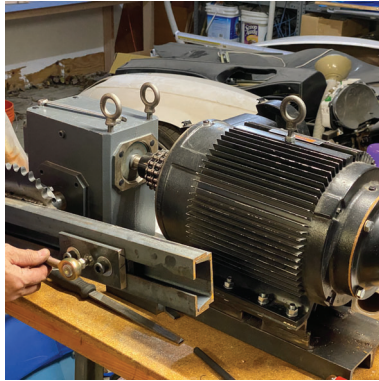
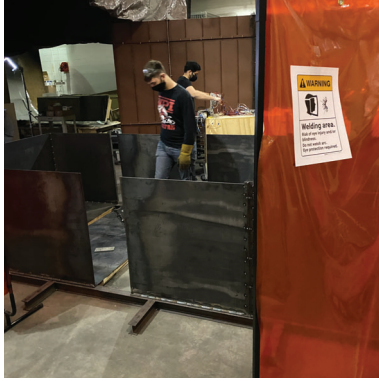
```

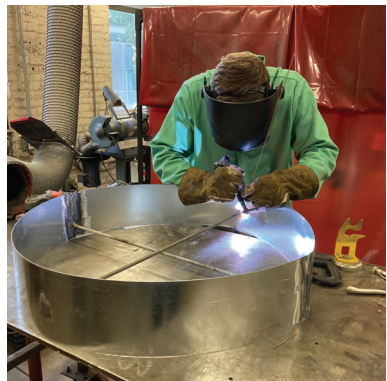
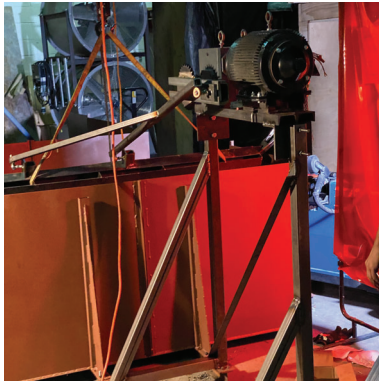
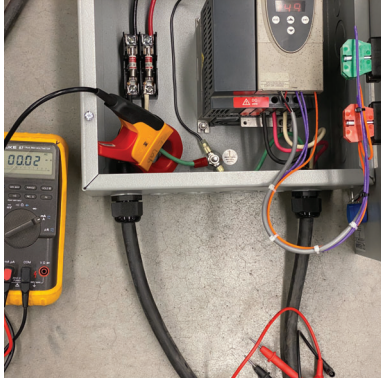
C.3.6 Wavetank Construction Photos

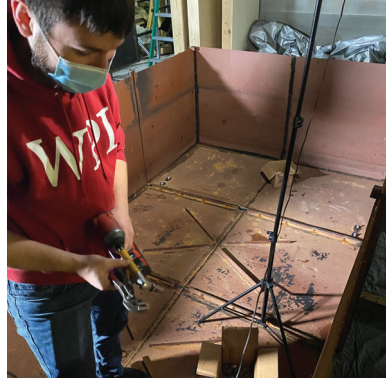
These photos are presented in the chronological order over which the medium scale wavetank construction took place. View from left to right across one row, then down to the next row to continue. Some additional photos of instrumentation and experimental apparatus construction are also included. Photos of initial design and modeling phases are not included, nor are any references to material or equipment prices.

Specific details including CAD models, dimensions, and cost can be made available upon request.









C.4 Large Scale

This section contains some of the codes used for the analysis of the data from the large scale. The main hurdles of this dataset were the large number of sensors and the long acquisition time. This required some data manipulation methods that wouldn't be needed for smaller datasets, such as separating the data from many columns on a single excel sheet into fewer columns on discrete excel sheets.

C.4.1 Data Separation Matlab Code

This code is written for MATLAB, and was used after the large-scale experiments for separating data contained within many columns of a single excel file into separate excel files for analysis.

```
A=xlsread('C:\Users\sauer\Desktop\CRREL_Tests\1_Baseline.xlsx','A1:ES10000');
2 %read excel file to matrix A 10,000 A1:ES10000 is rectangle to reference

4 B=A(:,(1:62)); %select columns 2-63 and put into matrix B use form B=A((2:63):,);
    to select ROWS 2-63
%names the header for each column
6 headerB={'Center_0','Center_1','Center_2','Center_3','Center_4','Center_5','
    Center_6','Center_7','Center_8','Center_9','Center_10','Center_11','Center_12',
    'Center_13','Center_14','Center_15','Center_16','Center_17','Center_18','
    Center_19','Center_20','Center_21','Center_22','Center_23','Center_24','
    Center_25','Center_26','Center_27','Center_28','Center_29','Center_30','Outer_0
    ','Outer_1','Outer_2','Outer_3','Outer_4','Outer_5','Outer_6','Outer_7','
    Outer_8','Outer_9','Outer_10','Outer_11','Outer_12','Outer_13','Outer_14','
    Outer_15','Outer_16','Outer_17','Outer_18','Outer_19','Outer_20','Outer_21','
    Outer_22','Outer_23','Outer_24','Outer_25','Outer_26','Outer_27','Outer_28','
    Outer_29','Outer_30'};
%combines the header with the data into a cell array
8 LiqTemp=[headerB;num2cell(B)];

10 C=A(:,(63:107));
headerC={'Flame1_0','Flame1_1','Flame1_2','Flame1_3','Flame1_4','Flame1_5','
    Flame1_6','Flame1_7','Flame1_8','Flame1_9','Flame1_10','Flame1_11','Flame1_12',
```

```

    'Flame1_13','Flame1_14','Flame2_0','Flame2_1','Flame2_2','Flame2_3','Flame2_4',
    'Flame2_5','Flame2_6','Flame2_7','Flame2_8','Flame2_9','Flame2_10','Flame2_11',
    'Flame2_12','Flame2_13','Flame2_14','Flame3_0','Flame3_1','Flame3_2','Flame3_3',
    'Flame3_4','Flame3_5','Flame3_6','Flame3_7','Flame3_8','Flame3_9','Flame3_10',
    'Flame3_11','Flame3_12','Flame3_13','Flame3_14'}];
12 GasTemp=[headerC;num2cell(C)];

14 D=A(:,(108:143));
headerD={'Slot8_0','Slot8_1','Slot8_2','Slot8_3','Slot8_4','Slot8_5','Slot8_6','
Slot8_7','Slot8_8','Slot8_9','Slot8_10','Slot8_11','Slot8_12','Slot8_13','
Slot8_14','Slot8_15','Slot8_16','Slot8_17','Slot8_18','Slot8_19','Slot8_20','
Slot8_21','Slot8_22','Slot8_23','Slot8_24','Slot8_25','Slot8_26','Slot8_27','
Slot8_28','Slot8_29','Slot8_30','Slot8_31','Slot9_0','Slot9_1','Slot9_2','
Slot9_3'}];
16 FRTemp=[headerD;num2cell(D)];

18 E=A(:,(144:148));
headerE={'Rad_1','Total_1','Rad_2','Total_2','Total_3'}];
20 HFGs=[headerE;num2cell(E)];

22 xlswrite('C:\Users\sauer\Desktop\seperated\1_LiqTemp Baseline.xlsx',LiqTemp);
    %write cell array 'LiqTemp' to excel file LiqTemp baseline
xlswrite('C:\Users\sauer\Desktop\seperated\1_GasTemp Baseline.xlsx',GasTemp);
24 xlswrite('C:\Users\sauer\Desktop\seperated\1_FRTemp Baseline.xlsx',FRTemp);
xlswrite('C:\Users\sauer\Desktop\seperated\1_HFG Baseline.xlsx',HFGs);

```

C.4.2 Data Averaging in Excel

Below is an example and excel formulas used to average data for some experiments in this work and especially the large scale. This translated data from 1 data point per second (1 Hz) to 1 data point per minute. This is accomplished by a moving average method, where for example the 2-minute data point is generated by averaging data from 90 seconds (30 seconds before 2-minutes) to

150 seconds (30 seconds after 2-minutes). This is accomplished by using excel's 'indirect' function inside of an "=AVERAGE" function as normal. Then directing this "INDIRECT" to a sheet of 'timecodes' in which the cells contain automatically generated text telling the formula where and over what range to calculate the average. This is helpful for calculating the average for a large number of points, when data for each point is needed. Whereas normally excel would only calculate the moving average as a trend-line.

	A	B	C	D	E	F	G
1	0		0	C	D	E	F
2	30	:	90	sheet1!C3:sheet1!D30:D90	sheet1!E3(sheet1!F3)		
3	90	:	150	"&D\$1&	sheet1!D90:D150	sheet1!E9(sheet1!F9)	
4	150	:	210	sheet1!C1:sheet1!D150:D21	(sheet1!E1:sheet1!F1)		
5	210	:	270	sheet1!C2:sheet1!D210:D27	(sheet1!E2:sheet1!F2)		
6	270	:	330	sheet1!C2:sheet1!D270:D33	(sheet1!E2:sheet1!F2)		
7	330	:	390	sheet1!C3:sheet1!D330:D39	(sheet1!E3:sheet1!F3)		

Figure C.8: Sheet and formula for generating 'timecodes' for averaging.

	A	B	C	D	E	F	G
1	Time sec	Time(min)	Center_0	Center_1	Center_2	Center_3	Center_4
2	0	0	15.5976154	15.71199187	15.64867	15.69561	15.48656
3	60	1	15.711197	15.65002057	15.70287	15.48359	15.21394
4	120	2	15.7023235	15.63553531	15.68909	15.47482	15.1985
5	180	3	15.6107163	15.66861382	15.55132	15.55461	15.22635
6	240	4	14.9212102	15.57779052	14.80466	15.57959	15.10028
7	300	5	14.4946312	15.51604897	14.30162	15.40631	15.18475
8	360	6	14.6474337	15.53135156	14.49487	15.4471	15.18475

Figure C.9: Calculation of time window on the averaged data sheet.

	A	B	C	D	E	F	G
1	Time sec	Time(min)	Center_0	Center_1	Center_2	Center_3	Center_4
2	0	0	15.5976154	15.71199187	15.64867	15.69561	15.48656
3	60	1	15.711197	15.65002057	15.70287	15.48359	15.21394
4	120	2	15.7023235	15.63553531	15.68909	15.47482	15.1985
5	180	3	15.6107163	15.66861382	15.55132	15.55461	15.22635
6	240	4	14.9212102	15.57779052	14.80466	15.57959	15.10028
7	300	5	14.4946312	15.51604897	14.30162	15.40631	15.18475

Figure C.10: Calculation of the averaged data point.

C.4.3 Thermal Penetration Rate in Excel

Below is the method and excel formulas used for finding the thermal penetration rate for the large scale. For each timestep and for each thermocouple an excel formula is used that determines if the

temperature at that time is above or below a certain value, 120°C for the analysis used for the large scale. The formula for this is shown in the screenshot in Fig. C.11 for the first thermocouple at the first timestep. Eqn. C.5 shows the format of the excel IF function used as the basis for this analysis. Eqn. C.6 shows the values used, demonstrating if the temperature is above 120°C the formula will print the current timestep, if below 120°C the formula will print zero.

$$= IF('logictest', [value if true], [value if false]) \tag{C.5}$$

$$= IF(T > 120, t, 0) \tag{C.6}$$

	A	B	C	D	E	F	G	H	I	J
1		Outer_0	Outer_1	Outer_2	Outer_3	Outer_4	Outer_5	Outer_6	Outer_7	Outer_8
2		-6.5	-6	-5.5	-5	-4.5	-4	-3.5	-3	-2.5
3		Time (min)	14	15	15	14	14	11	11	10
4		0	0	0	0	0	0	0	0	0
5		1	0	0	0	0	0	0	0	0
6		2	0	0	0	0	0	0	0	0
7		3	0	0	0	0	0	0	0	0
8		4	0	0	0	0	0	0	0	0
9		5	0	0	0	0	0	0	0	0
10		6	0	0	0	0	0	0	0	0
11		7	0	0	0	0	0	0	0	0
12		8	0	0	0	0	0	0	0	0
13		9	0	0	0	0	0	0	0	0
14		10	0	0	0	0	0	0	0	10
15		11	0	0	0	0	0	11	11	11
16		12	0	0	0	0	0	12	12	12
17		13	0	0	0	0	0	13	13	13
18		14	0	14	0	0	14	14	14	14

Figure C.11: Excel formula for determining if a thermocouple has passed a threshold temperature or not, for this case this threshold is 120°C

The final equation is at the top of each column (each thermocouple has a column), this formula displays the smallest value in the column, but only examines values that are larger than zero. Fig. C.12 shows this formula in place at the top of one of the columns. This set of formulas then gives you the first time that each thermocouple crosses the temperature threshold. The result is an array of zeros, with an advancing line of times corresponding to when each thermocouple crosses the threshold temperature. Fig. C.13 shows this array of zero and non-zero values, with zeros shaded as blue, showing a visual representation of the thermal wave progressing with time.

	A	B	C	D	E	F	G	H	I
1		Outer_0	Outer_1	Outer_2	Outer_3	Outer_4	Outer_5	Outer_6	Outer_7
2		-6.5	-6	-5.5	-5	-4.5	-4	-3.5	
3	Time (min)		+1)	15	15	14	14	11	
4		0	0	0	0	0	0	0	0
5	1	0	0	0	0	0	0	0	0
6	2	0	0	0	0	0	0	0	0
7	3	0	0	0	0	0	0	0	0
8	4	0	0	0	0	0	0	0	0
9	5	0	0	0	0	0	0	0	0
10	6	0	0	0	0	0	0	0	0

Figure C.12: Excel formula used for determining the first time at which the thermocouple crosses the threshold temperature.

	Outer_0	Outer_1	Outer_2	Outer_3	Outer_4	Outer_5	Outer_6	Outer_7	Outer_8	Outer_9	Outer_10	Outer_11	Outer_12	Outer_13	Outer_14	Outer_15
Time (min)	-6.5	-6	-5.5	-5	-4.5	-4	-3.5	-3	-2.5	-2	-1.5	-1	-0.5	0	3	3
0	0	0	0	0	0	0	0	0	0	0	0	0	0	0	0	0
1	0	0	0	0	0	0	0	0	0	0	0	0	0	0	0	0
2	0	0	0	0	0	0	0	0	0	0	0	0	0	0	0	0
3	0	0	0	0	0	0	0	0	0	0	0	0	0	0	3	3
4	0	0	0	0	0	0	0	0	0	0	0	0	4	4	4	4
5	0	0	0	0	0	0	0	0	0	0	0	0	5	5	5	5
6	0	0	0	0	0	0	0	0	0	0	0	0	6	6	6	6
7	0	0	0	0	0	0	0	0	0	0	0	7	7	7	7	7
8	0	0	0	0	0	0	0	0	0	0	0	8	8	8	8	8
9	0	0	0	0	0	0	0	0	0	9	9	9	9	9	9	9
10	0	0	0	0	0	0	0	0	10	10	10	10	10	10	10	10
11	0	0	0	0	0	0	0	11	11	11	11	11	11	11	11	11
12	0	0	0	0	0	0	12	12	12	12	12	12	12	12	12	12
13	0	0	0	0	0	13	13	13	13	13	13	13	13	13	13	13
14	0	14	14	14	14	14	14	14	14	14	14	14	14	14	14	14
15	0	15	15	15	15	15	15	15	15	15	15	15	15	15	15	15
16	0	16	16	16	16	16	16	16	16	16	16	16	16	16	16	16

Figure C.13: Thermal penetration analysis, increasing time to threshold temperature with increasing TC depth.